ALMA MATER STUDIORUM
UNIVERSITÀ DI BOLOGNA

DOTTORATO DI RICERCA IN

FISICA

Ciclo 37

Settore Concorsuale: 02/A1 - FISICA SPERIMENTALE DELLE INTERAZIONI FONDAMENTALI

Settore Scientifico Disciplinare: FIS/01 - FISICA SPERIMENTALE

THE KM3NET EXPERIMENT: METHODS FOR TIME, POSITION AND POINTING CALIBRATION OF THE DETECTOR.

Presentata da: Francesco Benfenati Gualandi

Coordinatore Dottorato

Alessandro Gabrielli

Supervisore

Annarita Margiotta

Co-supervisore

Maurizio Spurio

Esame finale anno 2025

Contents

Abstract

Neutrino astronomy is an emerging field in astroparticle physics, focused on measuring astrophysical neutrino fluxes and identifying their sources to better understand cosmic ray origins and acceleration mechanisms. Neutrinos, due to their lack of electric charge and since they interact solely via the Weak interaction, can travel vast distances across the Universe without being absorbed or deflected by magnetic fields, making them ideal probes of high-energy astrophysical phenomena. Their detection is achieved by neutrino telescopes, placed deep underwater or under ice. Since the early precursors, started in the 1970s, significant progresses have been made and the second generation of detectors is now being deployed.

The development of this thesis has been carried out within the KM3NeT experiment, which consists in two underwater detectors, KM3NeT/ARCA and KM3NeT/ORCA, under installation and taking data in the depths of the Mediterranean Sea. Recently, the KM3NeT Collaboration has announced the detection with KM3NeT/ARCA of KM3-230213A, the most energetic cosmic neutrino observed so far, demonstrating the capabilities of the detector even in a partial configuration. At completion, the two detectors are going to reach an overall volume greater than $1\,\mathrm{km}^3$ of sea water instrumented with thousands of optical sensors arranged in vertical strings. To reach the desired performances in terms of angular resolution on the reconstructed direction of neutrinos, the calibration of the detector plays a crucial role. The key parameters to optimize in order to improve the angular resolution are the time synchronization of the optical sensors and the precise determination of their position. Moreover, the correct pointing of the detector and the evaluation of its accuracy is pivotal in order to search for point-like neutrino sources.

After an introduction on neutrino astronomy in Chapter 1, updated with the most recent results in the field, and a description of the KM3NeT neutrino telescope in Chapter 2, the time synchronization of KM3NeT detectors at the current stage (March 2025) is described in Chapter 3. In October 2024, the KM3NeT/ARCA detector has completed its first development stage, Phase 1, with KM3NeT/ORCA following in 2025. The second stage, Phase 2, involves a re-design of the networking and of the time synchronization of the optical elements, with a change of paradigm. KM3NeT/ARCA has started the data taking of Phase 2 early in 2025, after the deployment of the first strings with the updated design that occurred on October 2024.

In Chapter 4, the time synchronization of the optical modules for Phase 2 is described, and the proposed strategy for the time calibration is discussed. In addition, the first results from the time calibration of the optical modules from strings of the Phase 2 design are presented.

In Chapter 5, the KM3NeT/ARCA Calibration Unit is illustrated: this is a dedicated

string, hosting oceanographic instrumentation, whose goal is the characterization of the water properties along the column water of the detector. By measuring the sound velocity in water and the sea current velocity, it will help improving the position calibration of the optical sensors, which is based on an acoustic positioning system. The Calibration Unit of KM3NeT/ARCA has been partially deployed in October 2024.

Finally, in Chapter 6, the analysis of the Moon shadow performed with data acquired with the KM3NeT/ARCA detector composed of 19 and 21 string is presented. The analysis exploits the deficit in the atmospheric muon flux in the direction of the Moon caused by the blockage of primary cosmic rays from the Moon, and aims at studying the detector pointing accuracy, evaluating a possible shift of the measured direction of the Moon with respect to the expected one. The analysis has been used as a cross check to verify the pointing of the detector and thus to assign the correct coordinates of the KM3-230213A neutrino event.

Sommario

L'astronomia dei neutrini è una branca emergente della fisica delle astroparticelle, focalizzata sulla misurazione e lo studio dei flussi di neutrini di origine astrofisica e sull'identificazione delle loro sorgenti, ai fini di comprendere meglio l'origine dei raggi cosmici e i meccanismi della loro accelerazione. I neutrini, grazie alla loro neutralità di carica elettrica e al fatto che interagiscono solo tramite l'interazione Debole, possono percorrere enormi distanze attraverso l'Universo senza essere assorbiti o deviati dai campi magnetici, costituendo quindi uno strumento ideale per studiare fenomeni astrofisici ad alta energia. La loro rilevazione è effettuata tramite telescopi per neutrini, rivelatori posti in profondità sott'acqua o sotto il ghiaccio. Dall'avvento dei primi esemplari di telescopi di neutrini, negli anni '70, sono stati compiuti progressi significativi ed è ora in fase di installazione la seconda generazione di rivelatori.

Lo sviluppo di questa tesi è stato condotto nell'ambito dell'esperimento KM3NeT, che consiste in due rivelatori sottomarini, KM3NeT/ARCA e KM3NeT/ORCA, attualmente in installazione e presa dati sul fondale del Mar Mediterraneo. Recentemente, la collaborazione KM3NeT ha annunciato la rivelazione con KM3NeT/ARCA di KM3-230213A, un neutrino cosmico con l'energia più elevata mai osservata finora, dimotrando le potenzialità del rivelatore anche in una configurazione parziale. Al loro completamento, i due rivelatori raggiungeranno complessivamente un volume strumentato superiore a 1 km^3 d'acqua, con migliaia di sensori ottici disposti lungo stringhe verticali. Per raggiungere le prestazioni desiderate in termini di risoluzione angolare nella ricostruzione della direzione dei neutrini osservati, la calibrazione del rivelatore svolge un ruolo cruciale. I parametri chiave da ottimizzare per migliorare la risoluzione angolare sono la sincronizzazione temporale dei sensori ottici e la determinazione della loro posizione. Inoltre, il corretto puntamento del rivelatore e la valutazione della sua precisione sono fondamentali ai fini della ricerca di sorgenti puntiformi di neutrini.

Dopo un'introduzione all'astronomia dei neutrini nel Capitolo 1, aggiornata con i risultati più recenti nel campo, e una descrizione del telescopio per neutrini KM3NeT nel Capitolo 2, viene descritta la sincronizzazione temporale dei rivelatori di KM3NeT allo stato attuale (Marzo 2025) nel Capitolo 3. A Ottobre 2024, il rivelatore KM3NeT/ARCA ha completato la sua prima fase di sviluppo, Fase 1, mentre KM3NeT/ORCA la completerà l'anno successivo. La seconda fase, Fase 2, prevede una riprogettazione della rete e della sincronizzazione temporale degli elementi ottici secondo un nuovo, differente, paradigma. KM3NeT/ARCA ha iniziato la raccolta dati della Fase 2 all'inizio del 2025, dopo l'installazione delle prime stringhe di nuovo design avvenuta nell'Ottobre precedente.

Nel Capitolo 4 viene descritta la sincronizzazione temporale dei moduli ottici per la Fase 2, e viene discussa la strategia proposta per la loro calibrazione temporale. Vengono

inoltre presentati i primi risultati della calibrazione temporale dei moduli ottici delle stringhe di nuovo design.

Nel Capitolo 5 viene illustrata la Calibration Unit di KM3NeT/ARCA, una stringa dedicata ad ospitare strumentazione oceanografica e il cui obiettivo è la caratterizzazione delle proprietà dell'acqua lungo la colonna d'acqua del rivelatore. Misurando la velocità del suono nell'acqua e la velocità della corrente marina, la Calibration Unit contribuirà a migliorare la calibrazione della posizione dei sensori ottici, basata su un sistema di posizionamento acustico. La Calibration Unit di KM3NeT/ARCA è stata parzialmente installata nell'Ottobre 2024.

Infine, nel Capitolo 6 viene presentata l'analisi dell'ombra della Luna eseguita con i dati acquisiti dal rivelatore KM3NeT/ARCA composto da 19 e 21 stringhe. L'analisi è basata sullo studio del deficit nel flusso di muoni atmosferici nella direzione della Luna causato dal blocco dei raggi cosmici primari da parte della Luna, e mira a determinare la precisione del puntamento del rivelatore, valutando un possibile spostamento della direzione misurata della Luna rispetto a quella attesa.

Chapter 1

Neutrino astronomy

Neutrino astronomy, along with Gravitational Waves observation, represents the most recent and promising branch of Multi-messenger Astrophysics. It aims at the detection of neutrinos emitted from astrophysical sources in order to investigate the nature of those object and study the origin and acceleration mechanisms of cosmic rays (CRs).

In the last decades, significant progresses have been made in the study of CRs thanks to the advent of the first generation of γ-ray detectors in space and on Earth that measured the high-energy (100 GeV - 100 TeV) and ultra-high-energy ($>$ 100 TeV) range of the spectrum. The production of these γ-rays is expected to occur in the acceleration mechanisms of charged CRs (electrons, protons, and heavy nuclei with $Z \geq 2$) and in their propagation, and unlike charged CRs their trajectories are not deflected and scrambled by the Galactic or intergalactic magnetic fields. Thus, the measurement of γ-rays direction allows one to trace back the production source. This has represented a breakthrough in the comprehension of CRs, and since the first results of γ-ray measurements several classes of Galactic and extra-galactic CR accelerators and sources have been discovered.

Despite this, questions remain unanswered for which we cannot rely exclusively on γ-rays. As a matter of fact, γ-rays can be produced both in electromagnetic and hadronic processes. The former include synchrotron radiation emission from relativistic electrons and inverse Compton scattering, while the latter include decays of π^0 produced in pp or processes or in photoproduction processes. In addition, high-energy photons with energy larger than several TeV can interact with the infrared background radiation and the cosmic microwave background radiation in the Universe producing a e^+e^- pair, and they can also be partially absorbed by interstellar dust.

On the other hand, neutrinos are produced only in hadronic mechanisms, in the decay of $\pi^\pm, K^\pm$ resulting from hadronic interactions. Moreover, being neutral-charged particles, neutrinos trajectories just like photons ones are not deflected by magnetic fields. Hence, their detection is the smoking gun of the presence of hadronic processes in the source.

In this chapter a short review of the experimental status of high-energy astroparticle physics and its theoretical underpinnings is shown, with particular focus on neutrino properties and neutrino astronomy.

1.1 Neutrinos

As a desperate attempt to solve the puzzle of the apparent non-conservation of energy in the β-decay process, in a famous letter [1] W. Pauli firstly hypothesized in 1930 the existence of a neutral particle with extremely low mass. This idea was afterward carried over in the following years by Enrico Fermi who developed his theory of the beta decay in analogy with electrodynamics. The theory, which explained the continuous energy spectrum of the emitted electron in the β-decay as the result of the emission from the nucleus of a *neutrino* (as he named the new particle), together with the electron, also foresaw the existence of the neutrino antiparticle counterpart: the antineutrino. Several years later, the existence of electron neutrinos was experimentally confirmed by Reines and Cowan in 1956, in an experiment [2] which exploited the inverse β-decay process originating from electron antineutrinos emanating from a nuclear reactor.

After the discovery of new leptons, the muon and the tau, the existence of a different neutrino flavor for each lepton was postulated; their discoveries were experimentally confirmed only in 1962 [3] and in 2000 [4], respectively, strengthening the validity of the Standard Model (SM) of particle physics. In the SM framework, neutrinos are massless elementary particles with spin 1/2, no electric charge, no color charge and with three different flavors: ν, ν_μ, ν_τ, grouped in three families with their corresponding charged leptons (e,μ,τ).

However, the observation of the *neutrino oscillation* phenomenon contradicted the SM by requiring the postulation of a non-zero mass for the neutrino. This quest for the absolute values of neutrino masses and their hierarchy breach represents the most promising bridge towards new physics beyond the Standard Model.

1.1.1 Neutrino interaction

In the Standard Model neutrino interactions are described by the interaction electroweak Lagrangian that describes the coupling of the leptons with the gauge bosons. For neutrinos this can be separated into the charged-current Lagrangian $\mathscr{L}_{I,L}^{(CC)}$ and the weak neutral-current Lagrangian $\mathscr{L}_{I,\nu}^{(NC)}$ [5]:

$$\mathscr{L} = \mathscr{L}_{I,L}^{(CC)} + \mathscr{L}_{I,\nu}^{(NC)} \tag{1.1a}$$

$$\mathscr{L}_{I,L}^{(CC)} = -\frac{g}{2\sqrt{2}}\left(j_{W,L}^{\rho}\, W_\rho + j_{W,L}^{\rho\,\dagger}\, W_\rho^\dagger\right) \tag{1.1b}$$

$$\mathscr{L}_{I,\nu}^{(NC)} = -\frac{g}{2\cos\theta_W} j_{Z,\nu}^{\rho}\, Z_\rho \tag{1.1c}$$

In Eqs. 1.1b, 1.1c W_ρ and Z_ρ are the gauge boson fields, g is the coupling constant of the weak interaction, θ_W is the Weinberg angle, $j_{W,L}^{\rho}$ and $j_{Z,\nu}^{\rho}$ are the leptonic charged-current and the neutrino part of the leptonic neutral-current, respectively:

$$j_{W,L}^{\rho} = 2 \sum_{\alpha\,=\,e,\mu,\tau} \overline{\nu_{\alpha L}}\, \gamma^\rho\, \ell_{\alpha L} \tag{1.2a}$$

$$j_{Z,\nu}^{\rho} = \sum_{\alpha\,=\,e,\mu,\tau} \overline{\nu_{\alpha L}}\, \gamma^\rho\, \nu_{\alpha L}$$

(1.2b)

In eqs. 1.2a,1.2 ν_α are the spinorial fields of neutrinos and ℓ_α the spinorial fields of charged leptons, and the subscript L stands for the application of the left-handed projector $\frac{(1-\gamma^5)}{2}$. It is thus evident that only the left-handed chiral component of neutrino fields takes part in the interactions, i. e. left-handed chiral neutrinos and right-handed chiral antineutrinos, as a result of the weak interaction parity violation which was firstly discovered in 1956 by Chien-Shiung Wu in her experiment with the ^{60}Co β-decay [6].

Neutrino-nucleon interactions

At the relevant energy range for neutrino astronomy, i.e.,the high-energy range ($>$ 100 GeV), neutrino-nucleon interactions dominate over neutrino interactions with orbital electrons (with exception of the Glashow resonance, see 1.1.1). Depending on the neutrino energy, different processes are possible: here, only the relevant ones for energies larger than 0.1 GeV are summarized. The cross-sections of these processes are shown in Fig.1.1. At energies below 1 GeV, the dominant process is the *quasi-elastic* scattering (QE) in which the neutrino elastically scatters off the nucleon ejecting one or multiple nucleons from the target. At energies larger than few GeV the *resonance production* (RES) cross-section overcomes the QE one: in this case the incoming neutrino can excite the target nucleon to a resonance state. Above 100 GeV, the most significant process is the *deep-inelastic* scattering (DIS): the neutrino energy is high enough to scatter off the partons that make up the nuclueon and the final-state parton promptly hadronizes into hadrons.

Let us consider the DIS interactions, represented in the diagram of Fig.1.2:

$$\nu_\ell + N \to \ell^- + X \quad (CC) \tag{1.3a}$$

$$\bar{\nu}_\ell + N \to \ell^+ + X \quad (CC) \tag{1.3b}$$

$$\nu_\ell + N \to \nu_\ell + X \quad (NC) \tag{1.4}$$

where $N = p, n$, $\ell = e, \mu, \tau$ and X denotes any set of final hadrons.

In charged-current (CC) DIS, mediated by a charged W boson (Eqs.1.3a,1.3b), the final state contains in addition a charged lepton of the same flavor as the incoming neutrino. In neutral-current (NC) DIS, mediated by a neutral Z^0 boson (Eq.1.4), the final state contains instead a neutrino. Anti-neutrinos undergo the same DIS interactions, charge-conjugated.

Let us consider the CC DIS process in 1.3a. The transferred four-momentum q is:

$$q \equiv p_\nu - p_\ell = p_X - p_N = (q_0, \mathbf{q}) \tag{1.5}$$

where p_ν, p_ℓ, p_N, p_X denote the four-momenta of the neutrino, the lepton, the target nucleon and the hadron state, respectively. The process is described by the following Lorentz-invariant variables:

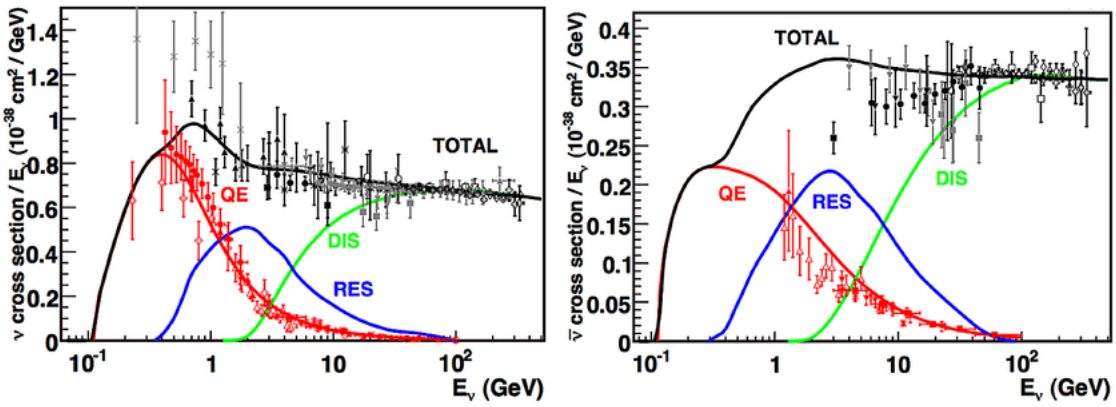

Figure 1.1: CC Neutrino-nucleon (left) and antineutrino-nucleon (right) cross-sections divided by neutrino energy, as a function of energy. The plot shows the total cross-sections (black lines) and the various contributing processes: quasi-elastic scattering (QE, red line), resonance production (RES, blue line), deep-inelastic scattering (DIS, green line). For prediction evaluation and plotted data refer to [7], whence the picture is taken.

$$s = (p_\nu + p_N)^2 \tag{1.6}$$

$$Q^2 \equiv -q^2 = 2p_\nu \cdot p_\ell \tag{1.7}$$

$$x \equiv \frac{Q^2}{2p_N \cdot q} \tag{1.8}$$

$$y = \frac{p_N \cdot q}{p_N \cdot p_\nu} \tag{1.9}$$

where s is the squared center-of-mass energy, x is the *Bjorken scaling variable* and y is the *inelasticity*. In the laboratory frame, assuming $E_\nu \gg m_N$, the inelasticity becomes:

$$y = \frac{q_0}{E_\nu} = \frac{E_\nu - E_\ell}{E_\nu} \tag{1.10}$$

where E_ν, E_ℓ are the neutrino and lepton energy: y is the fraction of energy transferred from the neutrino to the nucleon.

The differential cross-section can be expressed using variables in Eqs.1.7,1.8,1.9 ([8],[9]):

$$\frac{d^2\sigma_{CC}^{\nu,\bar{\nu}}}{dxdy} = \frac{G_F^2 m_N E_\nu}{\pi}\left(\frac{m_W^2}{Q^2+m_W^2}\right)^2\Big[(F_2(x) \mp xF_3(x))(1-y)^2 + (F_2(x) \pm xF_3(x))\Big] \tag{1.11}$$

where plus and minus signs refer to ν_l and $\bar{\nu}_l$ scattering, m_W is the $W^\pm$ boson mass and $F_i(x)$ are the *Bjorken structure functions*:

$$F_2(x) = 2\sum\left[x \cdot q(x) + x \cdot \bar{q}(x)\right] \tag{1.12a}$$

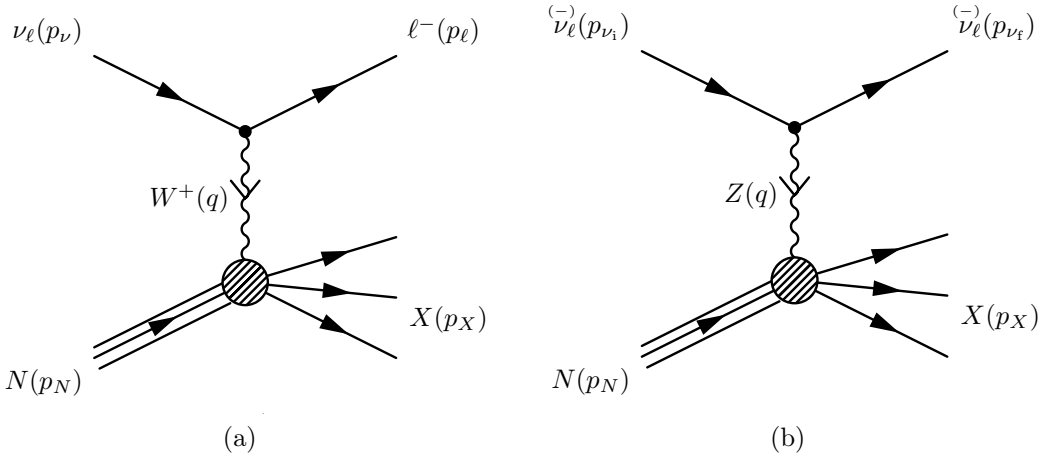

Figure 1.2: Feynman diagrams with four-momenta of the CC DIS process (left) and NC DIS process (right). Picture taken from [5].

$$x \cdot F_3(x) = 2 \sum [x \cdot q(x) - x \cdot \bar{q}(x)] \tag{1.12b}$$

In Eqs.1.12, $q(x)$ and $\bar{q}(x)$ are the quark and antiquark density distributions inside the nucleon.

For the NC DIS process, a similar computation after the substitution of the W-boson with the Z-boson leads to:

$$\frac{d^2\sigma_{NC}^{\nu,\bar{\nu}}}{dxdy} = \frac{G_F^2 m_N E_\nu}{\pi} \left(\frac{m_Z^2}{Q^2 + m_Z^2} \right)^2 \Big[(F_2(x) \mp xF_3(x))(1-y)^2 + (F_2(x) \pm xF_3(x)) \Big] \tag{1.13}$$

Integrating as in [8] Eq.1.11 and Eq.1.13 one obtains the total cross sections and finds the results that:

$$\frac{\sigma_{CC}^{\nu/\bar{\nu}}}{\sigma_{CC}^{\nu/\bar{\nu}} + \sigma_{NC}^{\nu/\bar{\nu}}} \approx 0.7 \tag{1.14}$$

i.e.,about the 70% of all neutrino-nucleon DIS scatterings are charged-current ones and that:

$$\sigma_{CC}^{\nu} / \sigma_{CC}^{\bar{\nu}} \simeq 2 \tag{1.15}$$

i. e. the probability for a high-energy antineutrino of interacting with matter is half the probability for a neutrino.

Assuming a small transferred four-momentum compared to the W-boson's mass, in the laboratory frame we have:

$$\sigma_{CC}^{0} \simeq \frac{G_F^2}{\pi} m_N E_\nu \tag{1.16}$$

which shows the linear dependence of the cross section on the neutrino energy E_ν. For larger transferred four-momentum cross-sections must take into account also the vector boson mass: for details of calculations with different parton distributions see [10]. The

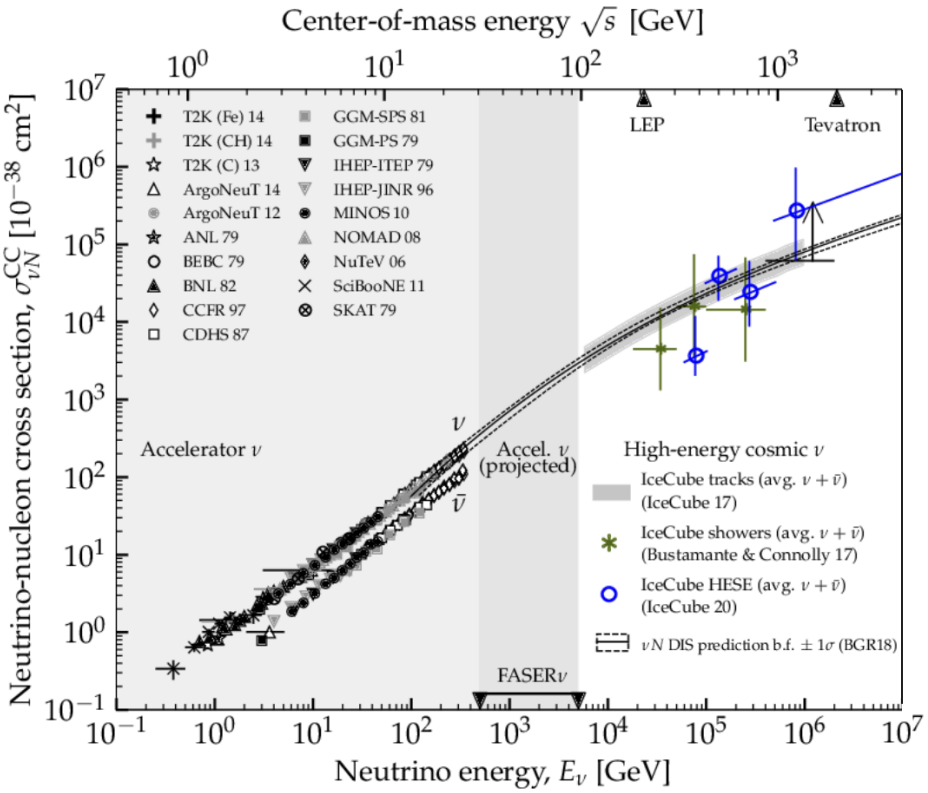

Figure 1.3: Neutrino-nucleon cross section measurements, compared to deep-inelastic scattering (DIS) cross section predictions. Values in the TeV-PeV range are based on IceCube measurements. Picture adapted from [11].

neutrino-nucleon cross section for DIS process is shown in Fig. 1.3, including predictions at the highest energy range.

Neutrino-electron interaction

Beside the charged and neutral current DIS with nucleons, another kind of interaction takes relevance for high-energy neutrinos: the interaction with electrons mediated by the W and Z bosons. The neutrino-electron cross section is in most cases smaller than the neutrino-nucleon one by orders of magnitude.

As one can see from Fig. 1.4, the neutrino-electron scattering cross sections for high-energy neutrinos is orders of magnitude smaller than the neutrino-nucleon cross section; nevertheless, this interaction becomes relevant for $\bar{\nu}_e$ scattering with atomic electrons when the center-of-mass energy approaches the W-boson mass. At this resonant energy, in the interaction $\bar{\nu}_e + e^- \to W^-$ a W^- boson can be produced, with the cross section reaching a maximum of $\sigma^{GR}_{\bar{\nu}_e e^-} \simeq 4.86 \times 10^{-31}$ cm^2 when the antineutrino energy is (electron assumed at rest)

$$E_{\bar{\nu}} = \frac{m_W^2 - m_e^2}{2m_e} \simeq 6.3\,\text{PeV} \tag{1.17}$$

as shown in Fig. 1.4. This process, known as the *Glashow resonance* [13], was hypothesized in 1959 by S. L. Glashow and due to the difficulties of detecting neutrinos of such

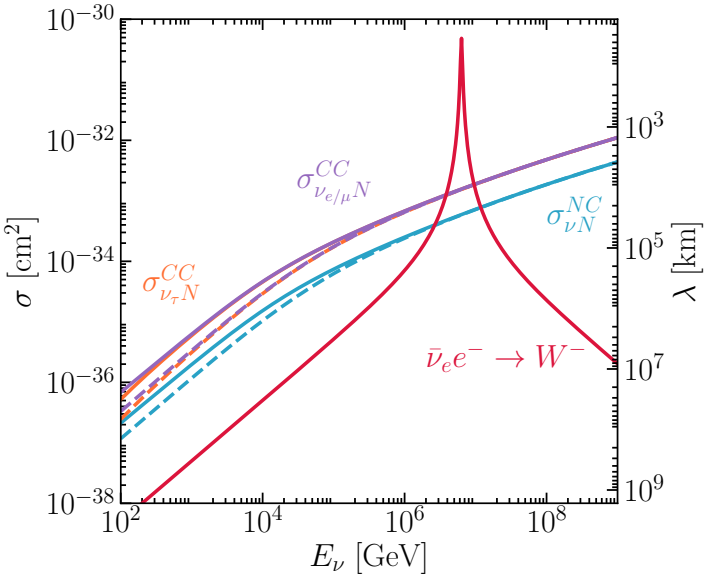

Figure 1.4: Neutrino scattering cross sections for different processes as a function of energy. The blue curves indicate neutral-current DIS processes for all neutrino flavors, while the purple and orange curves indicate the charged-current DIS processes for ν_e/ν_μ and ν_τ respectively. Solid curves refer to neutrinos and dashed ones to antineutrinos. The red curve instead refers to the Glashow resonance. The y-axis on the right represents the water equivalent mean free path of these interactions. Picture taken from [12].

high energies, it has been observed only very recently. In 2021 the IceCube collaboration reported [14] the detection of a shower event consistent with being created at the Glashow resonance. The measured event energy was 6.05 ± 0.72 PeV and the inferred neutrino energy, taking into account the non-visible part of the shower, was about 6.3 PeV. Given its energy and direction, it was classified as an astrophysical neutrino at the 5σ level.

1.1.2 Neutrino oscillations

According to the Standard Model, neutrinos are massless particles. Nevertheless, we know nowadays that the neutrinos must have a non-zero mass in order to explain neutrino oscillations. This phenomenon refers to the flavor changing of neutrinos in their propagation in vacuum or in a medium, based on the non-coincidence between neutrino flavor eigenstates and mass eigenstates, like it is for quarks. Indeed, the first hints of neutrino oscillations came in the '70s from solar neutrinos observed by the Homestake experiment. The discovery of neutrino oscillations occurred in 1998 from the SuperKamiokande observations using atmospheric neutrinos [15]. Oscillations in solar neutrinos had the definitive proof in 2002 with the Sudbury Neutrino Observatory (SNO) [16]. The flavor eigenstates ν_e, ν_μ, ν_τ must be then the mixture of *at least* three different mass eigenstates ν_1, ν_2, ν_3. The hypothesis of neutrino mixing was first anticipated by Bruno Pontecorvo in 1957 [17], though in terms of ν-$\bar{\nu}$ oscillations, and took further by Maki, Nakagawa and Sakata [18] on the basis of a two-neutrino hypothesis, then generalized to three neutrino families.

Three-neutrino families formalism

A neutrino mass term must be introduced accordingly in the Standard Model lagrangian, implying the violation of the conservation of the flavor lepton numbers L_e, L_μ, L_τ. Neutrino flavor eigenstates $|\nu_\alpha\rangle$ ($\alpha = e, \mu, \tau$) can be expressed as combinations of mass eigenstates $|\nu_i\rangle$ ($i = 1, 2, 3$) (and vice-versa) as:

$$|\nu_\alpha\rangle = \sum_i U^*_{\alpha i}|\nu_i\rangle\,, \quad |\nu_i\rangle = \sum_i U_{\alpha i}|\nu_\alpha \tag{1.18}$$

where:

$$\langle\nu_i|\nu_j\rangle = \delta_{ij} \tag{1.19}$$

and $U_{\alpha i}$ is the unitary 3×3 Pontecorvo-Maki-Nakagawa-Sakata (PMNS) mixing matrix:

$$U = \begin{pmatrix} U_{e1} & U_{e2} & U_{e3} \\ U_{\mu 1} & U_{\mu 2} & U_{\mu 3} \\ U_{\tau 1} & U_{\tau 2} & U_{\tau 3} \end{pmatrix} \tag{1.20}$$

The PMNS matrix can be parametrized by 3 mixing angles θ_{ij} and 1 complex CP-violating phase δ as follows:

$$U = \begin{pmatrix} 1 & 0 & 0 \\ 0 & c_{23} & s_{23} \\ 0 & -s_{23} & c_{23} \end{pmatrix} \begin{pmatrix} c_{13} & 0 & e^{i\delta}s_{13} \\ 0 & 1 & 0 \\ -e^{i\delta}s_{13} & 0 & c_{13} \end{pmatrix} \begin{pmatrix} c_{12} & s_{12} & 0 \\ -s_{12} & c_{12} & 0 \\ 0 & 0 & 1 \end{pmatrix} \tag{1.21}$$

where $c_{ij} = \cos\theta_{ij}, s_{ij} = \sin\theta_{ij}$. Consider now a neutrino mass eigenstate $|\nu_j\rangle$ with energy E(GeV). The propagation in time of mass eigenstate is described by the time-dependent Schrödinger equation, and since mass eigenstates are eigenstates of the Hamiltonian $\mathcal{H}$ with eigenvalue E one has:

$$i\frac{\partial}{\partial t}|\nu_j(t)\rangle = \mathcal{H}|\nu_j(t)\rangle = E|\nu_j(t)\rangle \tag{1.22}$$

The stationary state solution of Eq. 1.22 is

$$|\nu_j(t)\rangle = e^{-iEt}|\nu_j(0)\rangle \tag{1.23}$$

which due to the low-mass approximation becomes [5]:

$$|\nu_j(t)\rangle = e^{-ipt - im_j^2 L/2E}|\nu_j\rangle \tag{1.24}$$

where $t = L$ in natural units, replacing the propagation time with the distance between the source point and the detection point, and $|\nu_j(0)\rangle = |\nu_j\rangle$. Then, considering relationships in Eq. 1.18, the amplitude for the transition from a flavor state α to a flavor state β after a time t is:

$$\langle\nu_\beta|\nu_\alpha(t)\rangle = e^{-ipt}\sum_{k=1}^{3} U^*_{\alpha k}U_{\beta k}e^{-im_k^2 L/2E} \tag{1.25}$$

Hence, the probability of a neutrino produced with flavor α and energy E of being detected at a distance L with a flavor β is [5]:

$$P_{\nu_\alpha \to \nu_\beta}(L,E) = |\langle \nu_\beta | \nu_\alpha(t) \rangle|^2 = \sum_{k,j} U^*_{\alpha k} U_{\beta k} U_{\alpha j} U^*_{\beta j} \exp\left(-i \frac{\Delta m^2_{kj} L}{2E}\right) \tag{1.26}$$

which can be rewritten also as:

$$\begin{aligned} P_{\nu_\alpha \to \nu_\beta}(L,E) &= \sum_{j=1}^{3} |U_{\alpha k}|^2 |U_{\beta k}|^2 \\ +2 \sum_{k>j} \Re(U^*_{\alpha k} U_{\beta k} U_{\alpha j} U^*_{\beta j}) \cos\left(\frac{\Delta m^2_{kj} L}{2E}\right) \\ +2 \sum_{k>j} \Im(U^*_{\alpha k} U_{\beta k} U_{\alpha j} U^*_{\beta j}) \sin\left(\frac{\Delta m^2_{kj} L}{2E}\right) \end{aligned} \tag{1.27}$$

Eq. 1.26 can be seen as separated in two terms: the amplitude of the oscillation is determined by the elements of the mixing matrix, i. e. by the parameters θ_{ij} and δ, while the phase of the oscillation depends on the ratio L/E and on the difference of the squared masses $\Delta m^2_{kj} = m^2_k - m^2_j$. Since $\Delta m^2_{31} = \Delta m^2_{32} + \Delta m^2_{21}$ there are only two independent Δm^2_{ij} if there are only three neutrino flavors. The absolute values of neutrino masses (so far only upper limits have been set) and their hierarchy still need to be determined and are nowadays the main scientific goals of several experiments like KATRIN, DUNE, JUNO, Hyper-K, KM3NeT/ORCA.

Oscillations of high energy astrophysical neutrinos

Let us now consider the effect of the oscillation on the flavor content of high-energy neutrinos produced in astrophysical events. These neutrinos can travel undisturbed over very long baselines, from the kpc of Galactic neutrinos to Gpc of extragalactic neutrinos, in a medium that can be considered as vacuum. Thus, we can neglect matter effect and consider the limit $L \to \infty$ in Eq. 1.27: the probability of mixing becomes

$$P_{\nu_\alpha \to \nu_\beta}(L \to \infty) = \sum_{i=1}^{3} |U_{\beta i}|^2 |U_{\alpha i}|^2 \tag{1.28}$$

because both the sine and the cosine which make up the exponential in Eq. 1.27 vanish as a result of averaging over the rapid oscillations for $L/E \to \infty$. The cosmic neutrino at the detector can be then expressed as a product of a matrix P and the neutrino flux at the source:

$$\begin{pmatrix} \Phi(\nu_e) \\ \Phi(\nu_{mu}) \\ \Phi(\nu_{tau}) \end{pmatrix} = P \begin{pmatrix} \Phi^0(\nu_e) \\ \Phi^0(\nu_{mu}) \\ \Phi^0(\nu_{tau}) \end{pmatrix} \tag{1.29}$$

where the probabilities in P are evaluated inserting the measured values of the mixing parameters, as in [19]:

$$\begin{pmatrix} P_{ee} & P_{e\mu} & P_{e\tau} \\ P_{e\mu} & P_{\mu\mu} & P_{\mu\tau} \\ P_{e\tau} & P_{\mu\tau} & P_{\tau\tau} \end{pmatrix} \simeq \begin{pmatrix} 0.55 & 0.25 & 0.20 \\ 0.25 & 0.37 & 0.38 \\ 0.2 & 0.38 & 0.42 \end{pmatrix} \tag{1.30}$$

Considering different possible astrophysical production environments, the most general initial flux composition of high-energy neutrinos at the sources can be written approximately as $\Phi^0(\nu_e) : \Phi^0(\nu_\mu) : \Phi^0(\nu_\tau) = 1 : n : 0$ where n is characteristic of the emitting source and the production of ν_τ is considered extremely unlikely. In the "standard" scenario, it is assumed that $n = 2$, supposing neutrinos are produced mainly by pion decay chains $\pi^+ \to \mu^+\nu_\mu \to \bar{\nu}_\mu e^+\nu_e\nu_\mu$ (and equivalently for the π^-). In this scenario, after the oscillations during propagation, the expected detected flux on Earth is obtained exploiting Eq. 1.28 and it is about $\Phi(\nu_e) : \Phi(\nu_\mu) : \Phi(\nu_\tau) = 1 : 1 : 1$, i. e., an approximately equal neutrino flux for each different flavor is expected on Earth. Inverting the P matrix, the neutrino flavor composition at the source can in principle be inferred from the one measured on Earth. Also, from the experimental observable ratio

$$R_{exp} = \frac{\Phi(\nu_\mu)}{\Phi(\nu_e) + \Phi(\nu_\tau)} \tag{1.31}$$

one can derive the flavor ratio at the source

$$n = \frac{\Phi^0(\nu_\mu)}{\Phi^0(\nu_e)} = \frac{P_{e\mu} - (P_{ee} + P_{e\tau}) \cdot R_{exp}}{(P_{e\mu} + P_{\mu\tau}) \cdot R_{exp} - P_{\mu\mu}} \tag{1.32}$$

independently of any injection model. From 1.32, the separation among different extreme scenarios $n = 0, 2, \infty$ is conceivable.

1.2 Cosmic rays

Between 1911 and 1913 Victor Hess conducted several balloon flights at different heights carrying an electroscope in order to measure the variation of the rate of ionization in the atmosphere and discovered that it increases with the distance from the ground. This led him to the conclusion that there was radiation penetrating the atmosphere from outer space. His discovery, which later awarded him the Nobel Prize in 1936, was then confirmed by Robert Millikan in 1925 who gave the name *cosmic rays* to this radiation.

Nowadays we know that cosmic rays (CRs) are an isotropic flux of high-energy and stable charged particles originating and accelerated in astrophysical environments. They are classified into *primary* and *secondary* CRs. Primary CRs are fully ionized nuclei consisting mostly in protons and alpha particles, with a smaller fraction of heavier atomic nuclei and electrons. They impinge on the upper part of the Earth atmosphere at a rate of $\sim 10.000 m^{-2} s^{-1}$ (for particles with GeV energies). Part of this radiation can interact inside their acceleration regions or in their proximity, as well as during its propagation producing high-energy secondary particles. These can be either charged or neutral like γ-rays and neutrinos, which are are stable and can arrive on Earth together with the primary charged particles. Antiparticles, mainly positrons and antiprotons, are also produced and are present in the CR flux as well. Secondary CRs are all particles produced far from the acceleration regions, in interactions occurring during the propagation of primary CRs either in space or in the Earth's atmosphere.

Primary CRs and secondary CRs produced during propagation in space and arriving at the Earth atmosphere can be directly detected by space detectors and telescopes orbiting the Earth. Since the interaction of those particles with the atmosphere generate showers of secondary particles, detectors on Earth can only infer the flux of primary CRs in an indirect way by measuring these secondary particles.

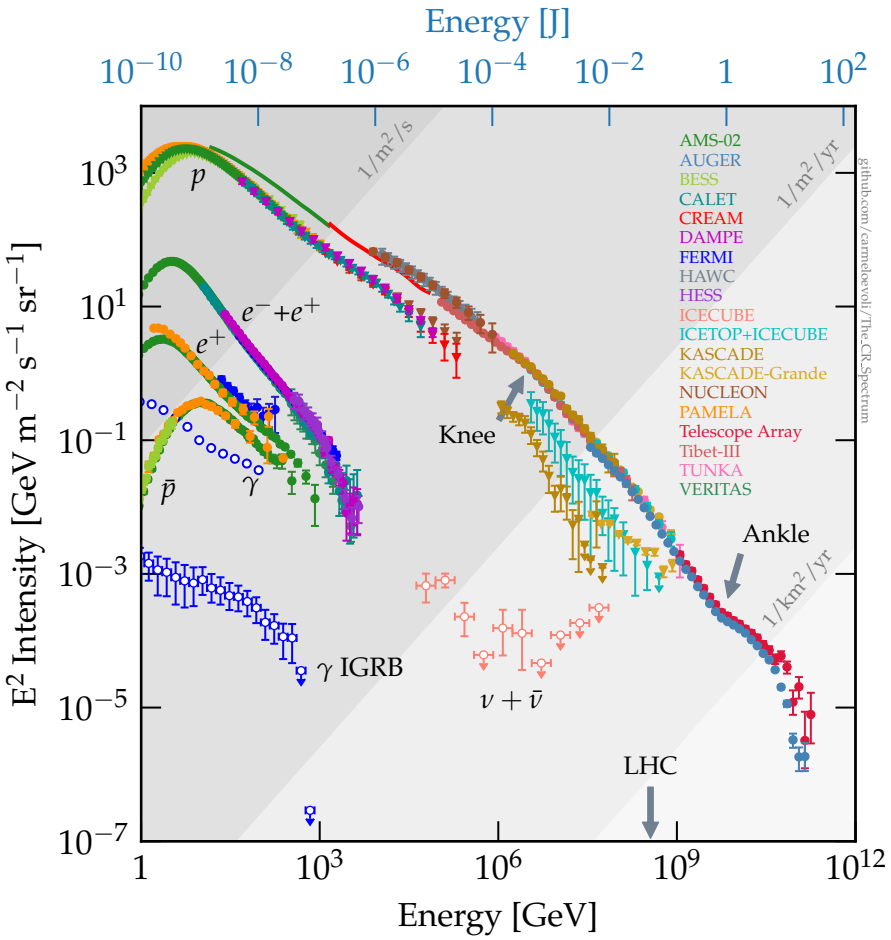

Figure 1.5: All-particle energy spectrum of cosmic rays. Data are taken from the labeled experiments. Picture taken from [21].

1.2.1 Energy spectrum

The CR energy spectrum spans many different orders of magnitudes, from 10^9 up to 10^{20} eV. The lower limit is somewhat constrained to a few GeV due to solar activity [20].

For energies larger than few GeV the spectrum is modelled by a power law of the kind:

$$\Phi(E) = KE^{-\alpha} \quad \frac{\text{particles}}{\text{cm}^2\,\text{s}\,\text{sr}\,\text{GeV}} \tag{1.33}$$

The all-particle spectrum obtained with measurements from direct and indirect experiments is shown in Fig. 1.5.

From the spectrum one can distinguish three different energy intervals above ~ 10 GeV (solar modulation affect the lower energy range, as stated before): from 10^{10} eV up to 10^{15} eV the extrapolated spectral index is $\alpha \simeq 2.7$. From 10^{16} eV to 10^{18} eV it is $\alpha \simeq 3.1$. Then, above 10^{18} eV the spectrum flattens again with $\alpha \simeq 2.6$ and it is cut off at about 10^{20} eV. The two transition regions between the different regimes, around 10^{15} eV and 10^{18} eV are called the *knee* and the *ankle*, respectively. Recent data from different space and ground experiment show that this simple framework presents additional features [22]. The three energy intervals are associated to different classes of astrophysical sources and accelerators which produce the CRs, as well as to differences in their composition and in

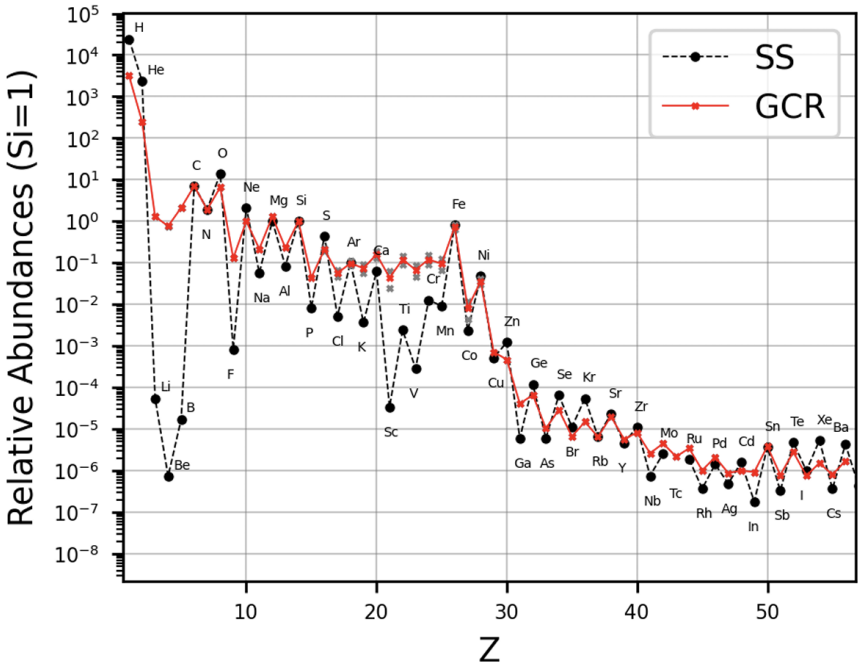

Figure 1.6: Elemental abundances of Solar system material (black dashed line) and Galactic cosmic rays (red solid line) at 2 GeV/nucleon, relative to the Silicon abundance. Picture taken from [24].

the interactions that occur during their propagation throughout the Universe.

1.2.2 Cosmic rays below the *knee*

CRs in the energy range between 10^{10} eV and 10^{15} eV dominate the energy spectrum. Their flux allows direct detection via satellite or balloon experiments. CRs below 10^{18} eV are considered of Galactic origin, due to their uniform flux along the Galactic plane. The Galactic magnetic field ($\langle B \rangle \simeq 4\,\mu$G) deflects charged particles, causing chaotic diffusion (as represented in Fig. 1.7)inside until they escape into intergalactic space, resulting in an isotropic flux from the Galactic plane. The chemical composition of Galactic CRs, studied by space-born experiments [23], show a dominance of protons ($\sim$ 85%) and Helium nuclei ($\sim$ 13%), followed by heavy nuclei ($\sim$ 1%), electrons ($\sim$ 1%) and antiparticles (less than 1%).

Comparing these abundances with solar system elements, as shown in Fig. 1.6, it can be noted that the two samples exhibit for most elements a remarkable similarity. This probably suggests that the source material for CRs has a similar chemical composition as the Solar System. Plausibly, it could be originated by the same mechanism that originated the Sun and its planets. Nevertheless, there are some elements for which the abundances show a clear difference: Li, Be, B and Sc, Ti, V, Cr, Mn are significantly more abundant in CRs. These are almost absent in stellar nucleosynthesis and result from spallation interactions of heavier nuclei (C, O, Fe) CRs with the interstellar medium during propagation. Taking into account the cross sections for such processes, one can infer the amount of matter that the CRs have traversed [19], which is about 1000 kpc;

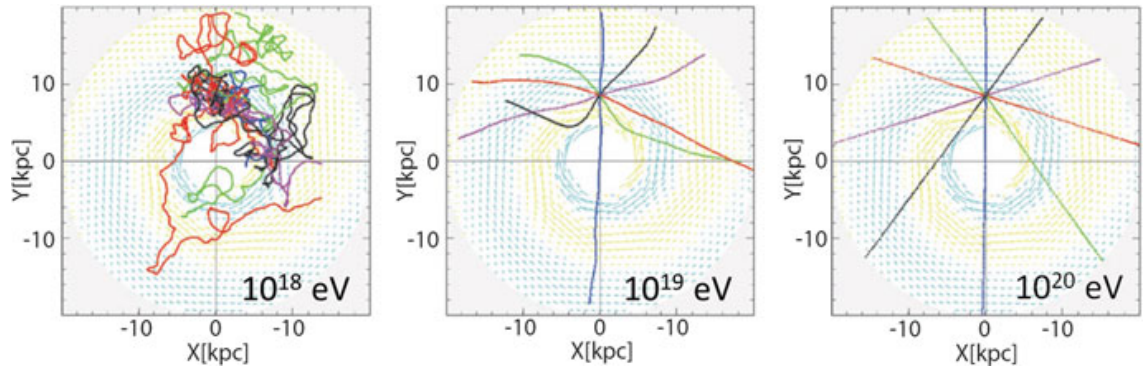

Figure 1.7: Simulated trajectory of charged CRs in the Galactic magnetic field. Trajectories of particles of energy up to 10^{18} eV are deflected by the magnetic field and undergo a chaotic motion inside the Galactic volume, whereas particles of energy of 10^{19} eV are only feebly deflected. Particles with energy of at least 10^{20} eV travel along almost straight lines, allowing the direct identification of their sources. Picture taken from [25].

this is much greater than the half-thickness of the disk of the Galaxy (0.1 kpc), indicating that CRs diffuse inside the Galaxy, in which they are confined for more than $3 \cdot 10^6$ years before escaping.

The Larmor radius $R_L = \frac{E}{ZeB}$ describes the trajectory curvature of a relativistic particle in a magnetic field. More energetic particles have less curved trajectories and shorter Galactic travel times. The the so-called *Leaky Box model* introduces an energy dependent exponentially decreasing term which must be convoluted with the emission spectrum at the astrophysical source to obtain the observed primary energy spectrum on Earth:

$$\Phi(E)|_{observed} \propto \Phi(E)|_{source} \cdot E^{-\delta} \tag{1.34}$$

Using measurements like the Boron-to-Carbon ratio, a value of $\delta \simeq 0.6$ was derived with a *leaky box* model applied to measurements of the TRACER detector and other experiments [26], leading to the source energy spectrum:

$$\Phi(E)|_{source} \propto E^{-2.1} \tag{1.35}$$

Galactic CRs are thought to be produced by Diffusive Shock Acceleration (DSA) processes (or *Fermi mechanism*) in supernova remnants, theorized by Enrico Fermi [27]. In the first-order Fermi mechanism, particles gain energy through head-on collisions with shock waves formed during supernova explosions. The shock wave propagates through the surrounding magnetized medium, where the upstream medium moves towards the shock wave and the downstream medium moves away. In the shock frame, a particle crossing the shock experiences head-on collisions, gaining energy until it is diffused away. Computations [19] show that for strong shocks as the ones occurring in supernova explosions, with this kind of mechanism an energy spectrum which follows a power law with the required spectral index ~ 2.1 to describe the Galactic CR spectrum is obtained.

In particular, type II Supernovae, are the most accredited sites for CRs acceleration below the knee. In these events, a shock wave is generated when a massive star's core,

composed of iron, collapses under gravity. The shock wave leads to a stellar explosion and to the presence of a remnant neutron star or a black hole, depending on the initial mass of the star, after the explosion. The gravitational energy is mostly released as neutrinos, with only a fraction going into photons and kinetic energy. This energy is sufficient to maintain the observed CR density, balancing the escape rate $P_{CR} \simeq 3 \times 10^{40}$erg/s; in fact, considering supernova frequency (about one every 50 years) and energy contribution (only $\sim 1 - 10\%$ of the 10^{51} erg released in kinetic energy of expanding material goes to high energy particles), the average output power of emitted CRs is of the order of $P_{SN} \sim 10^{40}$ erg/s. The maximum energy achieved in the shock wave mechanism is:

$$E^{max} \simeq 300 \cdot Z \text{ TeV} \tag{1.36}$$

Since the maximum energy depends on the electric charge of the CR, this produces different cut-offs for the different nuclei in CRs, and this would explain the knee structure. For all of these reasons and for others, supernova remnants are the most accredited sites for CRs acceleration below the knee.

1.2.3 Cosmic rays above the *knee*

In contrast to CRs below the knee, there is no general consensus on the acceleration model for CRs in the energy range between 10^{16}eV and 10^{20}eV (Ultra High Energy cosmic rays, or UHECRs). At such high energies, the Larmor radius is much larger than the Galaxy radius: if their origin would be inside our Galaxy, their arrival direction should point to their source as the trajectory is almost undeflected, as shown in Fig. 1.7. Since no UHECR excess of events is observed from the Galactic plane their origin is most probably extragalactic. In support of this hypothesis, there are some evidences from Telescope Array (TA) [28] and Pierre Auger Observatory (PAO) data [29] of large-scale anisotropies pointing away from the Galactic plane. The candidate sources must of course provide enough energy to reach the largest observed energies i. e., 10^{20} eV, and the source energy spectrum must fit the observed high energy spectrum after the propagation. One possibility to explain the high energies is that particles already accelerated in supernova remnants get re-accelerated by strong variable magnetic fields in the acceleration region. Proposed candidates which produce strong magnetic fields for this mechanism are Pulsars, Active Galactic Nuclei (AGN), Tidal Disruptive Events and Gamma-Ray Bursts (GRB).

Acceleration mechanisms above 10^{15} eV may involve the use of the Faraday's law:

$$\nabla \times \mathbf{E} = -\frac{1}{c}\frac{\partial \mathbf{B}}{\partial t} \tag{1.37}$$

allowing CRs acceleration up to the highest energy before the ankle. Despite the mechanism of this acceleration is complicate and not yet understood in detail [30], following the simple dimensional argument in [25] one can derive the maximum energy of a CR re-accelerated by a pulsar. Assuming that the region of magnetic field variation coincides with the pulsar radius R_{pulsar} (i.e., about 10 km), we can rewrite Eq. 1.37 as:

$$\frac{\mathscr{E}}{R_{NS}} = \frac{1}{c}\frac{dB}{dt} \tag{1.38}$$

and the maximum energy gained by a CR over a path length of the order of R_{pulsar} becomes:

$$E^{max} = \int Ze\mathscr{E}dx = \int Ze\frac{R_{pulsar}}{c}\frac{dB}{dt}dx = ZeR_{pulsar}B\frac{\omega_{pulsar}R_{pulsar}}{c} \tag{1.39}$$

where the typical magnetic field is $B_{pulsar} \sim 10^{12}\,\mathrm{G}$ and the angular velocity can reach values of $\omega_{pulsar} = 10^4\,\mathrm{rad/s}$. Thus, the maximum energy value becomes:

$$E^{max} \simeq 3 \times 10^{18}\,\mathrm{eV} \tag{1.40}$$

In general, a particle can no longer gain energy once it escapes the region where it is being accelerated. This condition sets an upper limit on its energy, which in SI units is given by:

$$E^{max} \leq ZeBR \tag{1.41}$$

obtained by requiring that the Larmor radius of the particle must not exceed the size of the acceleration region. This condition is known as the Hillas criterion: in order to be able to accelerate UHECRs to the limit energy of the spectrum the sources must necessarily have large enough values of magnetic field and size. In the Hillas diagram, shown in Fig.1.8, candidate sources are placed in a $B - R$ phase-space, taking into account the uncertainties on these parameters. Most astrophysical objects do not have the required $B\,R$ values to accelerate CRs to $10^{20}\,\mathrm{eV}$, leaving the best candidates for UHECR acceleration to be: neutron stars, Active Galactic Nuclei, Gamma Ray Bursts, and accretion shocks in the intergalactic medium.

1.2.4 The Greizen-Zatsepin-Kuzmin limit

During the same year of the discovery of the *Cosmic Microwave Background* (CMB), in 1966 [32] G. Zatsepin with V. Kuzmin [33] and independently K. Greisen [34] suggested that UHECRs would interact with the discovered CMB photons and that this process would have cut off the CR spectrum at an energy E_{GZK} just below $10^{20}\,\mathrm{eV}$. This limit is now known as the the Greizen-Zatsepin-Kuzmin (GZK) cut-off. According to it, no CR produced with energy larger than the cut-off could survive in the propagation from the source to us. The involved process in this flux suppression is the pion production through the Δ^+ resonance formation occurring in the interaction between UHECR protons and the CMB photons:

$$p + \gamma_{cmb} \rightarrow \Delta^+ \rightarrow \pi^+ + n \tag{1.42}$$

$$p + \gamma_{cmb} \rightarrow \Delta^+ \rightarrow \pi^0 + p \tag{1.43}$$

The neutral pion decays into two photons, while the neutron undergoes β-decay producing $p\,e^-\,\bar{\nu}_e$. Thus, in the final state a proton is present with an energy which is lower than the one of the initial proton. The proton energy threshold for this process, as shown in [19], is $E_p^{th} \simeq 7 \times 10^{19}\,\mathrm{eV}$ and protons above this threshold undergo pion production until their energy is below the threshold for the process. The result is a

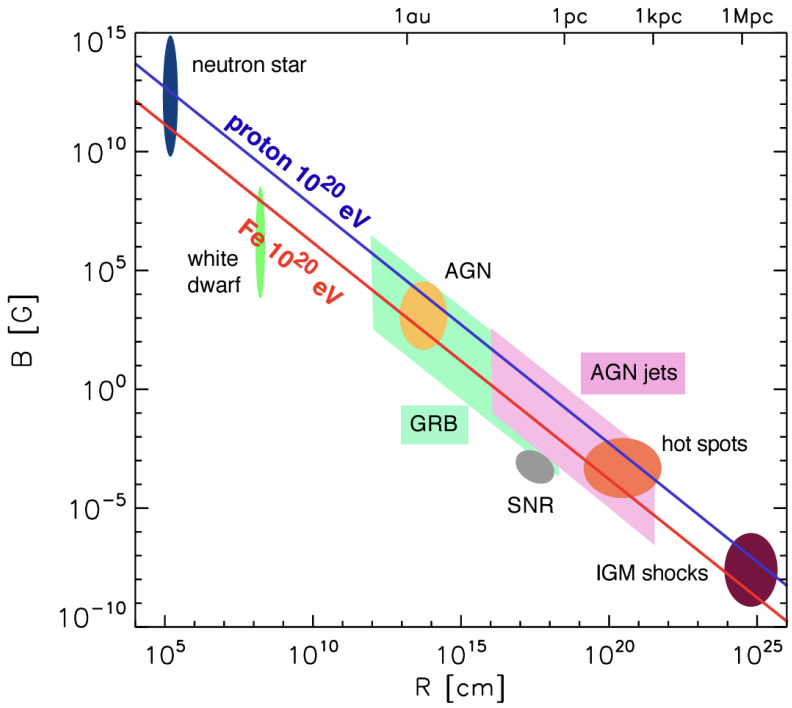

Figure 1.8: Hillas plot: sources above the blue (red) line are able to accelerate protons (iron nuclei) to a maximum energy of 10^{20} eV. Even if they are possible candidates in principle, neutron stars are discarded since we have no evidences of UHECRs emitted from Galactic neutron stars. Candidate sources are shown with the uncertainties in their parameters. Picture taken from [31].

suppression of the flux of protons above the threshold along with the production of high-energy photons and neutrinos.

Protons in the interactions in 1.42,1.43 can also be protons in heavy nuclei. In that case, the interacting proton in a nucleus with atomic number A and energy E has energy E/A, and the threshold energy therefore increases accordingly by a factor A for that nuclear species. Hence, the cut-off limits for heavy nuclei reach values of

$$E^{th}_{nuclei} \simeq E^{th}_{p}\, A. \tag{1.44}$$

CR composition at such energies would then reflect the different cut-offs for the nuclear species, with the CR atomic number increasing with energy. Unfortunately, inferring the chemical composition of UHECRs, detected by air-shower experiments, is extremely difficult as statistical shower-to-shower fluctuations prevent the precise measurement of the individual primary particle mass number which can only be deduced on a statistical basis. The latest dataset from the Pierre Auger Observatory (almost 20 years of data) [35] suggests a steepening of the mass spectrum as the energy increases. Lower uncertainties are expected in the next future, with the beginning of the upgrade [36] of the Pierre Auger experiment.

1.3 Atmospheric neutrinos

Protons in primary CRs impinging on Earth's atmosphere interact with the nucleons in nuclei of the atmosphere through the reaction:

$$p + N \rightarrow \pi^0, \pi^{\pm}, K^0, K^{\pm}, p, n, ... \tag{1.45}$$

The ellipsis indicate the production of higher mass hadrons, but most of the product particles consist in neutral and charged pions. These trigger a shower with an electromagnetic component and a hadronic one which propagates until the product particles energy is lowers than the interaction threshold.

The charged pions $\pi^{\pm}$ decay with a lifetime $\tau_{\pi^{\pm}} \simeq 2.6 \times 10^{-8}$ s through weak interactions:

$$\pi^+ \rightarrow \mu^+ \nu_\mu \tag{1.46a}$$

$$\pi^- \rightarrow \mu^- \bar{\nu}_\mu \tag{1.46b}$$

producing a muon flux. In turn, the muons can decay into:

$$\mu^+ \rightarrow e^+ \bar{\nu}_\mu \nu_e \tag{1.47a}$$

$$\mu^- \rightarrow e^- \nu_\mu \bar{\nu}_e \tag{1.47b}$$

with a lifetime $\tau_\mu \simeq 2.2 \times 10^{-6}$ s . Charged kaons $K^{\pm}$, produced in a smaller fraction in the shower, decay as in Eqs. 1.46a, 1.46b. The neutrinos flux produced in the decay of pions and kaons is called the *conventional neutrino flux*. From Eqs. 1.46a to 1.47b, the expected ratio ν_μ/ν_e is 2 but this ratio increases with energy as the muon decay length becomes larger than the length of the atmosphere; at such high energies, ν_e are mostly produced in the decays $K^0_L \rightarrow \pi + e + \nu_e$ and $K^{\pm} \rightarrow \pi^0 + e + \nu_e$.

Charmed meson produced by primary CR with sufficiently high energy also decay producing a flux of neutrino which has a harder energy spectrum and that is expected to overcome the conventional flux at energies larger than $\sim$ 100 TeV: this is known as the *prompt neutrino flux*. The reason behind it is that charmed mesons have very short lifetime of the order of $\sim 10^{-12}$ s and they decay before interacting with other particles. Thus, the produced neutrinos show an energy spectrum which is the same as the one of the parent primary CR. At lower energies, the prompt flux is too low to be measured and so far, only upper limits have ben set by the IceCube detector [37]. Instead, the conventional neutrino flux has been measured from the GeV range by experiments like Frejus and Super-Kamiokande [39] up to hundreds of TeV by the IceCube [40] and ANTARES neutrino telescopes [41]. These measurements are summarized in Fig. 1.9. The conventional neutrino flux has been calculated from numerical simulations through dedicated MonteCarlo models, based on available measurements of CR energy spectrum and composition and on hadronic interaction models for the production of charged pions and kaons in Eq. 1.45. Assuming a single power law with spectral index α for the primary CR, the expected conventional flux is:

$$\Phi_\nu(E) \propto E^{-\alpha-1} \tag{1.48}$$

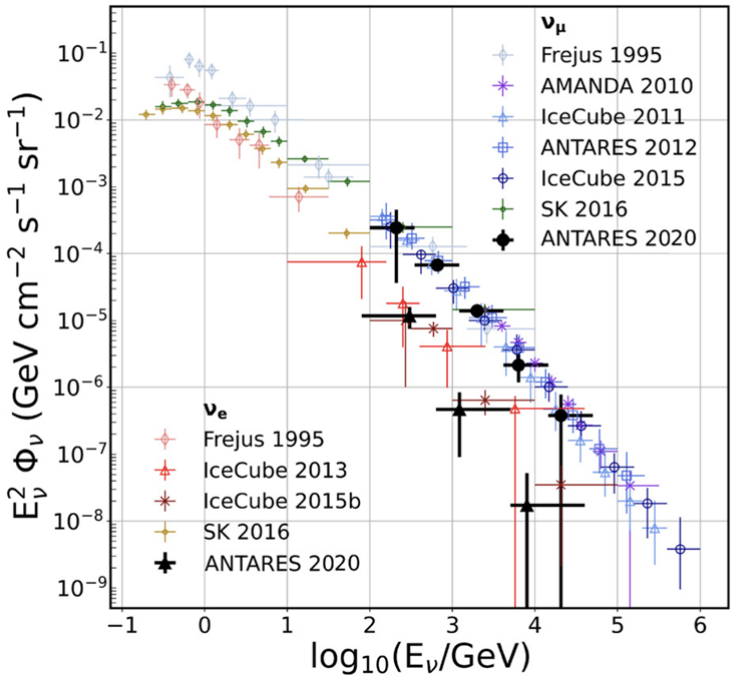

Figure 1.9: Measured energy spectra of the atmospheric ν_e ν_μ from different experiments. The vertical error bars include all statistical and systematic uncertainties. Picture taken from [38].

where $\alpha \simeq 2.7$ is the spectral index for CRs below the knee. At high energies (i. e., above the TeV) the flux of ν_e is heavily suppressed so that only ν_μ contribution can be taken into account. The experimental measurements in Fig.1.9 are in agreement with the expectation in Eq.1.48.

1.4 Astrophysical neutrinos and gamma rays

As discussed in Sec.1.2.2 we cannot rely on CR measurements for the localization of their sources since their trajectories are scrambled by the effect of the Galactic magnetic field. The solution to this problem is to exploit electrically neutral particles produced in CR interactions at the sources or nearby; photons (gamma rays) and neutrinos would not be deviated by the magnetic fields and their reconstructed direction on Earth can be traced backward to the originating point. Gamma rays can be produced in different mechanisms and at different wavelengths; their detection and multi-wavelength observation would also shed light on the nature of the source. They have much larger cross-sections than neutrinos and are therefore easier to detect; nevertheless, the drawback is that they are more likely to interact with material within or near the source or with interstellar medium during propagation and their flux could then be suppressed. Neutrinos, while being more challenging to be detected having small cross-sections, propagate without interacting along their path and they are the only particles that are unambiguous signatures of hadronic processes. Astrophysical neutrino detection primarily targets energies beyond a few tens of TeV, where the atmospheric neutrino flux diminishes and the astrophysical

flux becomes dominant.

1.4.1 Gamma rays production mechanisms

Gamma rays are produced in two different mechanisms which distinguish two different models. In the leptonic model gamma rays are produced by relativistic electrons via brehmsstrahlung radiation and via inverse-Compton scattering on low-energy photons or, most probably, via the combination of the two. In the hadronic model, protons produce gamma rays primarily via neutral pion decays $\pi^0 \to \gamma\gamma$ where each γ carries $1/2$ of the parent pion energy. Neutral pions are produced in the interaction of CRs with the gas in the interstellar medium:

$$p + p \to \pi^0, \pi^{\pm}, K^0, K^{\pm}, p, n, ... \tag{1.49}$$

with a cross-section of about $40 - 50\,\mathrm{mb}$, and in photoproduction processes, where high-energy protons interact with low-energy photons in the surroundings of the source as in Eqs. 1.42, 1.43 where now the target photons are ambient photons γ_ϵ mostly produced by electrons near the source via bremsstrahlung and have frequencies which span from the radio to the UV band:

$$p + \gamma_\epsilon \to \Delta^+ \to \pi^0 + p \tag{1.50a}$$

$$\to \pi^+ + n \tag{1.50b}$$

Even though the cross-section at resonant energy is two orders of magnitude smaller ($\sim 250\,\mu\mathrm{b}$) than the one for Eq. 1.49 for environment characterized by a high density of ambient photons the photoproduction processes can be significantly more frequent than proton-proton interactions. Energetic considerations in this section are taken from [42]. In the hadronic process 1.49 $\pi^+\,\pi^-\,\pi^0$ are produced with the same probability and the highest energy pion carries on average $1/5$ of the proton energy. In photoproduction processes instead, the probability of a π^0 being produced is $1/3$ and $2/3$ for the π^+; also in this case the π carries on average $1/5$ of the proton energy. In the hadronic model, the number of produced gamma rays is proportional to the number of produced neutral pions which in turn is proportional to the number of primary CRs; thus, the spectral index of observed γ-rays flux reflects the one of the primary CR flux:

$$\Phi_\gamma(E) \propto \Phi_{pions}(E) \propto \Phi_{CR}(E) \tag{1.51}$$

with $\alpha_{CR} \sim \alpha_\gamma$.

1.4.2 Neutrino production mechanisms

The same processes Eq. 1.49 and Eqs. 1.50a, 1.50b which lead to the production of γ-rays also produce a flux of astrophysical neutrinos via the decay of the charged pions:

$$\begin{aligned} \pi^+ &\to \mu^+\,\nu_\mu \\ &\hookrightarrow \mu^+ \to e^+\,\nu_e\,\bar{\nu}_\mu \end{aligned} \tag{1.52a}$$

$$\begin{aligned} \pi^- &\to \mu^-\,\bar{\nu}_\mu \\ &\hookrightarrow \mu^- \to e^-\,\bar{\nu}_e\,\nu_\mu \end{aligned} \tag{1.52b}$$

where after the chains each of the four produced leptons carries 1/4 of the pion energy. Thus, the astrophysical neutrino spectral index is related to the one of γ-rays and CRs: $\alpha_{CR} \sim \alpha_\nu \sim \alpha_\gamma$. However, neutrinos can only be produced in hadronic processes and their detection is a valuable handle to distinguish between hadronic and leptonic scenarios for a candidate source. Taking into account the considerations from Sec. 1.4.1 on the energies of γ-rays, pions and the parent originary proton one can derive the following relations:

$$E_\nu \sim \frac{E_\gamma}{2} \sim \frac{E_\pi}{4} \sim \frac{E_p}{20} \tag{1.53}$$

which holds both for hadronic and photoproduction processes. However, there are differences in the neutrino energy spectrum between the two production mechanisms. The photoproduction process has a defined threshold which depends on the energy of the ambient photon:

$$E_p > \frac{m_\Delta^2}{4E_\gamma} = \left(\frac{100\,\mathrm{eV}}{E_\gamma}\right) \times 4\,\mathrm{PeV} \tag{1.54}$$

The neutrino spectrum will thus reflect the energy spectrum of the ambient photons. Considering for instance a target photon in the UV band with energy $E_\gamma \sim 10\,\mathrm{eV}$, the parent proton must have a threshold energy of 40 PeV and the produced neutrino, according to Eq. 1.53, an energy of $\sim 2\,\mathrm{PeV}$. The hadronic mechanism is instead characterized by the hypothesis of limiting fragmentation, or scaling [43]. This means that the energy spectrum of the produced secondary particles scales like the one of the primary particle. Starting from a CR spectrum at the source which follows a power-law, then also the γ-ray and neutrino spectra will follow a power-law with an almost identical spectral index which, as we said, for a Fermi mechanism is:

$$\Phi_\gamma \approx \Phi_\nu \propto E_\nu^{-\alpha} \tag{1.55}$$

with $\alpha_{CR} \simeq \alpha_\gamma \simeq \alpha_\nu \sim 2$. Other differences are related to the proportions of the produced neutrinos and γ-rays. Considering that CRs are in general nuclei, hadronic processes with protons in CR nuclei can produce neutrinos while the interaction of ambient photons with nuclei will mostly lead to their photo-disintegration, reducing the secondary neutrino production. Moreover, the relative production rates of γ-rays and neutrinos ultimately depends on the ratio of the produced charged and neutral pions respectively and due to isospin conservation the branching ratio for neutral pion production is almost twice the one for the charged pions.

1.4.3 Neutrino and gamma ray astronomy

Although the fluxes of gamma rays and neutrinos are closely related to each other, and in turn to the one of primary CRs, a direct connection between them is not straightforward. In the first place, gamma rays can be produced both in hadronic and leptonic mechanisms whereas neutrinos are generated only in hadronic scenarios. Additionally, gamma rays can be absorbed both inside or near the source, if it is dense enough, and during their propagation by opaque objects along its path or in the interaction with background photons through a e^+e^- pair production mechanism:

$$\gamma + \gamma_{\mathrm{bkgr}} \rightarrow e^+ + e^- \tag{1.56}$$

The probability that a gamma ray will be absobed before reaching the Earth is:

$$P(E_\gamma) = 1 - e^{-\tau(E_\gamma)} \tag{1.57}$$

where $\tau = \sum_i \tau_i$ is the total opacity of the interstellar medium, including all i different background components (e.g. cosmic microwave background). According to [44], if we consider for example the cosmic microwave background photonsa gamma ray with energy $E_\gamma = 100\,\text{TeV}$ would be absorbed during propagation over 100 Mpc with probability $P \simeq 72\%$. But also for a Galactic distance of 8.5 kpc, a gamma ray of 1 PeV is absorbed with 60% of probability. If we take into account also the infrared background contribution, the Universe becomes opaque already at TeV energies. Thus, gamma ray absorption is very relevant for propagation over extragalactic distances but it is not negligible also for the highest energy gamma rays coming from within the galaxy. Therefore, at the highest energies the connection between extra-Galactic gamma rays and neutrinos is indirect and dedicated numerical simulations are necessary.

In other scenarios, instead, the link between the two is more evident. As an example, the supernova remnant (SNR) RX J1713.7-3946 is a study-case. If the hadronic processes occur in a SNR, comparable fluxes of gamma rays and neutrinos are expected. So far, it is not yet clear which among the hadronic, leptonic or mixed scenario best describes the source. The study of the gamma ray flux from RX J1713.7-3946, measured by HESS and Fermi LAT, thus put a constraint on the expected neutrino flux from it [45]:

$$E_\nu^2 \frac{d\Phi_\nu}{dE_\nu} \simeq 10^{-11}\,\text{TeV}\,\text{s}^{-1}\,\text{cm}^{-2} \tag{1.58}$$

The catalogue of gamma ray sources has been recently expanded after the discovery of ultra-high-energy ($E > 100\,\text{TeV}$, reaching 1.4 PeV) gamma rays by the LHAASO experiment in 2021 [46] [47] from several sources. The relevant aspect of this discovery is that at such energies the inverse Compton process is severely limited so that the only remaining production process is the π^0 decay in the hadronic scenario where the pions are produced by CRs in 1.49, which represents a strong evidence of accelerated Galactic CRs. Despite SNR being considered the best candidate for Galactic CRs, in this catalogue no SNR are present so far, while it includes massive Star Clusters and Pulsar Wind Nebulae. The discovery is of particular interest for the latters, which were previuoulsy believed to be be only leptonic accelerators but now have become candidates for CRs acceleration in hadronic processes. Neutrino detection from these source would shed light on the underlying gamma ray production processes.

1.4.4 Neutrino fluxes

Neutrino fluxes on Earth span several orders of magnitidues in energy. For what concerns neutrino astronomy, only the scales larger than the GeV (the lower limit of the atmospheric neutrino flux, as shown in Fig. 1.9) are of interest. The atmospheric neutrino flux, composed by a conventional and a prompt component, was already discussed in Sec. 1.3.

From energies larger than few tens of TeV, the astrophysical diffuse neutrino flux overcomes the atmospheric one. This is the flux primarily addressed by neutrino telescopes. In the $10^{14} - 10^{18}\,\text{eV}$ range the extra-Galactic diffuse neutrino flux is constrained

by the observed flux of UHECRs and the upper bound was derived by Waxman and Bahcall in [48]. A clear diffuse neutrino flux in this energy range has been observed by IceCube, with $E^2\Phi_\nu \approx 10^{-8}\,\mathrm{GeV\,cm^{-2}\,s^{-1}\,sr^{-1}}$. Upper limits for the flux at energies between 3 PeV and 100 EeV have been set by the IceCube collaboration [49].

At this high energy scale the dominant flux is from *cosmogenic* neutrinos, produced in the interaction 1.42 between UHECRs above the GZK threshold and CMB photons during their propagation over cosmological distances. The produced neutrinos have typically energies of 1/20 of the parent proton energy (see 1.53), whereas for nuclei this process is significantly suppressed due to nuclei photo-disintegration. Hence, a sizeable flux of cosmogenic neutrinos energies is expected only if UHECRs with energies above the cut-off are protons. Predicted fluxes have been compared to the experimental limits of IceCube and Pierre Auger [50]. Predictions are done exploiting propagation codes to study CR interaction with cosmic matter and assuming two different initial CR composition scenario: a pure proton UHECR composition and a mixed one (protons and heavy nuclei). Moreover, different cosmological evolution of UHECR sources are considered which can be also constrained by observed neutrino fluxes [51]. In the pure proton scenario, AGN-like evolution of sources results in a total neutrino flux larger than the experimental limits set by PAO and IceCube limits, while extremely low neutrino fluxes at energies $> 100\,\mathrm{PeV}$ are expected for the mixed composition scenario since nucleons of the nuclei involved in 1.42 would have less energy. In February 2025, the KM3NeT Collaboration has announced the breakthrough detection of a neutrino event with an estimated energy exceeding 100 PeV [52]. The extreme energy of the event exceeds the upper limits set by IceCube and PAO, and though the hypothesis of it being a statistical upward fluctuation cannot be discarded with extremely high confidence, it suggests a possible origin in a class of cosmic accelerators distinct from those responsible for the lower-energy astrophysical neutrinos observed so far. Alternatively, this may represent the first detection of a cosmogenic neutrino. Details of this discovery are illustrated in Sec. 1.6.

1.5 Astrophysical neutrinos detection

The IceCube detector provided the first evidences of astrophysical neutrinos by detecting an excess of high-energy neutrinos in independent samples, compared to the expected conventional atmospheric flux. The first all-sky search, done in 2013 with 2 years of livetime, was performed with events known as *High Energy Starting Events* (HESE), characterized by interaction vertices contained within the instrumented volume, with energy from 30 TeV to 1.2 PeV: 28 events were observed, with a background expectation of 10; the atmospheric origin was excluded at 4σ level [54]. The sample was later increased adding 4 years of data [55]: the hypothesis of background-only events was rejected at more than 6σ. The best fit to the data indicated a neutrino spectrum with a spectral index of approximately $\alpha_\nu \simeq 2.87$.

Another analysis has been performed by selecting charged-current upgoing ν_μ events, utilizing a sample from 9.5 of data collected from 2009 to 2018 [53] and comprising approximately 650k ν_μ candidates with energy between 15 TeV to 5 PeV, with a negligible contribution from atmospheric muons. A clear excess above $\sim 100\,\mathrm{TeV}$ was found (shown in Fig. 1.10), which is inconsistent with expectations for atmospheric neutrinos

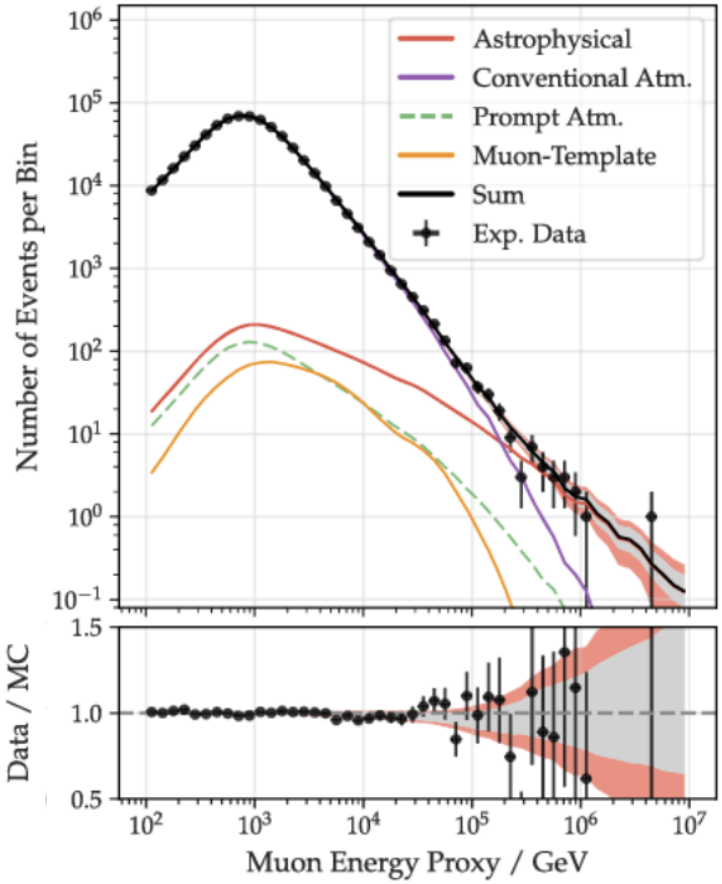

Figure 1.10: IceCube results for the 9.5 years of HESE events: experimental data (black dots) are shown together with the best-fit expectations from MonteCarlo simulations. The conventional atmospheric neutrino flux (purple) dominates the total flux energies below 100 TeV and is thus hidden below the overall sum (black). The atmospherical prompt neutrino component is shown in green. The astrophysical neutrino flux (red) is modeled as a single power law. The best-fit expectation for the remaining background of muons is shown by the orange line. The central 68%range of the best-fit expectation is drawn as a gray band. Figure taken from [53].

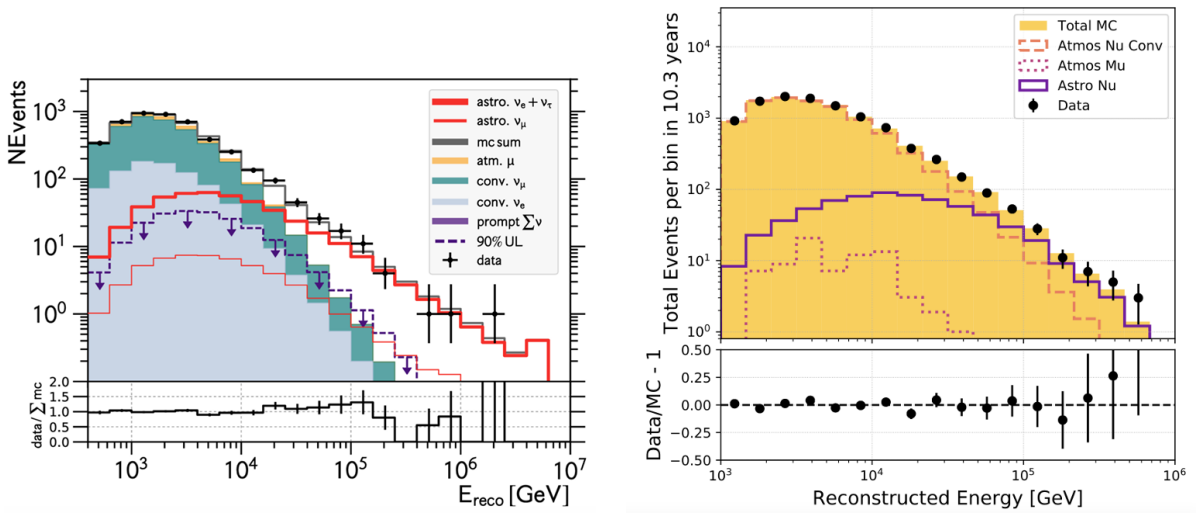

(a) (b)

Figure 1.11: Energy distributions of the events for the cascade (left) and ESTES (right) samples of IceCube. Data are compared to compared to MonteCarlo predictions from simulations. Figures taken from [56] and [57].

only. In this case the background-only hypothesis was rejected at 5.6σ. The spectral index resulting from the best fit of a power-law is $\alpha_\nu \simeq 2.37$, with normalization $\Phi^{\nu_\mu+\bar{\nu}_\mu}_{@100TeV} = 1.44 \cdot 10^{-18}\,\mathrm{GeV}^{-1}\mathrm{cm}^{-2}\,\mathrm{s}^{-1}\mathrm{sr}^{-1}$. A third sample consisted in cascade events from 2010 to 2015 [56] observed in the sensitive energy range from 16 TeV to 2.6 PeV, dominated ($\sim 90\%$) by electron and tau neutrinos. The fitted spectral index for the flux in this study was $\alpha_\nu \simeq 2.53$, with flux normalization for each flavor $\Phi^{\nu_i+\bar{\nu}_i}_{@100TeV} = 1.66 \cdot 10^{-18}\,\mathrm{GeV}^{-1}\mathrm{cm}^{-2}\,\mathrm{s}^{-1}\mathrm{sr}^{-1}$.

Finally, down-going starting track events (Enhanced Starting Tracks, ESTES) have been studied in 10 years of data taking [57] in the sensitive energy range between 3 TeV and 550 TeV, finding a best fit spectral index of $\alpha_\nu \simeq 2.58$ and normalization $\Phi^{\nu_i+\bar{\nu}_i}_{@100TeV} = 1.68 \cdot 10^{-18}\,\mathrm{GeV}^{-1}\mathrm{cm}^{-2}\,\mathrm{s}^{-1}\mathrm{sr}^{-1}$. Energy distribution of the events of the cascade and ESTES samples are shown in Fig. 1.11.

A global fit from the combination of the above-mentioned analyses has been recently perfomed [58] by the collaboration and is shown in Fig. 1.12. Results from ANTARES (tracks and cascades, 9 years) and Baikal-GVD (3 years of cascade events) analyses gave $\alpha_\nu \simeq 2.4$ at 1.6σ [59] and $\alpha_\nu \simeq 2.58$ at 3.05σ [60].

The first correlation of a neutrino event in IceCube with an astrophysical source occurred in 2017 [61]. IceCube detected a muon-like event caused by a neutrino with an energy of approximately 300 TeV and issued an alert to other experiments to search for the γ-ray counterpart. Both the Fermi-LAT satellite and the MAGIC telescope reported a coincidence with the direction of a known γ-ray source, the blazar TXS 0506+056. This correlation was found to be statistically significant at the 3σ level. Motivated by this finding, the IceCube collaboration examined the datasets from previous years in correspondence of the blazar's location and found an excess between September 2014 and March 2015 [62]. Allowing for a time-variable flux, this data provided an independent $3.5\,\sigma$ evidence for neutrino emission from TXS 0506+056. This suggests that blazars are

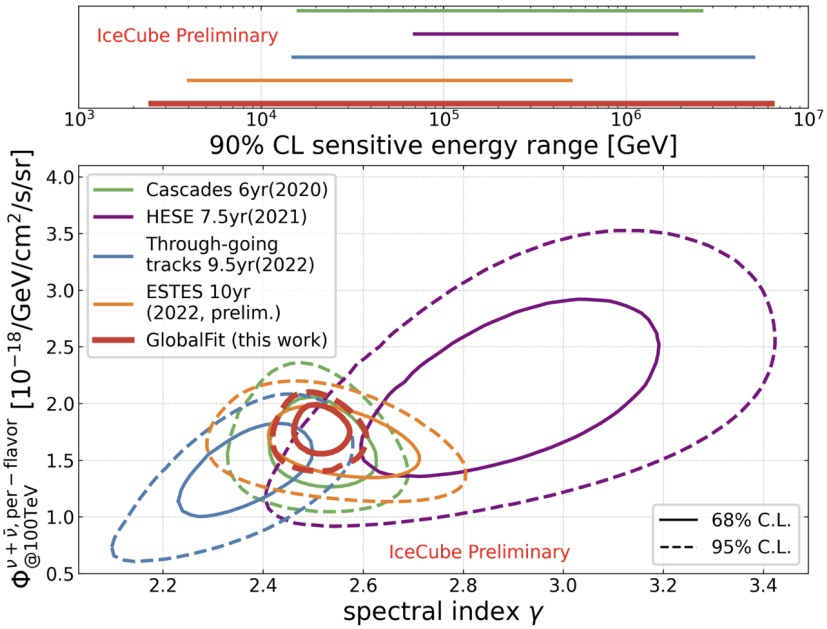

Figure 1.12: IceCube results for the combined fit of tracks and cascades under the assumption of an astrophysical single power-law neutrino flux. Results from the different individual samples, along with their sensitive energy regions, are show for comparison. Figure taken from [58].

potential sources of high-energy neutrinos.

After that, from increased datasets IceCube confirmed the neutrino excess emission from TXS 0506+056 and found other statistically significant coincides between neutrinos and other sources, in particular the active galaxy NGC1068 (at $4.2\,\sigma$) [63] from which gamma ray emission was observed by Fermi-LAT in the GeV energy range but not by MAGIC in the higher energy range, and three possible events in association with Tidal Disruptive Events (at combined significance of 3.7σ) [64] [65] [66].

1.6 The KM3-230213A event

In February 2025, the KM3NeT Collaboration announced the detection of a neutrino event with exceptionally high energy [52]. An extremely high-energy muon was detected, on 13 February 2023 at 01:16:47 UTC, by the underwater KM3NeT/ARCA neutrino telescope when it was consisting of 21 Detection Units (for details on the KM3NeT detectors, see Chap. 2). The event has been named KM3-230213A. The muon energy has been estimated to be 120^{+110}_{-60} PeV. This estimate has been made according to the event brightness by counting the number of photosensors (PMTs) hit by the Cherenkov light emitted along the passage of the muon in the water: for the KM3-230213A event 3672 PMTs (i.e., 35% of the total number of active PMTs in the detector) were triggered in the detector. Monte Carlo simulations of the event muon with energy of 10 PeV, 100 PeV and 1000 PeV are shown in Fig. 1.13.

The muon direction was horizontal, coming from 0.6° above the horizon at an azimuth of 259.8°; this is consistent with the extremely high energy of the parent neutrino, since

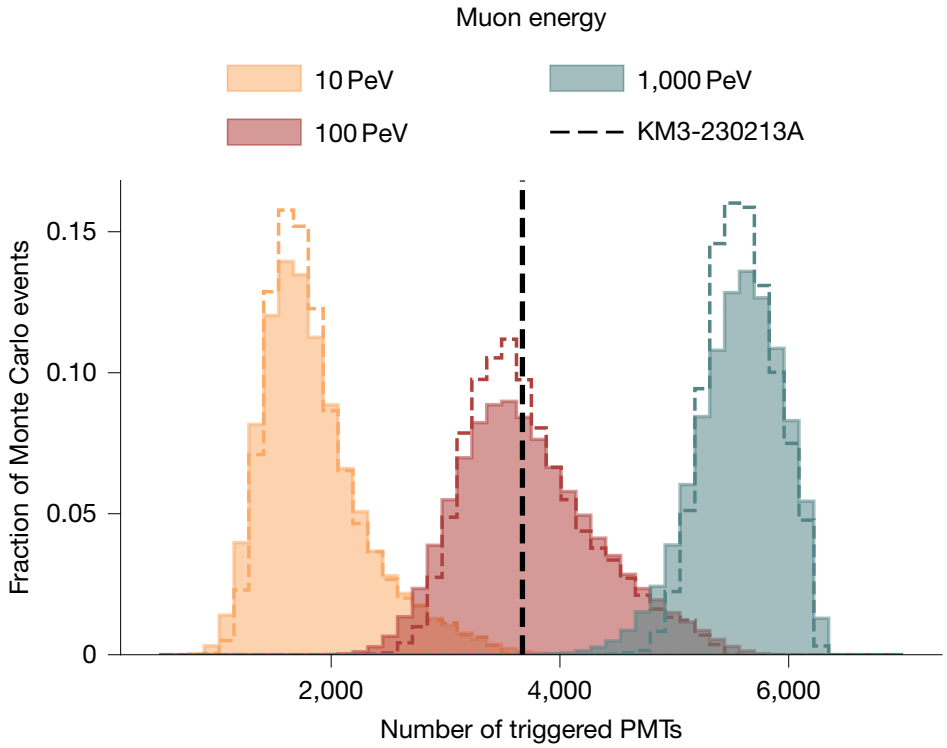

Figure 1.13: Normalised distributions of the number of PMTs triggered in the event for simulated muon energies of 1 PeV, 10 PeV and 1000 PeV. The vertical dashed line corresponds to the observed value for KM3-230213A, with $N_{trig}^{PMT} = 3672$. The dashed histograms represent the distributions from the nominal simulations. Filled histograms include systematic uncertainties by weighting the simulations according to a normal distribution, centered at the nominal value of the nuisance parameter and with a $\pm 10\%$ uncertainty. Muons simulated at 10 PeV almost never generate the amount of light that was observed in this event. Figure taken from [52].

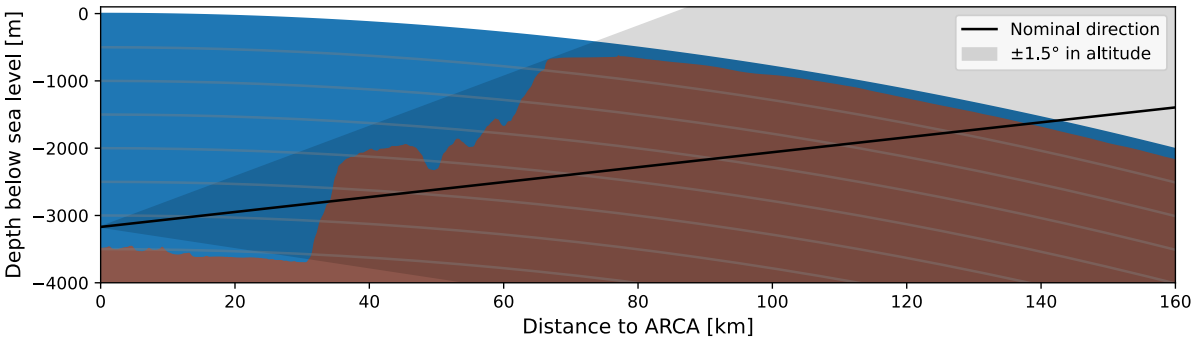

Figure 1.14: Illustration of the topography in the direction of the KM3-230213A event using bathymetric data from EMODnet [67]. A sectional view along the incoming direction and position of the event is provided, with the sea shown in blue and the seabed and the rock beneath in brown. The x-axis indicates the total distance from the KM3NeT/ARCA site, while the y-axis and the grey lines represent the depth with respect to the sea level. The shaded area shows the effect of a variation of ±1.5° in the direction reconstruction, corresponding to the 68% error region from the evaluation of systematic uncertainties. Figure taken from [52].

Earth is opaque for neutrinos at the PeV scale, as shown in Fig. 2.3. The uncertainty on the direction is estimated to be 1.5° (68% confidence level), dominated by the present systematic uncertainty on the absolute orientation of the detector. The direction also most likely excludes the possibility of the muon being an atmospheric muon reaching the detector: this was estimated and found to be negligible along the reconstructed direction (also considering possible directional uncertainties), given the amount of material that muons would need to traverse, which is shown in Fig. 1.14. In fact, a muon with the observed direction would have traversed about 300 km water-equivalent of material, which exceeds the maximal range of any atmospheric muon. The upper limit on the muon contamination at 100 PeV, considering an error on the zenith angle estimate as large as 2°, has been estimated to be 10^{-10} events per year. At the same time, given the high quality of the KM3-230213A event reconstruction, it is very unlikely that the event was produced by coincident muons from the same cosmic ray air shower or from coincident air showers. Considering its exceptionally high energy and the expected rate of atmospheric muons at the KM3NeT/ARCA detector, shown in Fig. 1.15, the atmospheric origin of the event was most likely discarded: with this respect, the Collaboration has also computed the probability of the event to be produced by the prompt component of the atmospheric neutrino flux, finding it negligible: the expected rate of atmospheric neutrinos above 100 PeV is on the order of $(1-5)\times10^{-5}$ events per year.

The parent neutrino energy was estimated from the measured muon energy (and its uncertainty), which represents a lower limit. In the simulations, the median neutrino energy that produces such muons is 220 PeV; 68%(90%) of simulated events from the whole sky fall in the 110–790 PeV (72 PeV–2.6 EeV) energy range, under the assumption that the incoming neutrino energy spectrum is $\propto E_\nu^{-2}$.

The equatorial coordinates (J2000) of KM3-230213A are: RA = 94.3°, dec. = −7.8°. Searches were performed for a potential source counterpart within a 3° radius around the event coordinates with publicly available multiwavelength data. Four hypotheses were

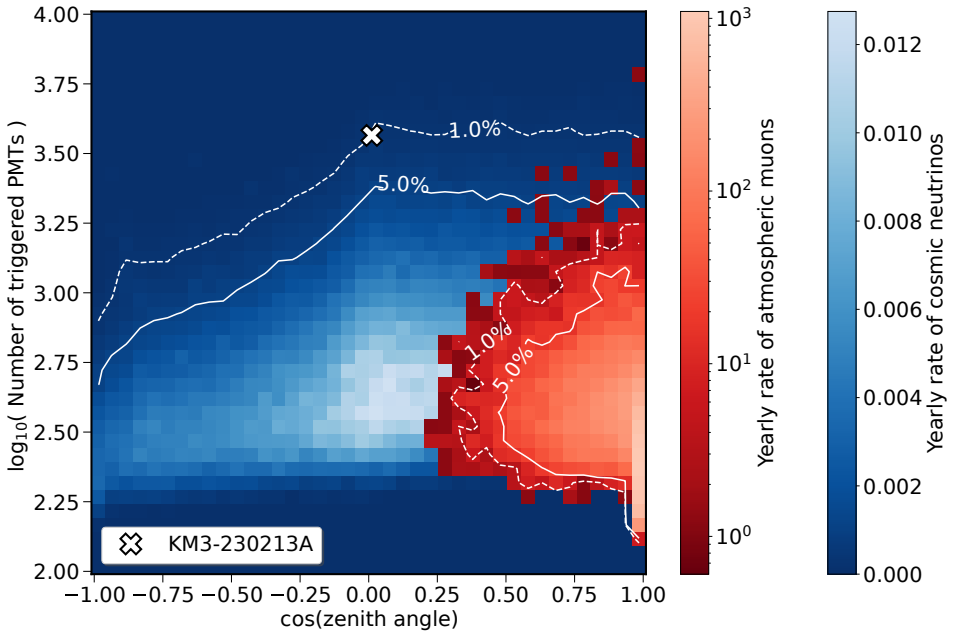

Figure 1.15: Expected yearly rate of atmospheric muons and cosmic neutrinos (according to the best-fit flux of [53]) in KM3NeT/ARCA per bin of N_{trig}^{PMT} and cos(zenith angle). The white solid (dashed) lines mark the boundary of the phase-space outside of which 5%(1%) of the muon and neutrino distributions are contained. KM3-230213A is shown as a white cross. Figure taken from [52].

tested: galactic, local Universe, transient and extragalactic origin but no compelling association was found. In order to associate a cosmic neutrino flux to the event, the steady isotropic flux that would produce one event, considering the detector exposure and the central (90%) 72 PeV–2.6 EeV energy range, was computed and is:

$$E^2\Phi(E) = 5.8^{+10.1}_{-3.7} \times 10^{-8}\,\mathrm{GeV\,cm^{-2}\,s^{-1}\,sr^{-1}} \tag{1.59}$$

Figure 1.16 shows the flux associated with KM3-230213A, alongside current measured and predicted neutrino fluxes and upper limits. The KM3NeT measurement exceeds the existing constraints from IceCube and Auger. One possible explanation is that this is a statistical upward fluctuation: based on current exposure, such an event would be expected once every 70 years, corresponding to a $2.2\,\sigma$ excess. An extrapolation of IceCube's single power-law flux would predict at most 0.12 events in the 335 days of KM3NeT data considered here, making the observation marginally compatible with expectations. This could suggest the emergence of a new flux component. Alternatively, the event could be of cosmogenic origin. Depending on the cosmic-ray injection spectrum, mass composition, and source evolution, the expected number of cosmogenic events ranges from 1.5×10^{-3} to 0.47. Figure 1.16 also shows this envelope, along with other diffuse emission models from source environments.

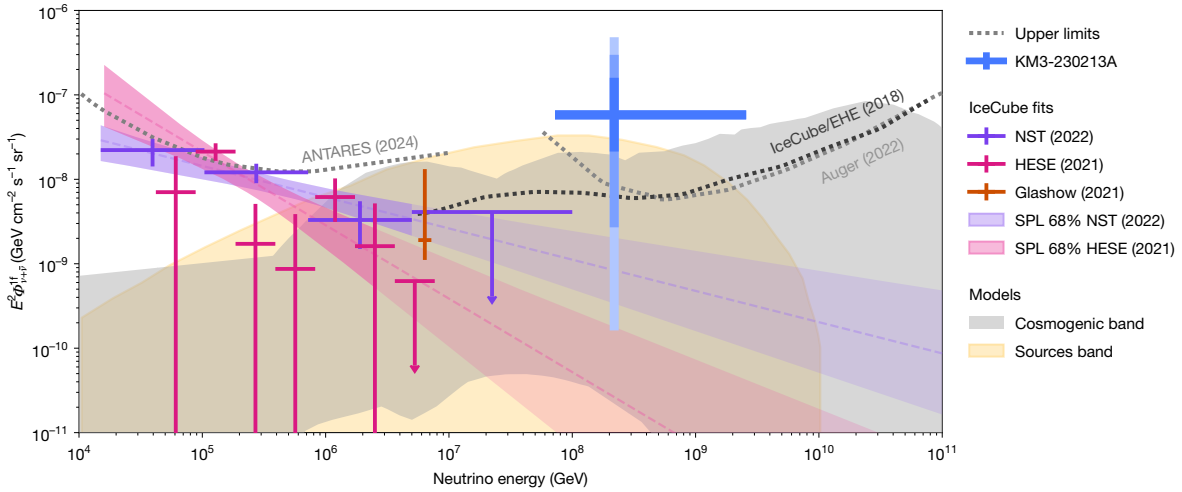

Figure 1.16: Per-flavour astrophysical neutrino flux inferred from KM3-230213A, assuming equal flavour ratios. The blue cross indicates the flux required to expect one event in the central 90% energy range (horizontal bar), with vertical bars showing $1\sigma - 3\sigma$ Feldman–Cousins confidence intervals. The purple and pink shaded areas show the 68% C.L. contours from IceCube's single-power-law fits, with darker shades marking the 90% energy range and lighter areas indicating high-energy extrapolations. Crosses represent piece-wise fits and the Glashow event (orange). Upper limits from ANTARES, Auger, and IceCube are shown with dotted lines. The grey and yellow shaded bands represent expectations from cosmogenic models and diffuse extragalactic source scenarios, respectively. Figure taken from [52].

1.7 Multi-messenger astrophysics and gravitational waves

The first detection of a gravitational wave (GW) was performed in September 2015 by the LIGO collaboration [68] and opened a new window on the Universe. Since then, many other GWs have been detected, but a new milestone in the multi-messenger astronomy was reached in 2017 when the VIRGO/LIGO collaboration observed the first GW event coinciding with an electromagnetic counterpart signal [69]. This event originated from the merger of two neutron stars approximately 40 Mpc away from Earth. Additionally, the study of the electromagnetic follow-up in the days after the event revealed the signatures of heavy element synthesis, including gold and platinum, solving the long-standing mystery of the origins of the heaviest elements in the periodic table. The follow-up for a neutrino counterpart performed by IceCube, ANTARES, and Pierre Auger collaborations [70] resulted in no statistically significant excess in the neutrino flux. To date, no neutrino/GW coincidence has been observed despite the detection of several GWs. The ANTARES collaboration, along with IceCube and other CR and gamma ray detectors, analyzed the events observed up to the O3 run and found no coincidences with neutrinos (see e.g. [71] for ANTARES, [72] for IceCube). The discovery of a coincident emission would provide important information about physics of the source. Currently, the emission of high-energy neutrinos from a GW source is expected to come from formed jets that characterize these mergers, as binary neutron stars, neutron star-black hole, and binary black holes. In the jets, charged particles are accelerated and these would produce mesons: from their decays and the decays of their secondaries, high-energy neutrino emission is expected. A neutrino detection would be a direct evidence of hadronic processes at work. Moreover, an eventual detected neutrino would constrain the location in the sky of the source more precisely.

A coincident neutrino/GW observation would be highly significant not only for CR and astrophysics studies but also for neutrino physics as it could impose stringent constraints on neutrino mass ordering and potentially on the absolute mass of the neutrino itself. This could be achieved by measuring the arrival time difference between the GW and the incoherent neutrino wave packet.

These results are expected to become attainable with the advent of the second generation of neutrino telescopes, including the KM3NeT detector.

Chapter 2

KM3NeT: a neutrino telescope in the Mediterranean Sea

The detection of astrophysical neutrinos is extremely challenging since the expected fluxes, as discussed in previous sections, are very low and the particle interacts with very small cross-sections. Thus, in order to observe a measurable flux not only a detector must have a very large target mass but it should also allow for a good background rejection. The first proposed solution came from M. A. Markov of 1960 [73], who suggested to instrument a large volume of water under a sea or a lake with an array of optical sensors to detect Cherenkov light emitted in water along the tracks of charged particles produced in the interactions of neutrinos occurring in the detector volume or close to it. The direction and the energy of the parent neutrino would be inferred by the measurement of the direction and energy of the secondary charged particle and these in turn would be obtained starting from the arrival times of Cherenkov photons on the optical sensors and from the released charge on them. At the same time, water sorrounding the detector would shield it from the background atmospheric muons. This is the concept of neutrino telescopes. Due to the technical complexity of this solution, it took almost 40 years to put in place the first attempt to test the feasibility of such a detector: in 1987 the Deep Underwater Muon and Neutrino Detector (DUMAND) project [74] deployed for few days from a ship a single instrumented string in the ocean, off-shore the Big Island of Hawaii. Then, the first successful neutrino telescopes were Baikal [75], deployed in the Siberian Baikal lake (Russia) in 1999 and the [76] completed in 2000 and installed under ice at the Amundsen-Scott South Pole Station. These prototypes had volumes smaller than the gigaton scale and were the precursors of the km^3 scale current Baikal-GVD (under construction) and IceCube (in operation) telescopes [77], respectively. In the Mediterranean sea, near Toulon, the ANTARES detector with 12 strings of optical modules was operational from 2008 to 2022, covering a surface area of about $0.1\,km^2$ [78]. The KM3NeT detector will be intensively described in the second part of this chapter.

2.1 High-energy neutrino detection

When a high energy neutrino traverses the Earth, it can interact with nucleons of the medium nuclei via charged current (CC) or neutral current (NC) weak interactions (see processes 1.3a 1.3b 1.4). In these interactions, secondary tracks or showers induced by

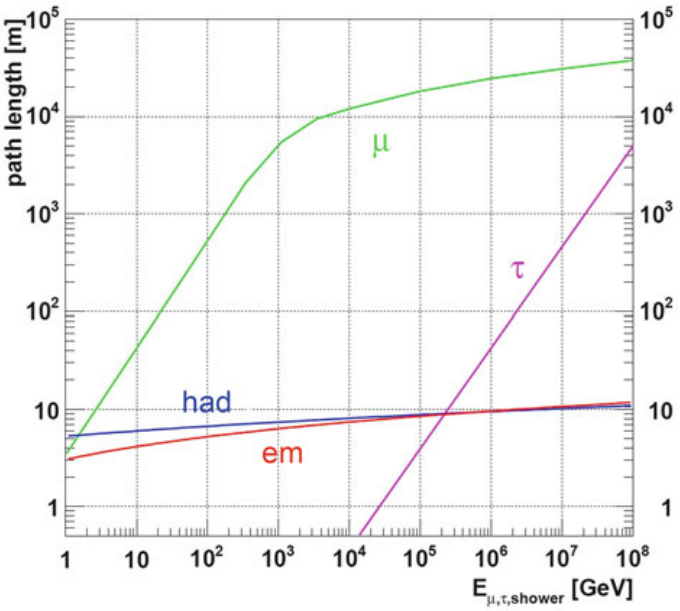

Figure 2.1: Path length of muons (μ), taus (τ), electromagnetic (em) and hadronic (had) showers in water as a function of energy. Figure taken from [79].

charged particles are generated. If the interaction occurs enough in proximity of the instrumented water (or ice) volume the secondary particles can reach the volume before stopping and induce in the medium along their path the production of optical Cherenkov photons. The detector, consisting in an array of optical sensors which are usually photompultiplier tubes (PMTs), collects these Cherenkov photons and exploits the related signals to determine direction and energy of the secondary particle track. These PMTs are located in optical modules, arranged in vertical strings which are several hundreds of meters high. Hundreds of strings, deployed in water or under the ice, form a detector volume which is of the order of km^3.

The need of km^3 scale volumes stands from the small neutrino cross sections and the expected cosmic neutrino fluxes (as derived from gamma ray fluxes): simple considerations in [79] show that $1\,\mathrm{km}^3$ of target volume is needed to observe few events per year. The water (ice) above the detector suppresses the huge flux (about 10^{11} larger than the expected flux of astrophysical neutrinos) of atmospheric muons on Earth surface, which still remains the largest flux of reconstructed events in telescopes. On the other hand, atmospheric muons from other directions other than the vertical are stopped well before arriving at the detector. In fact, the range of the highest energy muons in water is $\sim 40\,\mathrm{km}$ as shown in Fig. 2.1: thus, no charged particle can reach the detector from the hemisphere below.

Atmospheric neutrinos are instead an irreducible background, at least for what concerns the study of astrophysical fluxes, and come also from below the horizon. A simple scheme of neutrino telescopes detection principle is illustrated in Fig. 2.2. The expected flux of cosmic neutrinos depends on the energy, since high-energy (i.e., tens of TeV) upgoing neutrinos coming from the vertical, and thus transiting deep through the Earth, have not negligible absorption probability. Instead, neutrinos coming from within few degrees below the horizon provide a nearly absorption-free baseline at all relevant ener-

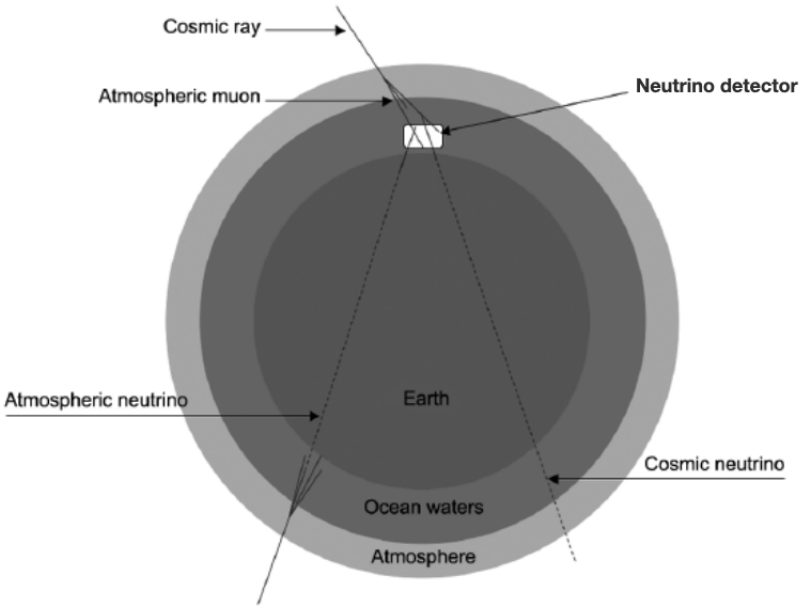

Figure 2.2: Detection principle of an underwater neutrino telescope. The whole thickness of Earth acts as a shield from the CR-induced shower of charged particles, and its field of view is mainly restricted to the hemisphere below the horizon. Instead, atmospheric neutrinos originated in the showers in the opposite hemisphere will always be present.

gies. The transmission probability as a function of the neutrino energy and zenith of the direction is shown in Fig. 2.3.

Neutrino telescopes would identify a cosmic neutrino signal over the background using different methods:

1. for up-going events with a track that can be accurately reconstructed, by the observation of an excess of events in a very small solid angle region $\Delta\Omega$ over the background of atmospheric neutrinos;

2. for all neutrino interaction candidates, by the observation of an excess of events above a given observed energy. This can include also down-going events with the interaction vertex reconstructed inside the detector. The expected cosmic signal is harder than the atmospheric neutrino spectrum.

The first method requires that neutrino detectors have good tracking capabilities: usually, only the track produced by a ν_μ CC interaction can be reconstructed with precision much better than 1°. The sky visibility for neutrino telescopes is reduced to the bottom hemisphere to avoid contamination from the huge flux of atmospheric muons. The second method relies on the calorimetric capabilities of the detector. It is usually more efficient for showering events, due to the fact that most of the neutrino energy is released inside the instrumented volume. A third method for identifying possible hadronic acceleration regions is:

1. The detection of a neutrino candidate in temporal/spatial coincidence with an external trigger, such as that resulting from a γ-ray burst observation, from a gravita-

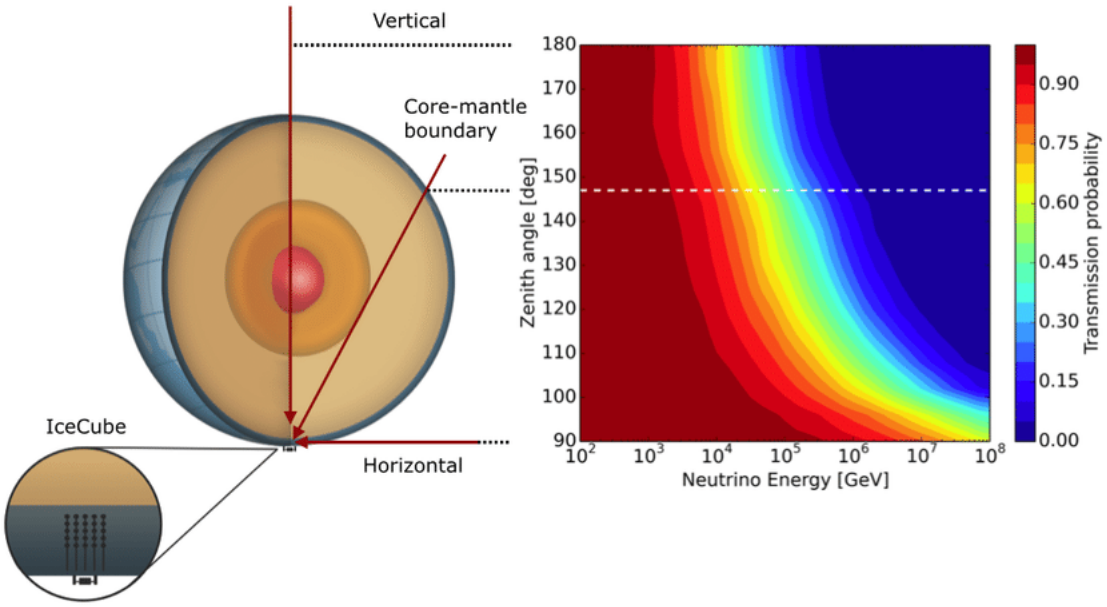

Figure 2.3: Transmission probability predicted by the Standard Model for neutrinos to transit the Earth as a function of the energy and the zenith angle. Figure taken from [80]

tional wave event, or from other transients observed by space-based or ground-based observations.

2.1.1 Cherenkov radiation

When a charged particle propagates in a medium at a velocity larger than the velocity of light in that medium, it polarizes the medium molecules along the path in a dipole arrangement. After the particle has passed, the molecules rapidly revert to their ground state, emitting electromagnetic radiation. A coherent conical luminous wavefront is emitted at a defined angle θ_C which depends on the charged particle velocity $\beta = v/c$ and on the refractive index of the medium n:

$$\cos(\theta_C) = \frac{1}{\beta n} \tag{2.1}$$

This is called the *Cherenkov angle*, and the effect is known as the *Cherenkov effect*. The minimum velocity of the particle β_{thr} for the effect to occur is:

$$\beta_{thr} = \frac{1}{n} \tag{2.2}$$

which corresponds to a threshold energy of:

$$E_{thr} = \frac{mc^2}{\sqrt{1 - 1/n^2}} \tag{2.3}$$

where m is the mass of the particle. This translates in a threshold kinetic energy of $T_{thr} = E_{thr} - mc^2$. This situation is depicted in Fig. 2.4. The number of photons [81]

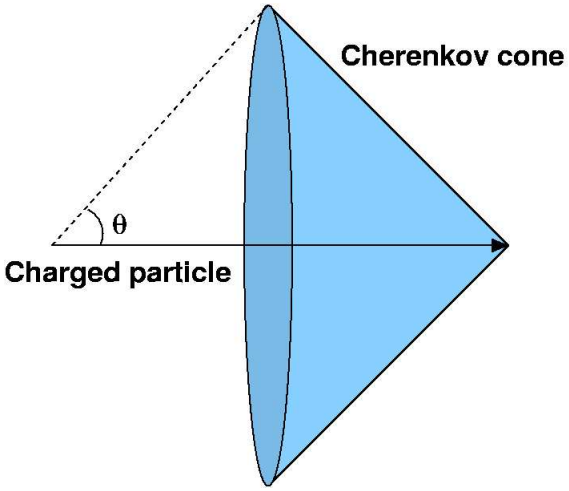

Figure 2.4: Illustration of the Cherenkov light cone emission at the passage of a charged particle. The wavefronts are emitted at the Cherenkov angle θ_C.

emitted per unit wavelength $d\lambda$ and path dx is:

$$\frac{d^2N}{d\lambda dx} = \frac{2\pi z^2 a}{\lambda^2}\left(1 - \frac{1}{\beta^2 n^2(\lambda)}\right) \tag{2.4}$$

where α is the fine structure constant and z the atomic number of the medium. The number of emitted photons in a wavelength range is obtained by integrating 2.4 over the wavelengths. For water, in the wavelength range between 300 nm and 600 nm for which the water is transparent, this gives:

$$\frac{dN}{dx} \simeq 340\,\text{photons/cm} \tag{2.5}$$

The refractive index of water in this range is $n \approx 1.35$, which for a highly-relativistic particle with $\beta \simeq 1$ results in a Cherenkov angle $\theta_C \simeq 42°$ and in threshold kinetic energies of $T^e_{thr} \simeq 0.25\,\text{MeV}$ for electrons, $T^\mu_{thr} \simeq 53\,\text{MeV}$ for muons, and $T^p_{thr} \simeq 450\,\text{MeV}$ for protons.

2.1.2 Water properties

The propagation of light in a medium is affected by both absorption and scattering of photons. For neutrino telescopes, the absorption decreases the number of photons reaching the PMTs, while scattering alters the direction of Cherenkov photons, delaying their arrival time at the PMTs. Hence, both these effects degrade the telescope's event reconstruction capabilities, worsening the angular resolution of the event direction. A photon beam of initial intensity I_0 and wavelength λ is degraded by absorption along the path, resulting in an effective intensity:

$$I(x) = I_0 \exp(-x/\lambda_{abs}) \tag{2.6}$$

where x is the distance travelled by the photons and λ_{abs} is the *absorption length* which depends on the medium and the wavelength. Sea water has maximum transparency

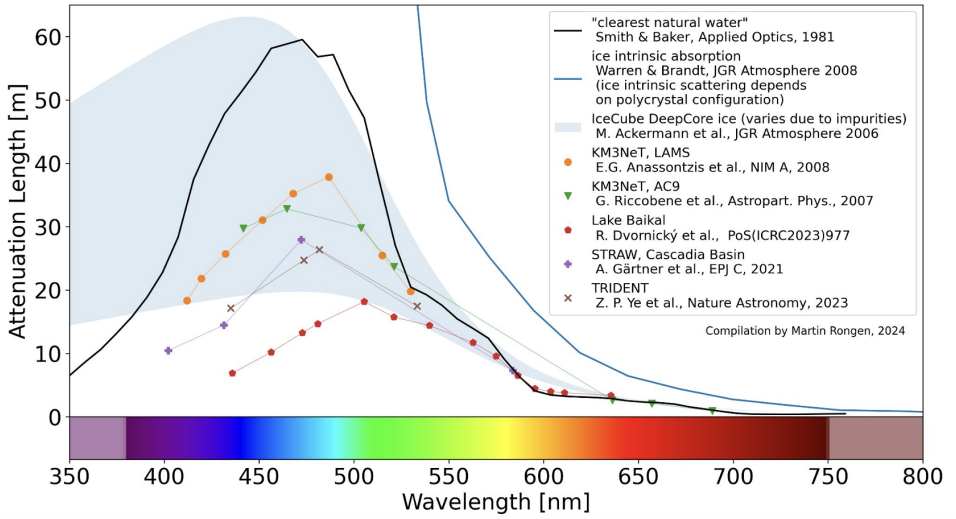

Figure 2.5: Measured water attenuation lengths for different current and future neutrino telescopes. Picture from M. Rongen, private communication.

for $\sim$ 400 nm photons, for which the corresponding absorption length is $\lambda_{abs} \approx 60$ m. Scattering is instead characterized by the *scattering length* λ_s and the light propagation is described by:

$$I(x) = I_0 \exp(-x/\lambda_s) \tag{2.7}$$

An effective scattering length λ_s^{eff} can be defined which takes into account, together with λ_s, the angular distribution of the momentum of the outgoing particles. Scattering typically takes place on water molecules ("Rayleigh scattering") or on larger particulates ("Mie scattering") [82]. The effective scattering length is:

$$\lambda_s^{eff} = \frac{\lambda_s}{1 - \langle \cos\theta_s \rangle} \tag{2.8}$$

where $\langle \cos\theta_s \rangle$ is the average scattering angle. The combination of absorption and scattering effects is referred to as light *attenuation*, and is charachterized by the *attuenuation length*:

$$I(x) = I_0 \exp(-x/\lambda_{att}) \tag{2.9}$$

where: $1/\lambda_{att} = 1/\lambda_{abs} + 1/\lambda_s^{eff}$. Measurements at the Mediterranean site of KM3NeT/ARCA, shown in Fig. 2.5, gave $\lambda_{att} \approx 35$ m, as measured for photon wavelength of 470 nm [82]. The angular distribution of scattered photon affects the telescope angular resolution, as it has a relevant impact on the event direction reconstruction. In this respect, water presents a better scattering length than ice, whose impurities worsen the scattering effect.

2.2 Neutrino signatures

Neutrino interactions near or inside the telescope give rise to two distinct topologies of events characterised by their signature: *track*-like events and *shower*-like events. These are summarized in Fig. 2.6. Track-like events are the reconstructed tracks of muons,

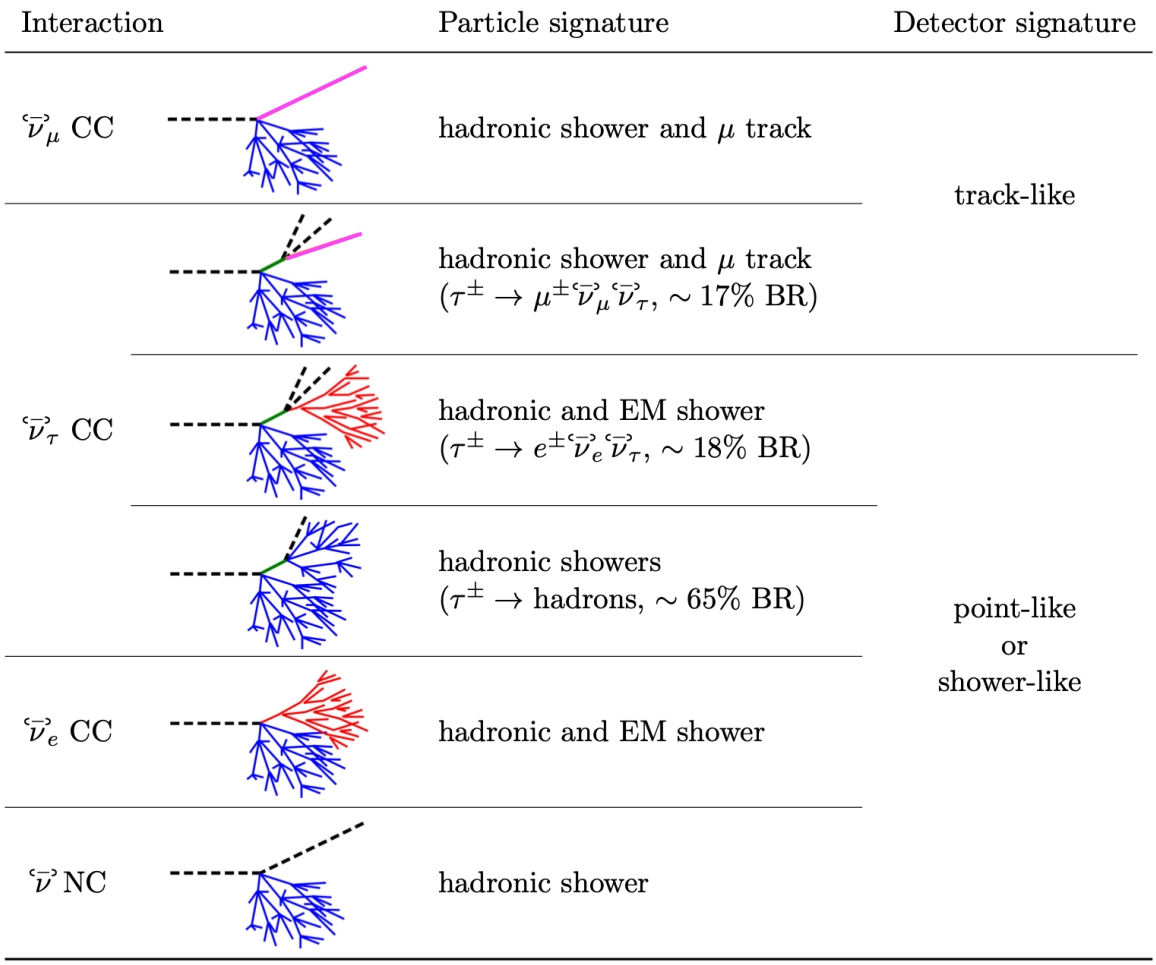

Figure 2.6: Event signatures of events in neutrino telescopes. Neutrinos are identified by dashed black lines, muons by straight purple lines, e^+, e^- in EM showers by straight red lines, secondary particles in hadronic showers by straight blue lines and τ by straight green lines. Adapted from figure taken from [83]

which are hundreds of meters long, generated in ν_μ CC interactions or in ν_τ CC interaction through the following $\tau \to \mu\nu_\mu\nu_\tau$ decay. Shower-like events instead are the results of ν_e, ν_τ CC interactions and ν_e, ν_μ, ν_τ NC interactions and they are characterized by an electromagnetic (EM) or a hadronic shower (or both) generated by the produced electrons and secondary particles. The showers extend only for a few tens of meters. For both types of signatures, no separation between particles and antiparticles can be made and thus a neutrino telescope is not sensitive to the distinction between neutrinos and anti-neutrinos.

2.2.1 Muon neutrino track-like events

From Fig. 2.1 one can see that for a km^3 telescope muons tracks in water exceed the dimension of the detector just after ~ 200 GeV. These tracks produce a clean signal on the PMTs and can be reconstructed with a high angular resolution. This in turn allows for an accurate reconstruction of the parent neutrino track, since those are closely

correlated. The kinematics of the interaction is such that the transversal momentum of the produced muons decreases with the energy and it is small, and so is the angle between it and the parent neutrino:

$$\delta\theta_{\nu\mu} \sim \frac{0.6}{\sqrt{\frac{E}{TeV}}} \tag{2.10}$$

Muons lose energy in a material via ionization and by stochastic processes, such as bremsstrahlung, pair production, and photonuclear interactions. The total average energy loss of the muon is:

$$\langle -\frac{dE}{dx} \rangle = a(E) + b(E)E \tag{2.11}$$

where a accounts for the energy loss due to ionization and b for the energy loss due to the stochastic processes. Both parameters a and b depend on the material as $a \propto Z/A$ and $b \propto Z^2/A$ and slowly vary with energy, especially above ~ 100 GeV, where radiative contributions dominate [84]. At such high energies, the parameters can be considered constant and in water they are $a \simeq 0.274\,\mathrm{GeV\,m^{-1}}$ and $b \simeq 0.000349\,\mathrm{m^{-1}}$ [85]. While for lower energies ionization dominates, muons with $E > 1\,\mathrm{TeV}$ lose energy stochastically and generate electromagnetic showers along their path, characterizing the signatures of TeV-PeV ν_μ. Energy loss by Cherenkov radiation constitutes only a small fraction of the total energy loss, and this makes the neutrino energy reconstruction much more complicated for track-like events than for shower-like events. When the neutrino interacts inside the telescope, both Cherenkov photons and photons from the hadronic shower can be detected, leading to a reliable estimate of the neutrino energy. If instead the neutrino has interacted far outside the telescope, most of the photons produced by the muon and all the photons of the hadronic shower never reaches the PMTs, leading to an underestimation of the neutrino energy.

2.2.2 Shower-like events

Electron neutrinos

A ν_e CC interaction produces a high-energy electron which propagates for few tens of cm (the radiation length in water is ~ 36 cm) and eventually emits a photon via bremsstrahlung and initiates an electromagnetic shower. In addition, near the interaction vertex (the nuclear interaction length in water is ~ 83 cm), the hadronic system X in the process 1.3a starts an hadronic shower. The longitudinal extension of the electromagnetic and hadronic showers is approximately few meters, as shown in Fig. 2.1, while the transversal extension is negligible. In neutrino telescopes aiming at astrophisical neutrinos, the distances between consecutive optical modules are of the order of tens of meters, i.e., larger than the distances covered by the showers. As a result, showers are detected by the telescope as point-like sources of Cherenkov photons induced by shower particles: this results in a worse angular resolution with respect to track-like events, but in a better energy estimation since all neutrino energy is released in the showers.

Electromagnetic showers allow a precise calorimetric measurement since the total Cherenkov light yield is proportional to the initial energy with small fluctuations in the number of secondary particles in the shower. Hadronic showers instead induce less

Cherenkov photons because hadrons, being more massive than $e^{\pm}$, have larger thresold energies according to Eq. 2.3. Also, event-to-event fluctuations in the Cherenkov light yield are more important in hadronic showers due to the fluctuations in the particles numbers and types. Nevertheless, if the initial energy is large enough that all the secondary particles reach the energy threshold, the average Cherenkov light yield for hadronic showers approaches that of electromagnetic showers. For what concerns the direction of the secondary particles with respect to the parent particle, the distribution for hadronic showers is more spread than for electromagnetic showers. This results in several Cherenkov cones with different directions. As the energy increases, the collinearity increases and approaches that of electromagnetic showers so that the different cones overlap: for TeV neutrinos, the different types of shower give the same signature in a neutrino telescope.

Neutral Current channel

The NC interactions for ν_e, ν_μ, ν_τ (see. 1.4) have the same event topology in a neutrino telescope, that is the presence of an hadronic shower generated by the hadronic system X. However, not all the initial neutrino energy is released in the shower since a fraction is carried away by the outgoing neutrino, reducing the energy resolution of the event.

Tau neutrinos

The event topology for ν_τ interactions depends on the neutrino energy. If the energy is smaller than $\sim 1\,\text{PeV}$, the τ track (see Fig. 2.1) is shorter than the shower longitudinal extension and cannot be resolved by the detector. In this case, the τ produces a second hadronic shower (or an electromagnetic one if it decays in $e^{\pm}$) and the event is seen as a shower-like event. If the τ produces a muon, then the muon track is resolved and the signatures is given by a track-like event. Instead, if the ν_τ has energy larger than $\sim 1\,\text{PeV}$, the τ track is usually long enough for the two showers, i.e., the first one due to the hadron X and the second one due to the τ decay, to be distinguishable, connected by the τ track. This topology is referred to as the *double-bang event*.

2.3 Background sources

Neutrino telescopes must face a *physical* background, which is independent of the type of telescope, and an *environmental* background which is peculiar of underwater telescopes.

2.3.1 Environmental background

A neutrino telescope located under the sea, as KM3NeT, is affected by two sources of optical background: the Cherenkov photons induced in the decays of radioactive elements in sea water and the photons emitted by bioluminescent organisms.

Radioactivity

Among the dissolved salts in sea water, ^{40}K constitute approximately the 1%. Since it is a radioactive element, it undergoes β-decay and the produced electron can induce

Cherenkov light. ^{40}K has two main decay channels:

$$^{40}K \rightarrow {}^{40}Ca + e^- + \bar{\nu}_e \qquad \text{B.R.} = 89.3\% \tag{2.12a}$$

$$^{40}K + e^- \rightarrow {}^{40}Ar + \nu_e + \gamma \qquad \text{B.R.} = 10.7\% \tag{2.12b}$$

The electron in Eq. 2.12a has often an energy above the Cherenkov threshold energy, and the photon in Eq. 2.12b has an energy of 1.46 MeV, which is enough to accelerate electrons via Compton scattering to energies above the threshold one.

Bioluminescence

Bioluminescence is emitted by organisms which inhabit the marine environment and can be divided into two contributions: a continuous and almost constant component, with seasonal variability (shown in Fig. 2.14), that is related to bioluminescent bacteria, and a component presumably due to larger size organisms that emits bursts with duration of several seconds. This background source depends on the abundance of these types of organisms, which in general differs with the geographical location, the depth and the time, but a general decrease pattern as depth increases is observed.

2.3.2 Physical background

Most of the reconstructed events in a neutrino telescope are not from astrophysical origin, and constitute thus a background to be rejected (except for studies aimed at atmospheric neutrinos). Down-going muons can be either produced in the development of CR showers in the atmosphere or by the interaction of atmospheric neutrinos: at the considered depths, the flux of direct atmospheric muons exceeds by several orders of magnitude the flux of muons induced by atmospheric neutrinos, as shown in Fig. 2.7. The background is thus almost exclusively constituted of down-going muons, which can be filtered out by selecting only up-going track-like events. However, a number of down-going events may be mis-reconstructed by the reconstruction algorithms as up-going events, contaminating the up-going sample. This contamination largely depends on used algorithms.

Up-going events must come from neutrino interactions only, since the muon maximum range is orders of magnitude shorter than the Earth's diameter. Nevertheless, the selection of up-going events leaves the atmospheric neutrino flux component, which represent an always present source of background. For energy larger than about 100 TeV however, the astrophysical neutrino diffuse flux is expected to dominate over the atmospheric one.

2.4 The KM3NeT detectors

KM3NeT [86], which stands for "Cubic Kilometer Neutrino Telescope", is a neutrino telescope and underwater observatory which is currently under installation, yet already operative and taking data, in the Mediterranean Sea. It is composed of two detectors: KM3NeT/ARCA and KM3NeT/ORCA. The KM3NeT/ORCA site is located at 40 km offshore Toulon, France at a depth of 2500 m and KM3NeT/ARCA site is located at about 100 km offshore Portopalo di Capo Passero, Italy at a depth of 3500 m; the

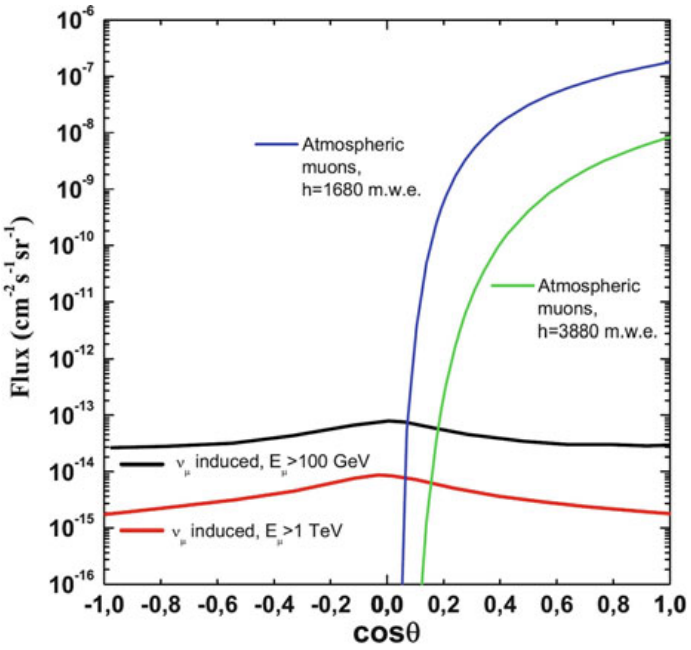

Figure 2.7: Background muon fluxes as a function of the zenith angle. Down-going atmospheric muon fluxes are calculated at depths of 1680 and 3880 meters of water equivalent, while atmospheric neutrino induced muon fluxes are calculated for two different muon energy thresholds: $E_\mu > 1$ TeV (red line) and $E_\mu > 100$ GeV (black line). Figure taken from [25].

locations are shown in Fig. 2.8). The aimed target volume at completion is about 1 km^3. KM3NeT design, construction, and operation inherits the experience of the predecessor ANTARES telescope. Being located in the Northern hemisphere, KM3NeT detectors are able to observe the sector of the sky with the Galactic plane, which is complementary to the one observed by Ice Cube located in the southern hemisphere.

Both detectors consist of a three-dimensional array of optical modules (*Digital Optical Modules*), that host the PMTs for Cherenkov photons detection. The optical modules are aligned and grouped in vertical strings (*Detection Units*) that are anchored to the seabed. The two sites differ in the density of optical modules, which is optimized for different energy ranges that reflect the different scientific objectives of the two detectors. In addition to the main physics goals, the observatory also houses instrumentation for Earth and Sea sciences for long-term studies and on-line monitoring of the deep sea environment. The optimization of the configurations of the KM3NeT/ORCA and KM3NeT/ARCA detectors has been studied with Monte Carlo simulations [87] according to the different physics goals of the two sites. The main physics objective of the KM3NeT/ORCA detector is the determination of neutrino mass hierarchy and of the oscillation parameters Δm^2_{31} and θ_{23} through ν_μ disappearance exploiting atmospheric neutrinos baselines spanning from tens of meters for down-going events to $\sim$ 13000 km for up-going events. Its configuration is optimized for studies at oscillation region energies, spanning from 100 MeV up to 100 GeV: the inter-distance between the Detection Units is 20 m and the Digital Optical Modules in a string are vertically spaced by 9 m. At completion, the full KM3NeT/ORCA detector will consist in one building block

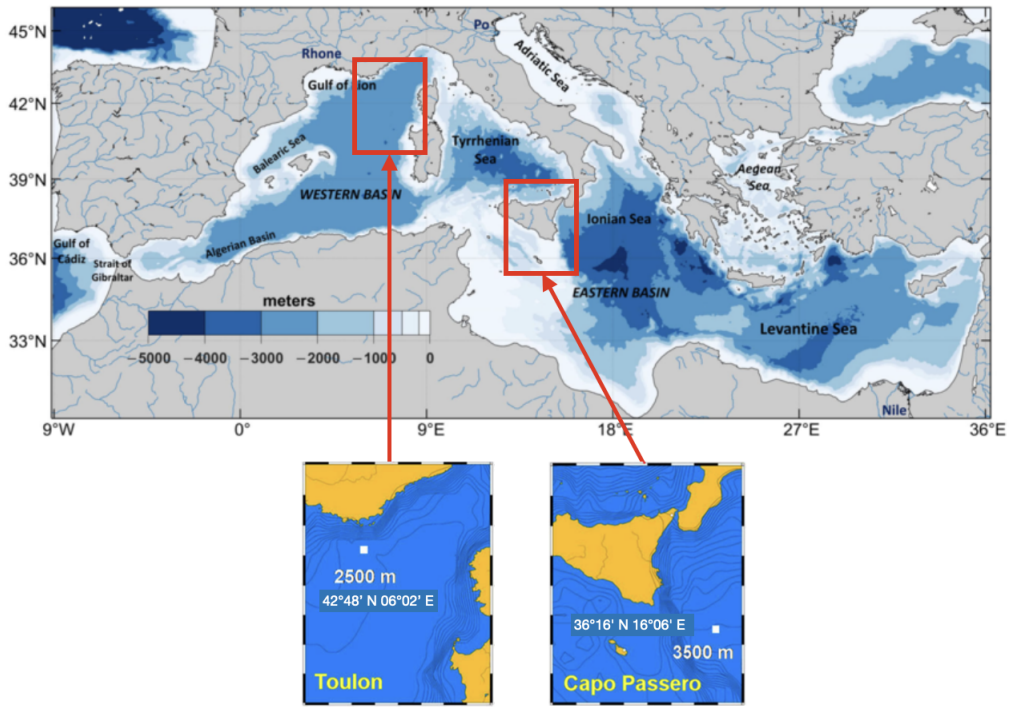

Figure 2.8: Bathymetric map of the Mediterranean sea with geographical locations of the KM3NeT/ARCA and KM3NeT/ORCA neutrino telescopes.

of 115 Detection Units. Currently (March 2025), 24 Detection Units are deployed and taking data.

KM3NeT/ARCA detector targets at high energy astrophysical neutrinos, and thus is optimized for detection of neutrinos at up to 100 PeV. To accomplish this, KM3NeT/ARCA must have a large extension, aiming at the size of at least 1 km^3 of instrumented volume. For this reason, the horizontal spacing between the KM3NeT/ARCA Detection Units is $\sim$ 90 m and the space between optical modules on each Detection Unit is $\sim$ 36 m. The final configuration will be divided in two building blocks of 115 Detection Units each. At present (March 2025), KM3NeT/ARCA consists in 34 Detection Units.

2.5 Digital Optical Modules

The sensitive elements of the KM3NeT detectors are the PMTs on the Digital Optical Modules [88] (DOMs). These modules are 17-inch glass spheres designed to withstand the high pressure at the sea bottom. DOMs are aligned in vertical strings anchored to the seabed called Detection Units, which host 18 DOMs each. The DOM contains 31 3-inch PMTs, along with their associated readout electronics, power boards, and additional sensors, as illustrated in Fig. 2.9. A metallic dome-like support glued on the sphere dissipates the heat transferring it to the sea water. The PMT high voltage and discriminating threshold are set individually for each PMT and can be adjusted from configurations during the detector operation [89]. The PMTs are supported by a foam structure and encapsulated inside the glass sphere, with optical gel filling the gaps between photocathodes and glass to ensure optical contact. Additionally, a reflector ring

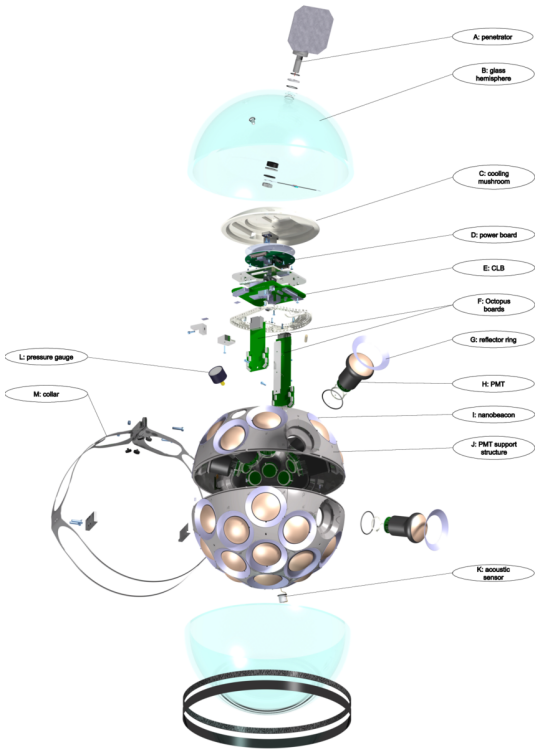

Figure 2.9: Internal structure of a Digital Optical Module. Figure taken from [88].

is placed around each photocathode to increase photon collection efficiency by up to 20-40%, depending on the incident angle of the photons [90]. The PMTs are arranged in five rings at zenith angles of 50°, 65°, 115°, 130°, and 147°, respectively. Six PMTs are positioned along these rings, with an additional PMT located at the bottom at a zenith angle of 180°. Consequently, the lower hemisphere of the DOM contains 19 PMTs, while the upper hemisphere contains 12 PMTs.

The PMT photocathodes are made of standard bi-alkali material and exhibit a quantum efficiency of approximately 27% at 404 nm and 22% at 470 nm [91]. This configuration of multiple small PMTs, as opposed to the traditional designs with fewer large-area PMTs, offers several advantages: it provides a larger total photocathode area within the sphere, it is less sensitive to the Earth's magnetic field (thus eliminating the need for metal shielding), increases the segmentation of the detection area, thereby enhancing the discrimination between single-photon and multi-photon signals and allowing better photon direction determination, and provides a better timing calibration due to the lower Transit Time Spread. In fact, PMTs in the DOM record the arrival time of Cherenkov photons generated in the seawater and provide geometrical information about the direction of these photons. When a photon hits a PMT, it generates a small electrical pulse. This pulse is then amplified and converted into a square wave pulse using the time-over-threshold technique. The pulse information, including its arrival time and duration, is sent to a Field Programmable Gate Array (FPGA) housed on the Central Logic Board (CLB), where it is stored for subsequent transfer to the shore.

In the deep sea the position of DOMs is affected by sea currents. Since a precise knowledge of each DOM position, with accuracy better than 20 cm, is required to reach a sub-degree angular resolution, DOMs also contain a piezo-acoustic sensor used to de-

Figure 2.10: Left: an assembled Digital Optical Module. Right: schematic representation of a part of a Detection Unit.

tect sound waves emitted by acoustic beacons located nearby the telescope array and on the bases of some Detection Units. The employment of this positioning system, which includes also hydrophones mounted in the Detection Unit bases, is able to provide the necessary accuracy [92]. DOMs feature also other sensors aimed at measuring the module heading: a compass to infer the pointing, accelerometers to measure yaw, pitch and tilt, and a gyroscope to measure the rotation. Temperature and humidity sensors are monitored as well. Finally, each module is equipped in the top hemisphere with a 470 nm LED emitter, called *nanobeacon*, which is produces fast light pulses towards DOMs located above in the Detection Unit. The operation of the nanobeacons, which is restricted to dedicated periods of measurement (*runs*, as explained in Sec. 2.7), is used for the timing calibration of neighbouring DOMs by measuring the time of flight of photons from one DOM to the other.

2.5.1 Central Logic Board

The DOM Central Logic Board (CLB) [93], shown in Fig. 2.11, is the main electronics board in the readout chain of KM3NeT. The PMT bases generate low voltage differential signals from the PMT electrical pulses, which are digitized with a resolution of 1 ns by Time to Digital Converters (TDCs) running in the Xilinx Kintex-7 (FPGA). After being time stamped in the Central Logic Board, TDC data are transferred on-shore enclosed in UDP packets. The CLB board also houses the monitoring instrumentation and provides the connection for the nanobeacon and the piezo sensor. The CLB implements a tunable crystal oscillator (25 MHz base frequency) required for reconstructing the White Rabbit clock. The oscillator signal is also used for achieving the 1 ns resolution for the TDCs: it is first transferred from a clock pin to a buffer in the FPGA, and then fanned out to the inner phase locked loop to provide two high frequency clocks of 250 MHz but with a 90-deg phase shift needed by the TDC core. With an oversampling technique, two others clocks with a 90-deg phase shift are obtained from those, resulting overall in a 1 GHz sampling capability. For the optical communication, a small form-factor

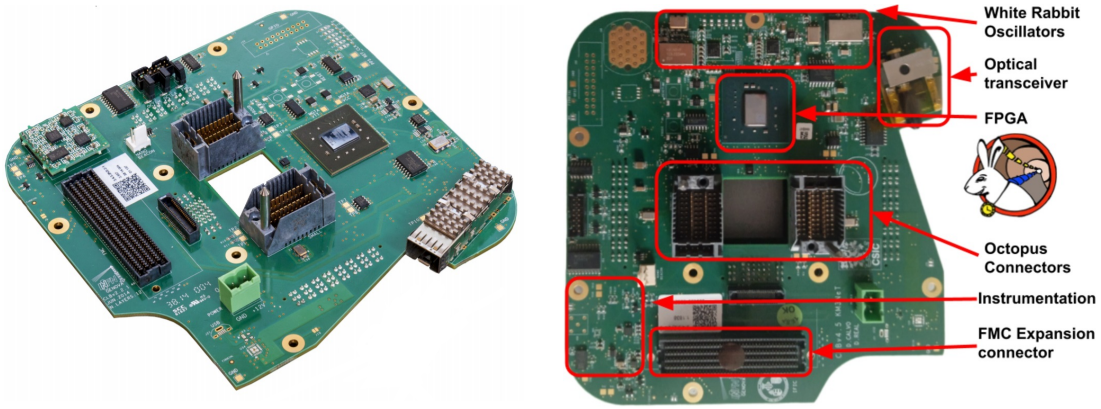

Figure 2.11: Pictures of a Central Logic Board v2 (Left) and v4 (Right), where the different components are highlighted.

pluggable transceiver is installed on the CLBs v2 deployed in DOMs of the Broadcast architecture. The newer version v4 [94], used in DOMs of the standard White Rabbit architecture, instead feature a bidirectional optical transceiver provided by Glenair [95] and new oscillator models which guarantee better phase noise and stability.

2.6 Detection Units

The Detection Units (DUs) are flexible vertical structures anchored to the seabed. Each has 18 DOMs and consists of two Dyneema ropes to which DOMs are anchored through their titanium collar with polyethylene bollards, as illustrated in Fig. 2.10 (right). The vertical spacing between consecutive DOMs is different from KM3NeT/ORCA and KM3NeT/ARCA, with 9m in the former and 36 m in the latter. Since the first DOM is placed at 100 m above sea bottom, KM3NeT/ARCA DUs reach a length of $\sim$ 750m. The DUs are kept taut by buoys on top, which also reduce the effect of sea currents in transversal displacements. On the anchoring structure of DUs, a pressure-resistant container called *base module* is located. The base module contain the electronic boards which convert the High Voltage received from shore to the +375 V for powering the DOMs, and the required devices for data transmission via optical fibers which in the case of KM3NeT/ARCA differ between the two architectures of the detector, the Broadcast and the Standard White Rabbit (details will be given in Chapters 3 and 4). Copper power wires and 18 optical fibers for DOMs are enclosed in an oil-filled vertical electro-optical cable (VEOC) which connects the base module and the DOMs, running along the DU ropes; at each DOM, the power lines and the respective optical fiber enter the DOMs through a penetrator located on the top of the sphere. Inside the DOM, a DC/DC converter steps down from 375V to 12V. DUs are deployed exploiting a submarine launch vehicle, called Launcher vehicle for Optical Modules (LOM) [96]. Each DU is rolled up around a LOM as in Fig. 2.12, which during deployment is first lowered to the seabed and then unhooked from the anchoring frame so that it freely floats to the surface while gradually unfurl the DU. Once emerged, the LOM is recovered and can be re-used for future deployments.

Figure 2.12: KM3NeT/ARCA Detection Units mounted on LOMs and ready to be deployed. The Base Module titanium cylinders (of the Standard White Rabbit architecture type) can be seen.

Power lines and optical fibers are provided to base modules by interlink cables which connect them to Junction Boxes (in KM3NeT/ARCA) or Nodes (in KM3NeT/ORCA) laid on the seabed. A single Junction Box can host interlink cables for several DUs. These in turn are connected to a Cable Termination Frame structure, from which a main electro-optical cable connects the shore station almost 100 km away providing power and data transmission from sea to shore and viceversa.

2.7 Trigger and Data Acquisition system

The KM3NeT Trigger and Data Acquisition system is designed according to a modular approach, similar to the off-shore detector's construction. This scalable design facilitates data collection and processing incrementally as Detection Units are deployed, even if the detector is not yet complete. The system does not use a hardware trigger within DOM electronics. Instead, all detected optical signals, along with acoustic data for detector positioning and other monitoring data, are sent to shore. The three different types of data are divided in three different data channels. This "all-data-to-shore" approach simplifies the electronics within the optical modules. However, it also means that data throughput is largely driven by the optical environmental background, resulting in approximately 0.2 Gbps per Detection Unit. In its final configuration, KM3NeT/ARCA is expected to handle a maximum overall data traffic of up to 500 Gbps, including acoustic and monitoring channels, in the most conservative scenario with rates exceeding 20 kHz per PMT. The traffic from shore to sea instead is constituted by the slow control commands to DOMs, which set the proper configurations for the electronics and the PMTs and regulate the data-taking. Once data arrives on-shore, they are redirected through a switching network to the computing infrastructure: the so-called Trigger and Data Acquisition System. The first stage of the processing is a queueing stage where

a modular number of processes (called optical and acoustic DataQueues) takes care of collecting and assembling in common time frames the data packets from DOMs and then send the resulting packets to the second stage, i.e., the filtering. At the filtering stage, a modular number of processes (called optical and acoustic DataFilters) apply the trigger algorithms to data. Eventually, filtered data are routed to a process which writes to ROOT files and store them on a local storage. Copies of the ROOT [97] files are also stored on remote storages. The orchestration of the routing of the packets from the different stages of data processing, as well as of the configuration and data-taking from DOMs, is done by the so-called Control Unit [98]: a collection of software processes and a web-server-based interface, through which users can start and stop data acquisition sessions, segmented into *runs*, with the desired DOMs and trigger and data acquisition settings. The Control Unit is also responsible for collecting and logging data from DOMs ancillary instruments to the central database.

2.7.1 Data acquisition network

The KM3NeT DAQ networking infrastructure is formed by 3 main subnetworks:

- Raw data network: connects the off-shore detector elements (DOMs and base modules), the on-shore optical and acoustic DataQueues), and the Control Unit;
- Managed data network: connects the DataQueues with optical and acoustic DataFilters;
- Filtered data network: connects DataFilters with the DataWriter and other processes dedicated to analysis of post-trigger data.

The RAW-LAN architecture which has been chosen for the first 32 Detection Units of KM3NeT/ARCA (and the first 48 DUs of KM3NeT/ORCA), the so-called *Phase 1*, is an asymmetric hybrid LAN which exploits 10 Gbps and 40 Gbps optical Ethernet links in the shore-station for routing the incoming traffic from the detector to the computing farm, and 1 Gbps Ethernet links to implement connections between the detector elements (DOMs and Base Modules) and the shore-station. The asymmetry of the raw data network, which represents its peculiarity, lies in the fact that while each DOM has a unidirectional 1 Gbps uplink through which it delivers its data streams to the shore-station, the latter exploits only few 1 Gbps downlinks (one per Junction Box in KM3NeT/ARCA, for a total of three), split by dedicated split-points, to *broadcast* the Slow Control commands (and timing) to all DOMs and steer them. This is why this is referred to as the "Broadcast" architecture. This solution reflects not only the topology of the data network but also the timing synchronization of the detector. In fact, in KM3NeT the synchronization of DOMs is provided by means of a White Rabbit [99] network.

In the Broadcast architecture a White Rabbit switch specifically customized for KM3NeT broadcasts the timing through a single optical fiber to all DOMs of the DUs connected to a Junction Box, this way diverting from the standard White Rabbit synchronization technology where every node of the network is synchronized through a single point-to-point link. For the rest of the DUs, the so-called *Phase 2*, the network topology differs, so to follow a standard White Rabbit timing synchronization approach. In this

case, standard White Rabbit switches on-shore implement point-to-point bidirectional connections with two WRS inside each DU base module, which in turn are connected point-to-point to the DOMs of the DU, split between the two switches. These symmetrical links grant a 1 Gb/s data transmission from each DOM towards its switch in the base module, and 1 Gb/s for both connections between the two White Rabbit switches in the base module and the ones on-shore. Details of these topology will be thoroughly discussed in the following chapters.

2.7.2 Trigger

The Central Logic Board subdivides the acquisition of data in time frames of 100 ms. When photons hit a PMT, if the analogue pulses exceed a defined threshold (typically set at 0.3 photoelectrons) and which represent a first level (level-zero, L0) of trigger, the arrival times and the time-over-threshold of the signals are registered and organized by the Central Logic Board into the time frames, encoded as User Datagram Protocol/Internet Protocol packets and subsequently sent to shore. In those frames, data packets are preceded by a header which contains the absolute timestamp of the frame (i.e., the UTC second provided by the White Rabbit network) and the serial number of the time frame contained in that second. DataQueue processes assemble frames coming from all DOMs and send over to the optical DataFilters processes all frames belonging to the same time period. Thus, optical DataFilters collect all frames related to the same 100 ms period, and combine all information in order to create a *timeslices* of 100 ms, to which they apply the trigger algorithms. The trigger algorithms, summarized in Tab. 2.1, are based on the requirement of space-time correlations between the registered photon hits in the timeslice:

- Level-one (L1) trigger: it requires a temporal coincidence of two or more L0 hits on different PMTs of the same DOM, within a fixed time window. The duration of the time window is determined by possible delays occurring during photon propagation in water, e.g. due to scattering, and is typically set to 25 ns.

- Level-two (L2) trigger: it requires a stricter coincidence between PMTs of a DOM, which takes into account an additional constraint on the direction angles between the PMTs.

- SuperNova trigger: it is implemented for supernova detection and is based on L1 hits with additional constraints on the number of hit PMTs.

2.7.3 Event reconstruction

DataFilters apply then optimised algorithms for track-like and shower-like *events*, looking at the correlations between triggered hits on different DOMs. For track-like events, reconstruction algorithms analyze the observed hits by fitting them to the hypothesis that the muon is traveling in a straight line, emitting Cherenkov light at a constant angle along its path. Fitting a muon track to the observed hits on PMTs is a non-linear problem, and a multi-step approach is used for this purpose. The main step in the fitting process involves determining the direction and vertex position of the track

Trigger	Description
L0	Photon hit on a PMT, with analogue pulse over the threshold
L1	Temporal coincidence of two or more L0 hits on different PMTs on the same DOM
L2	L1 hits with additional constraints on the hit PMTs direction angles
SuperNova	L1 hits with additional constraints on the number of hit PMTs

Table 2.1: Summary of the KM3NeT triggers at the photon hit level.

using a maximum likelihood method: the likelihood quantifies the match between the track hypothesis and the characteristics of the observed hits. The optimal track is the one that maximizes this likelihood. Once the track direction is determined, the energy is estimated considering the probability of hit and non-hit PMTs, within a predefined width around the muon trajectory. On the other hand, for shower-like events a dedicated algorithm firstly determines the position and starting time of the vertex, by minimising an estimator based on the difference between expected and observed hit times; then, it estimates the direction and energy of the shower from the probability of hit and non-hit PMTs.

2.7.4 Environmental background

The intensity of background light from ^{40}K decays depends on the ^{40}K concentration in sea water: since the salinity in the Mediterranean Sea has small geographical variation and is approximately constant with depth below few hundreds meters, this contribution is the same for both KM3NeT detectors, ORCA and ARCA. The Cherenkov photons from decay 2.12a produce coincident hits on neighbour PMTs in a DOM (L2 trigger), which are exploited to perform in-situ timing calibration of different PMTs within a DOM (details explained in Sec.3.3.1) and to find the PMT relative efficiencies by comparing the expected integrated coincident rates on PMT couples with the observed ones. An example of this study for a DOM of KM3NeT/ARCA is shown in Fig.2.13.

On the other hand, background light due to bioluminescent organisms has large fluctuations depending on the site and on the year season, and decreases with depth. Thus, the mean background rate due to this contribution is larger for KM3NeT/ORCA than for KM3NeT/ARCA: considering both ^{40}K decay and bioluminescence, the mean rate per PMT is O(10) kHz in KM3NeT/ORCA and $\sim$ 7 kHz in KM3NeT/ARCA (mostly due to ^{40}K). Mean PMT rates for KM3NeT/ORCA over a period of almost two years are shown in Fig.2.14. Unlike ^{40}K hits, these backgrounds hits are randomic and can be rejected to an acceptable level after applying the event reconstruction algorithms during data filtering.

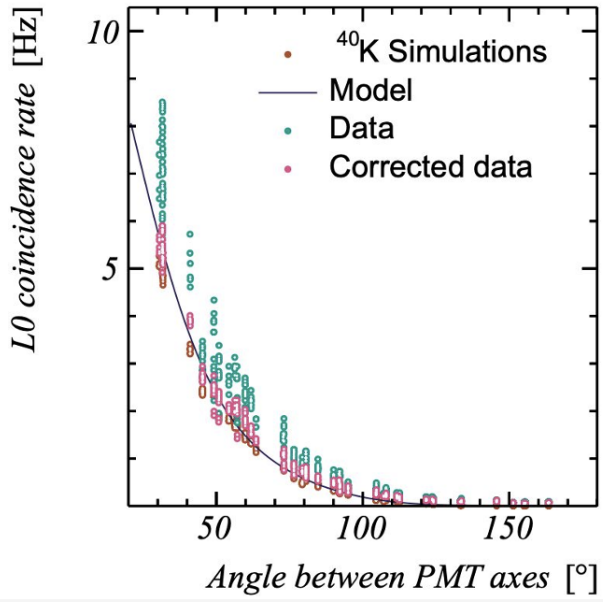

Figure 2.13: Distribution of the ^{40}K coincident rates (integrated over the allowed time-window which defines the hits coincidence) between all PMT pairs in a KM3NeT DOM, as a function of the opening angle between the pointing of the PMTs in the considered pair. Observed data are compared to a model, and the correction to the relative PMT efficiencies which align data to the model are applied. Picture from V.Kulikovskiy, private communication.

2.8 Detector performance

The number of detected neutrinos per unit time as a function of its energy can be expressed as [100]:

$$dN(E) = \Phi(E) \cdot \sigma(E) \cdot N_A \cdot \rho \cdot V_{eff}(E) \cdot dE \tag{2.13}$$

where Φ is the neutrino flux, σ the cross section, N_A the Avogadro's constant, ρ the density of the interaction medium, and V_{eff} the *effective volume* of the detector. The effective volume is defined as the volume in which a neutrino interaction produces a detectable muon and it is related to the performance of the detector and the trigger. The higher the effective volume is, the more events the telescope can detect. The number of neutrinos per unit time can also be expressed as:

$$dN(E) = \Phi(E) A_\nu^{eff}(E) dE \tag{2.14}$$

where A_ν^{eff} is the *effective area* of the telescope. This quantity represents the equivalent area of a detector with 100% detection efficiency and can be obtained through Monte Carlo simulations (as well as the effective volume):

$$A_\nu^{eff} = \frac{N_{det}}{N_{gen}} A_{gen} \tag{2.15}$$

Here, N_{gen} is the number of neutrino events generated in the Monte Carlo, distributed over the area A_{gen}, which covers the detector geometrically, and N_{det} is the number

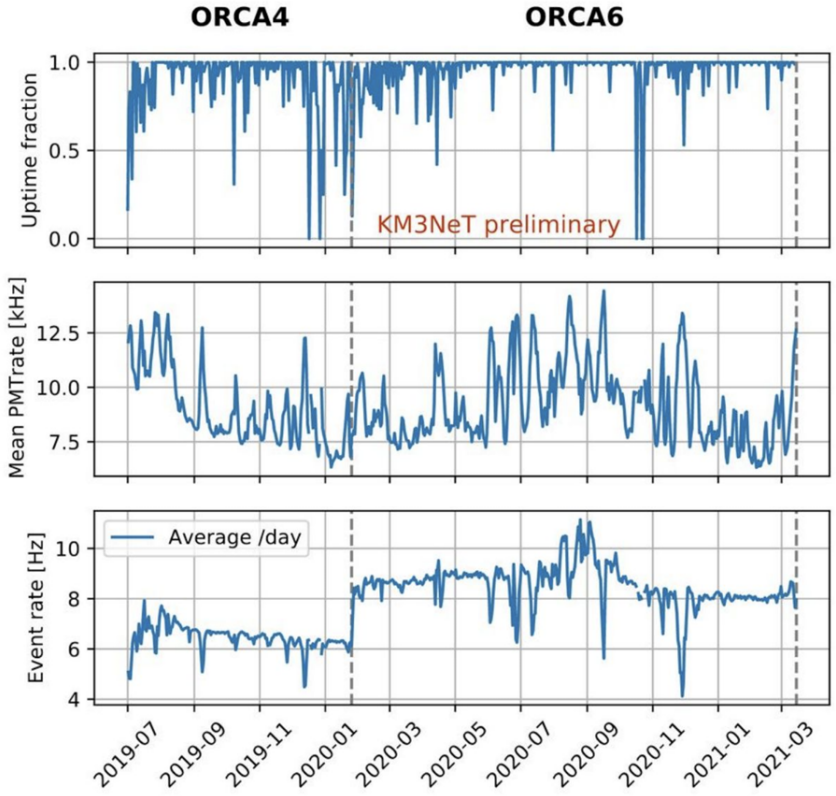

Figure 2.14: Time serie of mean PMT rate, in comparison with the event rate, for KM3NeT/ORCA detector (from ORCA4 to ORCA6). A varying mean PMT rate due to seasonal modulation in bioluminescence can be appreciated. Occasional bursts, which last several seconds, are averaged out in this plot. Picture from V.Kulikovskiy, private communication.

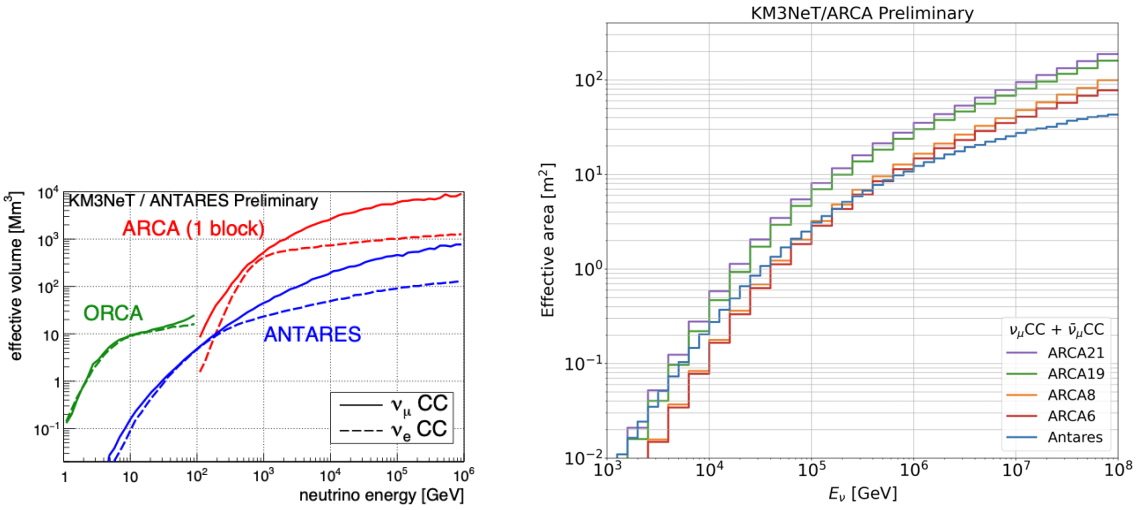

Figure 2.15: Left: Detector effective volumes as a function of neutrino energy: comparison between ANTARES, KM3NeT/ORCA and KM3NeT/ARCA (1 building block). Solid lines refer to track event signatures (ν_μ charged coupled interactions) while dashed ones to shower signatures (ν_e charged coupled interactions). Picture taken from [101]. Right: Effective areas for the different KM3NeT/ARCA detectors during construction for a flux of $\nu_\mu + \nu_{\bar{\nu}}$ that interact with CC interaction. The effective areas are compared with the ANTARES effective area for upgoing events. Picture taken from [102].

of detected events (given a considered analysis). The effective volume and area, being proportional to the expected rate of reconstructed events, serve as indicators of detection performance and can be used to compare different neutrino telescopes. In Fig. 2.15 (left), the effective volumes of KM3NeT/ARCA (1 building block) and KM3NeT/ORCA (full detector) are compared to that of ANTARES: KM3NeT detectors at that completion stage are expected to surpass ANTARES by nearly an order of magnitude across a wide energy range. Recent calculations of the KM3NeT/ARCA effective area has shown, see Fig. 2.15 (right), that even with just 21 DUs, has already exceeded ANTARES in effective area.

Monte Carlo simulations were used also to compute the angular deviation between the reconstructed neutrino tracks and their true directions as a function of energy. The figure of merit of the KM3NeT/ARCA angular resolution, computed for the full detector configuration, is shown in Fig. 2.16 (left). A smaller angular resolution is obtained for track-like events than for shower-like events, due to the different topology of the event. For neutrino energies larger than few hundreds of TeV, a median angular resolution below 0.1° is obtained for track-like events, while for shower-like events from neutrinos with energies larger than 100 TeV it is below 2° with the current reconstruction algorithm.

The relative energy resolution, defined as the ratio between the standard deviation of the energy measurement and the true energy of the neutrino is, for the case of KM3NeT/ARCA, $\sim 60 - 70\%$ in the neutrino visible energy range (i.e., the sum of energies of all particles producing light in the detector) $10\,\text{TeV} < E_\nu < 10\,\text{PeV}$ for track-like events and $< 5\%$ for $E_\nu > 50$ TeV for shower-like events.

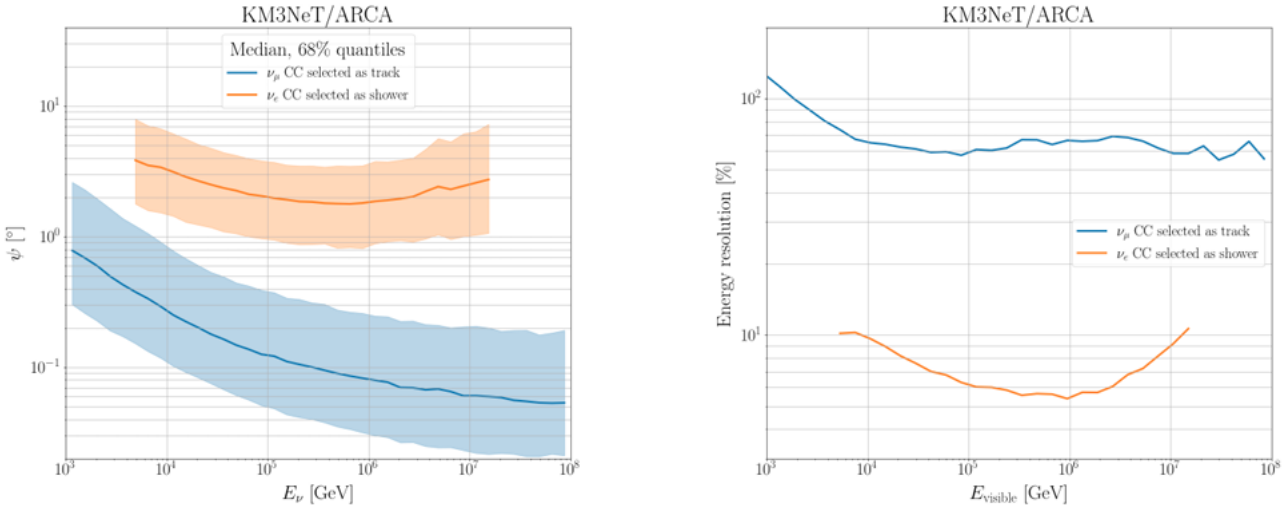

Figure 2.16: Angular deviation between the true and reconstructed neutrino direction (left) and energy resolution (defined as $\Delta E/E$) (right) as a function of the neutrino visible energy for KM3NeT/ARCA (MC simulations), for ν_μ CC track-like events and ν_e CC shower-like events. Figure taken from [103].

Chapter 3

The KM3NeT timing synchronization

The key observables in order to reconstruct the Cherenkov cone are the arrival times and number of photons on the PMTs. For the neutrino event reconstruction with a precision better than 1°, Digital Optical Modules (DOMs) need to be synchronized with nanosecond precision [104] and their position determined with less than 20 cm accuracy [105]. A preliminary study of the impact of the time synchronization uncertainties on the angular resolution of ν_μ tracks in KM3NeT/ARCA showed that in order to optimise the angular resolution to desired values for neutrino astronomy (i.e., at least $< 0.25°$) the total uncertainty between hits on any PMTs of the detector should be smaller than about 3.5 ns. This is the combination between the uncertainty on timing between different PMTs on a DOM (intra-DOM), different DOMs of a Detection Unit (inter-DOM), different DOMs of different Detection Units (inter-DU), in addition to intrinsic uncertainty on PMT hits. Taking into account that:

1. the uncertainty on DOM position, of approximately 20 cm, due to the accuracy of the acoustic positioning system corresponds to ~ 1 ns

2. PMT hit times have an intrinsic uncertainty due to the Transit Time Spread (defined as the full width at half maximum of the hit time distribution), which is ~ 2 ns for the small PMTs used in KM3NeT [91]

3. PMT hit time sampling by the Time to Digital Converters in the Central Logic Board (CLB) of the DOM is 1 GHz, corresponding to 1 ns of time resolution

the requirement for uncertainty on the timing between any PMTs in KM3NeT is to be lower than one nanosecond. While updated Monte Carlo studies are needed for more recent reconstruction algorithms which provide better angular resolutions, this requirement still holds true. The other requirement concerns the absolute timing of the detected events: this should be known with an accuracy of the typical timescale of astrophysical phenomena, i.e., of the order of milliseconds for fast transient sources, in order to characterize their time evolutions. Both requirements are fulfilled in KM3NeT by the adoption of the White Rabbit technology for timing synchronization, which extends standard Ethernet to provide a sub-nanosecond accuracy in synchronization between different nodes of a network, along with reliable data distribution over optical fibers. On-shore, a GPS provides a highly accurate and stable reference Coordinated Universal Time to a network of White Rabbit switches which distribute the common clock to all the CLBs inside

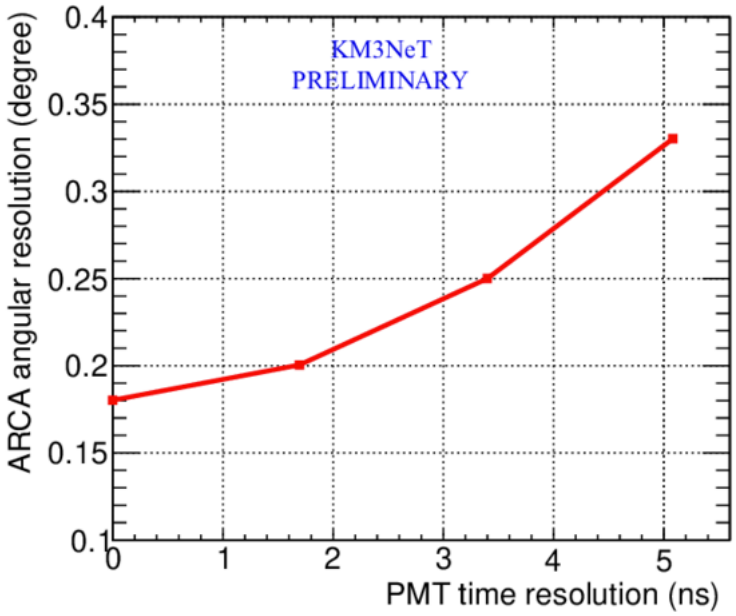

Figure 3.1: Angular resolution of KM3NeT/KM3NeT/ARCA for ν_μ CC track-like as a function of the time resolution between any of the PMTs in the detector, considering an energy spectrum E^2 with $E_\nu \geq 10$ TeV. The PMT time resolution includes different sources of timing uncertainties, in addition to standard PMT Transit Time spread: between different PMTs of a DOM, between different DOMs of a DU, between DOMs of different DUs. Picture taken from [104].

DOMs off-shore. These exploit the White Rabbit protocol to synchronize their clock to the common received. The use of a GPS ensures compatibility and synchronization with external time references; moreover, ranging the accuracy of standard GPS time servers between tens of nanosecond to one microsecond, it grants the fulfillment of the absolute timing requirement for the detector. The two different implementations of the White Rabbit solution (see Sec. 2.7) are going to be simultaneously in use in the detectors: the custom *Broadcast*, diverting from the standard design, is adopted for Phase 1, and the standard one, called *Standard White Rabbit* in this context, has been chosen for Phase 2.

Thus, the general layout of the KM3NeT detector can be considered as a large Ethernet network with thousands of nodes in the deep sea and on-shore. For the real-time filtering of digitized PMT data and for the offline analyses, an accurate time calibration of each PMT is required. The time calibration of each PMT is obtained by the combination of the calibrations of the shore station, the seabed infrastructure, and the DUs in the darkroom (see Sec. 3.4.2). The complete time calibration procedure is a three-stage process, which consists of

1. Pre-calibration: determination of the time offset of each PMT, by determining the data path length asymmetries in various subsystems in KM3NeT. This is mostly carried out prior to deployment.

2. Position calibration: to achieve sufficient accuracy in the in situ calibration, the position of all the DOMs need to be determined. The positions of the DOMs are required to be known at a level of 10-20 cm accuracy.

3. in situ calibration: the time calibration is finalized in situ using the signals from ^{40}K decay in the sea water and from atmospheric muons along with optical signals from the nano beacons installed in the detector as well as from laser beacons installed around. The obtained time calibration will also be monitored for stability using these sources.

Calibration procedures have been developed for both pre-calibration as well as in situ calibration for the relevant subsystems. The DOM position calibration is described in 5.

3.1 White Rabbit protocol

White Rabbit [99] (WR) is an Ethernet-based technology which ensures sub-nanosecond synchronization, with a precision of few tens of picoseconds, and deterministic data transfer between devices in a network, integrating Precision Time Protocol (PTP) and Synchronous Ethernet. A typical WR network employs a hierarchical topology consisting of WR-compliant nodes, in which multiple WR links are replicated. An example is shown in Fig. 3.2. A WR link is represented by a pair of nodes, a Master and a Slave, that are connected via a bidirectional optical point-to-point link, i.e. a single optical fiber plugged into optical transceivers, usually Small-Factor Pluggable modules (SFP). White Rabbit nodes can be either White Rabbit switches (WRS) or electronic boards implementing the White Rabbit PTP Core in the FPGA. In KM3NeT, WR nodes are both WR switches and the CLBs inside DOMs. White Rabbit extends the ordinary PTP message flow, adding an initial step called *White Rabbit Link Setup* initialization, illustrated in Fig. 3.3. This stage is performed by the exchange of WR-exclusive packets. After the White Rabbit Link Setup, the standard PTP flow begins.

The WR link setup includes the syntonization (i.e., disciplining clocks in relation to the master) of the slave clock over the physical layer, retrieval of the fixed delays information (i.e., the intrinsic delays in the transmission and reception of packets), and distribution of this information over the link. The synthonization is achieved thanks to Synchronous Ethernet: it uses phase locked loops to lock the slave oscillators from the retrieved clock which arrives from the incoming signal. After establishing the WR link, PTP is used for synchronizing the WR slave clock with the Master clock, which in turn can derived from a GPS. The synchronization process is done in two steps:

1. Initial synchronization: determines the master-to-slave offset and fixes the slave's phase shift accordingly

2. Phase tracking: maintains synchronization by monitoring and updating the phase shift

These two steps make use of the PTP message exchange protocol which is periodically repeated to adjust the master-to-slave delay.

3.1.1 White Rabbit link delay model

In the WR protocol the knowledge of the fixed delays, indicated by Tx_M, Rx_M, Tx_S, Rx_S, is necessary for calculating the link asymmetry and consequently determine the precise master-slave clock offset. In fact, each WR Master and WR Slave has some constant transmission and reception delays:

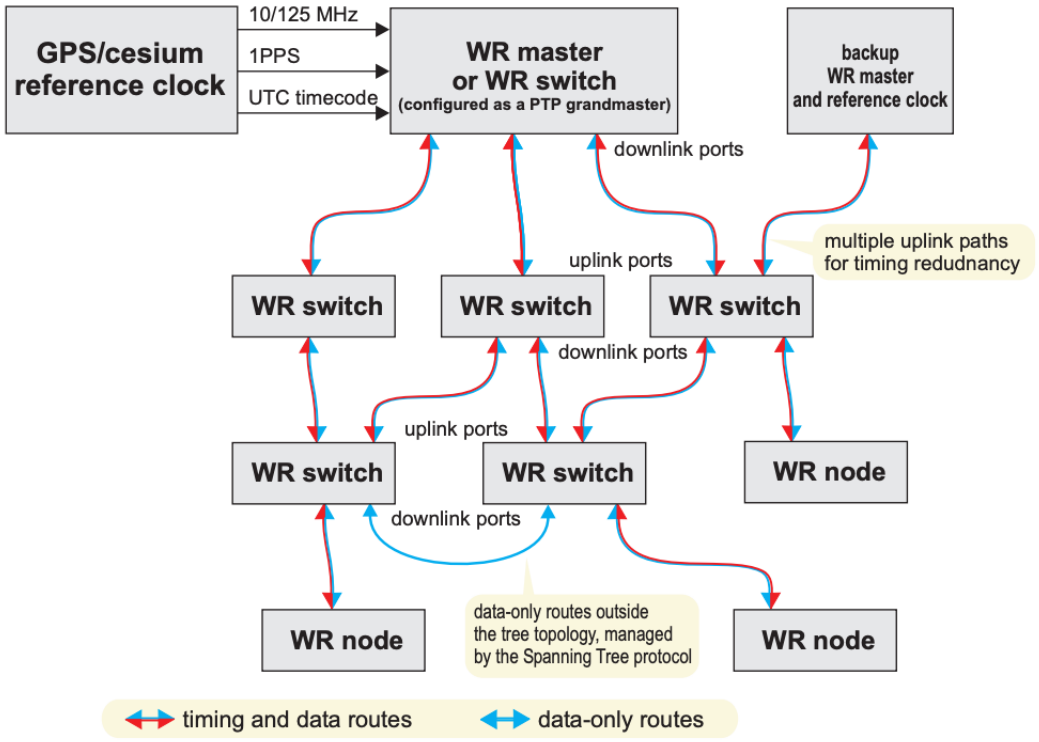

Figure 3.2: Example of a White Rabbit network. Picture taken from [106].

- Tx_M is the transmission delay of the WR Master from the moment in which a packet is time stamped inside the FPGA, to the moment when it reaches the fiber link.
- Rx_M is the reception delay of the WR Master, from the moment a packet reaches the receiving SFP module to the moment it is time stamped inside the FPGA.
- Tx_S is the transmission delay of the WR Slave
- Rx_S is the reception delay of the WR Slave

These delays are the summed result of the delays of the SFP transceiver, of the traces on the printed circuit board, and of the electronic components as well as the delays inside the FPGA chip. Additional reception delay, called bitslide value ϵ, is also caused on both sides by an internal alignment process in the serializers/deserializers circuitry:

- ϵ_M is the bitslide of Master's Rx path
- ϵ_S is the bitslide of Slave's Rx path

Except from hardware delays, packets transmitted in fiber are affected by propagation latencies in both directions:

- δ_{MS} is the Master-to-Slave fiber latency
- δ_{SM} is the Slave-to-Master fiber latency

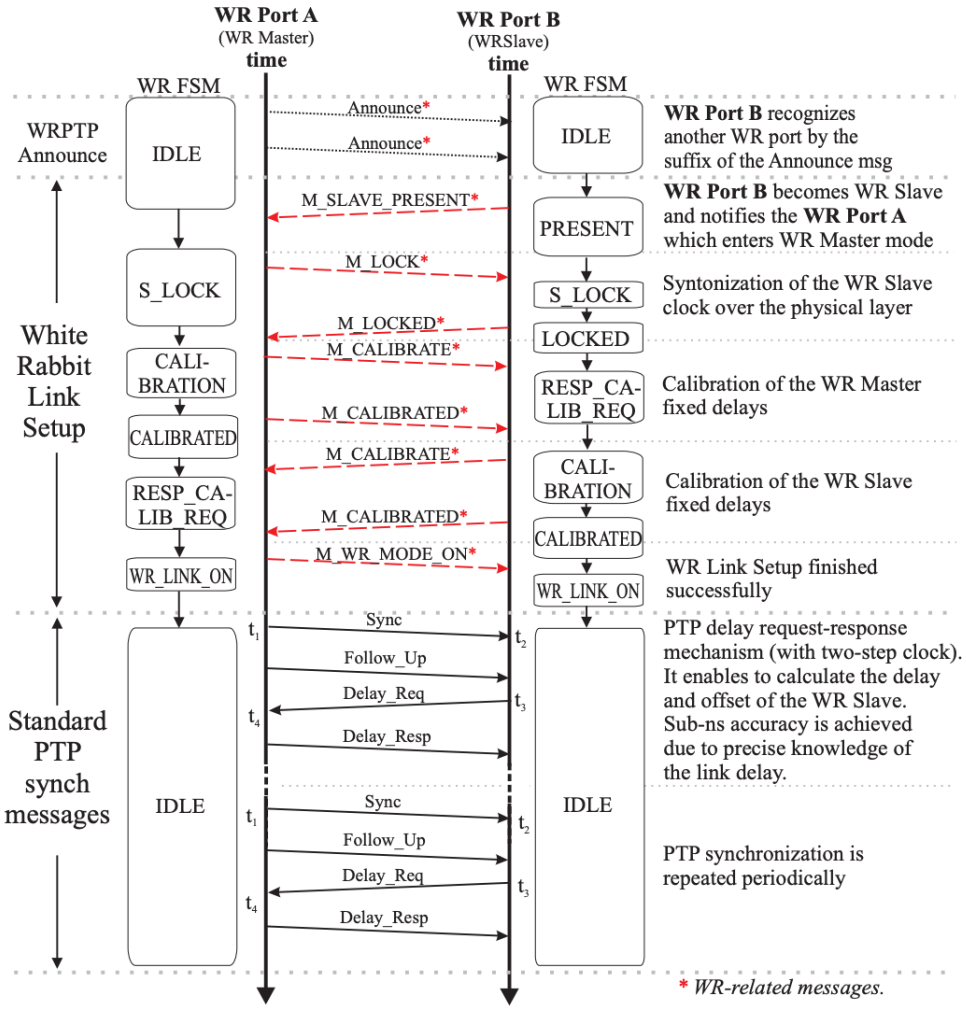

Figure 3.3: Overview of the message flow in the White Rabbit PTP exchange. Picture taken from [106].

Fiber propagation latencies are not equal since different light wavelengths are used to communicate simultaneously in both directions via a single fiber. For estimating the fiber asymmetry White Rabbit uses the α asymmetry parameter, which is constant for given wavelengths and type of fiber. Users should perform the WR Calibration procedure before deploying WR hardware to determine correct values of delays and fiber asymmetry factor. WR software features a dedicated file, called *dot-config* file, containing the calibration tables for each port (in the case of WRS) or configuration variables (in the case of a White Rabbit PTP core node) for storing these delays. The slave device, during the synchronization protocol, corrects its time with the values obtained from the fixed delays of both its Master and its own calibration table.

3.1.2 Round Trip Time measurements

WR continuously performs round trip time (RTT) measurements to maintain the time synchronization between master and slave. The RTT, also known in the protocol as the delay master-to-master $delay_{MM}$, is obtained from accurate hardware timestamps; these are the PTP timestamps t_1, t_2, t_3, t_4 shown in Fig. 3.3:

$$delay_{MM} = (t_4 - t_1) - (t_3 - t_2) \tag{3.1}$$

Starting from the RTT value and the fixed delays of the link, the protocol is able to determine the Round Trip Time of the cable ($RTTC$) i.e., of the fiber link:

$$RTTC = delay_{MM} - Tx_M - Rx_M - Tx_S - Rx_S \tag{3.2}$$

The RTT values can be retrieved from the WR device monitoring tool. Then, knowing the fiber asymmetry α parameter, from the RTT the protocol computes the one-way link delay $delay_{MS}$ (delay master-to-slave):

$$delay_{MS} = \frac{1+\alpha}{2+\alpha} \cdot RTTC + Tx_M + Rx_S \tag{3.3}$$

and uses it to align the Slave clock to the Master's one and to maintain the alignment over time.

3.2 White Rabbit networks in KM3NeT

An important point to consider when addressing the time calibration of the KM3NeT detectors is that two different network and timing architectures will be in operation simultaneously. Both architectures are based on the White Rabbit technology, although with two different network implementations, namely the Broadcast and the Standard WR, corresponding respectively to two different sectors of the detectors. Indeed, due to a technical transition that was decided during the early years of construction, 32(48) KM3NeT/ARCA(ORCA) DUs (Phase 1) will be operating within the *Broadcast* WR paradigm, while the remaining 198(67) KM3NeT/ARCA(ORCA) will be operating in the *Standard* WR paradigm (Phase 2). As a consequence of the staged development of the detector, the collaboration has undergone two phases of implementation of the WR architecture for data transport and clock transmission.

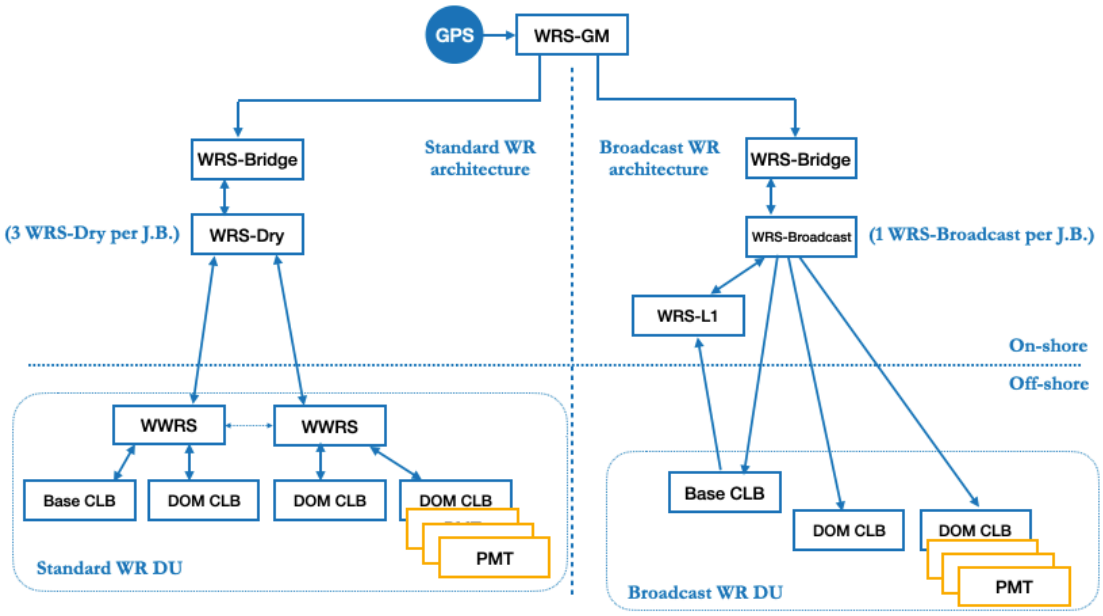

Figure 3.4: Conceptual scheme of the two KM3NeT timing architectures. On the left, the Standard WR implementation is sketched, while on the right the Broadcast implementation is shown. Number of on-shore WRS is representative for 1 Junction Box. The number of "Level-1" WRS differs between KM3NeT/ARCA and KM3NeT/ORCA detectors. Off-shore, 1 Detection Unit is represented (the number of DOMs included in the Detection Unit is not indicative).

For timing alignment purposes, the reference timeplane of the KM3NeT detectors is represented by the arrival of optical photons at the PMT surface (optical window). All calibration procedures, either for Phase 1 or Phase 2 detectors, employ this timing reference scheme to measure and compensate detector time delays. This element will be further developed in the following sections dedicated to the calibration procedures.

3.2.1 Broadcast architecture

In Phase 1, a customized version of WR has been developed by an external company. In this "Broadcast" WR implementation, the CLBs in DOMs are not connected with a point-to-point link to a Master WRS on-shore: several different DUs share a common uplink (the "broadcast" fiber) from a "Broadcast" WRS shore station, while on their way back each CLB makes use of its own fiber link. For this reason, the standard WR protocol cannot be established and individual CLBs are not able to find the correct master-to-slave offset. The Broadcast WRS receive timing through two layers of standard WRS named the "Bridge" WRS and the "GrandMaster" WRS, that ultimately is connected to the GPS, currently a Meinberg ® microSync RX200SQ/AD10, which provides a *Pulse Per Second* and 10 MHz clock via low voltage TTL signals. Coarse date and time information is distributed from the GPS to the WR fabric and to the whole data acquisition servers in the detector shore station over Network Time Protocol communication. Only a subset of CLBs i.e., those in the base modules, implements the automatic correction of the clock phase, though not through a one-to-one connection. In fact, another layer of

customized White Rabbit switches, the "Level-1", receives the White Rabbit packets from CLBs in base modules and communicate with the Broadcast WRS to complete their synchronization. The situation is depicted in Fig.3.4. CLBs in DOMs will set their clock using only the timestamp included in the incoming packets from the broadcast link, without adjusting it for the master-to-slave offset.

The due correction for each CLB of DOMs is in this implementation performed offline, by measuring the master-to-slave offset from dedicated calibration procedures and including it in the total time offset of the PMT hits (that takes into account also the other relevant delays). These total time offsets T_0 for each PMT channel in DOMs are corrected offline, during the filtering stage, using a set of time calibration parameters ("Broadcast" T_0 set) that are measured during the DU darkroom calibration and the optical network calibration. Eventually, when needed, this set of time offsets can be updated and adjusted with specific in situ calibration, e.g., exploiting ^{40}K and atmospheric muons as described in the next section.

3.2.2 Standard WR architecture

In Phase 2, a standard White Rabbit architecture is used. In this case, time information is dispatched from the GrandMaster WRS to the CLBs off-shore, through a chain of point-to-point master-slave links with automatic correction of the clock phase, thanks to the presence of two WRS (named Wet WRS, WWRS) inside the base module of the DU, as shown in Fig.3.4 (left). The additional time offsets due to the optical network asymmetries and peculiar hardware delays of specific boards are corrected offline, using (as for the broadcast approach) a set of time calibration parameters: the Standard WR T_0 set, measured during the DU darkroom calibration and the calibration of the optical network, as described in Chap.4. In situ calibration is also foreseen in this approach.

3.3 Calibration methods

From the calibration point of view, the two sectors of the detector are automatically set at the same phase, once the two T_0 sets are applied to data, offline. Indeed, the calibration procedures used to determine the time offsets of the Broadcast and Standard WR DOMs (PMTs) are both defined by setting the PMT surface, hit by the photon, as the reference time plane. This approach guarantees the correct reconstruction of the events, starting from the PMT hits. The development of the time calibration procedure to measure the time offsets that allow the synchronization of PMT signals with respect to the GPS time in the Standard WR scenario, in which I contributed within the KM3NeT time calibration working group and which is described in Chap.4, is based on the procedure used for the Boradcast scenario. The different time offset contributions are reported below.

3.3.1 Intra-DOM time offsets

Intra-DOM offsets refer to the subset of time difference between PMT channels with respect to a reference PMT in the DOM. These values include PMT Transit Time (as a function of PMT HV bias), front-end electronics delays and cable routing, and CLB TDC

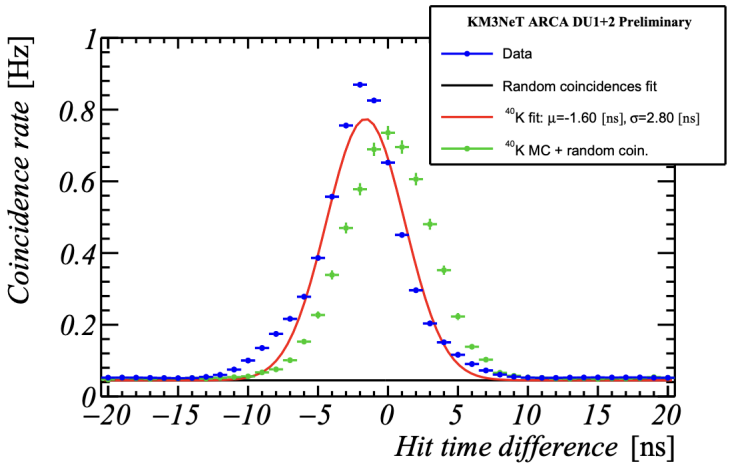

Figure 3.5: Coincidence rate as function of the hit time difference for a pair of PMTs in a KM3NeT/KM3NeT/ARCA DOM. Blue points are the observed data, and the result of the fit with Eq. 3.4 with fit is shown in red. The tails of data distrubution are used to estimate the background rate estimated from the tail. Green points are the simulated hits from MC assuming that the PMTs are synchronized. Picture taken from [107].

multiplexing. These are measured in situ, exploiting coincidence events in close PMTs originated by Cherenkov photons following a ^{40}K beta decay. Data that are collected during normal operation of the detector can be used for this analysis, specifically the L1 triggered hits, which contains all hit-coincidences within 25 ns on any given DOM. These coincidences consist mostly of the background signals from ^{40}K decays in the water. Such a decay produces a sizable number of Cherenkov photons, as described in Sec. 2.7.4. For those decays occurring in the vicinity of a DOM (typically within a few meters), the Cherenkov photons can produce a time coincidence of two (or more) hits in the DOM. The PMT time calibration exploits the time correlation between these hits [107].

The distribution of the hit time difference ΔT between these coincident hits is expected to be approximately gaussian distributed, where the mean is the difference between the transit times t_i^0 of the involved PMTs, the width is related to the PMT transit time spreads TTS_i and the integral scales with the product of the PMT efficiencies E_i:

$$R_{i,j}(\Delta T) = R(\theta_{i,j}) \cdot E_i \cdot E_j \cdot \frac{1}{\sqrt{2\pi}\sigma_{i,j}} e^{\frac{(\Delta t - t_i^0 - t_j^0)^2}{2\sigma_{i,j}^2}} + R_{i,j}^{random} \tag{3.4}$$

where $\sigma_{i,j}^2 = TTS_i^2 + TTS_j^2 + \sigma_{40K}^2$. Parametrization of the expected total coincidence rate for a PMT pair $R(\theta_{i,j})$ and the intrinsic time spread, σ_{40K}, due to the spatial distribution of the ^{40}K decays are determined from Monte Carlo simulations. The flat background from random coincidences $R_{i,j}^{random}$ is determined by a fit of the tails of each distribution and added to the simulated hit tim difference distribution. Fitting hit time distributions with Eq. 3.4 of all PMT pairs in a DOM provides the 31 PMT time offsets, transit time spreads and PMT efficiencies. An example on a DOM of KM3NeT/ARCA is shown in Fig. 3.5. The calibration procedure of these delays is identical for the Broadcast and Standard WR DOMs.

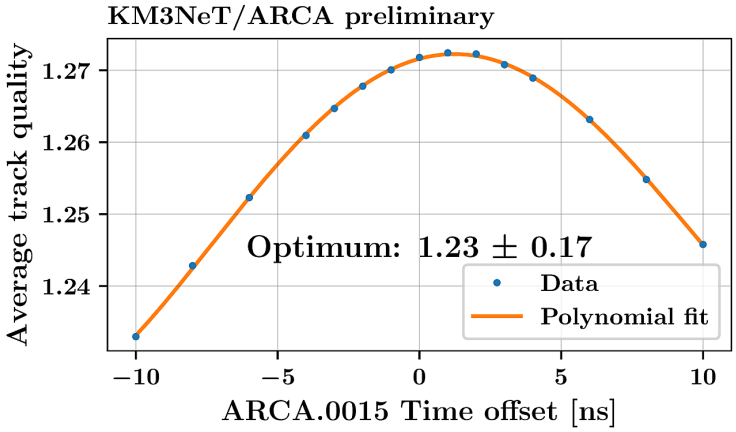

Figure 3.6: Track quality scan for the time offset of a DU of KM3NeT/ARCA. In this case, the offset is applied to all DOMs of the DU, fixing the offsets of other DUs with the nominal values. Picture taken from [108].

3.3.2 Inter-DOM time offsets

Inter-DOM time offsets refer to the relative time offsets between the reference PMTs of all DOMs in a DU. These delays are measured on-shore, prior the DU deployment, in a darkroom where reference PMTs in all the 18 DOMs of a DU are simultaneously flashed using single-photon laser pulses emitted at known GPS times. The measurement of inter-DOM intervals takes into account for each reference PMT: the transit time, the front-end electronics time latencies and the WR hardware delays of the CLB (Tx_S, Rx_S), if not corrected beforehand. For the Standard WR DUs, these offsets include also the Tx_M, Rx_M of the Wet WRS port to the CLB of the DOM, which we decided to not correct beforehand (see Sec. 4.4.1). In the Broadcast scenario these offsets also include the travel time of the time signal along the optical fiber network of the DU.

Inter-DOM offsets can be monitored and corrected with in situ measurements with auxiliary calibration devices as nanobeacons and laser beacons (see Sec. 3.5), and also analyzing reconstructed atmospheric muon tracks. The latter relies on a principle of track quality method, i.e., to add, on top of the track reconstruction process during which the best track properties are found, a step where the best PMT hit properties are found (time, position and orientation). These are the values which maximize the *quality* of the track, given by the likelihood resulting from the fit divided by the number of hits used. Analyzing a set of events, the optimal calibration can be determined by reconstructing the same data with different values of the detector parameters and monitoring the quality of the reconstructed tracks [108]. By varying the time offsets of DOMs within a DU (inter-DOM) or of all DOMs of a DU fixing the times of the other DUs (inter-DU, see below), a quality curve like the one shown in Fig. 3.6 is obtained from which the optimal offsets can be determined and used to correct the calibrations.

3.3.3 Inter-DU time offsets

The inter-DU time offsets are the offsets needed to align the time of DOMs indifferent DUs. In the Broadcast WR case, inter-DU time calibration is achieved through precise WR measurement of the Round Trip Time RTT between the master WRS on-shore

and each DU base module. After measuring the RTT, it is necessary to correct it by accounting for all relevant asymmetries in the propagation of the clock signal along the path. Time asymmetry arises from the different signal paths in the Junction Box, which is minimally affected by wavelength, and from chromatic dispersion in the fibers of the main electro-optical cable that connects the detector to shore. Chromatic dispersion results from the difference in wavelengths used for the downlink and uplink data transmission to/from the CLB in the base module. The knowledge of the correct RTT for each DU is required in order to obtain the correct T_0 offsets of related DOMs, based on the difference between the RTT measured in situ and in the darkroom.

In the Standard WR case, despite the fact that DOMs are synchronized in a standard way by the Wet WRS, the measurement of the asymmetries in the propagation of the clock from shore to sea is needed to correct the time of the Wet WRS received from shore, ultimately adjusting the T_0 set for DOMs. Also in this case, atmospheric muons can be exploited in situ to check and eventually correct these offsets, by evaluating different DU time offsets and determining the value which gives the best quality of the track fit.

3.3.4 Time alignment between Broadcast and Standard White Rabbit DOMs

As already mentioned, trigger algorithms are applied on-shore considering all hits recorded from the detector within a timeslice of 100 ms. The trigger processing implies a preliminary calibration of the raw data, e.g., applying the T_0 set and then inspect hits in the timeslice searching for coincidences among PMTs and DOMs within due time intervals. Due to the intrinsic design, the time front of DOMs of the Broadcast sector will anticipate the timing of Standard White Rabbit DOMs of an offset which is the delay master-to-slave for each CLB: although during triggering the hit times are corrected, in the case of events occurring at the edge between consequent timeslices this may lead to hits on the Broadcast DOM falling in the first timeslice and hits on the Standard White Rabbit DOMs falling in the second timeslice, causing the loss of the triggered events. To guarantee the correct operation of the trigger system (including hits from both Broadcast or Standard DUs for events at the edge of timeslices), we have considered to introduce a coarse time shift offset in the time synchronization algorithm of the CLBs of Broadcast DOMs. This offset will be equal to half of the RTT measured by the CLB in the base module, and will reduce the time skew between CLBs in DOMs of the Broadcast (on-shore timestamp) and Standard WR sectors (WR corrected timestamp); thanks to this solution, hits from DOMs in the Broadcast sector occurring near the edge of a timeslice will then fall in the same timeslice of the hits from DOMs in the Standard White Rabbit sector. To achieve this goal, we plan to shift the timestamp of hits from Broadcast DOMs by acting on the CLB firmware. After that, the same time shift offset must of course be subtracted from the Broadcast T_0 sets in order to maintain the true hit times.

3.4 Time calibration of the Broadcast White Rabbit system

The peculiar, custom topology of the Broadcast paradigm was implemented to optimize the number of fiber optic links available with the state-of-the-art data transport technology. The Coordinated Universal Time information, provided from a GPS receiver onshore, is broadcasted to all the detector CLBs by a set of few (one in KM3NeT/ORCA and three in KM3NeT/ARCA i.e., one per each Junction Box/Node) customized WR switches, nicknamed as Broadcast WRS. The unidirectional downlink from the Broadcast WRS to CLBs in DOMs is a unique 1 Gb/s link called the "broadcast", *slow control* link. That is, the same slow control data/clock packets sent by the Broadcast WRS reach all the CLBs subsea. On the other hand, two different classes of uplinks are implemented in this architecture:

1. a quasi-standard WR link to connect CLBs in the base modules;

2. an ethernet link to connect CLBs in DOMs;

Only the CLBs in the base modules effectively reply to the WR synchronization messages, using the so called *detector control* uplink to shore. The detector control packets are received by a layer of WR switches, the "Level-1" WRS, synchronized with the Broadcast WRS, to calculate the link RTT. The Cable Round trip time $RTTC$ of the link between shore and the DU base module is one of the parameters needed to time calibrate the DOMs in a specific DU, as explained in next sections. It is worth mentioning that in the time calibration procedures of the KM3NeT Broadcast section, the clock delay-phase of the CLBs in base modules remains uncalibrated (or better it can be determined only within a few tens ns accuracy). That is, the clock phases of the CLBs in DU bases are not synchronized. This has no effect on the time calibration of DOMs, as discussed later. In practice: in the calibration table of the CLBs in base modules, the hardware Tx and Rx delays and the α parameter are set to 0. The default Open Hardware White Rabbit calibration values are used for the Broadcast WRS (port 18) and Level-1 WRS (port 3 to 18). The CLBs in DOMs do not reply to WR messages distributed by the WRS Broadcast over the slow control link. They just set their clock frequency, set a constant phase delay once the WR link is established, and receive the broadcasted absolute time information from shore. Data acquired by the sensors in the DOM are time stamped by the CLB, and then sent back to shore on a different fiber. This link uses a standard ethernet protocol and CLBs' data are routed to standard ethernet switches on-shore. The phase-clock delay between the Broadcast WRS and each CLB in the DOMs is determined in several steps of the time calibration procedures implemented by the collaboration, stored in the so-called T_0 set of time offsets and corrected offline. The time calibration of the Broadcast sector, though it requires more complex steps and measurements, as shown in Sec. 3.4.3, than the one of the Standard WR sector (described in Chap. 4), it has successfully granted a reliable sub-nanosecond synchronization of the KM3NeT detectors resulting in a sub-degree angular resolution (statistical value obtained from MonteCarlo simulations, see Fig. 2.16). This has led to the discovery with KM3NeT/ARCA of the KM3-230213A event.

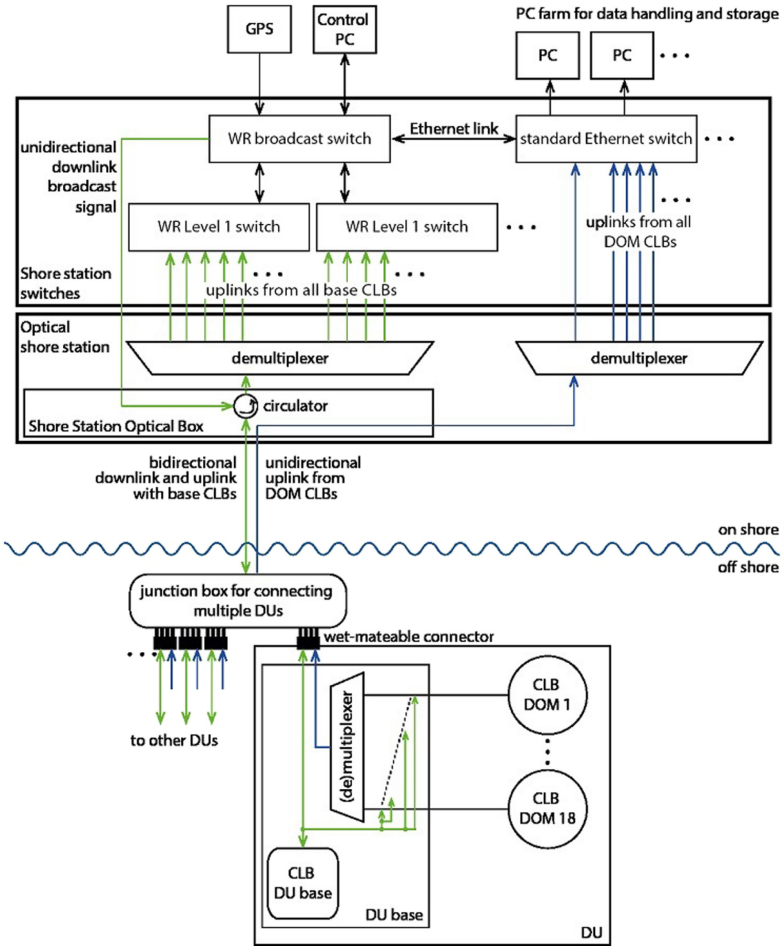

Figure 3.7: Scheme of connections for 1 KM3NeT Junction Box/Node. The green arrows denote the White Rabbit slow control/detector control uplink and downlink, the blue lines indicate the standard Ethernet uplinks from the DOM's CLBs to shore. Picture taken from [104].

3.4.1 Optical network

Each Broadcast WRS controls all the DUs connected to one Junction Box/Node (i.e., 12 for KM3NeT/ARCA and 25 for KM3NeT/ORCA). When more Junction Boxes are installed off-shore an additional level of WRS must be deployed. This level, nicknamed as *Bridge* WRS, interfaces the Broadcast WRS with GPS. A standard WR link connects the Bridge and Broadcast WRS. With the beginning of Phase 2, another switch, the GrandMaster WRS, will interface the Bridge WRS with the GPS. It is mandatory that all the Broadcast WRS installed in the shore station are synchronized with the Bridge WRS, and in turn the Level-1 WRS connected to each Broadcast WRS. In Fig. 3.7 the optical connections between the Broadcast on-shore and off-shore parts is schematized. As illustrated in the previous sections all the asymmetries of the optical fiber network, that is the difference between the travel time of optical signals in the slow control and detector control link, must be measured and accounted for to synchronize the detector. In the Broadcast architecture fiber length asymmetries appear in the shore station, in the Junction Box/Node and in the base module as different optical fiber path lengths

due to the presence of optical amplifiers, and as different travel time of slow control and detector control signals in the main electro-optical cable due to chromatic dispersion on the optical fiber.

3.4.2 Darkroom time calibration

In the Broadcast configuration, DOMs are not properly synchronized with the WR protocol since each CLB receives the clock from the Broadcast WRS without adjusting for the master-slave delay. This means that DOMs of a DU have staggered time fronts, with the stagger given by the propagation time of the clock signal in the optical fiber from a DOM to the following one (in addition to other delay components such as the PMT transit time, electronic delays etc.).

The determination of these offsets is the goal of laser measurements performed on reference PMTs inside a darkroom, at the KM3NeT test site in Caserta and at the Laboratori Nazionali del Sud in Catania. Since the optical connections inside the DU do not change after the darkroom calibration, the time delays between each DOM (more precisely, between reference PMTs in each DOM) and the CLB in the base module of the DU can be measured in the darkroom and kept the same in situ, unless a change of PMT High Voltage is applied, that would change the transit time. The darkroom calibration setup is sketched in Fig. 3.8.

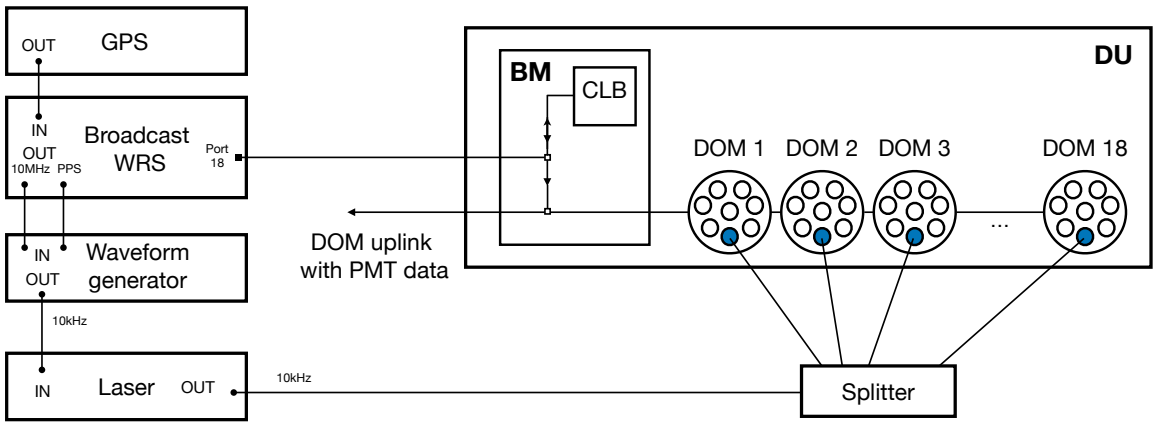

Figure 3.8: Sketch of laser system for the darkroom time calibration setup. The Level-1 WRS, needed to establish communication with the CLB in the base module of the DU is not drawn for simplicity.

The Pulse Per Second (PPS), a high-precision timing signal in WR that generates a pulse at the start of every second, from the Broadcast WRS is the trigger that is used to generate the laser calibration signals. Based on the PPS signal, a waveform generator produces a train of pulses at 10 kHz that drives, in turn, a picosecond laser emitter. The laser produces blue light to which the PMTs are sensitive. The laser head is connected to a fiber optic splitter, of which one fiber is addressed to each DOM. The fibers of the splitter have the same length (with cm accuracy) and the optical coupling is such that

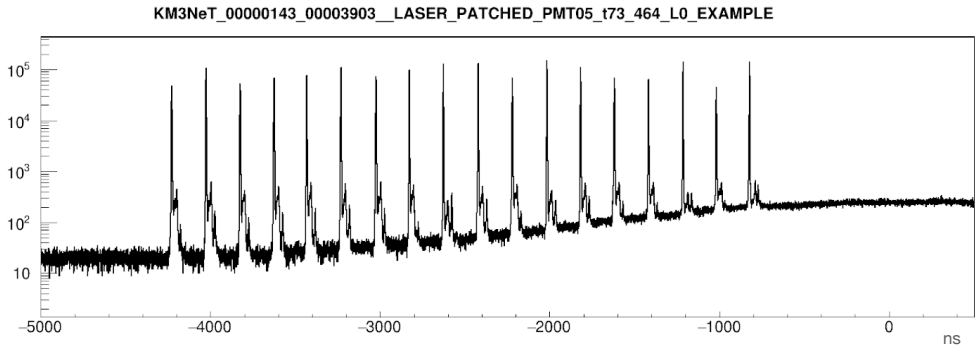

Figure 3.9: Typical histogram of the laser photon hit times (in ns) obtained during the calibration of a Broadcast KM3NeT/ARCA DU. The inter-DOM time delays for KM3NeT/ORCA DUs correspond approximately to 50 ns (10 m optical fiber length between DOMs) Figure produced by the KM3NeT timing calibration working group.

all DOMs receive the same light intensity (±6dB). The fiber output is placed in front of two reference PMTs of each DOM: typically PMT 7 (top hemisphere) or 15 (bottom hemisphere) are used. Laser intensity close to a single photoelectron per pulse is used for the time calibration measurements. All the electronics and optical time delays of the laser system are measured in advance and are remeasured when needed and monitored, to determine the absolute time offset between the PPS of the Broadcast WRS and the emission of the laser signal. The test station WRS fabric also uses a Level-1 WRS to establish communication with the CLB in the base module of the DU.

Synchronization of the test station WRS fabric is a mandatory step to measure reliable values of the $RTTC$ between the WRS fabric and the CLB in the base module. The measured value of $RTTC$ for each DU later enters in the inter-DU offset calculation together with the asymmetry of the shore-to-sea and sea-to-shore fiber paths in the shore station rack and with the calibration tables of the WRS Broadcast and Level-1 WRS. After the test station is set-up and calibrated, the measurements of inter-DOM time offsets takes place. During laser runs, the uplinks from the DOMs contain the TDC data with the laser signal. The average difference between the time of the photon hit, t_{hit}, and the measured arrival time of the laser light at the reference PMT, t_{meas}, provides the time calibration offset, t_0^{DR}, for the DOM j in DU i:

$$t_0^{DR}(i,j) = t_{hit}(i,j) - t_{meas} \tag{3.5}$$

Hence, the laser calibration effectively provides time relative calibration offsets between the DOMs of a DU and the CLB in the base module. Instead, the absolute time of the photon hit cannot be recovered, directly, from the darkroom calibration: this requires measurements of inter-DU time delays. In Fig. 3.9 a typical histogram of the laser photon hit times detected by the reference PMTs in DOMs of a KM3NeT/ARCA DU during the darkroom calibration, performed in the Caserta test site, is shown. Each peak is from the reference PMT in a DOM and the difference between peaks is approximately 200 ns, that is the travel time of light in about 40 m of optical fiber. For each DU calibrated in the darkroom, the T_0 set is stored together with the test station time offsets. An uncertainty in Eq. 3.5 arises from the undetermined offset between the laser trigger pulse and the laser output signal: this is typically calibrated to zero from factory (i.e., it is

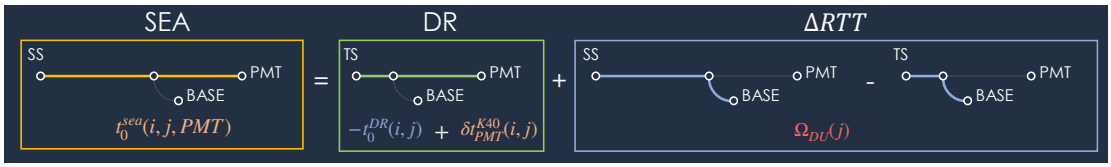

Figure 3.10: Overview of the darkroom to sea calibration procedure, used to obtain the PMT time offsets in sea $t_0^{sea}(i,j,PMT)$ (for a PMT in DU j, DOM i), starting from the darkroom measurement $t_0^{DR}(i,j)$ and the in situ ^{40}K measurement $t^{K40}(i,j,n)$. The correction $\Omega_{DU}(j)$ represents the difference ΔRTT in the round trip times measured in the shore station (SS) and in the test station (TS). Picture taken from an internal presentation of the KM3NeT timing calibration working group.

synchronous with laser photon emission).

3.4.3 Full time calibration

The t_0^{DR} offsets found in Fig. 3.9 are calculated with the DU connected to the test station (TS) facility. Once deployed and connected to the shore station (SS), such values must be translated to the new ones which take into account the different delays and asymmetries of the shore station configuration. Finally, the ^{40}K calibration gives the values for all PMTs of a DOM:

$$\Delta t_0^{sea}(i,j,PMT) = -t_0^{DR}(i,j) + \delta t_{PMT}^{K40}(i,j) + \Omega_{DU}(j) \tag{3.6}$$

Here, $\delta t_{PMT}^{K40}(i,j)$ is the time offset for each PMT in DOM i, DU j with respect to the reference PMT used in the darkroom calibration, and $\Omega_{DU}(j)$ is the difference between the RTT measured after the deployment and in the darkroom test station. A minus sign is applied to $t_0^{DR}(i,j)$ because of the intrinsic negative value of the offset (the clocks of the CLBs anticipate the clock of the Broadcast WRS). This procedure is outlined in Fig. 3.10. Indeed, changing from the test station to the sea, the change in the clock path until from the WRS to DOMs will be equal to the change of the clock path until the CLB in the base module (whose $RTTC$ can be measured), since the base module is a relatively fixed reference to the DOMs. Yet, using the $RTTC$ as given by the WR tool on the CLB in the base module for this purpose, asymmetries in both architectures (test station and sea) must be taken into account. The global constant with all these factors that must be added to the whole DU to properly correct the T_0 measured in the darkroom is the Ω_{DU}:

$$\Omega_{DU}(j) = \tfrac{1}{2}\left[RTTC_{BASE}^{sea} + RTTC_{BASE}^{DR} + ASY^{SS} + ASY^{MEOC} + ASY^{JB_j} + ASY^{TS}\right]$$

$$+ Tx_M^{SS} - Tx_M^{TS} + \Delta Rx_S^{sea-DR} + \Delta T_{GPS-WRB}^{SS}$$

where:

- $\Delta T_{GPS-WRB}^{SS}$: delay between the GPS in the shore station and the Broadcast WRS

- $RTTC^{sea}_{BASE}$: measurable $RTTC$ in the sea from the shore station Broadcast WRS to the CLB in the base module, with CLB delays Tx_S,Rx_S set as 0. It must be updated simultaneously in all the DUs after each deployment.
- $RTTC^{DR}_{BASE}$: measurable $RTTC$ in the darkroom from the test station Broadcast WRS to the CLB in the DU base module, with CLB delays Tx_S,Rx_S set as 0.
- ASY^{SS}: asymmetry of the shores station between slow control and detector control fibers
- ASY^{MEOC}: chromatic asymmetry of the main electro optical cable
- ASY^{JB^j}: asymmetry of the Junction Box/Node where DU j is connected to
- ASY^{TS}: asymmetry of the test station
- Tx^{SS}_M: Tx_M of the Broadcast port in the shore station
- Tx^{TS}_M: Tx_M of the Broadcast port in the test station
- ΔRx^{sea-DR}_S: difference in the Rx_S of the CLB in the base module from the darkroom to the sea; this is usually null.

The Ω_{DU} value is specific for each DU, and its precise determination allows to perform a correct inter-DU calibration. Since in situ $RTTC$ depends daily and seasonally, dominantly on the temperature conditions in the shore end of the main electro-optical cable, a simultaneous update of the $RTTC$ reference of all the DUs in water is necessary, when a new DU is deployed. An eventual delay between the GPS and Broadcast WRS of the shore station represents a global offset and must hence be taken into account in order to assure the absolute synchronization of the detector.

3.5 In situ time calibration

In addition to the ^{40}K and atmospheric muons calibration, described in Sec. 3.3, the KM3NeT collaboration has developed other methods to perform time calibration checks of the detector elements, based on the measurement of the travel time of light emitted by dedicate devices. These methods represent an important tool to keep under control the synchronization of the detector and thus to provide a stable, sub-degree angular resolution and, as it is the case for the nanobeacons (Sec. 3.5.1), have already proven their reliability with the Broadcast architecture. In the context of the time calibration strategy that we propose for the Standard WR scenario, we foresee to employ them as well, as a further check on the synchronization.

3.5.1 Nanobeacons

Each DOM is equipped with a nanobeacon, which consists of a flashable LED (light emitting diode) at a wavelength of 470nm and an electronics board responsible for generating the trigger signal for the optical pulse. The LED is installed in the top hemisphere of the DOM, pointing upward to DOMs above in the DU. When operational, the LED produces

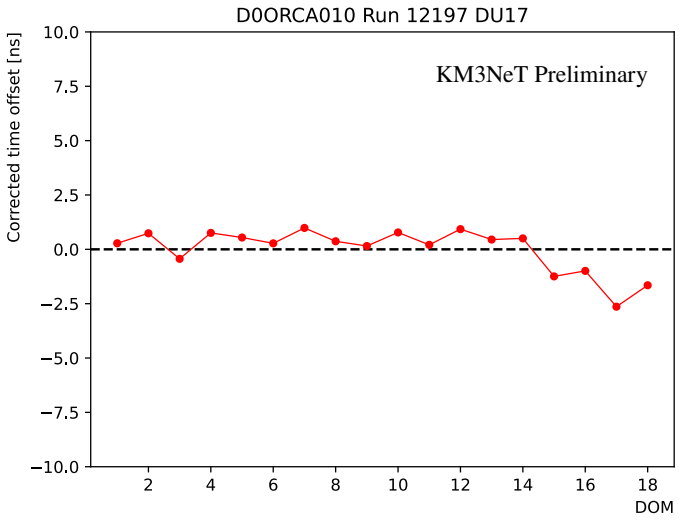

Figure 3.11: Correction to the nominal T_0 offsets found from a nanobeacon analysis for a KM3NeT/ORCA DU. Picture taken from [109].

short light pulses of $\sim$ 3 ns of rise time. The nanobeacons are used to determine the relative time offsets among DOMs of the same DU: during dedicate calibration runs, the nanobeacons are activated and the light from a LED beacon in a DOM is detected by the PMTs in the above DOMs. The difference between the time of the detection of the LED light on DOM j and the emission time of the light by the LED on DOM i, subtracted by the travel time of light in the medium between DOMs, which is $c_{water} \cdot \Delta x_{ij}$ (assuming a fixed DU geometry) where c_{water} is the sound velocity in water, gives the relative time offsets:

$$\Delta t_{i,j} = (t_j - t_i^{flash}) - c_{water} \cdot \Delta x_{ij}. \tag{3.7}$$

The emission time of the light is obtained by using the three closest PMTs to the nanobeacon within the DOM. The accuracy of the method is increased thanks to the redundancy given by considering all the possible pairs of illuminated DOMs, flashing all the nanobeacons of a DU [109]. This results in a system of $\frac{1}{2}18(18-1) = 153$ equations with 17 unknowns, fixing the offset of one DOM, e.g., the first one. This method is used to check the consistency of the inter-DOM offsets found in the darkroom and to determine the ones of the few DOMs that, due to technical issues, were not possible to calibrate in the darkroom. An analysis, performed in KM3NeT/ORCA, comparing offset corrections found with nanobeacons and atmospheric muons methods showed sub-ns agreements between the two [104].

3.5.2 Laser beacon calibration

This calibration is in development and provides an independent cross check of the inter-DU time offsets estimated with atmospheric muons. Reproducing the principle used in ANTARES, it relies on laser beacons consisting of titanium containers equipped with a battery powered laser source at with 532 nm, a diffuser, a quartz rod and the necessary control electronics. Each beacon is located in a position (on Junction Boxes within detector array in KM3NeT/ARCA, on dedicated frames called *Calibration Bases* outside the detector array in KM3NeT/ORCA) such that it can illuminate all DUs with light

pulses up to a distance of about 250 m and hence allowing the verification of the inter-DU time delays by measuring the relative time differences of the hit times on the DUs. Dedicated acquisition runs can be performed on a weekly basis, to provide the necessary statistics to evaluate the inter-DU time offsets through linear fits of the distance with respect to the detection time for each DU with at least two DOMs hit by the light pulses. Simulations taking into account Laser characteristics, diffuser, quartz rod and propagation in sea water predict a light pulse width of around 3 ns for closest DOMs, which has been confirmed with preliminary runs taken with KM3NeT/ARCA.

3.5.3 PMT high voltage dependence

During operation of the KM3NeT detector a re-tuning in situ of the PMT high voltage bias might be needed; since this affects the transit time of the PMT, this would affect the t_0 offset for that specific PMT. Hence, a re-calibration of the time offset is necessary, and can be done with the knwoledge of the PMT transit time (or, the hit arrival time) dependence on the high voltage.

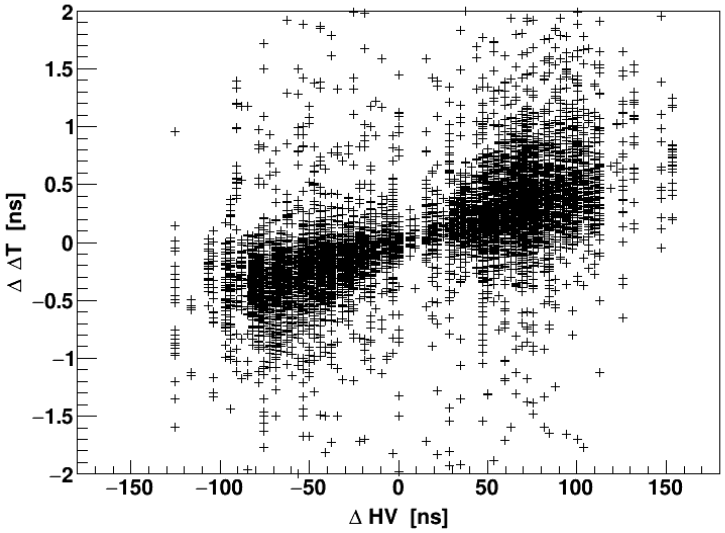

Figure 3.12: Time offset changes $\Delta(\Delta T)$ of ^{40}K hits time differences on PMTs as function of the HV change for a KM3NeT/ORCA DOM. Each point represents a PMT pair with only one PMT with a modified high voltage. Picture produced by the KM3NeT Calibration working group.

This dependence has been studied with a pulsed laser: the high voltage change from 900 V (usual voltage) to 1300 V (the maximum voltage used in the KM3NeT context) gives a transit time difference of $\sim$ 6 ns. Alternatively, the time differences can be measured in situ considering the Δt between ^{40}K hits on PMT pairs. Then, one of the high voltage of one of the PMT of the pair is changed, and the Δt re-measured. The distribution of the difference of the Δt as a function of the high voltage applied gives the desired correction. An example of this plot is shown in Fig. 3.12 and shows that for a closer, more realistic range of voltage variations the time differences are mostly contained within 1 ns.

Chapter 4

Time calibration of the Standard White Rabbit system

Phase 1 of KM3NeT/ARCA was completed in 2023, with the integration of all the 31 Broadcast DUs and the deployment of 28 DUs of KM3NeT/ARCA. In October 2024, the last three Broadcast DUs have been deployed, along with the first 3 DUs of Phase 2, i.e., which use the Standard WR. The Standard WR architecture must allow, as it is for the Broadcast, a sub-ns synchronization of the detector elements (i.e., between the PMTs) in order to reach the desired sub-degree angular resolution. Like for the Broadcast, the time calibration of the Standard WR system is crucial in order to achieve this goal. In this chapter, the strategy that, together with the working group of timing calibrations, I have conceived is illustrated, together with the results from the calibration of the first Detection Units of the Standard WR architecture, among which three have been deployed.

4.1 General overview

The implementation of the data transport and clock transmission system of KM3NeT Phase 2 is based on a standard, point to point, White Rabbit multi-layer architecture and an additional "sensor" layer composed by the PMT and its front-end electronics.

The WR hierarchy for KM3NeT Phase 2 is shown in Fig. 4.1. As for the Broadcast case, the reference time plane of the physics events is defined at the photocathode of the PMT, and the time calibration procedure aims at characterizing and measuring the time offsets between the detector clock (i.e., the reference absolute GPS time) and the photon hit time. The absolute time reference is provided by the same GPS in use for the Broadcast system, connected to a GrandMaster WRS. In turn, the GrandMaster WRS synchronizes, via bi-directional single-fiber links, a second layer of WRS: the Bridge WRS; in KM3NeT/ARCA the three Bridge WRS control and synchronize both the Phase 1 Broadcast branch (3 Broadcast WRS) and the standard WR fabric.

The third WR level of the Standard WR fabric is composed of a row of so-called *Dry* WRS. This is the last last layer of WRS on-shore, equipped with long-range tunable laser SFPs. The ports of the Dry WRS communicate, point-to-point, with a *Wet* WRS (WWRS) in the DU base module. The DU base module for the Standard WR scenario differs from the one of the Broadcast case: the re-developed, enlarged, titanium

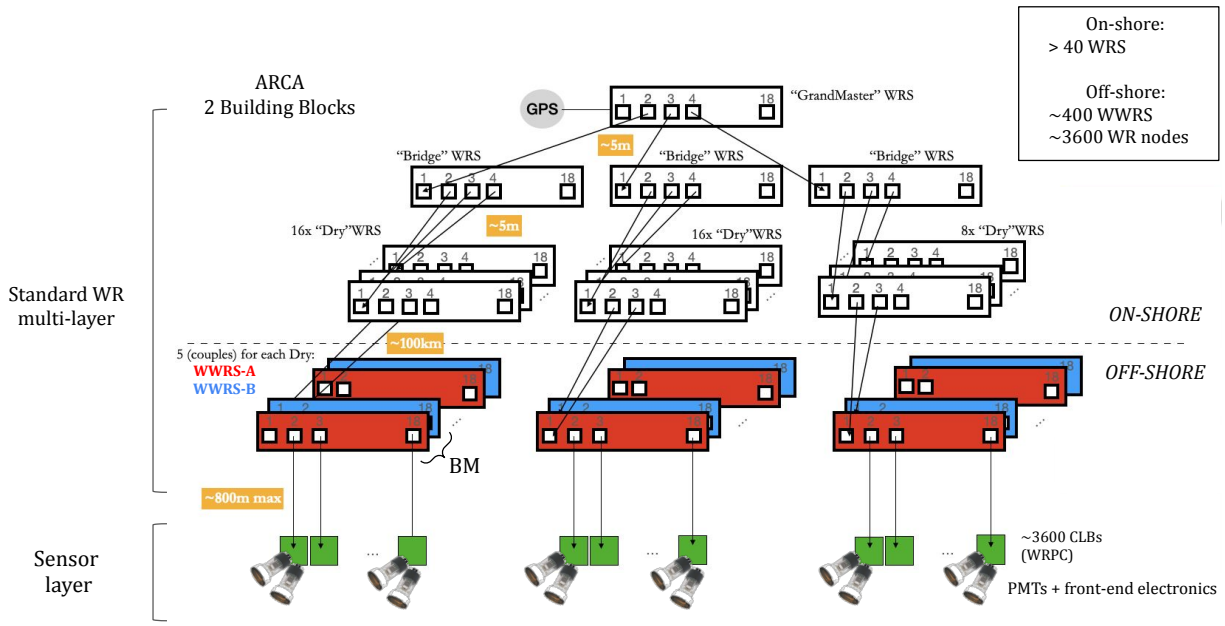

Figure 4.1: Scheme of the White Rabbit based KM3NeT/ARCA data/clock transport system for Phase 2.

container includes two custom WRS, identified as the WWRS-A and WWRS-B. These are composed of a standard White Rabbit switching core board mounted on a backplane developed by KM3NeT. The backplane is designed to host 18 Glenair® transceivers, to which the DOMs of the DU are connected, subdivided in the two WWRS, with bi-directional Glenair fibers. Ports 2 of the WWRS couple are connected among each other, to implement a backup interlink which is activated to re-direct data traffic from one WWRS to the other in case of failure of one of the two WWRS.

A complex optical-fiber infrastructure (described in Sec. 4.3) ensures communication between the Dry WRS and the WWRS. The number of Dry WRS in the shore station depends on how many DUs are connected to each of them, taking into account that out 17 ports are available, out of which for every DU two ports are needed for the links with the WWRS and one port is needed for the redirection of data from/to the data acquisition system. In KM3NeT/ARCA, a maximum of five DUs are connected to each Dry WRS, resulting in a total minimum number of 40 Dry WRS when KM3NeT/ARCA will be completed (199 Standard WR DUs). Off-shore, about 100 km distant, almost 400 WWRS and approximately 3600 WR nodes (the CLBs) will be present making KM3NeT/ARCA the largest and widest White Rabbit network in the world.

The last layer of the WR architecture is formed by the CLB hosted in the DOMs, directly connected to the ports of the WWRS. Eventually, each CLB interfaces the "sensor" layer composed of the 31 PMTs and their front-end electronics. In a standard White Rabbit network all the WRS devices are automatically synchronized and have the same time phase upon two conditions:

1. All the time latencies of the opto-electronic components (e.g. board, ports, transceiver) are calibrated and corrected;

2. All the point-to-point optical connections between each master and slave use a

single fiber (or two fibers of the same length) and the chromatic dispersion of the fiber is known or negligible.

The implementation of the KM3NeT Standard WR data/clock transport system is subject, however, to two main complications:

1. The asymmetries in the time propagation delays between shore-to-sea and (transmission) and sea-to-shore (reception) are present in the system due to:
   - the different fiber lengths, mainly due to the presence of optical amplifiers in the Junction Box in the transmission channel;
   - the chromatic dispersion of the optical fiber, that is the different propagation time of signals used for transmission and reception along the main electro-optical cable (mainly).
2. The effort to measure the Tx/Rx fixed delay values, described in Sec. 3.1.1, of each WWRS port and of each CLB (several thousands) is too much demanding in terms of time and manpower, thus so far not compatible with the detector completion time.

Together with the other members of the working group dedicated to timing calibration, I have therefore implemented the following "mixed" approach to calibrate the time delays:

- All the WRS on-shore (the fabric, from the GrandMaster WRS to the Dry WRS layer) and their optical transceivers has been calibrated by us at the KM3NeT/ARCA shore station during the summer of 2024 using the standard Open Hardware White Rabbit procedure (as described in Sec. 4.2.3). I have also verified again the synchronization of the fabric after the installation at the shore station. Re-calibration can be always performed at the shore station, in case of need.

- All WWRS will have port 1 (connection to the Dry WRS onshore) and port 2 (backup interlink between WWRS-A and WWRS-B) and their transceivers calibrated before integration (as described in Sec. 4.4.1). The calibration will be verified during the DU integration process. In this early stage, I have decided to adopt a temporary solution, also described in Sec. 4.4.1.

- Optical fiber network asymmetries are measured by the optics working group before the integration of the detector (see Sec. 4.2.3). These contributions are presently intended to be added offline in the offsets of the T_0 set. As a viable alternative option, these values could be inserted in the WWRS calibration tables as additional offsets of the Tx/Rx fixed delays and in the alpha fiber asymmetry coefficient. In the latter case the WWRS would beat the same time of the WRS fabric onshore. However, we consider this approach at this stage not mature, since it requires a high level control and monitoring of the calibration tables of a very large number of devices.

- The time calibration of the DU is measured in a darkroom almost identically to what was done in the Phase 1 (Broadcast) production. That is, the electronics latencies of the communication ports (i.e., Tx/Rx) of the WWRS to the CLBs

and the ones of the CLBs themselves, in addition to the electronics delays of the sensor layer (i.e., the reference PMT transit time, front-end electronics, and photon hit timestamping by the TDCs in the CLB) are calibrated simultaneously using a pulsed laser source, synchronous with the GPS (as described in Sec. 4.4.2).

It is important to remind that the darkroom calibration, performed for two reference PMTs in each DOM (PMT-7 in the upper, PMT-15 in the lower hemisphere), accounts for the so-called inter-DOM time delays. In the Standard WR architecture the inter-DU delay is automatically calculated by the measurement of the optical asymmetries, and it does not need the measurements and recording of the *RTTC* and WR fabric Tx/Rx values. A scheme of the time delays in situ and in darkroom, according to the calibration strategy that we propose, is reported in Fig. 4.2. For KM3NeT/ARCA, two darkrooms are currently (March 2025) in use: one is located inside the Caserta KM3NeT laboratory and test station (in which I produced the results presented in the thesis), and another at the Laboratori Nazionali del Sud, in Catania. The two darkroom stations are conceptually identical, the only difference being the characterization of the laser delays, as different optical fiber splitters and models of lasers are used. In the next future, a third darkroom is foreseen to be prepared at the Istituto Nazionale di Fisica Nucleare in Genova.

4.2 Calibration of the White Rabbit fabric on-shore

The onshore WRS fabric is composed of standard WRS which run a customized version of WR firmware *v6.1* for KM3NeT specific purposes, namely the *6.1-rc*. The new feature introduced by the customization is the implementation of the so-called "jumbo frames" for the data packet size, which is relevant to the KM3NeT data acquisition system; this feature does not affect the synchronization protocol. When an official WRS firmware version is released by Open Hardware White Rabbit, a corresponding set of calibrated fixed delays is distributed and is configured in the *dot-config* file of the device. This is also the case for the firmware 6.1: https://ohwr.org/project/white-rabbit/-/wikis/Calibration#default-calibration-values-for-wr-switch. The KM3NeT custom firmware *v6.1-rc* comes with the same *dot-config* file as of *v6.1*. Nonetheless, the synthesization of the new custom firmware has introduced unknown fixed delays in the WRS electronic components, as well as inside the FPGA chip, which were not measured by the Open Hardware White Rabbit community. Thus, we cannot rely on the firmware *6.1* calibration constants, as we have experienced delays larger than 1 ns when connecting a WRS *v6.1* to a WRS *v6.1-rc*, if we used default calibration values for the latter.

Moreover, since we are going to deploy several layers of WRS in the shore-stations, the use of common default values for all the WRS, along with their uncertainties, could lead to the pile-up of the uncertainties from the first to the last layer, possibly resulting in synchronizations worse than 1 ns. For these reasons, a dedicated calibration of the KM3NeT WRS fabric must be performed.

4.2.1 White Rabbit switch calibration

The procedure for the calibration a WRS is illustrated in the Open Hardware White Rabbit Calibration document: https://ohwr.org/project/white-rabbit/wikis/Documents/White-

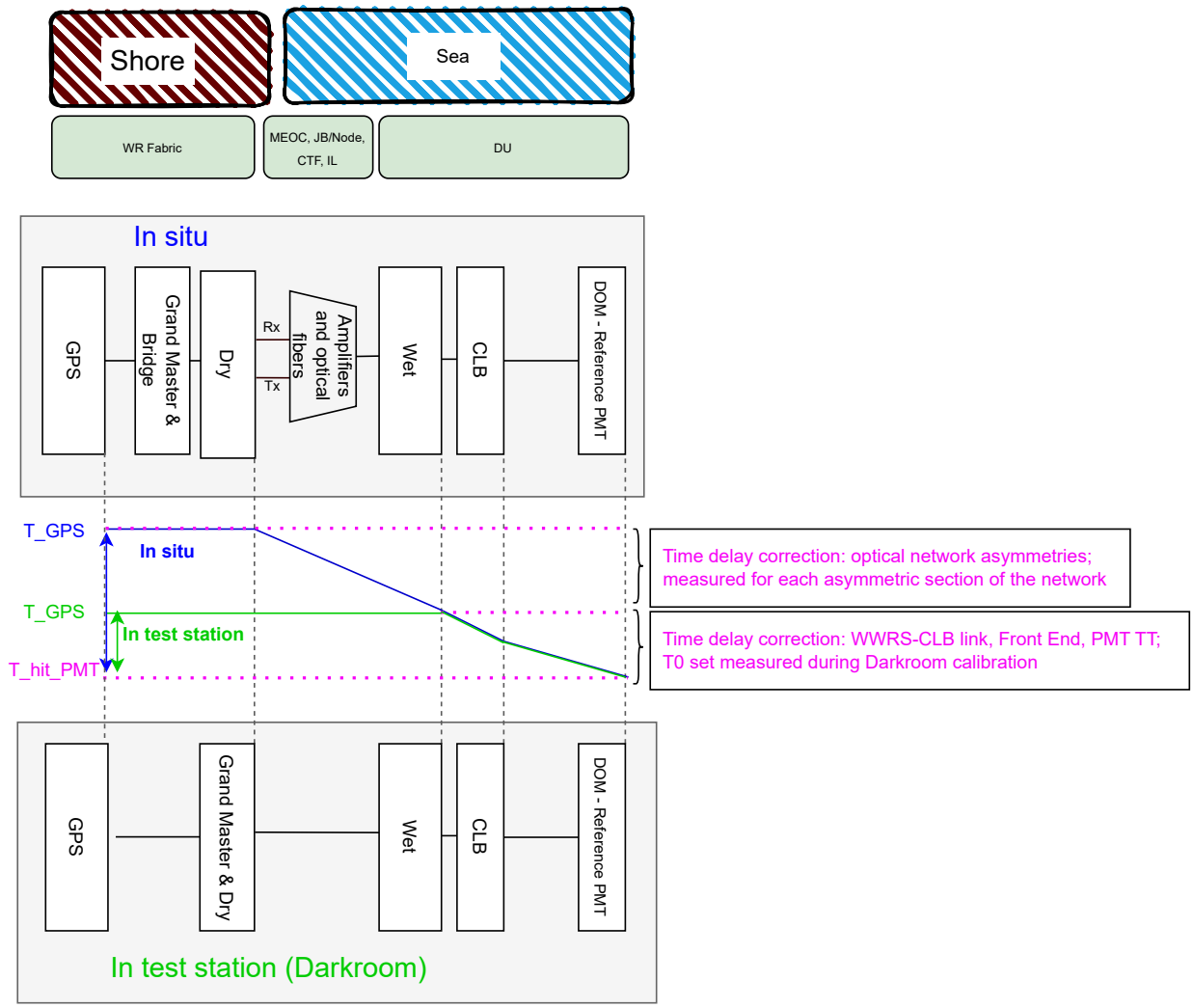

Figure 4.2: Scheme of the time delays in KM3NeT Standard White Rabbit architecture, in situ and in darkroom (at Caserta and Catania test stations).

Rabbit-calibration-procedure. The main concept of the calibration is that each White Rabbit switch (or node) has some constant transmission and reception delays on every port that are the summed result of the delays of the SFP transceivers, the electronic components and the traces on the printed circuit board, as well as the delays inside the FPGA chip. To achieve the best synchronization between WRS, those fixed delays for each port and for each WRS must be measured so that the WR protocol can automatically compensate for them. This is achieved by modifying the fixed hardware delay parameters in the configuration *dot-config* file in the WRS. The measurement of these delays is the goal of the WRS calibration procedure, that must be done before deploying the WRS fabric.

Unfortunately, there is no easy way of separating the contribution in the fixed transmission and reception delays of the WRS port itself and of the SFP plugged in the port. Thus, during the calibration procedure the measured fixed Tx/Rx delays are actually the overall delays of the port and of the corresponding SFP. Hence, substituting the SFP in a calibrated port could result in inaccuracies (potentially up to several hundreds of ps, as we observed during a measurement session performed at CERN in March 2024, described in [110]) if the SFP is substituted with a SFP from a different vendor or from a different production batch. In those cases, a re-calibration of the port and SFP couple is desirable. For these reasons, in the following the term "calibration" refers to the calibration of the coupled port and SFP, and the SFP used in the calibration process is meant to be left plugged in the WRS and to be used in the foreseen standard operation of that WRS.

The preliminary step in the procedure is to define the so-called *Golden Calibrator*. The Golden Calibrator is a standard WRS whose ports hardware fixed delays are known and measured, allowing one to use it as a known reference during the calibration of the other devices.

4.2.2 The Golden calibrator

The procedure for the creation of the Golden Calibrator is reported in the Open Hardware White Rabbit Calibration document [111]. The Calibrator has to be selected among the set of available WRS. The only constraint for the selection is having two instances of the same (as much as possible) switch: they must both have the same PCB layout and the same FPGA bitstream, and the selected port on the switches, that will become the Calibrator(s) reference port, should mount complementary SFPs from the same producer and same production batch. The procedure creates a couple of identical reference ports with same, known fixed delays on the Calibrator(s); the procedure can be repeated on other ports, also with different types of SFPs. The Golden Calibrator is how one of these two WRS is called, in the context of KM3NeT.

We ideated the Golden Calibrator for KM3NeT at CITIC-Granada in April 2024, starting from two WRS at CITIC-Granada, shown in Fig.4.5, that were known to be entirely produced (i.e., in all of their components) by the same company. The two WRS have the official *v6.1 fw*. Connecting two complementary AXGEN SFPs (Axcen Photonics Corporation®), one at 1310 nm and the other at 1490 nm, of the same production batch on port 1 (one set as Master, the other set as Slave) of both WRS, and leaving the same default calibration values in the *dot-config* of both WRS, the skew between the *Pulse Per Second* (PPS) of the two switches, which indicates the difference in time

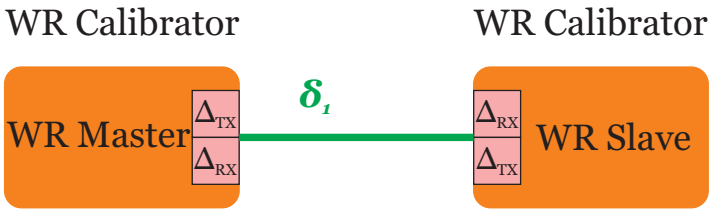

Figure 4.3: Pre-calibration of the Golden Calibrator(s) pair, using a fiber with known, measured latency δ_1. Picture taken from [111].

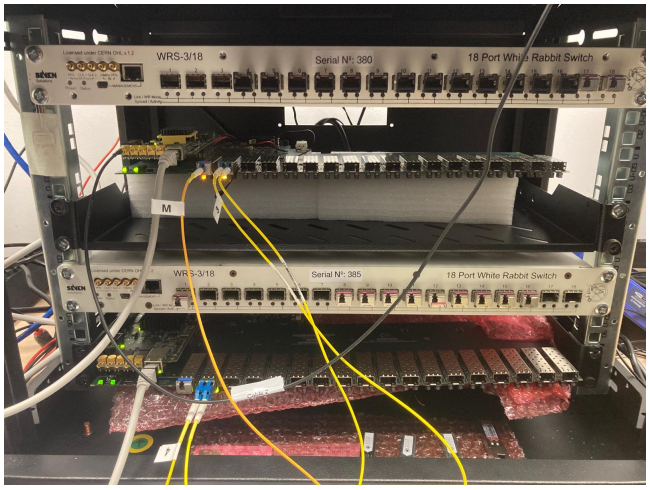

Figure 4.4: the selected Golden calibrator(s) pair, at CITIC-Granada. In ports 1, bi-directional AXGEN SFPs are plugged (1490 nm, 1310 nm). In ports 2 Lumentum tunable SFPS are plugged.

synchronization, was measured to be -35 ps at the oscilloscope. This showed that the two WRS on port 1 have almost identical fixed delays, and we can safely assume that:

$$Tx_M + Rx_M = Tx_S + Rx_S \tag{4.1}$$

This was indeed the smallest value that we observed among several pairs of WRS which we tested; thus, this couple of devices was selected.

Swapping the SFPs between the two WRS, the PPS skew was measured to be -43 ps. This negligible difference found after the swap of SFPs indicates that the two SFPs are symmetrical, i.e., introduce the same delay. At this point, following the procedure the total fixed delay of the two devices:

$$\Delta = Tx_M + Rx_M + Tx_S + Rx_S \tag{4.2}$$

Naturally, the Calibrator has some internal asymmetry, which means that $Tx \neq Rx$. To determine the exact values of Tx and Rx, one should take apart the Calibrator and measure the latency of PCB traces, electronic components, SFP transceivers, that is in principle possible but not trivial at all. Therefore, as in procedure, we assumed that the Golden Calibrator(s) have no asymmetry:

$$Tx_M = Rx_M \tag{4.3}$$

$$Tx_S = Rx_S \tag{4.4}$$

and we assigned:

$$\Delta/4 = Tx_M = Rx_M = Tx_S = Rx_S \tag{4.5}$$

to each fixed delay for port 1 in the *dot-config* files of the two WRS. This assumption does not affect the later calibration quality, as it is taken into account during the actual calibration of each WRS. One of the two WRS was selected to become the Golden Calibrator: its port 1, with the AXGEN 1310 nm and 1490 nm SFPs used in this pre-calibration step and set with $\Delta/4 = Tx_M = Rx_M$ can be used for calibrating other WRS ports which mount compatible (in terms of wavelength) Axcen or BlueOptics® SFPs, which are the models used in KM3NeT WRS. We performed the above-mentioned procedure also with ports 2 of the Golden Calibrator(s), plugging tunable Lumentum (Lumentum Operations LLC®) SFPs from the same production batch. In this case, leaving the same default calibration values in the *dot-config* of both ports the PPS skew between them was found to be -5 ps. Swapping the SFPs, the value did not change, showing a very good symmetry between the combined fixed delays of ports and SFPs. The Golden Calibrator port 2, with its Lumentum SFP and after this pre-calibration, can and has been used for calibrating other WRS ports which mount Lumentum SFPs.

4.2.3 White Rabbit switch calibration

Having defined the KM3NeT Golden Calibrator, the calibration of WRS of the KM3NeT WRS fabric can be performed following the standard procedure in [111]. In short, the switch under calibration (Slave) is synchronized by the calibrator (Master) through an optical fiber with known $RTTC$ on a selected port. The WR software of the Slave switch provides the user with the $delay_{MM}$ measured value. From the knowledge of the Master fixed delays and the fiber latency, the sum of the Slave fixed delays is given by reverting Eq. 3.2:

$$\Delta_S \equiv Tx_S + Rx_S = delay_{MM} - Tx_M - Rx_M - RTTC \tag{4.6}$$

where Tx_S, Rx_S are the summed contributions of the port and related SFP delays. Initially, Tx_S, Rx_S are both set to the coarse value $\Delta_S/2$. Then, by looking at the PPS skew between the calibrator and the WRS with an oscilloscope or a time interval counter, the values are corrected for their asymmetry:

$$Tx_S = \frac{\Delta_S}{2} - skew_{PPS} \tag{4.7a}$$

$$Rx_S = \frac{\Delta_S}{2} + skew_{PPS} \tag{4.7b}$$

The procedure is then repeated for all the ports and plugged SFPs of the switch. Once that the fixed delays of both the Slave and the Master are known and the switch is connected to another Master with a different fiber, the protocol infers and provides the user with the correct $RTTC$ from the $delay_{MM}$ measurement. At the end of the procedure, for each switch and for each combination of port and SFP, the values Tx, Rx are found and configured in the *dot-config* file of the switch. In a test that I conducted at CITIC-Granada in April 2024, results have shown that connecting six WRS calibrated in this way in cascade and comparing the PPS skew between the first and last WRS in

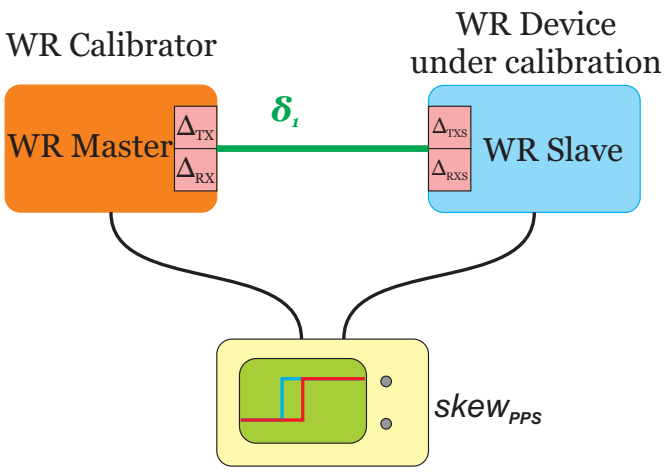

Figure 4.5: WRS calibration using a WRS Calibrator (e.g. KM3NeT Golden Calibrator) and a fiber with known, measured round trip time $RTTC$. Picture taken from [111].

the cascade, it was found to be smaller than 10 ps, as well as between any two layers in the cascade.

The Golden Calibrator port 2 not only can be used for the calibration of the WRS shore station fabric but in the future will also be used for the calibration of port 1 of the WWRS, where a Lumentum tunable SFP is plugged. Instead, ports 3-18 of the WWRS mount Glenair transceivers which cannot be easily handled and connected, leading to a complex and time-consuming calibration. The backup interlink ports of the WWRS (port 2) are calibrated, but not in a standard way. Details are given in Sec. 4.4.1.

Calibrated WRS, apart from the shore station, must be also used in:

- Base module integration sites, to allow the verification of the synchronization of the WWRS port 1 before integrating the WWRS inside the base module. In fact, the PPS skew between the base module integration site calibrated WRS and the WWRS port 1 should be smaller than 100 ps, if the calibrations have been performed correctly.

- Darkroom test station rack; this is crucial to grant the consistency of the measurements done in the darkroom with a DU, once the DU will be deployed offshore and connected to the shore station WRS fabric.

4.2.4 The KM3NeT Child Calibrator

The requirement to perform the calibration of a WRS port is the knowledge of the fixed delays of the calibrator WRS. After the calibration, the fixed delays of the port are known, and in turn that can be in principle used for the calibration of other WRS ports. In KM3NeT, we define as *Child Calibrator* a standard WRS that was calibrated from the Golden Calibrator, with some ports calibrated with AXGEN/BlueOptics SFPs and some others with the Lumentum tunable SFPs.

Thus, the Child Calibrator can be used to calibrate either WRS ports with AXGEN/Blue Optics SFPs or with Lumentum SFPs. In this way, the Child Calibrator is capable of calibrating any WRS of the KM3NeT fabric, just like the Golden Calibrator.

At CITIC-Granada, in April 2024, I have performed a test in order to demonstrate that the use of the Child Calibrator as calibrator device is equivalent, within 10 ps, to using the Golden Calibrator:

1. A WRS port was calibrated using port 1 of the Golden Calibrator WRS
2. The same WRS port was then calibrated using port 1 of a Child Calibrator WRS; eventually, the port was connected to port 1 of the Golden Calibrator in order to check the synchronization.

The Tx, Rx obtained after the two calibration are shown in Tab.4.1: differences are smaller than 10 ps.

calibrator (port 1)	calibrated port Tx (ns)	Calibrated port Rx (ns)
Golden Calibrator	256.377	260.637
Child Calibrator	256.386	260.630

Table 4.1: Calibration of a WRS port using the Golden Calibrator and the Child Calibrator. Resulting values of Tx, Rx are compatible within 10 ps.

The PPS skew when the port, calibrated with the Child Calibrator, was connected either to the Golden Calibrator was found to be 3 ps (shown in Tab.4.2), indicating that the calibration with the Child Calibrator is as accurate as the one done with the Golden Calibrator. The estimated link length, computed by WR from the $RTTC$, is identical in both cases, and compatible with the true fiber length of 2.66 m (measured in the lab), showing the correct determination of the port fixed delays. The difference in the PPS

Master (port 1)	Estimated link length (m)	$delay_{MM}$ (ns)	PPS skew (ps)
Golden Calibrator	2.658	1058.215±0.001	3±1
Child Calibrator	2.659	1058.609±0.001	8±1

Table 4.2: WR parameters when the WRS port, calibrated with the Child Calibrator, is synchronized by either the Golden Calibrator or the Child Calibrator. Errors are computed as $\sigma/\sqrt{N}$, where σ is the standard deviation from N measurements. 60 measures were taken from the WR software tool, while 300 measures were taken with the oscilloscope for the PPS measurement.

skew is 5 ps, consistent with the difference in the Tx, Rx values found between the two calibrations (-9 ps for the Tx and $+7$ ps for the Rx). The reason behind the creation of a Child Calibrator is the convenience for the experiment of having one (or more) calibrators, which are located in Italy (and France), that can be used in the integration sites and shore stations, to calibrate the necessary WRS equipment.

After having performed the proof of concept, at CITIC-Granada we have created two Child Calibrators:

- One has been shipped to Catania and is located at the LNS(Laboratori Nazionali del Sud)/Portopalo; we have used it from April to September 2024 to calibrate the WRS fabric at the KM3NeT/ARCA shore station, at the LNS darkroom test site, and the Dry WRS at the LNS base module integration site.

- One has been shipped to Bologna, and I have used it to calibrate the Dry WRS of the Bologna base module integration site, and the WRS fabric of the Caserta darkroom test site.

4.2.5 Synchronization of the WRS fabric onshore

Once that WRS in the shore station is deployed, and their final SFPs plugged, they can be calibrated. For this calibration, we have used the LNS/Portopalo Child Calibrator. The used SFPs are listed in Tab.4.3. Once the WRS were calibrated, the due fiber con-

SFP	type	WRS (port)
BlueOptics 1490 nm	singe-fiber	Bridge(1), Dry(1)
BlueOptics 1310 nm	single-fiber	GrandMaster(2-18), Bridge(2-18)
Lumentum tunable	dual-fiber	Dry(3-18), WWRS(1)
Glenair 1330 nm	single-fiber	WWRS-A(2-18), WWRS-B(3-18)
Glenair 1270 nm	singe-fiber	WWRS-B(2)

Table 4.3: SFP types used in the KM3NeT Standard White Rabbit system.

nections for the shore station were implemented. Due to the total large number of ports, the calibration of the WRS has been done using a dedicated setup which automatizes the procedure. The setup we created, shown in Fig.4.6, is based on the design of the setup which is present at CITIC-Granada, and it is composed of the Child Calibrator, a Raspberry Pi® board, a Keysight® 53230A time interval counter, a networking switch and a 1-to-32 fiber splitter. 18 fibers of the splitter, of which we measured the $RTTC$, are simultaneously connected to the ports of a switch in the fabric, and a script automatically calibrate ports one after the other. The time interval counter is used for the measurement of the PPS skew. Several calibration sessions have been performed during the summer of 2024 in order to calibrate the shore station WRS fabric which will be used for the operation of the first 17 DUs of the Standard WR system, that has been partially installed (3 DUs were succesfully deployed) in October 2024. With this procedure, the measured delay between the layer 1 (Bridge) and any of the layer 3 WRS (Dry) was found to be smaller than 100 ps. In a later stage, we foresee to employ the same setup, with the addition of a multiplexer required for coping with the large number of WRS, for a constant monitoring of the PPS skew between WRS of the fabric and, if necessary, for the re-calibrations in case of:

- shifts in the PPS skew over time during operation;
- substitution of SFPs;
- upgrade of WRS firmware.

Since after the DU deployments the WWRS PPS signal is no more available, in order to monitor the synchronization between the Dry WRS ports and the WWRS we plan to use an additional, spare, calibrated WWRS. This will be connected to a spare port of one of the Dry WRS. Their PPS skew will be verified and monitored, and in case of WWRS firmware updates, this spare WWRS will be used for measuring the time offset between the different firmware versions. This time offset will eventually be taken into account to correct the T_0 offset sets.

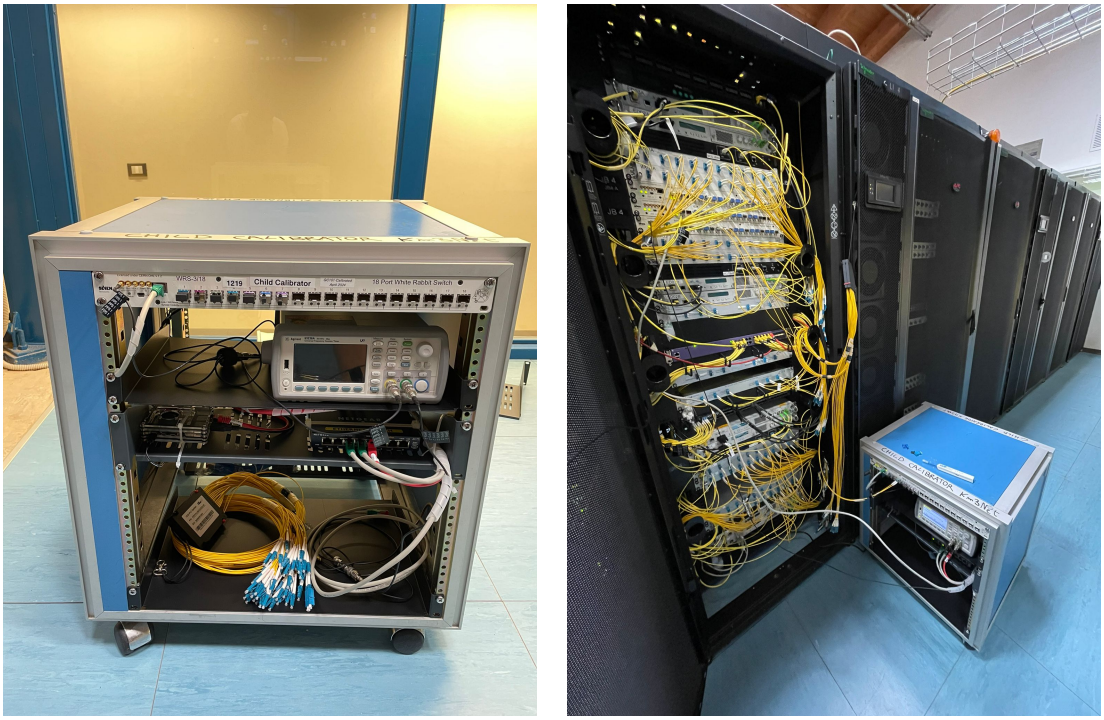

Figure 4.6: Left: the automatic setup of the LNS/Portopalo Child Calibrator. Right: the automatic setup during the calibration of a WRS in the KM3NeT/ARCA shore station.

4.3 Optical fiber network onshore and offshore

The optical network for KM3NeT Standard WR architecture has been designed to minimize the number of optical paths where Tx/Rx asymmetries may arise. A scheme of the optical fiber connections from the shore station to DOMs, highlighting the asymmetric path sections is shown in Fig. 4.7. The segments of optical connections, from sea to shore, are:

1. the optical link between the CLB in the DOM and the WWRS; this is implemented by a single bi-directional optical fiber. The maximum length of this link (700 m approximately for the highest DOM) is such that chromatic dispersion can be neglected. Beyond this, any asymmetry is absorbed in the darkroom calibration, described in Sec. 4.4.2, when the T_0 set is determined.

2. the optical connection between Lumentum transceiver on WWRS port 1 and the interlink cable that connects the DU to the Junction Box comes over two separated fibers for transmission and reception of an optical filter in the base module, which routes the two different wavelengths over a single fiber. Symmetric filters are used (i.e., the delay difference between the transmission and reception paths is smaller than 50 ps), but in any case the asymmetry is measured during the characterization of the filters at the integration stage, and taken into account.

3. A single fiber for transmission/reception is used inside the interlink subsea cable between the DU and the Junction Box. The length of the interlink is not larger

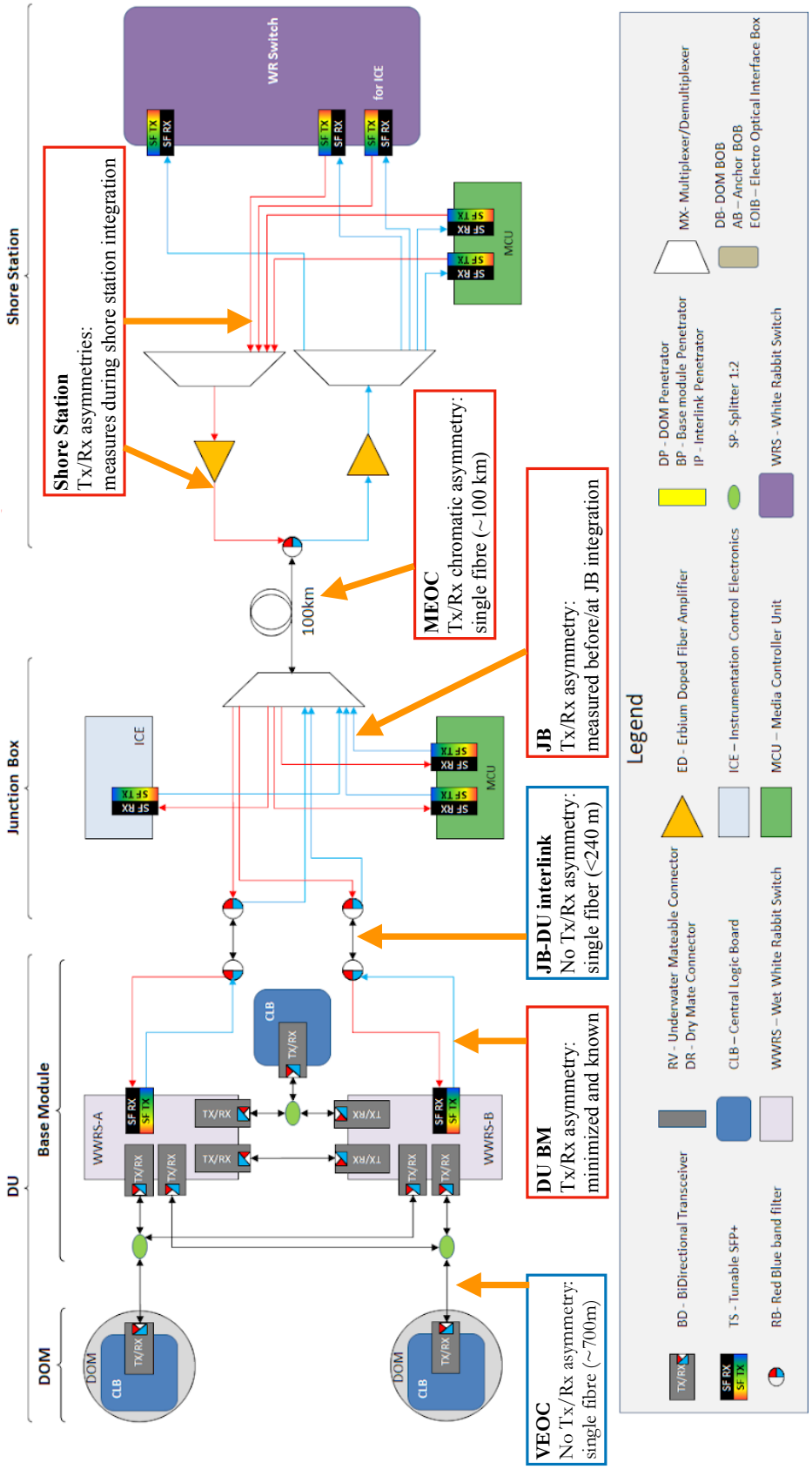

Figure 4.7: Scheme of the optical path of the Standard WR architecture. The optical lines from shore to sea are represented with red (meaning larger optical wavelengths) lines, the sea to shore connections are represented with blue lines. Black lines are bi-directional single fiber connections. Picture adapted from an original scheme provided by the KM3NeT optics working group.

than $\sim$ 250 m, which is a negligible distance to observe chromatic dispersion effects.

4. The optical link inside the Junction Box (or Node) is strongly asymmetric, due to the need of installing a pair of optical amplifiers to optimize the data transport from shore to sea. The two asymmetries in the transmission and reception paths for the two WWRS are measured by the optics working group during the Junction Box integration stage, by measuring the RTT along the transmission paths (2 for each of the 7 ports), and reception paths (2 for each of the 7 ports) of the Junction Box. This is done using an autonomous WR-based setup, composed of a WRS and a WRPC board. The Junction Box has two different optical amplifiers, and decribed measurements are done for both, activating them in turn.

5. The link between the Junction Box and the shore station is the main electro optical cable and is bi-directional. Optical fibers in the cable are approximately 100 km long, and suffer from chromatic dispersion over such a long distance. This asymmetry is parametrized by the α coefficient in WR, and can in principle be set in the calibration tables of the WWRS for automatic compensation. However, being this approach unnecessarily complex for the moment given the large number of nodes, we decided to set α to 0 (i.e., no asymmetry), as it is in the Broadcast case for the CLBs in base modules, and the asymmetry offset will be accounted for offline. The optics group conducted measurements of the KM3NeT/ARCA main electro optical cable for Phase 2 with a setup which is the same as the one used for measuring the Junction Box asymmetry, but with an optical amplifier onshore to allow transmission over loopback fibers ($\sim$ 200 km in total).

With respect to the main electro optical cable, an additional contribution to the travel time of optical signals should be considered, that is the dependence of the optical fiber length, and thus of the $RTTC$, as a function of fiber temperature. This effect arises mainly in the onshore and shallow water section of the cable, since the temperature change is negligible at depths larger than a few hundred meters. Daily and seasonal effects have been observed in the past: for the former, $RTTC/2$ oscillations of the order of few hundreds of ps for KM3NeT/ORCA and tens of ps for KM3NeT/ARCA were measured; for the latter, few nanoseconds variations were registered for both detectors. Variation of $RTTC$ as a function of temperature is coherent among all wavelengths on the same fiber and, with good accuracy, for all fibers of the same cable. In the Standard WR scenario this effect is negligible since it corresponds to a symmetric elongation or shrinking of the optical fiber. On the other hand this effect induces a common and equal time shift to all the CLBs of the DUs of the Broadcast sector. The reconnection of the time offsets of the Standard and Broadcast DUs would require in this case a dynamic calibration taking into account, offline, a correction coefficient for the gradient of travel time of optical signals in the cable.

4.4 Standard White Rabbit Detection Unit calibration

Time calibration of the offshore part of the network, that is of the DU with its DOMs and WWRS, is of uttermost importance since it relies on unique laboratory measurements carried out before the deployment, and non directly repeatable or verifiable after. Therefore, it represents a crucial step of the calibration of the detector required to reach the

sub-degree angular resolution. Due to the previous considerations, a reliable calibration of the "Wet" part of the links between the Dry WRS and the WWRS must be carried out during the commissioning of all DUs. Furthermore, the behaviour of the link must be closely monitored at run time, during laser runs in the darkroom. The calibration of the DOM, that is the CLB fixed delays, the delays of the electronics related to the PMT hit timestamp as well as the PMT transit times, are the goal of the darkroom process.

4.4.1 Calibration of the Wet White Rabbit Switches

The custom backplane board of the Wet WRS mounts 18 optical transceivers, just like the standard WR backplane. One of those, namely port 1, mounts a Lumentum tunable SFP where two fibers of an optical filter are connected, as shown in Fig.4.7. This is the port where the WWRS is synchronized by the Master Dry WRS onshore. The frequency of the SFP is tuned to a specific value for each WWRS, compliant to the multiplexing in the Junction Box and de-multiplexing onshore. Port 2 is dedicated to the backup interlink, with a Glenair transceiver at 1330 nm on WWRS-A and at 1270 nm on WWRS-B. All the other ports mount Glenair transceivers at 1270 nm, complementary to the Glenair at 1330 nm on the CLBs. The calibration of all the 18 ports must be taken into account. The scheme of the connections of the WWRS is shown in Fig.4.8. Redundancies are implemented by means of optical splitter: fibers from 12 DOMs are connected to both WWRS. The link with the CLB in the base module is also redundant. Hence, out of the 15 available ports in each WWRS for DOM connections, 3 are assigned to direct DOM connections, 6 by to the default DOM connections, and the remaining 6 are for the redundant connections. The redundant link is not activate during normal operation, when the laser of the related WWRS port transceiver is turned off. If the default connection to one of those DOMs is lost, the redundant link is activated by turning on the laser of the transceiver. In that case, the DOM is synchronized by the other WWRS and sends data to it.

Dry WRS - WWRS link

In production, according to our strategy, port 1 of the WWRS will be precisely calibrated at the board assembly stage with a Golden (or Child) calibrator. After that, the following checks are foreseen:

- During the base module integration process in the four different dedicated sites, where the WWRS is connected to a Dry WRS in the integration site, the check of synchronisation of WWRS will be performed by a measurement of the Pulse Per Second (PPS) skew. Since the Dry WRS in the integration site are calibrated with the Child Calibrator, the synchronization of the WWRS achieved with the Golden (or Child) calibrator during its assembly is recovered and consistent also with the Dry WRS in integration sites.

- During darkroom laser runs, any residual miscalibration on port 1 of the WWRS will anyhow be accounted for, since they will be included in the T_0 set.

However, so far for the first batch of DUs of the Standard WR architecture the calibration of port 1 was not done with the Golden (or Child) Calibrator; instead, we set the Dry

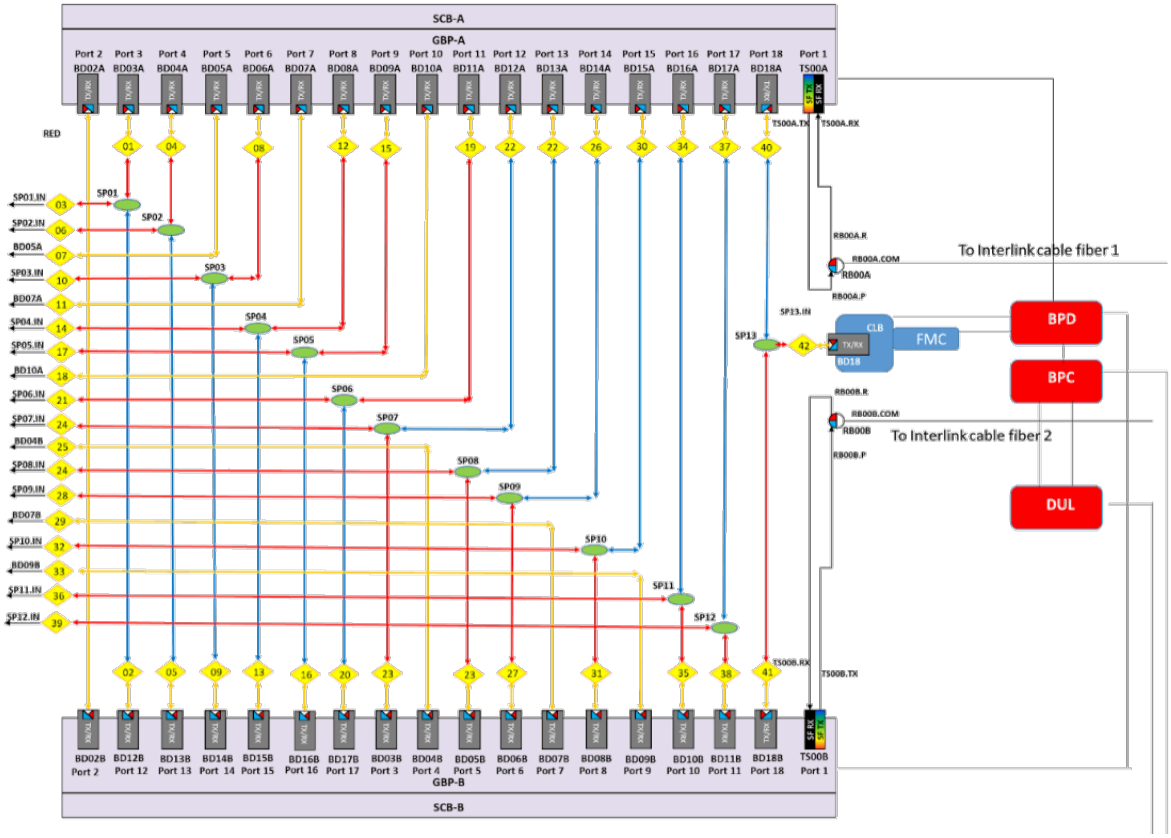

Figure 4.8: Scheme of the optical connections between the 18 DOMs (the yellow rhombuses on the left), the CLB in the base module and the two WWRS of a Standard WR DU, made of a switching core board (SCB) and a custom Glenair backplane (GBP). Green circles represent optical splitters. Yellow lines are the direct connections, while red and blue lines are the redundant connections. Picture provided by the KM3NeT optics working group.

WRS with a calibration table resulting from the average of the tables obtained from the calibration of two WRS with firmware *v6.1-rc*. Then, the same Dry WRS port in the different base module sites is used to calibrate the WWRS port 1 following the standard procedure. This means that discrepancies of hundreds of ps (possibly also of nanoseconds) are expected to occur in the synchronization once the WWRS are connected to the darkroom test station Dry WRS, but this difference is accounted for in the time measurements with the laser. Moreover, laser measurements of a DU with the WWRS calibrated in a base module integration site can show time offsets with discrepancies from the measurements of DUs with WWRS calibrated in other sites, corresponding to the difference in the fixed delays between the Dry WRS of the related sites.

WWRS-A/B backup interlink

Port 2 of the WWRS is employed as a backup interlink between WWRS-A and WWRS-B, for redundancy purposes needed in case of missing link between shore and one of the two WWRS. In that case, a manual intervention is required in order to set port 2 of the malfunctioning WWRS as Slave, and to activate the link between the two ports which are, by default, shut off to avoid a loop between the switches. The Master WWRS will then synchronize the other WWRS, and data taken by the WWRS affected by the fault condition is diverted to the other WWRS and from there to shore. This redundant backup is associated with the following procedures:

- At base module integration sites, the port 2 link is calibrated by activating it, and aligning the PPS signals of the two WWRS. This is not the official standard procedure for calibration but a simplified one that we decided to adopt: after the implementation of the interlink fiber, the PPS skew is measured and used to correct the default fixed values of port 2 of one of the two WWRS. The result is that the two PPS are aligned, so the two WWRS beat the same time, but the $RTTC$ as computed by the Slave WRS is wrong, because it is computed from a wrong initial assumption of total fixed delay value $Tx_M + Rx_M + Tx_S + Rx_S$. This means that the precise synchronization would not be recovered if the fiber was changed; however, since this is not the case and the $RTTC$ measurement is in this case not of interest, the procedure is valid for our purposes.

- The consistency of the calibration is checked with darkroom laser runs, by activating the interlink and comparing laser time measurements with the ones found from the default condition. If the calibration is correctly performed, no difference is expected between the two.

WWRS - CLB link

CLBs inside DOMs represent the last layer of the WR infrastructure. Links to/from CLBs are handled by ports 3 to 18 of the WWRSs. These ports are not calibrated, but have default values. The CLB fixed delays are set using nominal Tx, Rx delays, that I derived from the average values of a set of characterized production CLBs. In order to obtain those values, I calibrated 14 production CLBs in Bologna, and computed the average of the Tx and Rx distributions, shown in Fig. 4.9 for Tx only. The average values of Tx and Rx are respectively 248.710 ns and 193.950 ns, with an asymmetry of 54.760 ns

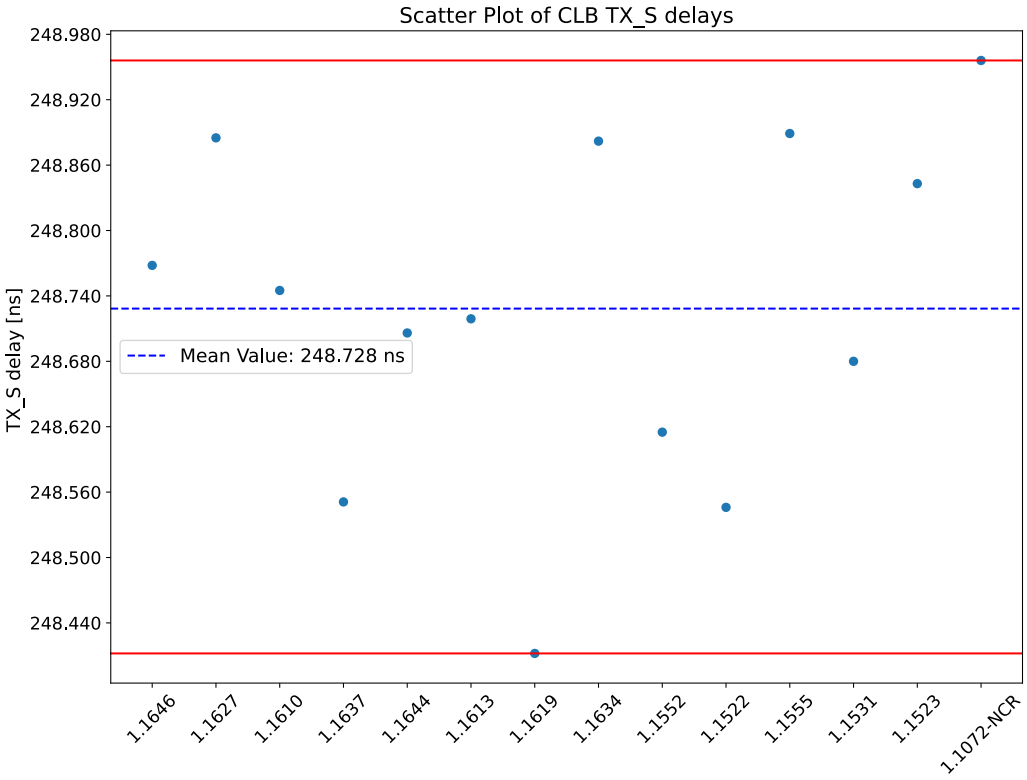

Figure 4.9: Tx values from the calibration of a set of 14 CLBs v4.5 performed in Bologna. The CLBs were calibrated connecting them to port 18 of a White Rabbit switch with firmware $v5$. The spread of CLB Tx values can be evinced, but not the absolute calibration values since they were not calibrated with the Golden/Child calibrator: differences up to few hundreds of ps may be expected.

resulting in a PPS skew of 27.38 ns (half the asymmetry). It is important to rembember that, according to Eq. 3.3, a given introduced asymmetry between transmission and reception in the network results in a PPS skew which is half of the asymmetry. Therefore, an optical asymmetry will be introduced as a consequence of component-to-component variations. As a result, a timing shift between CLBs and WWRs will be present. The choice of proceeding in this way derives from the fact that individual ports and CLB calibrations for the WWRS-CLB links are unnecessarily complex and time consuming, due to the large number of CLBs and WWRS ports to be processed, also in consideration of the fact that such timing shifts can be easily addressed and calibrated during darkroom laser runs, as discussed in the following. It is necessary to calibrate also the redundant links and respective ports; thus, laser measurements when the redundant links are active are necessary.

4.4.2 Darkroom calibration

The last step of the calibration is the determination of the absolute hit times on the reference PMT(s) in DOMs. This is done with laser runs in the darkroom, both in Caserta and at LNS (and in the future, starting from 2025, also in Genova), in a similar

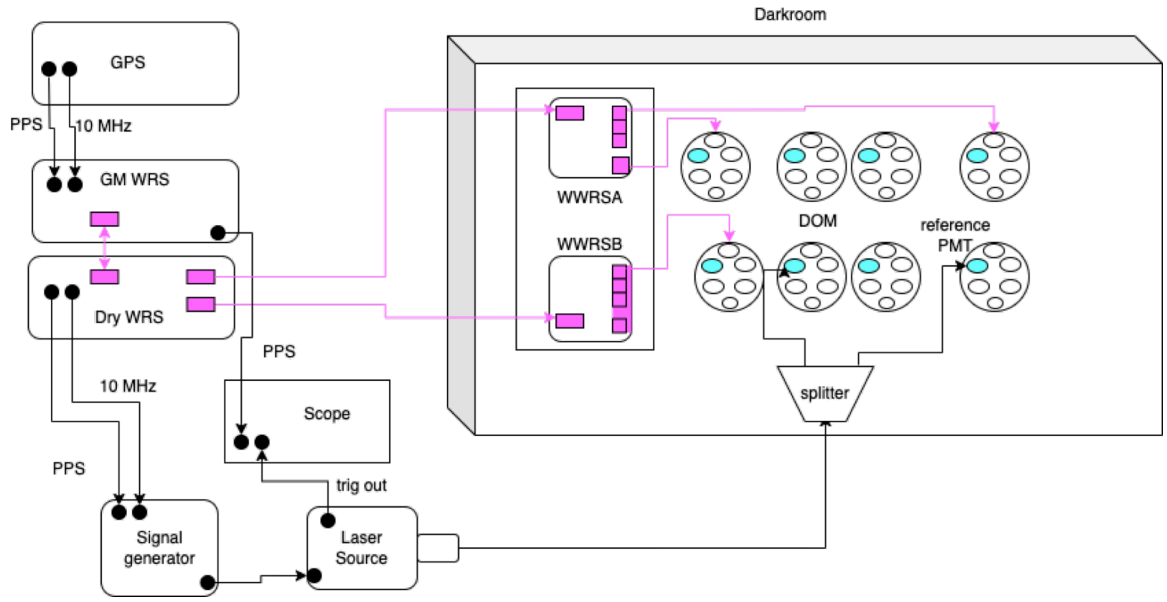

Figure 4.10: Scheme of the darkroom setup. GPS, GrandMaster and Dry WRS are shown on the left, along with the signal generator, laser system and oscilloscope for PPS measurements. The laser splitter (i.e., the laser distribution system) is shown in the darkroom box.

way to the Broadcast laser measurement, with the setup shown in Fig. 4.10. The setup is similar to one used for the Broadcast DUs (described in Sec. 3.4.2), with the difference being in the WRS fabric: in the Standard WR case two standard WRS (a GrandMaster and a Dry WRS), calibrated from the Golden Calibrator, are present. The PPS and 10 MHz signals of the Dry WRS are used for the generation of the laser trigger signal, while the PPS signal of the GrandMaster WRS, which is connected to the GPS and in this case acts as Master for the Dry WRS, is used for the time delay measurement between the the WRS fabric time and the laser out time. Moreover, the concept of the setup is identical for all the darkrooms used in KM3NeT, though some components, e.g., the optical splitter and the laser source, can differ and are thus characterized at each site.

The reference time plane is represented, as in the Broadcast scenario, by the arrival of optical photons on the PMT surface. In the calibration strategy that we propose for the Standard WR system, the measured time offsets include:

1. Residual asymmetries in the chain of links from the Dry WRS, to the WWRS, and finally to the CLB. The presence of such asymmetries is due to:

   - Miscalibration of WWRS port 1;
   - Miscalibration of WWRS ports 3 to 18 and of the CLB;

   and were discussed in Sec. 4.4.1.

2. Opto-electronic delays. An absolute time delay is present from the reference time plane (i.e., optical photon impinging at PMT surface) and the timestamped hit time in the CLB. These time shifts are not handled by the WR synchronization,

and require dedicated measurements carried out in the darkroom. Such delays can be summarized with the following opto-electronic contributions:

- PMT transit time;
- Delays in the readout chain (i.e., in the amplifier, threshold comparator, FPGA and the relative transmission lines).

The combined effect of all these contributions can be globally measured for each single DOM during the DU calibration in the darkroom and give the T_0 sets. The T_0 corrections are found for the pair of reference PMTs for each DOM, and are used to align the time of hits to the reference time plane, during triggering. The absolute time delays of the remaining, non-reference PMTs are later equalized from ^{40}K measurements.

All the timing measurements are carried out after the PMT high voltage tuning step: the tuned high voltage values, which give PMT gains of 3×10^6 and hit time over threshold of 26.4 ns are employed for all the reference PMTs during the laser runs.

4.5 Qualification Detection Unit

The very first Standard WR DU that we tested, in January 2024, in the Caserta darkroom and test station was the so-called *Qualification Detection Unit* (QDU). Its base module was left open during the darkroom tests and sealed only afterwards, in order for us to have access to the Pulse Per Second (PPS) signal from the two WWRS and monitor it with the oscilloscope. In fact, we carried out PPS skew measurements relative to all employed WR components to verify the synchronization of the system. For the tests of the QDU, a pair of uncalibrated WWRS was employed, along with non perfectly symmetric optical filters both in the base module and on the Dry WRS of the darkroom data acquisition rack. As a result, we carried out the calibration of the WWRS in the base module relying on the measurement of the PPS alignment, as done in production for the backup interlink only.

Firstly, we verified the PPS skew between the GrandMaster and Dry WRS (both calibrated with the Golden Calibrator): it was found to be 20 ps, so the two were properly synchronized. Then, we measured the PPS skew between the Dry WRS and the two WWRS, which was found to be 2.35 ns for WWRS-A and 2.30 ns for WWRS-B. These skews include both the misalignment of the WWRS clock due to uncalibrated fixed delays and the contribution of the asymmetrical optical filters (which was measured and accounted for additional ~ 200 ps of skew for both switches). The calibration tables of the WWRS were changed accordingly to correct the skews, and we measured again the values. The same was done with the backup interlink, thus in this case we followed the defined procedure for interlink calibration. Results are listed in Tab. 4.4.

After this step, we connected the PPS signal of the Dry WRS to the signal generator for the darkroom laser emitter. Since the reference time plane of the detector is fixed at the PMT photocathode, the characterisation of the laser delay, i.e., the delay between the PPS of the pulse generator and the arrival of the distributed optical pulses to the PMT surfaces, is of uttermost importance for the characterisation of the absolute hit times of DOMs. This was done before the darkroom runs by:

	PPS skew (ps)
GrandMaster - Dry	20 ± 5
Dry WWRS-A	2355 ± 5
Dry − WWRS-B	2298 ± 5
WWRS-A − WWRS-B	-57 ± 5
WWRS-A^{interlink} − WWRS-B^{interlink}	-495 ± 5
Dry − WWRS-A$_{corr}$	57 ± 5
Dry − WWRS-B$_{corr}$	38 ± 5
WWRS-A$_{corr}$ − WWRS-B$_{corr}$	-19 ± 5
WWRS-A$_{corr}^{interlink}$ − WWRS-B$_{corr}^{interlink}$	-3 ± 5

Table 4.4: PPS skew between WR components during the Qualification Detection Unit tests. WWRS^{interlink} refer to the situation in which the interlink is activated and either of the WWRS is Master of the other. Found offset was then corrected changing the fixed delays in the calibration table of WWRS-B, and afterwards the new skew between WWRS$_{corr}^{interlink}$ was measured.

- measuring the travel time of blue photons in the fiber splitter (equal for all fibers), using a 406 nm source laser, and in the fiber optic distribution system;
- measuring the trigger out signal from the laser controller, and trough knowledge of the typical optical emission delay, declared in the device calibration sheet, of the laser head between trigger and output;

The measured values, considering two different fiber splitters used, are shown in Tab.4.5

	delay (ns)
Dry WRS PPS - laser output	161.722
laser path (1)	51.661
laser path (2)	51.090

Table 4.5: Time delays introduced by the laser emission and the propagation of the light in the path from the laser head up to the PMTs.

The laser is operated using a 10 kHz repetition rate in data-taking runs with a typical duration of five minutes. We carried out laser runs on the reference PMT-8 of all 18 DOMs. Afterwards, from the acquired data root files we extracted the laser hit times using dedicated analysis codes. Laser hits are time-stamped with respect to the PPS and modulo the laser repetition period. Laser hit times distributions are approximately gaussian in shape: a gaussian with overimposed flat (to model ambient light noise) fit is applied on the hit times distributions of each reference PMT to extract the most probable value, hereby identified as *mean peak time*. As an example, a fit from the reference PMT of DOM-17 of the QDU is shown in Fig.4.11. These are distributed around a central value, corresponding to the sum of the contributions listed in Sec.4.4.2 and of the laser delay, shown in Tab.4.5, from the PPS of the signal generator up to the arrival of light at PMTs.

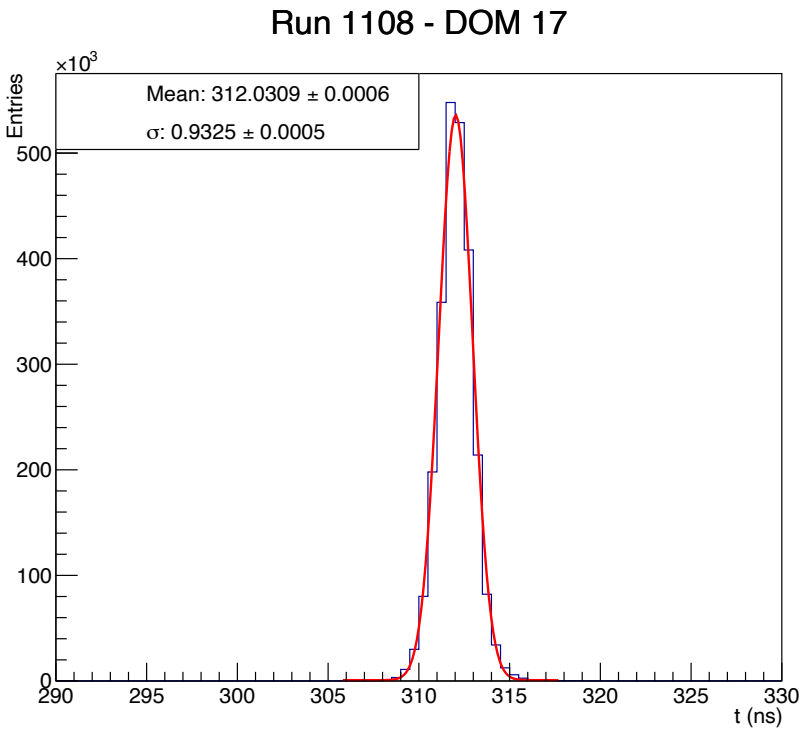

Figure 4.11: Example of laser hit times during darkroom test with the Qualification Detection Unit: DOM 17 in Run 1108 is shown, with a gaussian and overimposed flat (not visible in the scale) fit.

The sigma of the gaussian fits has a typical value of 2 ns, compatible with the expected PMT transit time spread [91]. The relevant laser runs taken with the QDU are listed in Tab. 4.6. At first (run 1108) we left the fixed Tx, Rx delays of CLBs set to 0; then, we set them with the average values found from the 14 CLBs calibration (explained in Sec. 4.4.1). The configuration of such delays on the CLBs, as well as the activation of the interlink or the redundant links on the WWRS occurs in an automatized way through dedicated codes which I developed for this specific purposes.

Run ID	Interlink	WWRS delay on port 1	WWRS delay on port 2	CLB delays
1108	inactive	Default $v6.1$	Default $v6.1$	0
1106	inactive	Corrected	Default $v6.1$	Average
1157	A Master	Corrected	Corrected	Average
1163	B Master	Corrected	Corrected	Average

Table 4.6: Laser runs taken with the Qualification Detection Unit. Average CLB delay refers to the average Tx, Rx values found from the calibration of a set of 14 production CLBs.

In particular:

- Run 1108 is representative of a starting situation with default (Open Hardware White Rabbit firmware $v6.1$) Tx, Rx values on all ports of the WWRS, and CLB Tx, Rx set to 0.

- Run 1106 is representative of a situation with calibrated port 1 on both WWRS and with nominal Tx, Rx correction on all CLBs configuration.

In Fig. 4.12 the distributions of the laser hit times obtained from the 18 DOMs in run 1108 are shown. Mean peak times distribute around a central value corresponding to the sum of laser photons travel time and opto-electronics delays; the residual relative spread corresponds to the residual asymmetries in the links to be corrected. The mean peak hit times are the T_0 used for the time correction. The obtained distributions from 1106 and 1108 are shown and compared in Fig. 4.13. In contrast with the Broadcast scenario, in this case the T_0 offsets are distributed with a standard deviation of ~ 2 ns, indicating the intrinsic goodness of the White Rabbit synchronization of the nodes in the adopted topology.

In particular, with reference to the run 1106, we can carry out the following theoretical delay estimations:

- The average DOM delay is ~ 288.7 ns
- The total laser delay from Tab. 4.5 is ~ 213.3 ns (laser path 1 was used)
- The opto-electronic delays of PMT/CLB (dominated by PMT transit time) are ~ 75.4 ns

The inferred value of the opto-electronic delay is fully compatible with the transit time of KM3NeT PMTs [112], which is ~ 72 ns.

Runs 1157 and 1163, which we took with the interlink active and each WWRS acting as Master of the other, were needed in order to verify the calibration of the interlink. As I show in Fig. 4.13, the mean hit times for DOMs 10:18 (i.e., the ones synchronized by WWRS-B) obtained in Run 1157 are almost perfectly superimposed to the ones of Run 1106, as well as DOMs 1:9 (i.e., the ones synchronized by WWRS-A) obtained in Run 1163, illustrating an accurate synchronization of the Slave switch through the interlink, as if it was directly connected to the Dry WRS.

We did not measure the T_0 set of the redundant configuration, when the synchronization of DOMs occurs via the redundant links, due to lack of time in the production process. In this case, if there will be the need to activate a redundant link, the new T_0 set for the DOM could be obtained starting from the available one and exploiting the in situ atmospheric muon calibration method to correct it.

4.6 Qualification Junction Box

We made a further test of the calibration procedure by introducing in the setup the Qualification Junction Box (QJB) and its test rack. The QJB is the first integrated Junction Box of a new type, specifically developed for the Standard White Rabbit topology and it has been deployed in October 2024. In January 2024, in Caserta, the QDU was connected to the QJB, whose test rack was in turn connected to the test station data acquisition rack. In this way, a situation compliant to the final one after the QDU and QJB deployment was achieved. The goal of the test was to verify that the time delay asymmetry introduced by the QJB optical path, along with its test rack, can be properly corrected from on shore. Thus, after having determined the QJB and QJB rack optical asymmetries, we verified the consistency of the introduced delays by:

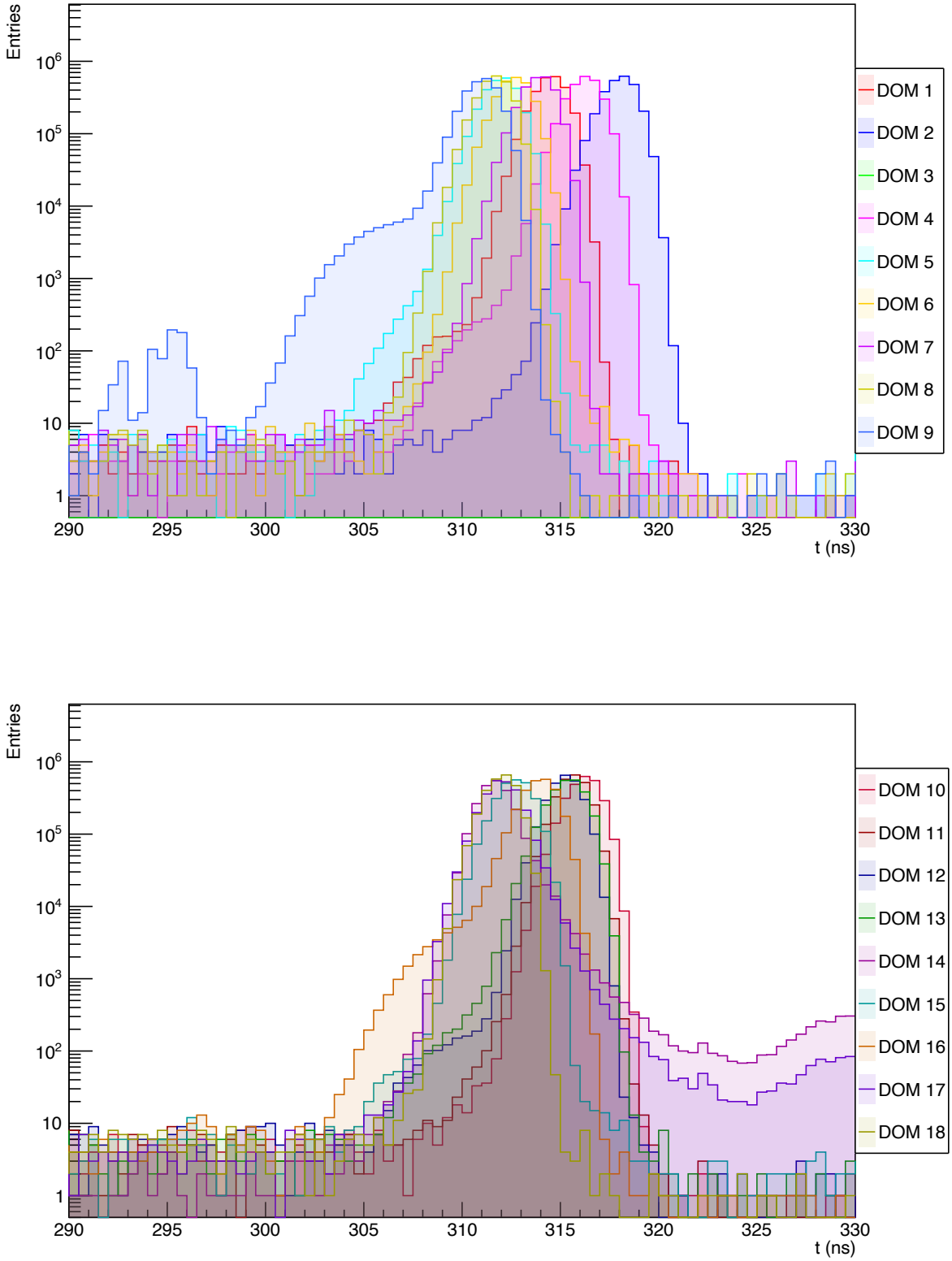

Figure 4.12: Superimposed laser hit times distribution from run 1108 for WWRS-A (top, DOMs 1 to 9), and WWRS-B (bottom, DOMs 10 to 18). Background noise, as well as pre-pulses and after-pulses, are visible due to the logarithmic scale.

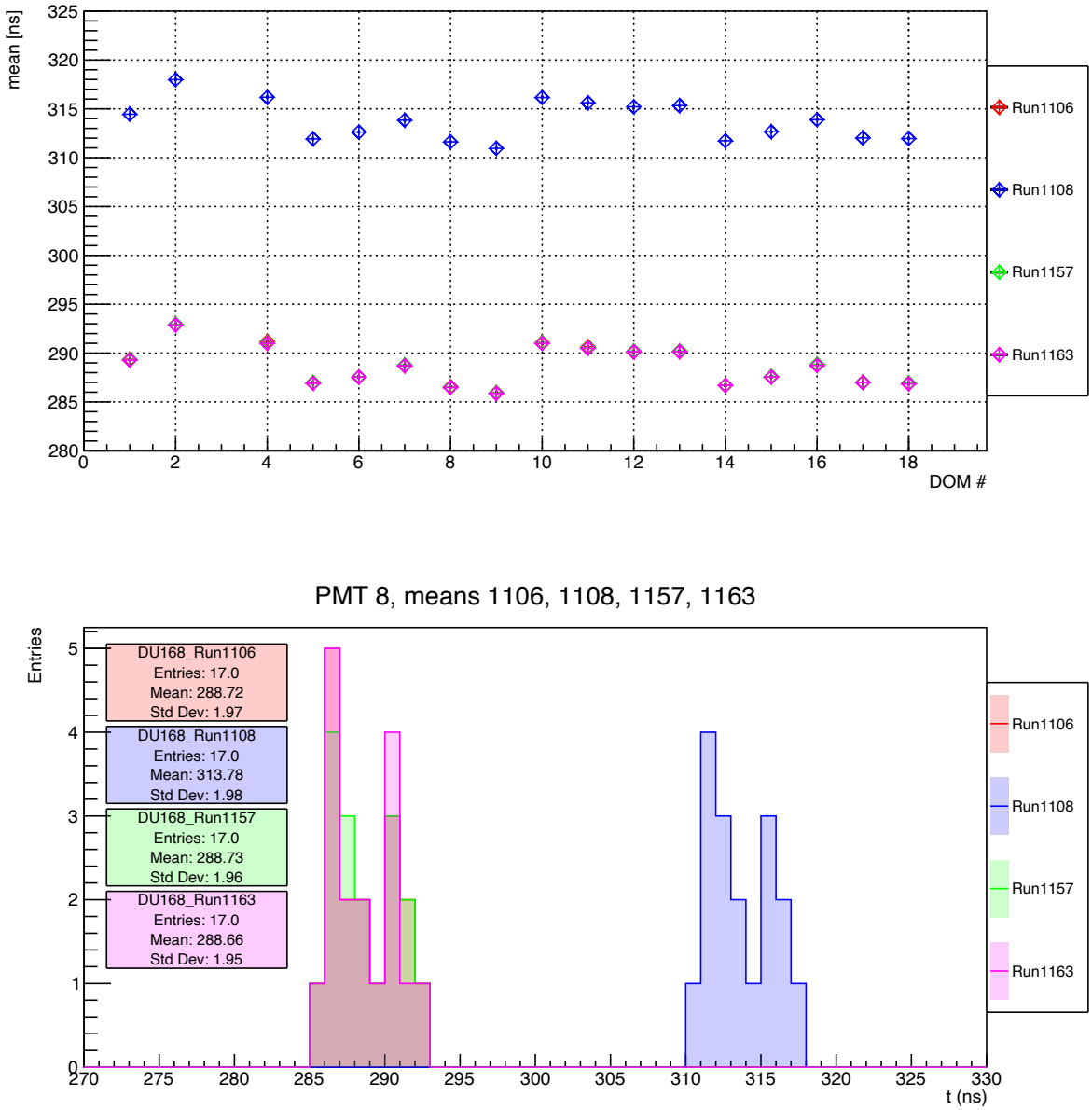

Figure 4.13: Top: mean laser hit times as a function of DOM floor for runs 1106, 1108, 1157, 1163. Error bars (corresponding to fit parameter uncertainty) are shown but hidden inside the marker. DOM 3 was not operative during the runs. Runs 1157, 1163 with the backup interlink activated are almost perfectly superimposed to run 1106, after the calibration of WWRS port 2. Bottom: distribution of mean laser hit times of all DOMs for runs 1106, 1108, 1157, 1163.

- Measuring the PPS skew between the Dry WRS and the WWRS-A/B, and comparing it with the values found for the QDU only setup;
- Measuring the T_0 set, and comparing it with the one found for the QDU only;

In both cases, the comparison with the QDU only setup reflected, as expected, the delay introduced by the QJB and its rack.

The QJB optical asymmetry, that is the asymmetry in fiber length between the shore-to-sea and sea-to-shore optical paths, was measured (as for all Junction Boxes) in advance during the integration. In particular, for each of the 7 ports of the Junction Box to which DUs are connected, the asymmetry of the optical path is measured for both connections to WWRS-A and WWRS-B and for both optical amplifiers. In fact, in the Junction Box two Erbium-Doped Fiber Amplifiers (EDFA) are used, referred to as the primary and secondary (as backup) EDFA, in order to amplify the optical signal from shore to sea. The same is done for the asymmetries in the shore-to-sea and sea-to-shore optical paths, for WWRS-A and WWRS-B connections, in the QJB test rack, which features a multiplexer/demultiplexer and fibers of different lengths. This is done by connecting two White Rabbit boards at the ends of the optical paths of the rack connections, in both stream directions, measuring the *RTT* and comparing them to find the difference. Ultimately, the asymmetry of the optical filters used in the setup with the stand-alone QDU, must be taken into account when comparing results to the QDU and QJB setup, since they are removed once the QJB is introduced. Details of the procedures of all these measurements are out of the scope of this thesis, but the results, which are of interest, are reported in Tab. 4.7.

Measured asymmetries	
Component	Asymmetry/2 (ns)
EDFA Primary Port 1, WWRS-A	86.027
EDFA Secondary Port 1, WWRS-A	89.491
EDFA Primary Port 1, WWRS-B	84.755
EDFA Secondary Port 1, WWRS-B	88.219
QJB test rack, WWRS-A	1.198
QJB test rack, WWRS-B	1.198
Total (EDFA Primary, WWRS-A)	87.225
Total (EDFA Primary, WWRS-B)	85.953
Total (EDFA Secondary, WWRS-A)	90.689
Total (EDFA Secondary, WWRS-B)	89.417
QDU optical filter, WWRS-A	0.140
QDU optical filter, WWRS-B	0.105

Table 4.7: Measured asymmetries (divided by two) for the different components in the Qualification Detection Unit setup with the Qualification Junction Box and stand-alone. The division by a factor two is reported for easiness of comparison, as it corresponds to the expected difference in the PPS skew.

Then, we measured the PPS skew between the Dry WRS and WWRS-A/B and took laser runs for the configuration with the QJB. Results are summarized in Tab. 4.8, where the PPS skew and the mean values of the mean peak PMT hit times distributions for

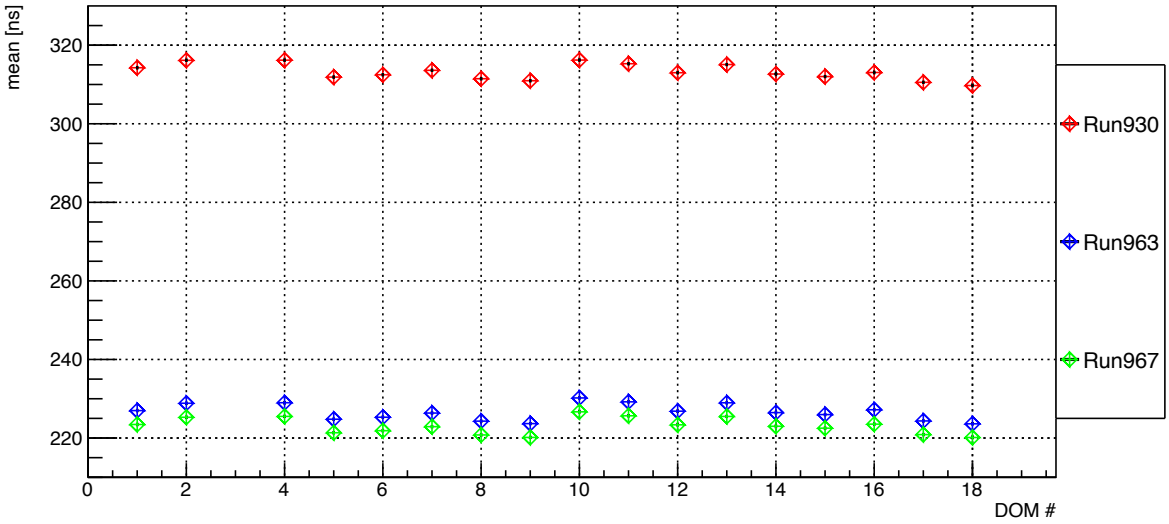

Figure 4.14: Reference PMT peak times for the runs listed in Tab.4.8. DOM #3 was not operative during the runs.

DOMs are compared. Reported reference measurements for the stand-alone QDU in this test differ for few hundreds of ps from results obtained in Sec.4.4, since different optical filters were used. Fig.4.14 show the reference PMT peak times that I obtained for those runs.

Run ID	EDFA	PPS skew (ns)		⟨PMT hit time⟩ (ns)	
		WWRS-A	WWRS-B	WWRS-A	WWRS-B
963	Primary	89.729	89.205	226.16	226.98
967	Secondary	93.193	92.682	222.66	223.47
930	QDU-only	2.336	2.871	313.38	313.09

Table 4.8: Results from the laser runs with the QDU stand-alone and with the QJB. In all runs, default WRS $v6.1$ delays for port 1 of the WWRS was set, and no Tx, Rx delays for the CLBs. PPS skew is measured with respect to the Dry WRS. The reported PMT hit time is the average of the distribution of peak times for the reference PMT (PMT-8 in this case) of DOMs.

From values in Tab.4.8, the delays ΔT introduced by the Qualification Junction Box can be inferred both by comparing measurements for the stand-alone Qualification Detection Unit and for the Qualification Detection Unit and Qualification Junction Box setup. The comparison can be done either with the measured PPS skews, or with the average PMT hit time sets obtained with the laser runs. The results are listed in Tab.4.9.

First, it can be noted that the measurements of the PPS skew and the average PMT hit time are well matched within ~ 200 ps but the sign is reversed. In particular, the QJB and its rack have longer fibers in the shore-to-sea direction than sea-to-shore, resulting in a shift of the PPS signal (namely, further in time) and thus in the origin of time of WWRS-A/B by a quantity equal to half of the total QJB asymmetry. As a consequence, the PMT hit times are shifted by the same quantity, but with opposite sign.

In addition, the expected ΔT must take into account the asymmetry of the optical filter used in the stand-alone QDU setup which are removed once the QJB is introduced. Thus, the expected delay is the sum of the filter half asymmetry and the total QJB half asymmetry, reported in Tab.4.7. Measured values for the PPS skew match the expectations at a level of few tens of ps for WWRS-A and less than 300 ps for WWRS-B, for both the QJB optical amplifiers employed. In the latter case, the larger discrepancy is probably attributed to a not identified optical component (or to a less accurate measurement of the asymmetry). For the average PMT hit time, all measurements match the expected values within ~ 150 ps.

These results indicate that the optical path asymmetries introduced by a JB, measured during its integration, can be corrected to re-synchronize the detector with accuracy of tens of ps, and in any case not worse than 300 ps. This asymmetry can be compensated either adding the known delays in the calibration table of WWRS-A/B, on port 1, or offline as part of the T_0 set.

			PPS skew (ns)		⟨PMT hit time⟩ (ns)	
WWRS	EDFA	ΔT exp.	ΔT meas.	Difference	ΔT meas.	Difference
A	Primary	87.365	87.393	0.028	-87.220	0.145
B	Primary	86.058	86.334	0.276	-86.110	0.058
A	Secondary	90.829	90.857	0.028	-90.720	0.109
B	Secondary	89.522	89.811	0.289	-89.725	0.098

Table 4.9: Comparison between the expected and measured delay ΔT introduced by the QJB, from both PPS skew measurements and average PMT hit time sets. Values are determined comparing runs 963, 967 to run 930 from Tab.4.8, and subtracting the optical filter asymmetry (divided by two) of the QDU stand-alone setup, reported in Tab.4.7. Expected values are the total half asymmetries from Tab.4.7, added to the half asymmetry of the QDU stand-alone optical filters.

4.7 Results from the first Detection Units

After the QJB, we have calibrated (up to September 2024) in the Caserta darkroom other ten DUs. Here, the results are reported. In Fig.4.15 the mean peak times I obtained for reference PMT-27 for the ten DUs are shown. The CLBs were configured with the average values for Tx and Rx, and the laser delays are subtracted in the shown time values. It is interesting to compare the mean peak times obtained for the same DOM number, since those refer to the same Wet WRS switch port and thus ideally the same port fixed delays. For all DOM numbers this spread of the mean peak times is very limited and contained within approximately 5 ns, as highlighted with the grey boxes in Fig.4.15, that include also the difference in the opto-electronic delays of the CLB and PMT of the different DOMs. This shows very small discrepancies in the synchronization by the same port of different Wet White Rabbit switches.

The standard deviation for the distributions of mean PMT hit times for each DU is approximately 2 ns, as shown in Fig.4.16 (Top). This is compatible with what already observed with the QDU. The different distributions reflect the different port 1 calibrations for the WWRS of the DUs; in fact, the base modules of DU-179,181,189,194 were

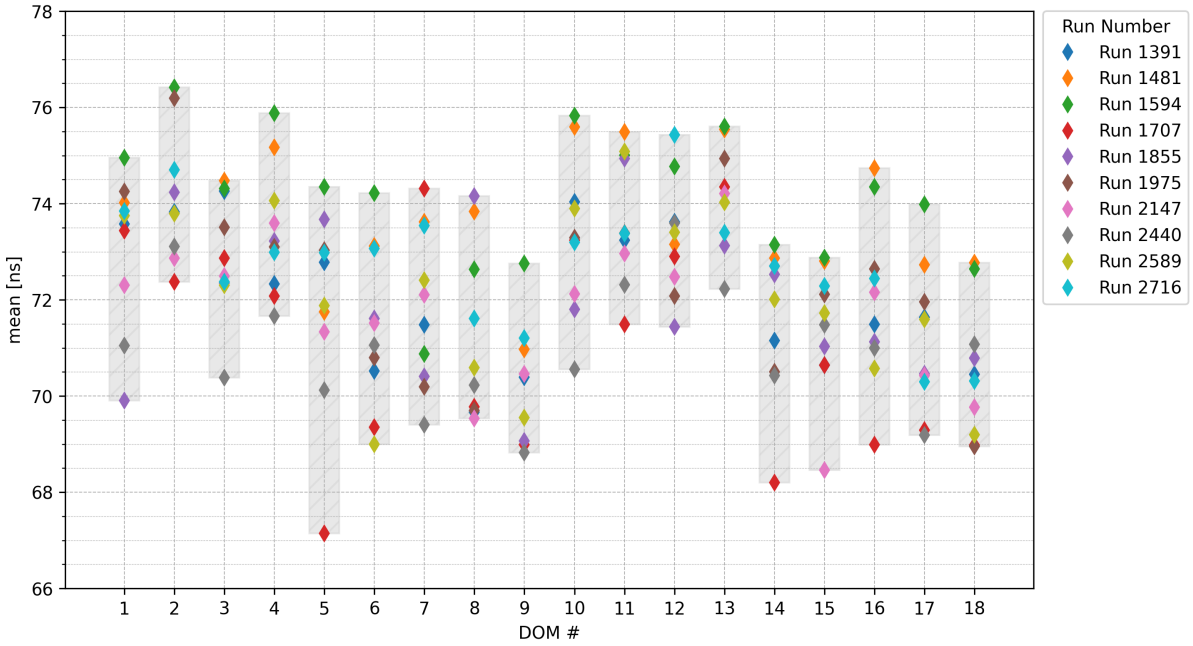

Figure 4.15: Reference PMT peak times for the first ten Detection Units of the Standard White Rabbit calibrated in the Caserta darkroom, as a function of DOM floor. Error bars (corresponding to fit parameter uncertainty) are shown but hidden inside the marker. The reference PMT is PMT-27. Here, the corresponding laser delays are already subtracted, and the Central Logic Boards are configured with the average Tx, Rx delays. The grey shadowed rectangular boxes highlight the spread of the peak times distribution for each DOM number.

integrated in Caserta, base modules of DU-180,183,191,205 in Bari and base modules of DU-198,203 in Bologna. Since each site use a different Dry WRS (at the moment not yet calibrated with the Golden/Child Calibrator, while instead configured with a common average calibration table) to calibrate port 1 of the WWRS, the residual mis-calibrations show up in the respective base modules. Nonetheless, as shown in Fig. 4.16 (Bottom), the overall distribution of mean hit times can be fitted with a Gaussian with $\sigma = 1.92$ ns, which is compatible with the standard deviation of the individual distributions, indicating that the discrepancies due to the different (unknown so far, but expected to be of the order of a few hundreds of ps) fixed delays between the Dry WRS of the base module integration sites are negligible with respect to the intrinsic spread of the mean PMT hit times. Among these, DU-179,189,194 have been deployed in October 2024 and are currently acquiring data.

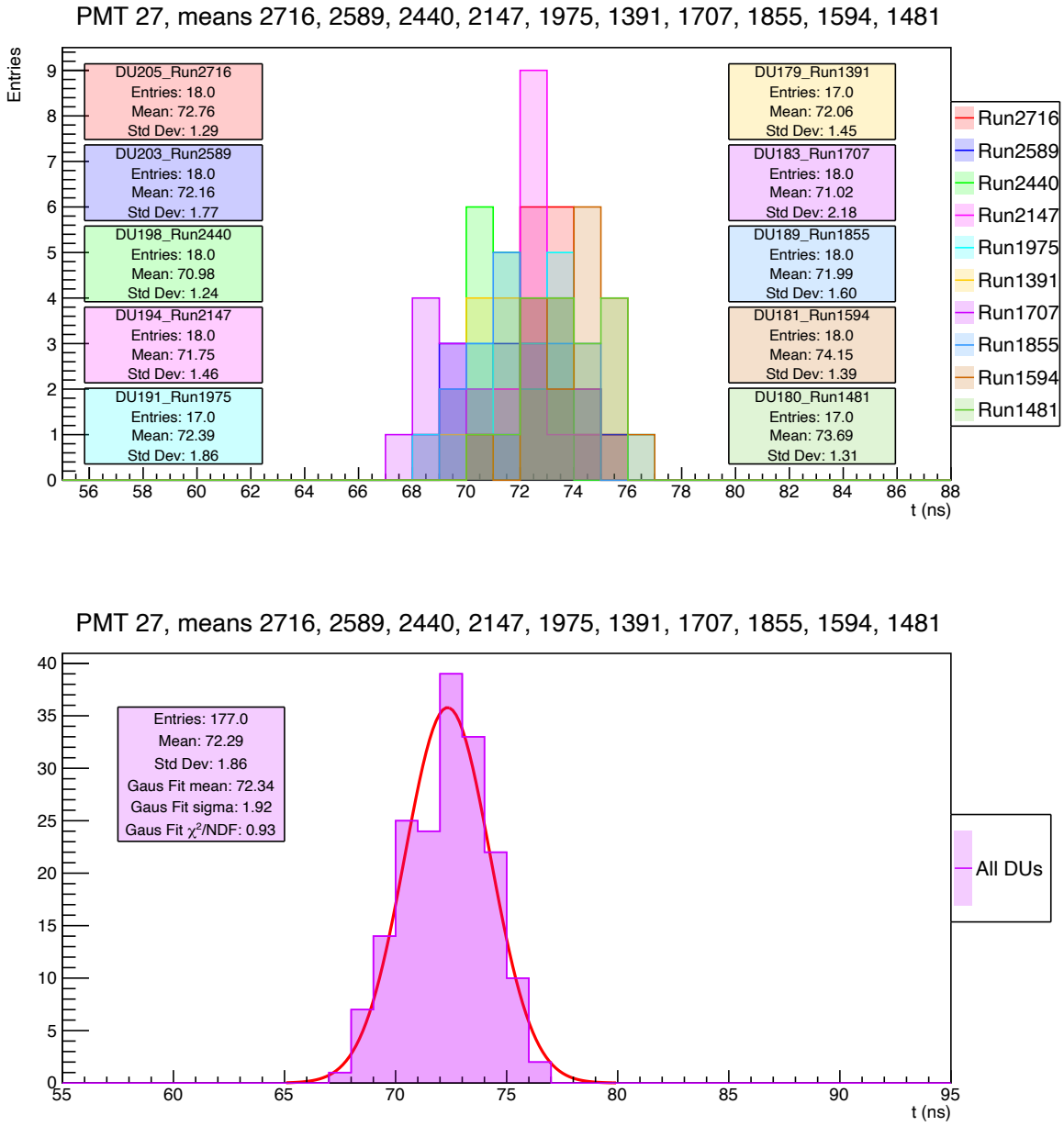

Figure 4.16: Top: histograms of mean laser PMT hit times of all DOMs for the first ten integrated Detection Units of the Standard White Rabbit system in the Caserta test site. Bottom: combined histogram of the distributions, with Gaussian fit.

Chapter 5

The KM3NeT/ARCA Calibration Unit

Together with timing synchronization, the other key parameter to optimize the detector angular resolution is the precise determination of the position in the sea of each individual Digital Optical Module (DOM. In fact, sea currents displace the DOMs up to O(10 m) in a manner that depends on their position along the Detection Units (DUs). The KM3NeT acoustic system primary goal is the implementation of the detector positioning system, based on commercial available technologies and systems and on the return of experience from the operation in ANTARES [113]. The data from KM3NeT acoustic system are also used by the Earth and Sea Science Community for several research items like marine monitoring, biology, geophysics and oceanography. The positioning system is planned to become a "hybrid" positioning system that will use acoustic positioning system data from hydrophones and piezoelectric-sensor, compass/tilt data and current meters data. While the formers come from sensors installed in DU bases and inside DOMs, current meter data will be provided by marine instrumentation installed on dedicated lines called *Calibration Units*. This information will be later used to develop a full DU *mechanical shape model*, capable to predict the behaviour of the line and interpolate the DOM positions in case of malfunctioning of some piezo sensor. In this chapter I will describe the first Calibration Unit of KM3NeT/ARCA and its role in the improvement of the detector acoustic positioning system. The integration and tests, to which I contributed and that led to its partial deployment in October of 2024, are illustrated.

5.1 The KM3NeT positioning system

With the "all-data-to-shore" approach, all acoustic data acquired by the acoustic receivers are continuously digitized and sent to shore, where they are managed and analyzed by the acoustic DataQueues and DataFilters (see Sec. 2.7). Two different acoustic sensors are present in the detector: a digital hydrophone, installed in each DU base, in the Junction Boxes, and in the Calibration Units, and a digital piezoelectric-sensor, installed inside each DOM. Two different acoustic positioning systems are needed to provide mandatory information during the deployment and the operation of the detector. During the deployment phase, an absolute acoustic positioning system (called *Navigation and Absolute Positioning System*) must provide the depth and position of the detector's mechanical structures anchored on the seabed, i.e., Junction Boxes, DU bases and Calibration Units, in a geo-referenced coordinate system with an accuracy

Figure 5.1: Left: the hydrophone used in KM3NeT, a Colmar® DG1330. Right: the acoustic beacon used in KM3NeT, a MAB 100 from Mediterraneo Senales Maritimas®.

of about 2 meters. The geo-referencing of the detector field is done by the Navigation and Absolute Positioning System using auxiliary commercial acoustic systems, such as a ultra-short baseline positioning system (in KM3NeT/ARCA) and a customisation of a commercial long baseline system (in KM3NeT/ORCA). However, evidence has shown that the system currently in use for KM3NeT/ARCA (until March 2025) provides an accuracy on the absolute position of the DUs only of the order of 10 m, resulting in a systematic uncertainty of the detector orientation of $\sim 1.5°$. This uncertainty has affected also the estimated direction of the KM3-230213A event. Therefore, starting from the sea operations of 2025, the same long baseline system used in KM3NeT/ORCA will be also adopted in KM3NeT/ARCA.

On the other hand, during the operation phase a *relative acoustic positioning system* is used to determine the positions over time of the DUs and DOMs in the geo-referenced field. In fact, under the effect of sea currents, DOMs tend to float around the vertical position which must hence be continuously monitored as well as their orientation. The relative acoustic positioning system must able to determine DOMs position continuously via triggered emission of acoustic signals whose repetition rate is of one every few minutes, which gives optimal position reconstruction given the slow movements of DOMs underwater (sensible position variations occur on a hourly scale). Combining the absolute and relative positioning systems, the system should be able to determine the absolute position of the detector elements, which is important for a safe deployment of the structures, and to determine the absolute pointing direction of the telescope, necessary for the localization of astrophysical sources.

The relative acoustic positioning system uses an auto-calibrating long baseline system of hydrophones, piezos and acoustic emitters (shown in Fig. 5.1) placed in the detector geo-referenced field. The acoustic emitters are long baseline beacons placed in the bases of some DUs, of the Calibration Unit, and in the Junction Boxes. Additionally, until the number of beacons in the bases is large enough, few external autonomous beacons, powered by batteries, are installed on tripods in the detector field. In KM3NeT/ARCA, up to Phase 1, four beacons are inserted on DUs, three on Junction Boxes, and three are present on external tripods. The position of the acoustic receivers is computed on-

shore by measuring the time of flight of the beacons signals on the acoustic receivers, determining via multilateration the position of the acoustic receivers with respect to the geo-referenced system. In addition, time of flight measurements between different beacons and hydrophones can be used to perform their auto-calibration, i.e., monitor their relative fixed distances with a better accuracy than the one obtained from the Navigation and Absolute Positioning System. Since the array of receivers is synchronous with the detector White Rabbit clock delivered from shore, the relative acoustic positioning system can perform precise time of flight measurement, with accuracy of about $5\,\mu$s, corresponding to an error of about 1 cm, considering a true sound velocity in water at the depth of sea bottom for KM3NeT/ARCA $c_{sound} = 1550\,$m/s. This is mostly driven by the sampling frequency of the receivers (195.3 kHz), and by the accuracy of the time response of acoustic sensors, i.e., the latency between receivers signal reception and timestamp by the Central Logic Board ($\sim 0.25\,\mu$s), and between beacons trigger reception and signal emission ($\sim 0.8\,\mu$s). The latter, i.e., the uncertainty on the time of emission, can however be reduced by exploiting the nearby hydrophone, located in the same structure of the beacon at a known, fixed distance, to time tag the signal emission. The uncertainty due to the White Rabbit time synchronization, below the nanosecond, is instead negligible.

However, as of March 2025, the triggered emission by the beacons is not yet operational and the beacons emit acoustic signals continuously at a predefined frequency. Thus, the distances between DOMs and beacons, as well as the time of signal emissions, are currently estimated from a global fit of the time of signal arrivals.

The value of sound velocity in water at the considered depths has been measured in advance during prior sea campaigns (via the Chen-Millero empiric formula [114] based on measurement of conductivity and temperature as a function of depth along the water column, performed with Conductivity Temperature and Depth probes, CTDs), but will be measured and monitored in situ using proper devices on the Calibration Unit, as sound velocimeters and CTDs. The latter measurements are especially important for the positioning of DOMs: sound velocity is only slightly affected by the small changes (measured during previous sea campaigns) of temperature and salinity at the sea bottom where the hydrophones are located, while the effect is more relevant over the 700 m water column of the DU. The uncertainty on the absolute value of sound velocity thus causes the largest error in the distance measurement: in combination with the signal sampling and latencies, the sound velocity must be known with relative accuracy of 0.04% to achieve a $\sim 20\,$cm accuracy at 500 m of distance. This is the accuracy needed to reach the desired sub-degree angular resolution.

Past results in KM3NeT/ARCA have demonstrated that the acoustic system, though incomplete, already achieves a resolution of $\sim 20\,$cm [115] [92], expected to improve further after the complete installation of the auto-calibrating long baseline array of beacons, together with the profiling of sound velocity with sound velocimeters (which have an accuracy of $0.001\,$m/s).

In a following stage the information provided by both the acoustic and compass-tiltmeter systems will be used together with the knowledge of the DU mechanical properties to develop a mechanical model for the DU, following what was already done with ANTARES [113]. The aim of the model is to determine the position of each DOM: using as fitting parameters the effective sea current direction and velocity, it is capable to reconstruct the shape of the line and interpolate the DOM positions for DOMs with piezo

sensors that have failures [116]. The reconstruction of the positions with the mechanical line fit model is considered an improvement with respect to the direct location from the acoustic positioning system [117], especially for the case of DOMs with missing or noisy acoustic data. At present, a calibration method based on an acoustic fit that takes as input a set of acoustic events and fits a model of the detector geometry to the acoustic data [92] has been used to determine the position of DOMs: this method was used in the reconstruction of the KM3-230213A event. Sea current data from direct measurements can be used to provide validation and predictive models for these line fit analyses.

In this context, the KM3NeT/ARCA Calibration Unit, is going to improve the acoustic positioning system (and thus, to improve the detector angular resolution) in several ways:

- adding a permanent pair of acoustic beacon and hydrophone in the network
- providing direct measurements and on-line monitoring of sea currents along the water column
- allowing the characterization of sound velocity in the medium with precise direct and indirect (through water properties characterization) measurements along the water column

The Calibration Unit is divided into two main structures, the Calibration Base and the Instrumentation Unit, connected by a 700m-long electrical interlink cable that can be operated by the submarine remotely operated vehicle during the deployment phase: The Calibration Base, consisting in anchoring frame which hosts an acoustic beacon, a hydrophone and a Base Module with the due electronics, will be connected to a Junction Box via a 300m-long standard DU electro-optical interlink cable for power and communication with the shore station. The Instrumentation Unit consists in a recoverable frame that will be connected for power and communication to the Calibration Base and a line made by an inductive rope mounting the oceanographic sensors. The sensors communicate with an inductive modem located in a base container on the frame, and are powered by batteries. Thus, the line needs to be recovered every two years for battery exchange and for the re-calibration of the sensors. For this reason, the Instrumentation Unit will be located outside the detector field in order to guarantee safe deployment and recovery operations. The Calibration Base and Instrumentation Unit positions in the KM3NeT/ARCA site are shown in Fig. 5.2. The deployment of a Calibration Unit for each building block of the KM3NeT/ARCA detector is foreseen, with the first one which has been deployed, in a partial configuration, in October 2024. In fact, due to technical constraints during the deployment operations, the inductive rope with the oceanographic sensors had to be temporary (i.e., until the next sea operations) disassembled from the Instrumentation Unit, of which only the frame with the inductive modem and the pressure sensor hosted on it was deployed.

5.2 The KM3NeT/ARCA Calibration Base

The main role of the Calibration Base is to contribute to the detector relative acoustic positioning system by adding a hydrophone and an acoustic beacon to the network.

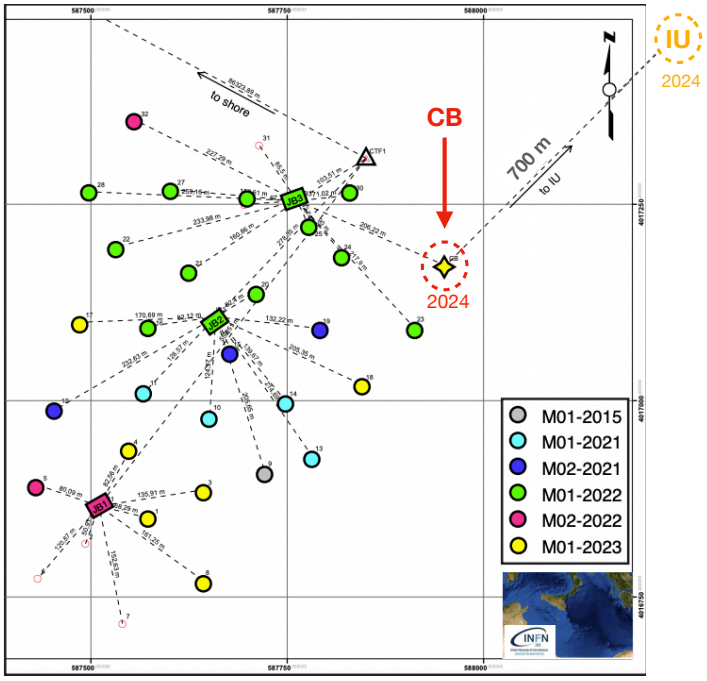

Figure 5.2: The KM3NeT/ARCA sea-floor map, as of March 2025; colored circles (boxes) indicate installed DUs (Junction Boxes), while the straight lines indicate the inter-link cables connecting the DUs to the Junction Boxes. The colour scheme follows the sequence of marine campaigns indicated by a progressive number and the year. Highlighted are the positions of the Calibration Base (CB) and of the Instrumentation Unit (IU). The Instrumentation Unit position is chosen to be in safe distance from the DU array and, according to the dominant current measured at site, to minimise the risk of line drifting into the field during deployment and recovery operations.

The instruments are mounted on the frame and are connected to a base module, similar to a DU base module, which contains the electronics for managing the power and communication both with the shore station, through the Junction Box, and with the Instrumentation Unit. The main components of the Calibration Base are described in the following subsections and are shown in Fig. 5.4. The Calibration Base has been assembled and integrated in the KM3NeT Caserta laboratory during several dedicated sessions from January 2022 to July 2023 by expert teams from Caserta, Catania, Bologna and Genova in which I participated.

5.2.1 Anchoring frame

The Calibration Base frame is a compact structure, weighting 1460 kg, made of primary and secondary iron crossbars welded together in a configuration which is expected to be effective against corrosion phenomena. It has a central load-bearing beam and two lateral beams to support the hydrophone and the acoustic beacon, and it features a high density polyethylene front panel where the Teledyne ODI® [118] plugs, made to be operated by the submarine remote vehicle, for the interlinks towards the Junction Box and the Instrumentation Unit are integrated. The structure was assembled in Genova and moved to Caserta in January 2022 in order to mount the other components. The

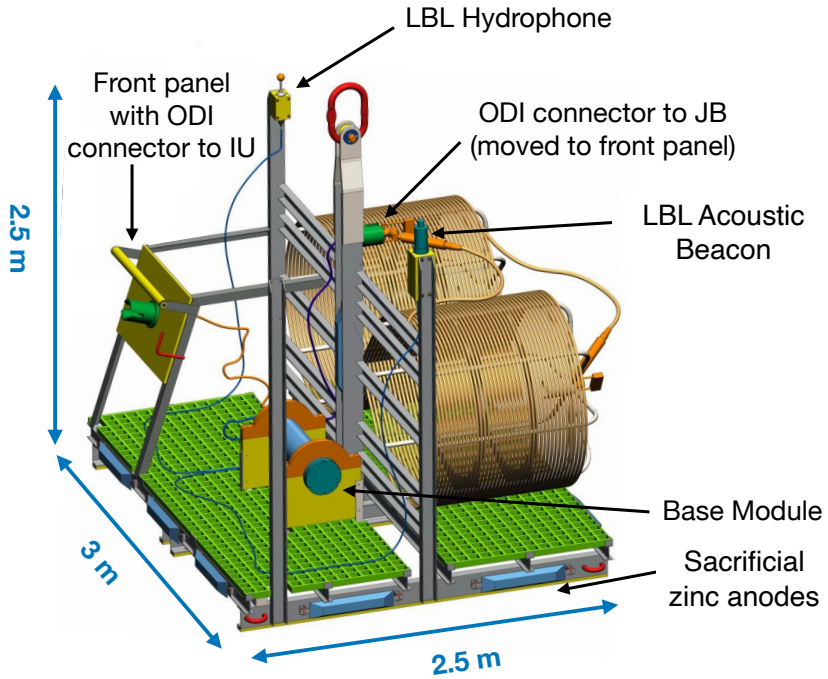

Figure 5.3: Mechanical structure of the Calibration Base: components and instrumentation are highlighted. Adapted from a picture in a KM3NeT internal documentation of the Calibration Unit working group.

polyethylene is used also for the supports that fix the base module, the hydrophone and the acoustic beacon to the structure. All the bolts and screws that we used to fix those to the supports are made of titanium, to avoid corrosion. Moreover, in order to guarantee protection against corrosion over long-term deployment, all the metal surface is coated with anti-corrosion painting (standard NORSOK M-501 [119]) and a cathodic protection system with eleven ∼12 kg sacrificial zinc anodes located on the bottom sides and on the central beam is applied. The floor of the structure was provided with fiberglass grids in order to facilitate the assembly and to prevent the anti-corrosion painting from scratching during the integration. Initially, the structure was built with a support for hosting the interlink towards the Junction Box and the corresponding ODI® connector, mateable by the submarine remote vehicle, was foreseen to be integrated on a panel adjacent to the central beam; however, since the interlink has already been separately deployed in advance during a previous marine campaign, the connector has been moved to the front panel to facilitate future operations of the remote vehicle during connection after the Calibration Base deployment.

5.2.2 Instruments

The selected hydrophone is the same model used for the DUs and Junction Boxes, i.e., the Colmar DG1330, a digital omni-directional hydrophone specifically designed and produced by the company for KM3NeT to be operated at a depth of 3500 m. It consists of a spherical piezo-ceramic element, read-out by an analogue board splitting the signal in two lines with different gains (+46 dB and +26 dB). The low gain channel has been implemented in order to prevent signal saturation due to the acoustic emission from the

Figure 5.4: The Calibration Base during the weighting test at the Caserta facility. The base module, laid on the frame floor, the two orange jumper cables which connect it to the front panel, and the hydrophone (with the green cable) are visible.

beacon in close proximity (∼3 m), while the high gain channel is used for analyzing data received from distant beacons, spanning up to a few kilometers, as well as for studying faint acoustic signals, such as those related to bio-acoustics, environmental noise, and acoustic neutrino detection [120]. It includes an analogue signal high-pass filtering stage at 700 Hz to reject the low frequency ambient sea noise and improve the signal to noise ratio in the detection of beacon pulses range (20-40 kHz). The sampling frequency is 195.3 kHz, and the acceptance frequency range is 5-90 kHz. The two streams are sampled with a stereo 24 bit commercial ADC (CS-4270) and converted into AES/EBU [121] protocol using a digital interface transmitter. The acoustic beacon is the Mediterraneo Senales Maritimas® [122] MAB 100, endowed with a FFR SX30 acoustic transducer. The electronic boards are contained in a shielded titanium case resisting up to 4000m of depth. Currently, I have programmed the beacon in autonomous mode, emitting every 30 seconds its unique modulation signature carried by a sweep signal ranging from 40kHz to 36kHz; in a future stage, the acoustic emission will be stimulated by external triggers. Both instruments are connected to the Calibration Base base module via a common GISMA® [123] MCIL6M connector, and linked through it to a Central Logic Board via the mezzanine board (see Sec. 5.2.3). Connection for power and communication is done via RS-485 with a RJ45 connector for the hydrophone, while the acoustic beacon power is taken directly from the base powering board and communication uses RS-232 lines connected to the mezzanine board. The clock from the Central Logic Board, synchronised to the master clock in the shore station, is exploited to timestamp data retrieved by the

hydrophone and can be used to emit synchronised triggers to the acoustic beacon.

5.2.3 Base module

The mechanical container of the KM3NeT/ARCA Calibration Base base module is made of titanium and it is identical to the base module of Broadcast DUs, except for the interface flange where the connectors for the Calibration Base instruments (made by GISMA®) and for the two jumper cables (made by Teledyne ODI®) towards the plugs for the Instrumentation Unit and the Junction Box inter-links are located. The internal frame is also identical, excluding the electrical and optical elements used to connect the DU base module to DOMs.

The base module hosts the following electronics boards, which we integrated in Bologna in March 2022 (see Fig. 5.5, top):

- The Base Power Supply board. This board, identical to the one installed in the base module of DUs which have a beacon, receives 375 V DC power from the Junction Box and converts it into low voltage to power other electronic boards installed in the base module, the Calibration Base instruments and the Instrumentation Unit.

- The Central Logic Board (CLB), identical to the ones installed inside each DOM and base module. Regardless of the detector element where they are integrated, all CLBs are identical except for the installed firmware. The firmware that I installed is a specific version, inherited from the KM3NeT/ORCA Calibration Unit, based on the one for the CLB in the base module of Broadcast DUs, and implements the communication with the Instrumentation Unit. At the current stage, this is done via a graphical user interface, shown in Fig. 5.6, which extends the one used for standard CLBs and allows the user to issue serial commands via RS-232 protocol to the inductive modem inside the Instrumentation Unit base container and to the beacon, and to read the answer messages. The CLB receives commands and the common clock from the shore station as it occurs for Broadcast DUs (i.e., the Rx is received from a Broadcast fiber, while the Tx line is connected to a Level-1 White Rabbit switch) and, through the mezzanine board, it interfaces the Base Power Supply board, the instruments and the Instrumentation Unit. As usual, communication between CLB and shore station is established using a Small Form Pluggable laser integrated into the CLB. The only optical component thus consist in a wavelength division multiplexing filter, which is on one side connected to the Tx,Rx fibers from/to the laser and on the other to the connector for the jumper cable, which connects it to the front panel plug.

- The FPGA Mezzanine Card is a piggy pack board mounted on the CLB. It enables CLB communication with the Base Power Supply board, instruments and the Instrumentation Unit, and gives power to the hydrophone.

After the integration of the electronic boards, the base module was moved to Caserta, where, in July 2022, we completed the integration of the optical components (see Fig. 5.5, bottom), i.e., the fibers, the optical filter and the connectors on the flange.

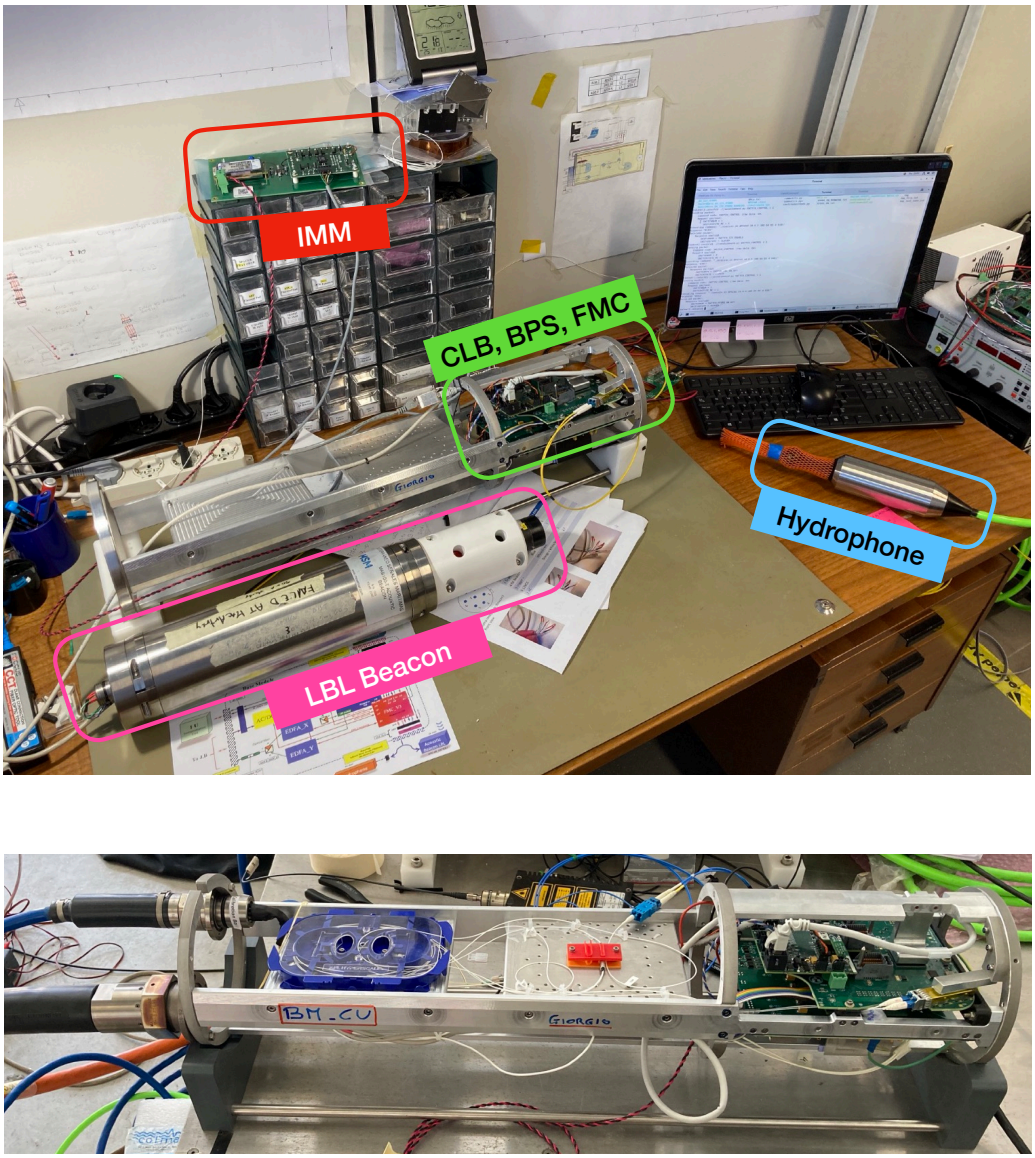

Figure 5.5: Top: the base module of the Calibration Base during the electronic boards (in the green box: Central Logic Board (CLB), Base Power Supply (BPS), FPGA Mezzanine Card (FMC)) integration and power tests in Bologna. An acoustic beacon (LBL Beacon, in the pink box), hydrophone (blue box) and an inductive modem module (IMM, in the red box) used for test purposes are highlighted. Bottom: the base module in Caserta during the integration of the optical fibers for communication to/from shore.

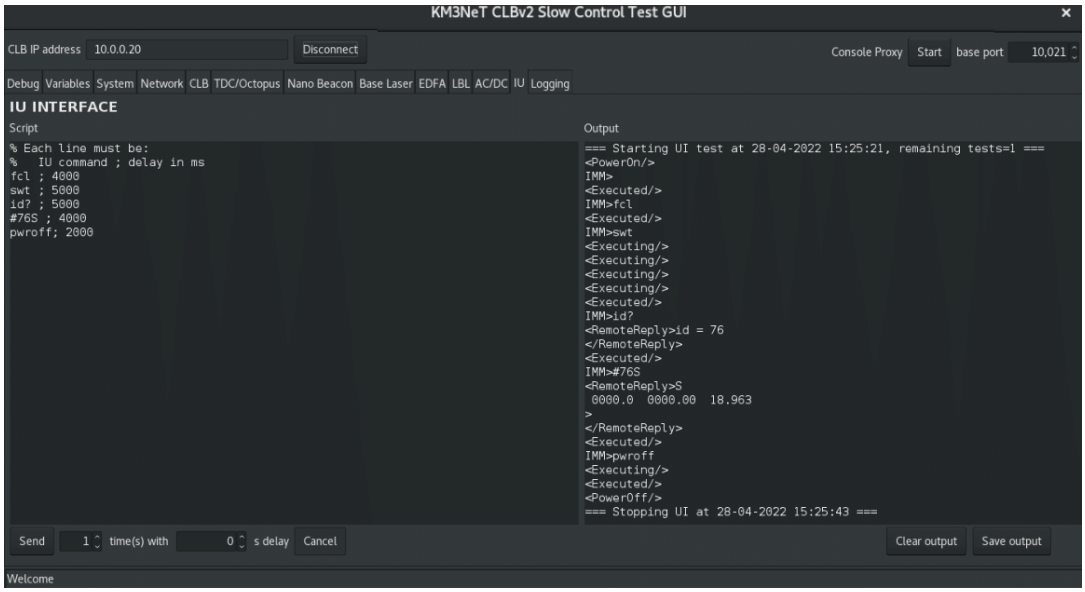

Figure 5.6: Screenshot from the graphical user interface during a communication test with the KM3NeT/ARCA inductive modem of the Instrumentation Unit.

5.3 The KM3NeT/ARCA Instrumentation Unit

The role of the Instrumentation Unit is to monitor oceanographic and acoustic properties of the water column, providing direct measurements of sea current, conductivity, temperature, pressure (the three allow the indirect sound velocity determination) and sound velocity. This data will be used primarily to recover the sound velocity profile and the currents of the water column.

It is composed of the Instrumentation Line and the recoverable frame: a scheme is illustrated in Fig. 5.7. The Instrumentation Line is an inductive line, which will be kept vertical by a top buoy, that both provides support for the oceanographic sensors and acts as transmission medium of the inductive transducers used to communicate with them, avoiding additional conductors. The line is connected to a base container on the frame, where an inductive modem is located. Each instrument on the line, either native inductive or interfaced to the cable via proper inductive modems, communicates through the inductive cable with the base modem. In turn, the latter is connected to the Calibration Base to perform on-line data taking and reconfiguration of the instruments. Each instrument is autonomously powered by internal batteries. This concept has been already tested by the Albatross (https://www.seanoe.org/data/00633/74513/) mooring inductive line of the European Multidisciplinary Seafloor and water column Observatory [124], installed offshore Toulon. The Albatross line is however totally autonomous and communicates the data to the shore through an acoustic modem connected to the node (which in turn is connected to shore), while in this case the communication from the inductive modem on the Instrumentation Unit frame to the Calibration Base occurs via serial RS-422 protocol (https://en.wikipedia.org/wiki/RS-422) with the interlink cable. This system allows for the deployment of up to 100 instruments, that can be positioned anywhere along the cable and that can be easily reconfigured by simply sliding and re-clampling the instrumenrs on the cable.

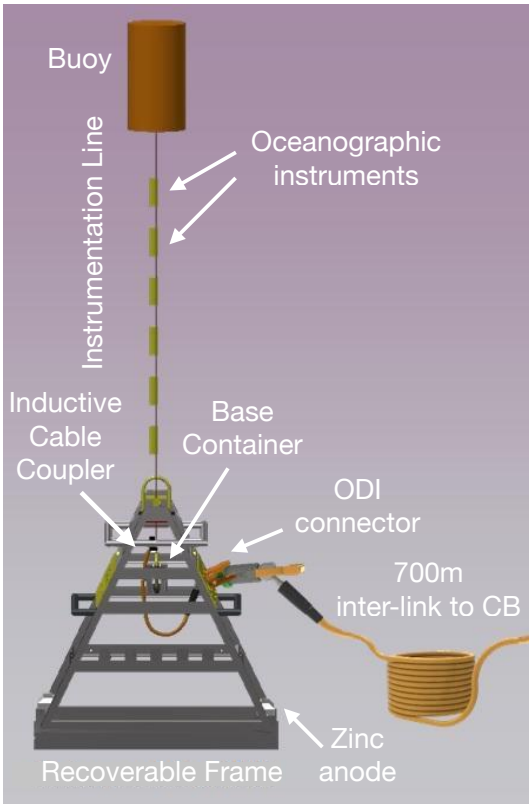

Figure 5.7: KM3NeT/ARCA Instrumentation Unit main components. In addition, on the frame a pressure sensor is also located. Adapted from a picture in a KM3NeT internal documentation of the Calibration Unit working group.

The frame consists in a metallic anchoring structure which hosts the base container where the electronic boards are located, a front panel with the bulkhead plug for the remote vehicle to connect the container to the Calibration Base, an absolute pressure sensor (with its inductive modem) and the inductive coupler for the line. The Instrumentation Unit has been integrated in Caserta by the Calibration Unit team from 2022 to July 2024, when we performed the last tests before the shipping in preparation for the deployment.

5.3.1 Recoverable frame

The recoverable frame structure is made of stainless steel coated with anti-corrosive painting (standard NORSOK M-501) and cathodic protection is granted by two ∼12 kg welded sacrificial zinc anodes. The front panel and the support floor for the base container and the other devices are built in high density polyethylene.

The frame has been designed in order to be recovered every two years, together with the Instrumentation Line, for batteries change and instrument re-calibration. To preserve the connector of the interlink cable from the Calibration Base to the Instrumentation Unit during the recovery operations, a long-term cap on a parking terminal frame, shown in Fig. 5.9, will be used.

Figure 5.8: The Instrumentation Unit recoverable frame: the front panel with the Teledyne ODI® interlink cable connected during a communication test can be seen; the pressure sensor is higlighted by the cyan box, its inductive converter by the purple box (left). The base container, behind the pressure sensor and the converter, can be seen as well (right).

Figure 5.9: Instrumentation Unit recoverable frame (on the left) and the parking frame for the connector of the interlink with the Calibration Base.

5.3.2 Base container

The base container is a titanium pressure vessel containing an electronic board that receives the power (12 V DC) and serial RS-422 communication lines from the base module of the Calibration Base. The base inductive modem is mounted on this board, from which it receives the 12 V power and which also includes a serial converter from RS-422 (used to transmit serial data over long distances) to RS-232 (https://en.wikipedia.org/wiki/RS-232) standard, used by the modem.

The board is connected to the Calibration Base through a circular DMS series connector (a type of connector which ensures durability and reliabilty in harsh environments) on one of the vessel flange via a jumper cable to the connector on the front panel, mateable by the remote vehicle. On the other flange, another circular DMS, high-reliability, connector is used for the connection of the base modem to the inductive cable coupler. We have performed the integration of the electronic board in Caserta in July 2022, while the connectors on the flanges were mounted in February 2023; when, we implemented the final connections and sealed the container. The base container, is shown in Fig. 5.10. The floor and the supports which fix the container and the instruments are made of high density polyethylene, while titanium screws are used.

5.3.3 Instrumentation Line

The inductive cable is a 750 m long, 3x19-strands galvanised jacketed wire rope with swaged socket terminations to allow grounding with seawater and current loop through the mooring cable. The line is equipped with the following instruments, delivered with their test and calibration certificates:

- Two native inductive Conductivity,Temperature and Depth (CTD) probes with pressure and optical dissolved oxygen sensors. They measure conductivity, temperature and depth and allow indirect calculations of sound velocity in water as a function of temperature, pressure and salinity through Chen-Millero [114] formula. Measurements of oxygen and salt concentration (the latter inferred from

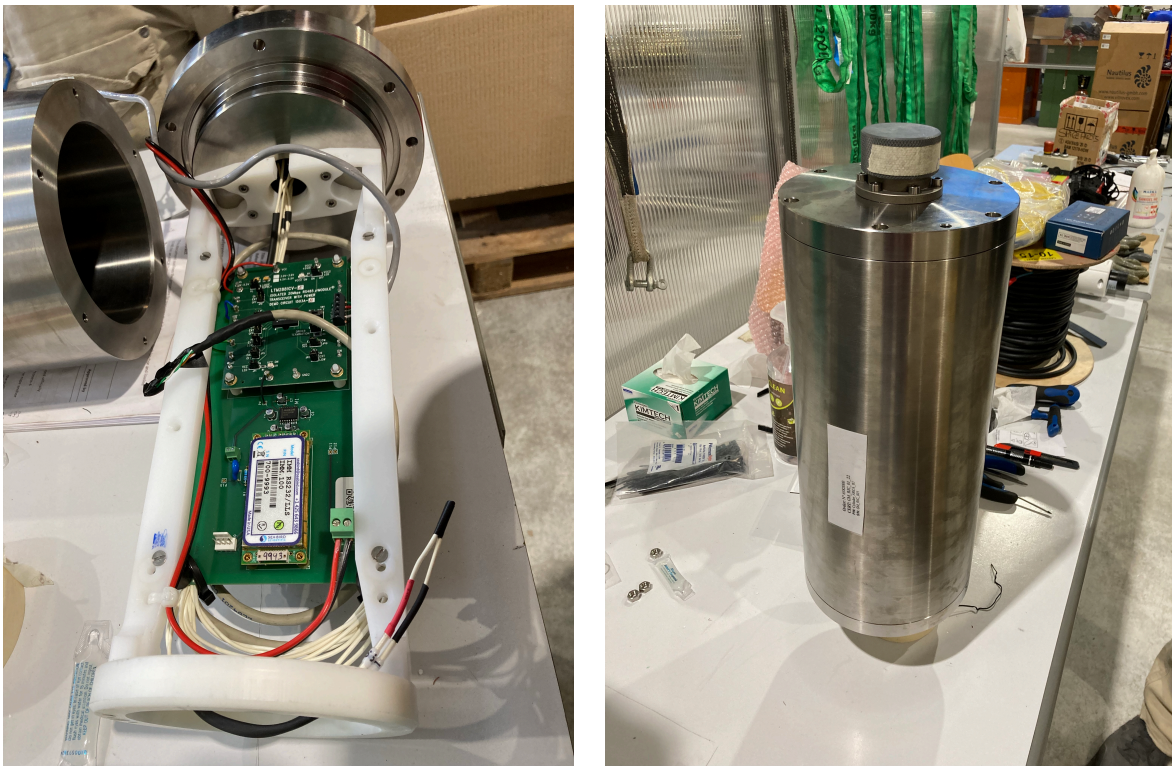

Figure 5.10: The Instrumentation Unit base container open during integration (left), and after sealing (right). The big electronic board is the one which converts the serial standards, from the RS-422 used for the long-distance communication, to the RS-232 for the Seabird Inductive Modem Module (the small board with white cover in the front) and provides it with the power supply of 12 V, received from the Calibration Base base module.

conductivity) in water, as well as its temperature, can be used for oceanographic studies;

- Two non-inductive sound velocity sensors. They perform a direct measurement of the sound velocity in water, thus contributing to improve the fits of the acoustic positioning system for the determination of the DOMs position.
- Two non-inductive Doppler current sensors. They perform measurements of the sea current along the 3 directions.
- One non-inductive pressure gauge, used as absolute depth reference to improve the accuracy of the acoustic positioning system; its measurements will also allow geo-oceanographic studies on the variation of sea depth and can be used to monitor earthquakes and tsunamis.

The inductive Conductivity, Temperature and Depth

The model of the selected Conductivity, Temperature and Depth (CTD) sensor is the Seabird® [125] SBE 37 IMP-ODO MicroCAT with titanium housing, a 7000 dbar pressure sensor, integrated inductive modem telemetry, and a 7000 meter optical dissolved oxygen Sensor. The device is a high-accuracy conductivity, temperature, pressure and and dissolved oxygen recorder with internal batteries, memory, and a pump which operates before and during data collection to flush sediments. Data can be either acquired in single measurements or recorded in memory and then transmitted in polling mode. Measured data and derived variables (salinity, sound velocity, specific conductivity) are output in engineering units. Given the provided accuracies on conductivity, temperature and pressure, the combined accuracy for the indirect sound velocity computation is $\simeq 0.1\,\mathrm{m/s}$.

The sound velocimeter

The selected sound velocimeter is a miniSVS by Valeport® [126]. The miniSVS sensor is fitted with a digital time of flight sound velocity sensor: the sound velocity is calculated from the time taken for a single pulse of sound to travel a known distance. The miniSVS therefore consists of a single circuit board controlling all sampling, processing and communications functions, and a sensor comprising a ceramic transducer, a signal reflector, and spacer rods to control the path length. A titanium housing provides waterproof protection to a depth up to 6000 meters. In addition, it features a Platinum Resistance Thermometer temperature sensor. The provided accuracy of sound velocity measurement is $0.001\,\mathrm{m/s}$, much better than the one provided by the indirect CTD measurement.

The current meter

The selected current meter is the Aanderaa® [127] ZPulse Doppler Current Sensor, version 4520R with depth rating of 6000 meters and serial ouput. The sensor is based on the backscatter acoustic Doppler principle. It has two orthogonal transducer axes with two transducers on each axis. This enables it to measure in both directions on each axis, making it insensitive to disturbance from vortex speeds around the sensor

itself. One transducer on each axis transmits short ultrasonic pulses simultaneously and receives backscattered signals from particles in the water. This gives an orthogonal x and y speed components to find the horizontal speed components. The North and East speed components are calculated based on the x and y speed components and the heading from the built-in solid-state electronic compass. The sensor takes several of these two-component measurements and finally calculates the averaged North and East speed components and the vector averaged absolute speed and direction. Accuracies are 0.15 cm/s for the current speed vector and 5° for the current direction.

The absolute depth sensor

The depth sensor, hosted in the recoverable frame, is a Paroscientific® [128] Digiquartz Intelligent Depth Sensor 8CB4000-I consisting of a pressure transducer and a serial interface board in a titanium waterproof housing. Measurement data are provided in engineering units with accuracy of 0.01% or better over a wide temperature range. Pressure measurements are fully temperature compensated using a precision quartz crystal

Height from seabed (m)	**Instrument**	**Measurement**
650	Valeport miniSVS	Sound velocity
600	Seabird SBE-37 IMP-ODO MicroCAT CTD	Conductivity, temperature, pressure, oxygen
550	AAndera ZPulse Doppler Current Sensor 4520R	Current velocity
200	Valeport miniSVS	Sound velocity
150	Seabird SBE-37 IMP-ODO MicroCAT CTD	Conductivity, temperature, pressure, oxygen
100	AAndera ZPulse Doppler Current Sensor 4520R	Current velocity
0	Paroscientific Digiquartz Depth Sensor 8CB4000-I	Pressure

Table 5.1: Oceanographic sensors mounted on the Inductive Line, and respective indicative height from the seabed.

During the clamping of the oceanographic instruments on the line, performed in July 2024, we spaced them according to the distances listed in Tab. 5.1 in order to properly monitor the full water column in which the detector is enclosed, and characterize the

sound and current velocity along it for the DOM positioning calibration. For what concerns the inductive modems, they are of two types: one type of modem is needed to interface and power the non-inductive oceanographic instruments to the inductive line and another is needed to allow the communication on one hand with the Calibration Base and on the other hand with the modems connected to the instruments. The first type is a Seabird® [125] SBE-44 Underwater Inductive Modem: it has a built-in inductive cable coupler (a split toroid) and cable clamp, providing data communications without the need for electrical connections, and an easy and secure attachment to any point on the jacketed inductive wire. An underwater bulkhead connector on the end cap provides the serial data connection to the coupled instruments, a control line, and switched power out. It is powered by batteries. The second type is the Seabird Inductive Modem Module, a low-

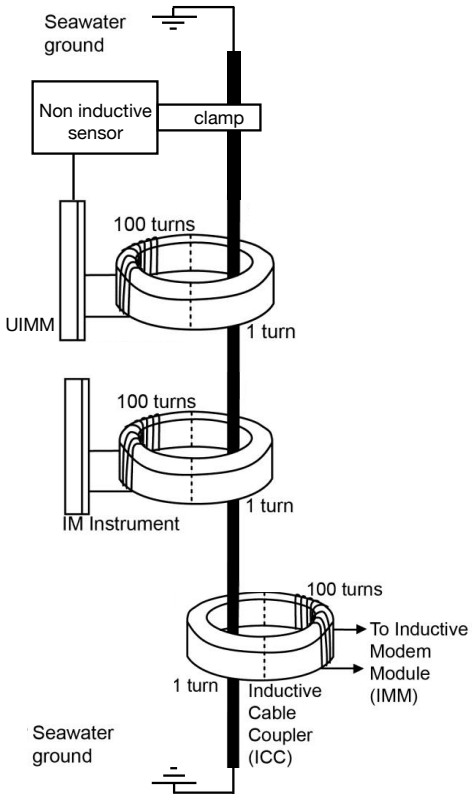

Figure 5.11: Representation of the inductive line, highliting the cable couplers made of toroidal transformers consisting in a circular ferrite core and two coils which share a magnetic field.

power microprocessor peripheral that interfaces serial RS-232 instruments to inductive moorings. It is shown in Fig. 5.10, connected to the interface board which converts the serial protocol. Power (12 V DC) is provided by the Base Power Supply board in the Calibration Base base module. The Inductive Modem Module includes capabilities that allow instrument self-discovery, inductive line status reporting, and cable coupler performance measurement. It is coupled to the line via the Inductive Cable Coupler.

5.4 Tests

We performed several tests during and after the integration of the Calibration Base and the Instrumentation Unit.

Preliminary tests

In March 2023, after the integration of the electronic boards of the Calibration Base base module in Bologna, I have conducted preliminary measurements in order to verify the compliance of current and power absorption with requirements set for the module. For these tests, an acoustic beacon, a hydrophone and an Inductive Modem Module with its interface board were connected to the base module (see Fig. 5.5). The Base Power Supply board was powered with the nominal +375 V DC by a power supply, and the current and power consumption of the electronic boards were registered. Then, the different instruments were powered on first individually, and then sequentially. In each case current and voltage values, both from the power supply and from the specific power terminals on the Base Power Supply board read via a dedicated software, were registered. All measurements matched the requirements. In addition, the White Rabbit time synchronization of the Central Logic Board (connected via optical fibers to a Broadcast White Rabbit switch) was verified, as well as the communication with the instruments.

Power and optics tests

We repeated the power tests in Caserta in July 2022 after completing the integration of the optical components of the base module, linking it to the test site rack (with a Broadcast White Rabbit switch and the due switching network and optical multiplexer/demultiplexer to establish communication with the boards) via a test jumper electro-optical cable, connected to the circular DMS series connector on the base module flange. The hydrophone and beacon were connected via their jumper cable to their connector on the flange. The interface board to the Inductive Modem Module, housed inside the Instrumentation Unit base container, was connected to the mezzanine board in the base module (still open) with a 800 meters long Ethernet cable for the communication lines (which we used in order to mock the subsea interlink) and to the Base Power Supply board for powering, with a 20 Ohm resistor (again, to mock the impedance of the 700 m subsea interlink). The configuration is shown in Fig. 5.12 (top). At this stage, the Instrumentation Unit base container was only connected to the base module, and not to the inductive line.

In a later stage, after the integration of the connectors that will be operated by the remote vehicle on the Calibration Base front panel, we tested again the system in February 2023 using two compatible test cables, plugged on the connectors, with their test boxes (see Fig. 5.12). The first was acting as the interlink with the Junction Box, and its test box was connected with optical fibers to the Data Acquisition rack; the second, acting as the interlink with the Instrumentation Unit, had the test box connected to the Instrumentation Unit base container via the 800 meters Ethernet cable and the power lines with the 20 Ohm resistor. Power and optics measurements were repeated. In both stages, all power measurements (reported here: [129]) fulfilled the requirements, as well as the optical power received from the Central Logic Board. After that, we sealed the

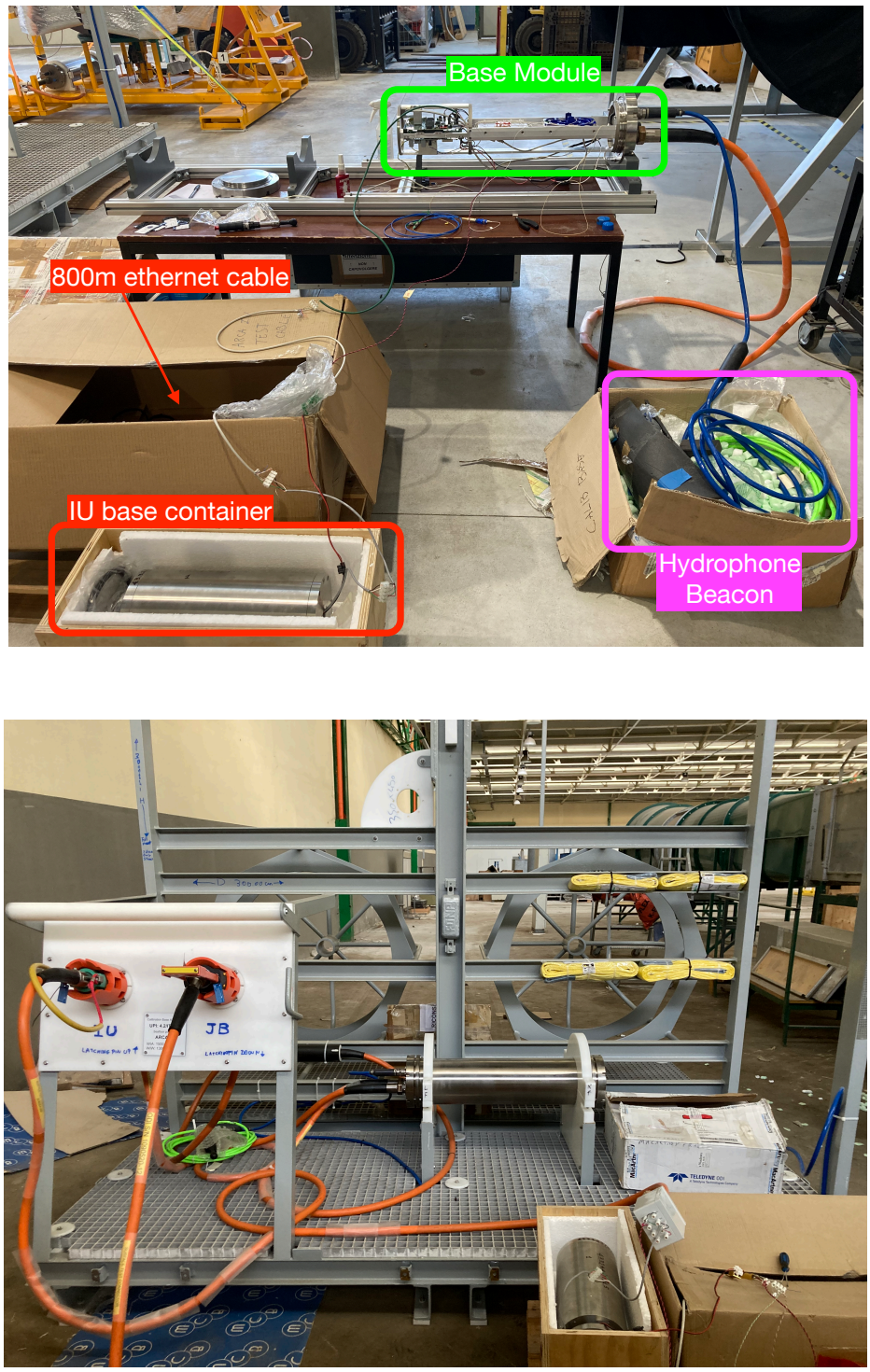

Figure 5.12: Tests of the Calibration Unit components. Top: open base module connected with the Data Acquisition test rack via a test cable (orange one). Hydrophone and beacon were connected via the GISMA® connector and jumper cable (blue one). The Instrumentation Unit base container was connected via a 800 m Ethernet cable and power lines with a 20 Ohm resistor. Bottom: sealed base module linked to the front panel connector handled by the remote vehicle. The communication was established through the cable, made by Teledyne ODI®, plugged to the front panel (connector on the right), with its test box connected to the Data Acquisition rack. The Instrumentation Unit base container was also connected with a cable with test box, and through 800 m of Ethernet cable.

base module and weighted the whole Calibration Base structure in air.

Data transmission

After the integration of the Calibration Base base module, I verified the communication with the hydrophone, beacon and Inductive Modem Module, exploiting the dedicated graphical user interface. I first checked the default beacon autonomous emission "manually" (by hearing the emitted sound) and then detecting it by the hydrophone, as shown in Fig. 5.13. This way, the functionality of the hydrophone was also verified, along with the stream of acoutic data packets from the Central Logic Board. Then, I configured the beacon to the current setting described in Sec. 5.2.2. The communication with the

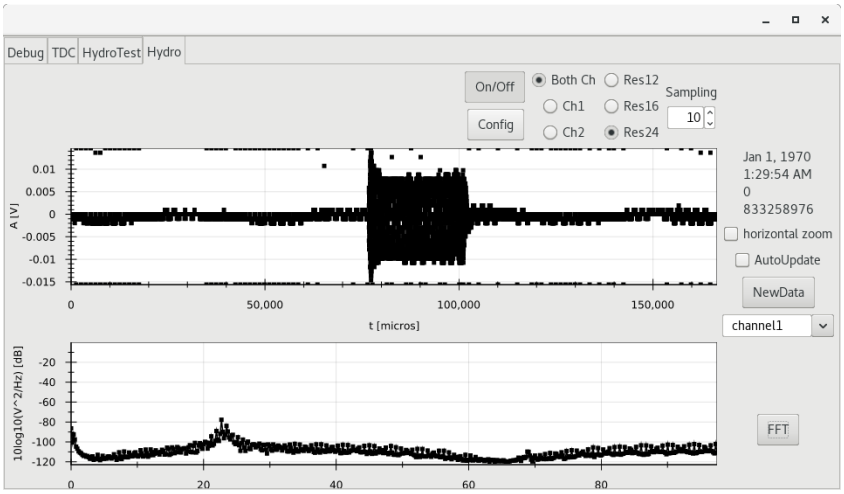

Figure 5.13: Screenshot from the graphical user interface showing the acquired data by the hydrophone, corresponding to the acoustic beacon emission. For this test, the beacon was configured to emit a sweep signal ranging from 23kHz to 24kHz. The plot on top shows the voltage amplitude of the signal on the piezo sensor as a function of time, while the bottom plot shows its Fourier transform. The peak in the frequency range is correctly identified at $\sim$ 23kHz.

Inductive Modem Module was established at this stage with the 800 m Ethernet cable, and verified by retrieving the configuration of the Modem. In the later stage of Fig. 5.12 (right), the communication was verified again. After that, we completed the base container integration by installing and cabling the two connectors on the flanges (one for the jumper cable to the Instrumentation Unit connector operated by the remote vehicle on its front panel, the other for the inductive cable coupler), and sealing it. We fixed the container, the inductive cable coupler and the pressure sensor (together with its SBE-44 coupler) to their supports on the frame floor, and connected the container to the cable coupler on one side and to the jumper cable on the other. In July 2024, we integrated the Instrumentation Line: after having configured with a laptop and serial connection all the oceanographic instruments, we wrapped the line around a spooler, shown in Fig. 5.14, and while the line was being wrapped, we clamped the instruments to it at the determined distances. The spooler will be used during the deployment of the Instrumentation Unit.

Figure 5.14: The spooler used for the deployment of the Instrumentation Unit. On its left, the Instrumentation Unit frame can be seen, connected with the 700 m cable to the Calibration Base (not visible) during the final functional test.

For our last tests in Caserta, we implemented all the connections as in their operational configuration: the final 700 m interlink cable were connected to the plugs on the front panels of the Calibration Base and Instrumentation Units; the inductive cable coupler was coupled at one end of the line, still on the spooler, and the communication between the Calibration Base base module and a PC in a test rack was established through a test cable plugged to the Junction Box connector on the front panel. With the graphical user interface, we successfully retrieved a set of measurements from all the instruments on the inductive line. Collected data, which at the current state of development are saved on text files from the graphical user interface, are going to be stored on the KM3NeT database, and will be eventually made available to the European Multidisciplinary Seafloor and water column Observatory. In the near future, we plan to automatize the communication of the Central Logic Board with the Inductive Modem Module so as to eliminate the need of user intervention. The Control Unit will take care of the communication with the Inductive Modem Module and perform a routine in which it will trigger a measurement from the sensors, extract the responses and store them in the database.

5.5 The Bologna Laboratory for User-ports

In order to develop and test the handling of the communication with the instruments by the detector Control Unit, in July 2024 I have set up in Bologna a dedicated test bench, named *Bologna Laboratory for User-ports*. The test bench takes advantage of the presence, in the same laboratory, of the *Bologna Common Infrastructure*: this is a unique setup, over the whole KM3NeT collaboration, which puts in place all the data processing key-points due to a real implementation of the full Data Acquisition chain inside a controlled environment. It integrates all main aspects from control and monitoring, to the time synchronization, networking, and online software for data processing. The Bologna

Common Infrastructure is used to develop and test Data Acquisition-related hardware, firmware and software components before their installation either on the shore-station servers or their deployment on the submarine infrastructure. It comprises two full DU-size test benches, each formed by 18 Central Logic Boards (CLBs) running with DOM firmware and a simplified base module (i.e., without the container and the optical components required for a real DU). In particular, one test bench implements the Broadcast network configuration, while the other implements the Standard White Rabbit configuration. The CLBs are connected to the necessary front-end switching fabric and their data is sent to servers running the Trigger and Data Acquisition System processes, recreating a setup which is compliant to the KM3NeT/ARCA shore-station one. As such, the data acquisition orchestration is handled by the Control Unit. The Bologna Laboratory

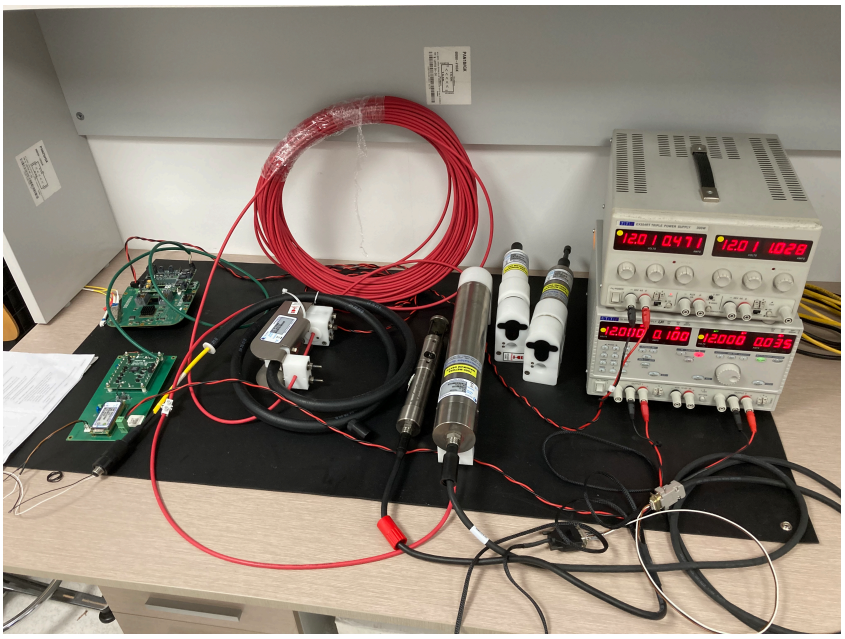

Figure 5.15: The test bench of the Bologna Laboratory for User-ports.

for User ports (see Fig. 5.15) simulates a Calibration Unit: the test bench is composed of a CLB, running the Calibration Base firmware, connected to an Inductive Modem Module mounted on its interface board. The modem is coupled to a 50 m copper test wire through an Inductive Cable Coupler. The CLB is connected via optical fibers to the Bologna Common Infrastructure networking and computing infrastructure, in order to integrate sensor data with the data acquisition system. In this way, it will allow the development and test of the process variable solution in order to implement the Calibration Unit control from the Control Unit. The test bench is currently equipped with the models of instruments that are present in the KM3NeT/ARCA Instrumentation Line, but it allows for testing of any kind of oceanographic sensor. In fact, the KM3NeT/ARCA detector infrastructure includes the *user ports*: dedicated ports of the Junction Boxes which serve as physical connection for power and data transmission to structures such as the Calibration Unit. These are meant to be possibly exploited by external users who intend to exploit KM3NeT infrastructure for deep-sea environmental studies. In this context, the test bench would provide a testing environment for those users.

Chapter 6

The Moon shadow analysis with KM3NeT/ARCA

As explained in Chap. 5, the KM3NeT relative acoustic positioning system measures the relative distances between Digital Optical Modules (DOMs) and acoustic emitters, but this does not constrain the absolute orientation of the telescope on Earth: the absolute positions of the Detection Units (DUs) and acoustic emitters must be also measured, and this is done by the Navigation and Absolute Positioning system. However, the absolute positioning system used so far in KM3NeT/ARCA is able to provide positions of DUs with an accuracy of O(10) m only, which produces a significant systematic uncertainty in the detector orientation. Nonetheless, comparing the measured beacons positions from acoustic data to the nominal positions provided by the navigation system, the Collaboration has been able to estimate the correction to the detector orientation. Moreover, starting from the KM3NeT/ARCA marine operation of 2025, novel acoustic emitters are going to be deployed, whose absolute position will be measured with ~ 1 m accuracy in each direction thanks to the adoption of a different absolute positioning system. An independent way to measure the pointing accuracy of the detector is to study the deficit of atmospheric muons (or other secondary particles, in other experiments) from the direction of the Moon due to the absorption of cosmic rays in the Moon, i.e., the Moon shadow. This approach has been already exploited in the past by multiple experiments such as MACRO [130], L3+Cosmics [131], MINOS [132], ARGO-YBJ [133], HAWC [134], IceCube [135], ANTARES [136] and others. In KM3NeT, this study was performed to evaluate the pointing accuracy of KM3NeT/ORCA and its angular resolution for down-going muons [137]. I have performed for KM3NeT/ARCA a similar analysis as the one done in ANTARES and KM3NeT/ORCA. This analysis served as an independent cross-check of the detector pointing in the study of KM3-230213A [**?**], in order to determine the correct event celestial coordinates.

6.1 Data and Monte Carlo samples

The analysis includes data collected by ARCA with 19 and 21 DUs, from 13/07/2022 to 11/09/2023 for a total of 335 days of livetime. The position of the Moon in the local altitude-azimuth coordinate system of the detector during the period is shown in Fig. 6.1. The data sample used in the analysis consist of all detected muon tracks whose direction

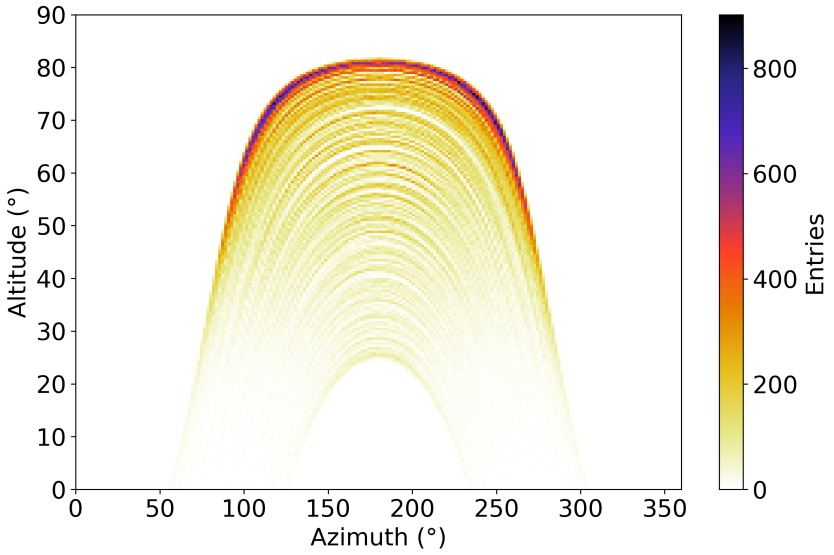

Figure 6.1: Altitude-azimuth coordinates of the Moon in the local sky of the KM3NeT/ARCA detector, from 13/07/2022 to 11/09/2023. Coordinates are obtained with *Astropy* package [138]. Here, the Moon position at the time of each detected event in the analyzed data sample is shown.

is located within a restricted field of view around the Moon position. Preliminary cuts were applied to the sample, in order to filter only well reconstructed, down-going muon tracks (i.e., with altitude defined as the angle between the horizon and the track, greater than 0). I have implemented the event selection, after the application of the preliminary cuts, according to the following procedure:

1. for each event, and at its related date and timestamp, the altitude and azimuth coordinates of the Moon in the local sky of the KM3NeT/ARCA detector was computed by means of the Astropy software [138];

2. for each event, the angular distance between the sky position of the Moon at the time of the event and the event was evaluated: if the distance is smaller than 12° the event is kept, otherwise is rejected. This is done in order to restrict the field of view around the Moon by an angular distance of 12°, which is large enough to host a good statistics for atmospheric muons in the chosen field of view;

The altitude distribution of the selected tracks, shown in Fig. 6.2, reflects the altitudes of the Moon throughout the period, which range above the horizon up to about 80°. A further, later, filtering step in the selection of the data sample consisted in the application of cuts on quality parameters of the reconstructed tracks, described in Sect. 6.2.1. The chosen cuts were determined from a study on the corresponding Monte Carlo sample of atmospheric muons.

The Monte Carlo sample is generated with the MUPAGE software [139], on a *run-by-run* basis, i.e., reproducing the effective data taking conditions of each detector *run* (see Sect. 2.7). The successive steps of the Monte Carlo simulate the propagation of the atmospheric muons in sea water and the emission of Cherenkov photons within a cylindrical volume around the detector, with a radius equivalent to the radius of the

detector instrumented volume enlarged by four times the light absorption length in water. Light is then propagated up to the PMTs of DOMs, whose efficiencies are simulated according to real measured values. The optical background, discussed in Sect. 2.7.4, is also simulated according to the measured rates during each run. Finally, the PMT hits are processed using the trigger and reconstruction software as done for real data. To each reconstructed event a date and timestamp is assigned, which is generated uniformly over the run duration. The same preliminary cuts used for data, which filter only the

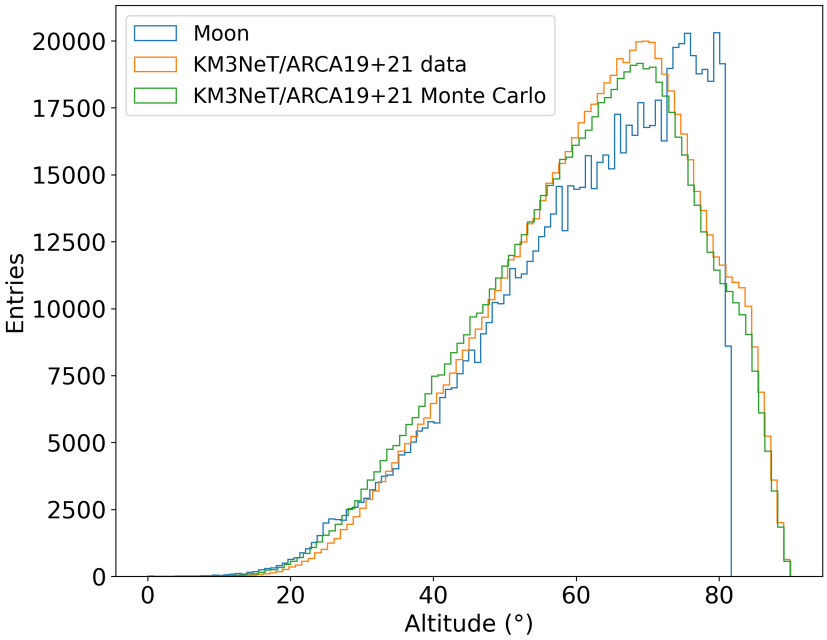

Figure 6.2: Distributions of the altitudes of the detected muon tracks in the analyzed data sample (in orange) and in the Monte Carlo sample (rescaled to data, in green), in the proximity of the Moon, whose altitudes during the data period are shown (in blue) for comparison.

well reconstructed, down-going muon tracks, were applied also to the simulated events.

In order to reproduce in the Monte Carlo sample the muon deficit due to the presence of the Moon in the sky, I have modified the described procedure used for the selection of the data sample adding the following additional step:

3. among the surviving events from step 2, the muon deficit due to the Moon disk is simulated by rejecting all muon tracks whose generation direction lies within 0.26° (the Moon angular radius) of angular distance from the Moon position.

The effect of the interplanetary magnetic field on the primary impinging cosmic ray trajectories was neglected from energetic considerations. Considering a proton with energy of 200 GeV and an average value of the interplanetary magnetic field at Earth's orbit of 6 nT [140], the Larmor radius $r_L = p/qB$ is of the order of 10^{11} m, much larger than the distance between Moon and Earth which is $\sim 3.8 \times 10^8$ m: such a proton undergoes no significant deflection in its path between the Moon and the Earth. Considering that the detected down-going muons in the KM3NeT/ARCA detector have energies larger than 500 GeV, which is only a fraction of the parent primary cosmic

ray, we can safely assume that the effect of the interplanetary magnetic field on the trajectories of primary cosmic rays of the detected muons is negligible. The effect of the geomagnetic field can also be neglected, since it has an intensity at most of the order of tens of μT on Earth surface, rapidly decreasing under a $\propto 1/r^3$ law if we approximate it with a dipole behavior. For this reason, the geomagnetic field extends only up to $O(10^7\,\mathrm{m})$ in space, i.e., a small fraction of the particle trajectory from Moon to Earth. The same assumption can be done also for the secondary muons produced in the cosmic ray interaction, since their Larmor radius is, considering the geomagnetic field and the minimum detected energy, at least three orders of magnitude larger than the distance traveled up to the detector. Moreover, the angular deflection between the secondary muon and the primary cosmic ray, due to the transverse momentum of the parent pion of the muon and in the pion decay, is limited by the large Lorentz factor.

6.2 Analysis method

The significance of the shadowing effect of the Moon is assessed using a likelihood ratio test, i.e., comparing the likelihood of a null hypothesis H_0 and the likelihood of the alternative hypothesis H_1, both evaluated on the 2-dimensional muon distribution over the field of view, centered at the Moon nominal position. The muon distribution is represented as function of the variables (x, y), representing the planar projection of the Cartesian components of the angular distance between the muon direction and the Moon position, as illustrated in Fig. 6.3. These coordinates are defined as:

$$\begin{aligned} x &= (\alpha_\mu - \alpha_{Moon}) \times \cos(h_\mu) \\ y &= h_\mu - h_{Moon} \end{aligned} \tag{6.1}$$

where (α_μ, h_μ) are the azimuth and altitude coordinates of the muon track and $(\alpha_{Moon}, h_{Moon})$ are the azimuth and altitude coordinates of the Moon, at the time of the detected event [1].

The field of view, centered at the nominal Moon position, is thus defined by a 2-dimensional grid in the (x, y) variables, whose bins are filled by the distribution of the muon events.

The null hypothesis corresponds to the background-only case, where no Moon is present in the field of view; the alternative hypothesis corresponds to the case of an *anti-signal* (i.e, a deficit of events) superimposed to the background due to the presence of the Moon in the field of view, which blocks the primary cosmic rays. The test-statistic used in the analysis is the log-likelihood ratio:

$$\lambda = -2 \ln \frac{L_{H_1}}{L_{H_0}} \tag{6.2}$$

where L_{H_1} and L_{H_0} are the likelihoods of data samples under the H_1 and H_0 hypotheses. Under the assumption that the distribution of events in each bin of the field of view

[1] The definition used here of the x coordinate is the same of the one adopted in [137], the only difference being the use in this analysis of the altitude variable, whereas the zenith angle (defined as the altitude plus 90°) is used in the KM3NeT/ORCA analysis This can be seen by comparing the events altitude distribution of Fig. 6.2 with the event zenith distribution of Fig. 2 in [137]. This difference implies the presence of a cosine factor here, instead of the sine factor in [137].

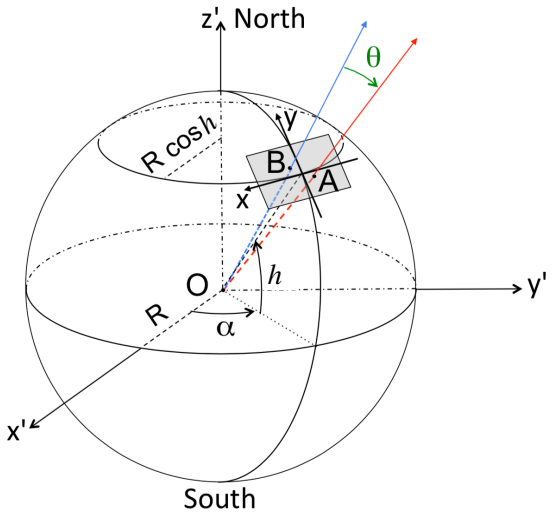

Figure 6.3: Representation of the angular distance between two celestial objects A and B in the local sky, projected on a plane. Objects positions are defined by their azimuth (α) and altitude (h) coordinates. In this analysis, the objects are the muon track and the Moon. Considering a unit sphere and centering the origin of the (x, y) plane on the Moon position, the projections on the x, y axes of the relative distance of the muon track are described by Eq. 6.1.

follows the Poisson distribution, the likelihood under hypothesis H (either H_0 or H_1) for N_{bin} of the field of view is:

$$L_H = \prod_{i=1}^{N_{bin}} \frac{e^{-N_{i,H}} N_{i,H}^{n_i}}{n_i!} \tag{6.3}$$

where n_i is the observed number of events occurring in the i-th bin, and $N_{i,H}$ is the expected number of events in the i-th bin under the H hypothesis. Defining

$$\chi^2_H = -2 \ln L_H \tag{6.4}$$

as in [141], Eq. 6.3 becomes:

$$\chi^2_H = 2 \sum_{i=1}^{N_{bin}} \left(N_{i,H} - n_i + n_i \ln \frac{n_i}{N_{i,H}} \right) \tag{6.5}$$

and the log-likelihood ratio in Eq. 6.2 becomes:

$$\lambda = \chi^2_{H_1} - \chi^2_{H_0} = 2 \sum_{i=1}^{N_{bin}} \left[N_{i,H_1} - N_{i,H_0} + n_i \ln \left(\frac{N_{i,H_0}}{N_{i,H_1}} \right) \right] \tag{6.6}$$

The advantage of the quantity λ in Eq. 6.6 is that, being based on a likelihood ratio, it asymptotically (i.e., for a large number of events) follows a χ^2 distribution with the due number of degrees of freedom, according to Wilks' theorem. This property is therefore used in the analysis to determine the probability of rejecting the null hypothesis, and to extract the significance of the Moon shadow.

The 2-dimensional distribution of the events is represented by a histogram with x, y axes ranging from $-6°$ to $+6°$, with bin sizes of $0.2° \times 0.2°$. The expected number of events in each bin of the histogram under the H_0 and H_1 hypotheses is obtained by fitting it with a background and a background plus anti-signal functions that model the hypotheses. The chosen range of the histogram is such that it is wide enough to properly model the background event density and to contain the entire detectable shadow anti-signal. Varying the range of up to $\pm 0.5°$ has shown to affect the background fit parameters estimation only at few percent level, and to not affect the position of the minimum of the λ test statistic. Following what has been done in the KM3NeT/ORCA analysis [137], the background function is parametrized with a polynomial function of the form:

$$p(x, y, \mathbf{k}) = k_0 \cdot P_x(x, \mathbf{k_x}) \cdot P_y(y, \mathbf{k_y}) \tag{6.7}$$

where $P_x(x, \mathbf{k_x})$ is a polynomial function of degree k_x of the variable x with coefficients $\mathbf{k_x}$, and $P_y(y, \mathbf{k_y})$ is a polynomial function of degree k_y of the variable y with coefficients $\mathbf{k_y}$. The polynomial functions are defined as:

$$P_z(z, \mathbf{k_z}) = 1 + \sum_{i=1}^{n_z} k_{zi} \cdot z^i \quad \text{for } z = [x, y] \tag{6.8}$$

and the degree of the polynomials has been determined according to the best match with the Monte Carlo sample, by finding the degree of the polynomial fit function that had the best agreement with the distribution of the events x and y variables. The expected number of events per bin under the H_0 hypothesis, N_{i,H_0}, is then determined from the fit of the background function. As in [137], the event distribution on x was found to be uniform (0-degree polynomial), while the projection on y is best parametrized with a second order polynomial function. The flat distribution of the events over the x variable is in agreement with the expected homogeneous atmospheric muon flux along the azimuth coordinate; on the other hand, the rising distribution of the events over the y variable reflects the increase of the muon flux with the altitude.

Even though the search of the degrees of the polynomial functions that parametrize the background distribution was done on the Monte Carlo sample which include the anti-signal at the $(x, y) = (0, 0)$, this procedure is made reliable by the following considerations: the chosen range of the fitted distribution ($\pm 6°$) is large enough, and the number of events blocked by the Moon small enough ($\sim 5 \times 10^2$ among $\sim 1 \times 10^6$ events in the field of view, before applying the quality cuts and without considering the effect of the detector angular resolution that lead to the mis-reconstruction of some events in the direction of the Moon even though their simulated original trajectory did not point in that direction) to consider the effect of the anti-signal negligible in the fit of the background function. Thus, using the definitions in Eq. 6.8, the function which parametrize the background, from Eq. 6.7, is:

$$p(x, y, \mathbf{k}) = k_0 \cdot (1) \cdot (1 + k_{y1} y + k_{y2} y^2) \tag{6.9}$$

In Fig. 6.4, the projections of the events distributions in the field of view over the x and y variables are shown, for both the Monte Carlo and data samples. The described reasons that supported the choice of evaluating the degrees of the background polynomial functions $P_x(x, \mathbf{k_x}), P_y(y, \mathbf{k_y})$ on the Monte Carlo event distribution regardless of the

presence of the anti-signal in the center of the field of view, holds true also in the case of the data events distribution, as shown in Fig. 6.4 by the goodness of the 0-degree and 2-nd degree polynomials fits on the x and y distributions for the data sample. Thus, the function in Eq. 6.9 is applied to the 2-dimensional histogram of the data event distribution to parametrize the background, and the estimation of the parameters $\mathbf{k} \equiv \{k_0, k_{y1}, k_{y2}\}$ from the fit gives $\mathbf{k} = \{67.2 \pm 0.2, (63.4 \pm 0.6) \times 10^{-3}, (2.6 \pm 0.2) \times 10^{-3}\}$. The values found from the fit of the Monte Carlo 2-dimensional event distributions are compatible, as expected, at few percent level with these values.

In the H_1 hypothesis the Moon is considered as a point-like anti-source which removes events from the muon sample. This choice comes from the fact that the expected angular resolution of the detector for the data sample is larger than the angular radius of the Moon. The deficit is smeared out by the point spread function of the detector: in this analysis, as a first approximation, the point spread function of the detector was parametrized as a two-dimensional Gaussian function, following what has been done in KM3NeT/ORCA [137] and ANTARES [136]. This results in a fit function defined as a bi-dimensional Gaussian deficit of events, superimposed to the background function as follows:

$$f(x, y, A, \sigma_{res}, x_s, y_s) = p(x, y, \hat{\mathbf{k}}) \cdot \left(1 - \frac{A\pi R_M^2}{2\pi\sigma_{res}^2} \exp\left[-\frac{(x^2 - x_s^2) + (y^2 - y_s^2)}{2\sigma_{res}^2}\right]\right) \quad (6.10)$$

where

- R_M is the apparent angular radius of the Moon, i.e., 0.26°;
- A is the relative amplitude of the Moon deficit;
- σ_{res} is the angular width of the Gaussian shadow. This can be interpreted as the detector angular resolution for down-going muons, since the expected detector angular resolution for these events is larger than the size of the Moon
- x_s, y_s are the assumed x and y coordinates from Eq. 6.1 of the Moon position in the field of view.

The significance of the shadow at the nominal Moon position $(x_s, y_s) = (0, 0)$ is determined by fitting A on the 2-dimensional event distribution, and deriving it from the corresponding value of λ, referred to as λ_O, i.e. the test-statistic in Eq. 6.6 evaluated at the bin centered in $(0, 0)$. The value of σ_{res} is fixed to the expectation value determined from the Monte Carlo sample. According to Wilks' theorem [142], the λ distribution asymptotically follows a χ^2 distribution with $m - n$ degrees of freedom, where $m(n)$ are the degrees of freedom of the fit of the $H_1(H_0)$ hypothesis. Here, the resulting parameter of interest is A.

The best-fit position of the shadow is obtained instead by fitting (A, x_s, y_s) and fixing σ_{res} to the value found from the Monte Carlo. Moreover, in order to determine the distribution of λ when x_s, y_s are varied, a scan is performed over the assumed coordinates of the Moon: this is done by defining a 2-dimensional grid, narrowed in the range ±2° (because the position of the Moon shadow, even considering possible mis-alignments of the detector, is expected to be well contained within this range) and with bin sizes of $0.01° \times 0.01°$. The concept of the grid is illustrated in Fig. 6.5: for each bin of the grid, the

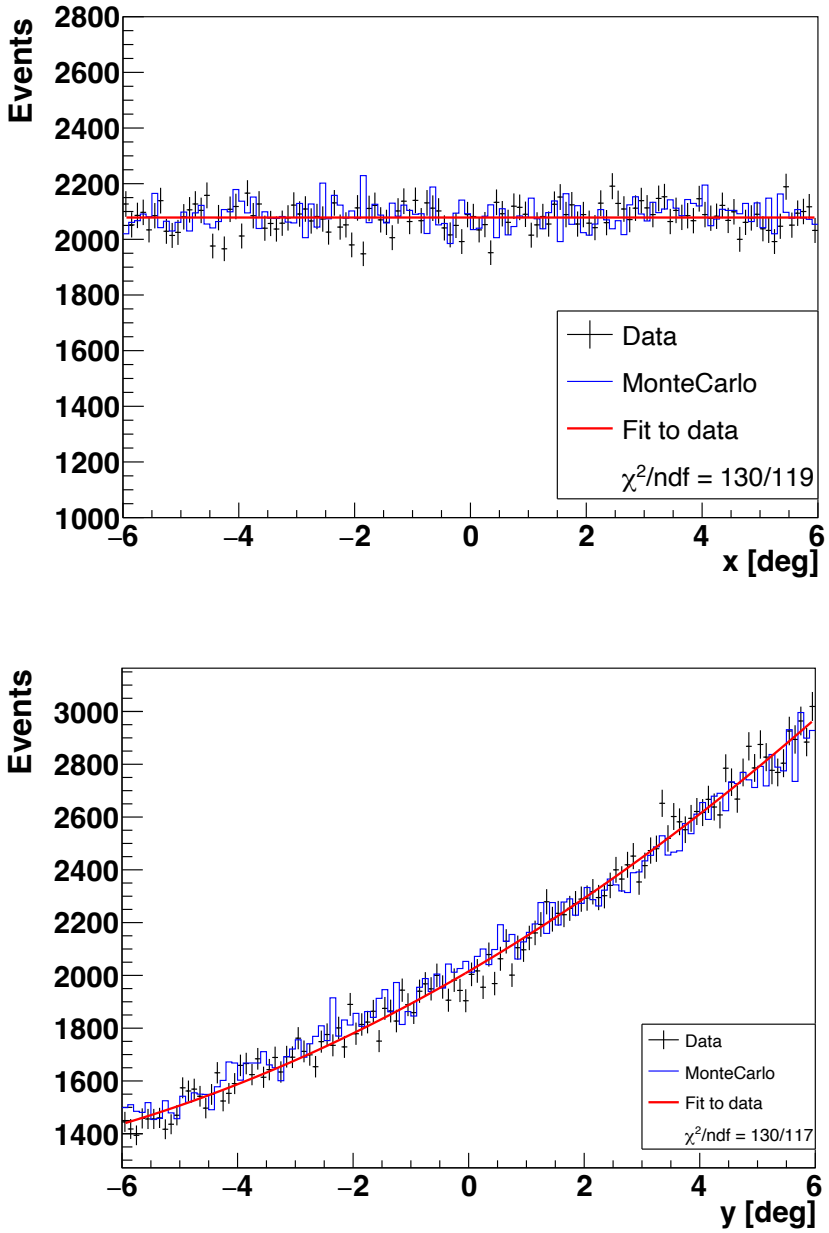

Figure 6.4: Distribution of the x (up) and y (bottom) coordinates of the events, compared to the polynomial fits (red lines) of the background H_0 hypothesis and expectation from the MonteCarlo (blue histogram, rescaled to data), after applying the selected quality cuts. The x distribution is fitted with a 0-degree polynomial function, while the y distribution is fitted with a 2nd-degree polynomial function.

Moon position is assumed with (x_s, y_s) corresponding to the center of that bin, and these values are used to perform the fit of the 2-dimensional event distribution histogram with the function in Eq. 6.10, with A as a free parameter and σ_{res} fixed to the value found from the Monte Carlo. This way, the 2-dimensional map of the λ values is constructed and the contour lines around the minimum value λ_{min}, corresponding to $1\sigma, 2\sigma, 3\sigma$ confidence levels can be drawn. The map can be interpreted as the profile-likelihood in the x_s, y_s parameters space, with A being the nuisance parameter, and thus with two degrees of freedom. The confidence level regions are obtained such that $\lambda \leq \lambda_{cut}$, with:

$$\lambda_{cut} = \lambda_{min} + Q(2, CL) \tag{6.11}$$

where $Q(\text{dof}, CL)$ is the p-quantile of the chi square distribution accounting for two degrees of freedom and the confidence level CL, and $Q(2, 68.27\%) = 2.30$, $Q(2, 95.45\%) = 6.18$, $Q(2, 99.73\%) = 11.83$ [143].

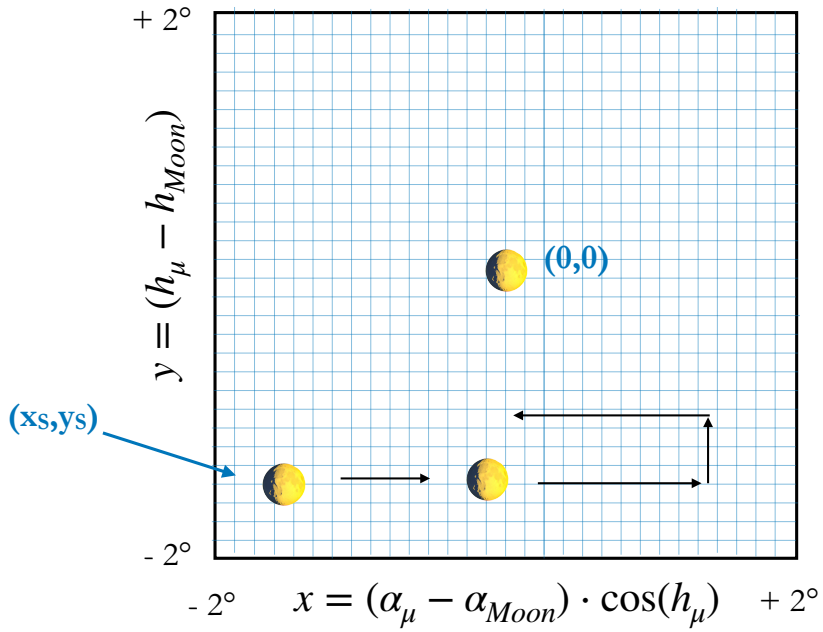

Figure 6.5: Illustration of the adopted technique for constructing the 2-dimensional map of the λ test statistic (here shown in a field of view within 2° in x and y from the Moon nominal position $(x, y) = (0, 0)$). The Moon position is varied and assumed at the center of each bin of the map, where the test statistic is then evaluated.

6.2.1 Results from Monte Carlo

The Monte Carlo sample in this analysis is exploited mainly to determine the best quality cuts to apply to the real dataset, and to estimate the value of σ_{res} to be used to evaluate the best-fit position of the Moon in the scan of the field of view with the data sample. The selected parameters which I considered for the optimization of the reconstructed muon tracks in the samples are the likelihood of the track-like event reconstruction fit, and the estimate on the angular error, called β_0. The criterion to determine the best cut values is to minimise the λ test-static considering the Moon at the nominal position, i.e.,

at the center of the field of view with $(x_s, y_s) = (0, 0)$: thus, the different cuts on the two parameters are scanned, and each time the corresponding value of λ_O is computed. For

Cut on *likelihood*	**Cut on β_0**
> 50	$< 0.4°$

Table 6.1: Optimization cuts found from the Monte Carlo sample.

this study, I used the ARCA21 Monte Carlo sample (2388 runs corresponding to 287.5 days of livetime) and increased the statistics, simulating six times the livetime of the dataset. This has been done by performing six times the selection procedure described in Sect. 6.1, each i-th time applying an offset of $2 \cdot i$ hours (with $i = [0, 1, 2, 3, 4, 5]$) to the time at which the Moon position is computed, at step (1) of the procedure. This way, different muon tracks of the original Monte Carlo sample are selected for every i-th sample, along the phase space of the coordinates of Moon in the local sky. The samples were then merged into one. The resulting scan of the cut parameters is shown in Fig. 6.6. The optimal cuts that I found, for which the λ_O has the minimum value, are illustrated in Tab. 6.1. Applying those cuts, the corresponding fraction of surviving events is 63%, and the fitted values of the shadow amplitude and of the angular resolution are $A = (0.62 \pm 0.08)$ and $\sigma_{res} = (0.31 \pm 0.03)°$.

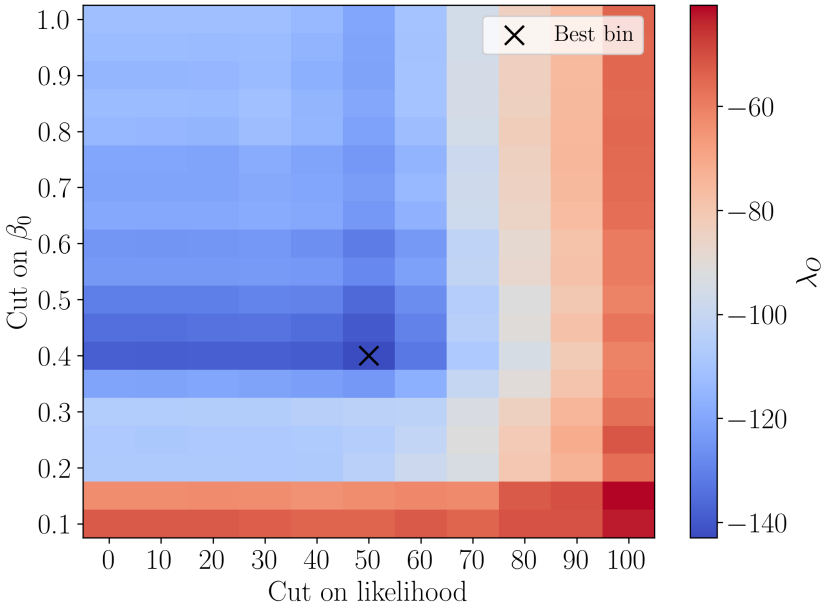

Figure 6.6: Distribution of λ computed at the nominal Moon position $(x, y) = (0, 0)$, i.e., λ_O, when different cuts on the track likelihood and on the angular error estimate β_0 are applied. The bin with the lowest value of λ_O, for which the best cuts are determined, is highlighted with a black cross.

In addition, the Monte Carlo is exploited to evaluate the uncertainty on the assumed rotation of the detector. If the detector is rotated around the vertical axis (i.e., a rotation

of the azimuth coordinate) by an unknown offset, a possible way to investigate the offset is to perform a scan over different assumed shifts of the azimuth coordinate of the real events and to determine for which value the significance of the Moon shadow in the nominal position $(x, y) = (0, 0)$ reaches its maximum. The associated error to this estimate on the shift of the azimuth can be evaluated from a study on the Monte Carlo: performing the scan of the significance of the Moon shadow when the azimuth of the events is varied, one can find the shift of the azimuth for which the significance reaches its maximum; the expected value of the shift is zero, as in the simulation the events coordinates are generated according to the fixed detector coordinate system. In other words, the detector in the Monte Carlo simulation cannot have an unknown rotation around the vertical axis. By repeating the same study over several Monte Carlo samples, the distribution of the best azimuth shift is obtained. To do this I considered 12 compatible, in terms of statistics, ARCA19+21 Monte Carlo samples (2767 runs, corresponding to 335 days of livetime) obtained as per procedure in Sect. 6.1, but for each sample i applying an offset of $2 \cdot i$ hours ($i = [0, ..., 11]$) to the time at which the Moon position is computed. For each sample, I varied the azimuth of the events in the range $\pm 3^\circ$ with steps of 0.2° and computed the λ_O for each shift in order to determine the value which corresponded to the highest significance. During the fit, the σ_{res} was fixed to 0.31° i.e., the best Monte Carlo estimate resulting from the cuts optimization. The confidence interval at 1σ is obtained increasing by one the minimum value of λ_O (here following a χ^2 distribution with one degree of freedom). The resulting distribution of the best azimuth offsets found for the 12 Monte Carlo samples, together with the 1σ confidence intervals is shown in Fig. 6.7.

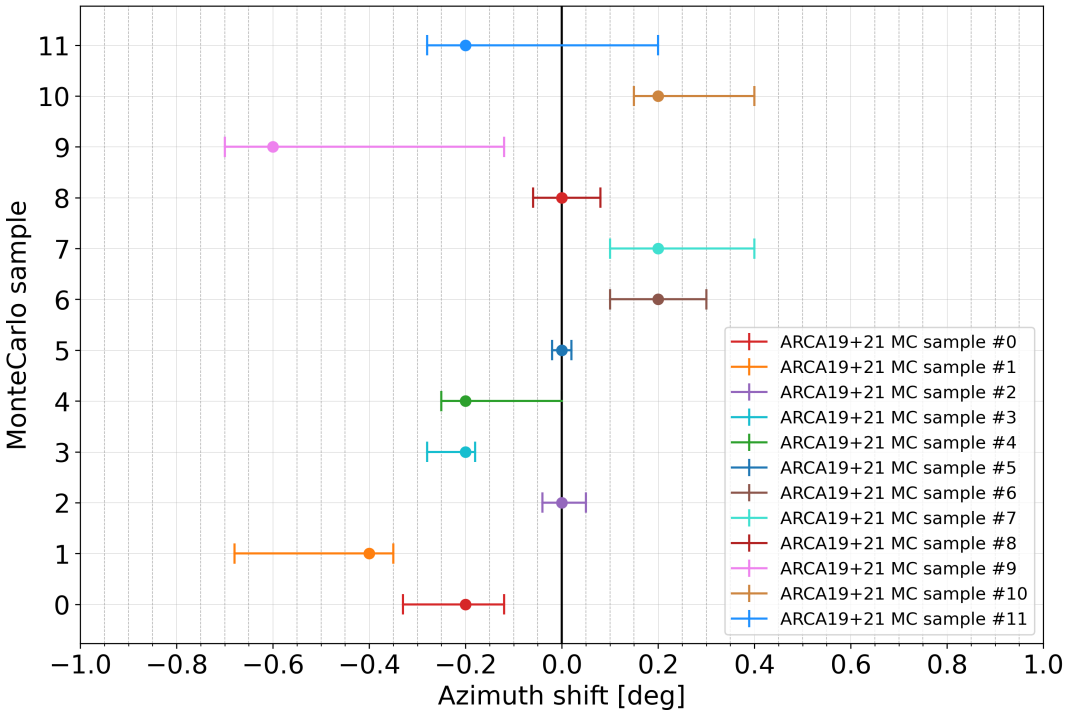

Figure 6.7: Azimuth offset, applied to the muon tracks, that maximizes the Moon shadow significance in the nominal position $(x, y) = (0, 0)$, i.e., minimizes λ_O, for each of the 12 different Monte Carlo samples. The dotted lines represent the corresponding 1σ confidence intervals.

The standard deviation of the distribution, equal to sdev $= 0.24°$, has been taken as the estimate of the uncertainty on the best azimuth offset.

6.3 Results from data

The final data sample, after having applied the optimal cuts found in Sect. 6.2.1, consists in 784128 muon tracks detected in 335 days of data taking. An average event density can be estimated from the densities of events contained in annuli of the field of view centered on the Moon position: doing this with steps of 0.2° gives an average density of 1700 events per square degree. The sample characteristics are summarized in Tab. 6.2.

I have performed the H_0 and H_1 hypothesis fits and built the 2-dimensional λ distribution, shown in Fig. 6.8. The distribution is obtained, as illustrated in Sect. 6.2, by defining a grid in the $\pm 2°$ range in both x and y with bin size of 0.005° (to create a smooth map), assuming the Moon position at the center of each bin, and computing λ under this assumption. The σ_{res} is here fixed to the value estimated from the Monte Carlo, i.e., $\sigma_{res} = 0.31°$.

The (x, y) coordinates corresponding to the smallest λ, that is $\lambda_{min} = -21.21$, are $x_s = (0.79 \pm 0.09)°$, $y_s = (-0.08 \pm 0.08)°$, which are taken as the best estimation the position of the Moon. The fitted relative shadow amplitude is $A_{min} = (0.57 \pm 0.12)$, compatible with the Monte Carlo expectation, and the p-value associated to λ_{min} is $p = 4.1 \times 10^{-6}$, corresponding to a significance of 4.5σ. The value of λ found in the nominal position $(x, y) = (0, 0)$ is $\lambda_O = -2.52$. Since at each bin the test statistic λ

Data sample	
Time period	13/07/2022-11/09/2023
Livetime (days)	335
Field of view around Moon	12°
Events	784128
Average event density	1700/deg^2

Table 6.2: Final data sample of KM3NeT/ARCA19+21 used in the Moon shadow analysis, after the optimization cuts.

follows asymptotically a χ^2 distribution with one degree of freedom, assuming H_0 as true, the p-value associated to λ_O is $p = 0.11$, corresponding to a 1.2σ significance of the shadow when the Moon is assumed in the nominal position. The low significance in the center is expected, since the orientation of the detector is known to suffer from a systematic shift.

The $y = 0$ coordinate is compatible within 1σ with the y_s found for the best position of the Moon. This means that the observed data are compatible, within statistical fluctuations, with the absence of a systematic offset on the tilt angles of the Detection Units (i.e., on the string inclination from the nominal position determined with the acoustic calibration). The $x = 0$ coordinate is beyond the 3σ compatibility with the x_s found for the best position of the Moon, indicating the presence of an offset in azimuth of the detector. According to the definition in Eq. 6.1, a shift in the x coordinate is connected with a shift in the azimuth α coordinate of the muon tracks by the factor $\cos(h_\mu)$ which reflects the distribution of the cosines of the altitude of the tracks. This distribution for the data sample is shown in Fig. 6.9, and has a mean value of ≈ 0.5. Using this mean value, a shift of the azimuth of the muon tracks can be inferred to be approximately within the range $\approx [+1.4°, +1.8°]$, obtained from the 68% confidence interval around the best position of the Moon $x_s = (0.79 \pm 0.09)°$.

An independent dedicated study has been performed by the Collaboration in order to determine the shift of the detector orientation. In this study, the acoustic beacon positions, as used in the calibration of the detector for the reconstruction of the events, are compared with their positions determined during their deployment. The results showed that there is a net rotation between these two positions, estimated to be of 1.35°: to recover the beacons positions as measured during the deployment, the detector should be rotated of +1.35° degrees in the clockwise direction, or the azimuth of the events should be rotated of 1.35° in the counter-clockwise direction. This value is only slightly outside the $[+1.4°, +1.8°]$ range of the azimuth shift of the events inferred from the best assumed position of the Moon.

According to this indication, I have built the 2-dimensional map of the distribution of the λ test statistic after having shifted the azimuth of the events by $-1.35°$. The distribution is shown in Fig. 6.10. The best fit point has $x_s = (0.13 \pm 0.14)°$ and $y_s = (0.12 \pm 0.11)°$ with $A_{min} = (0.46 \pm 0.12)$ and $\lambda_{min} = -13.87$. This corresponds to a p-value of $p = 2 \times 10^{-4}$, that is, a significance of 3.55σ. In the nominal position, the

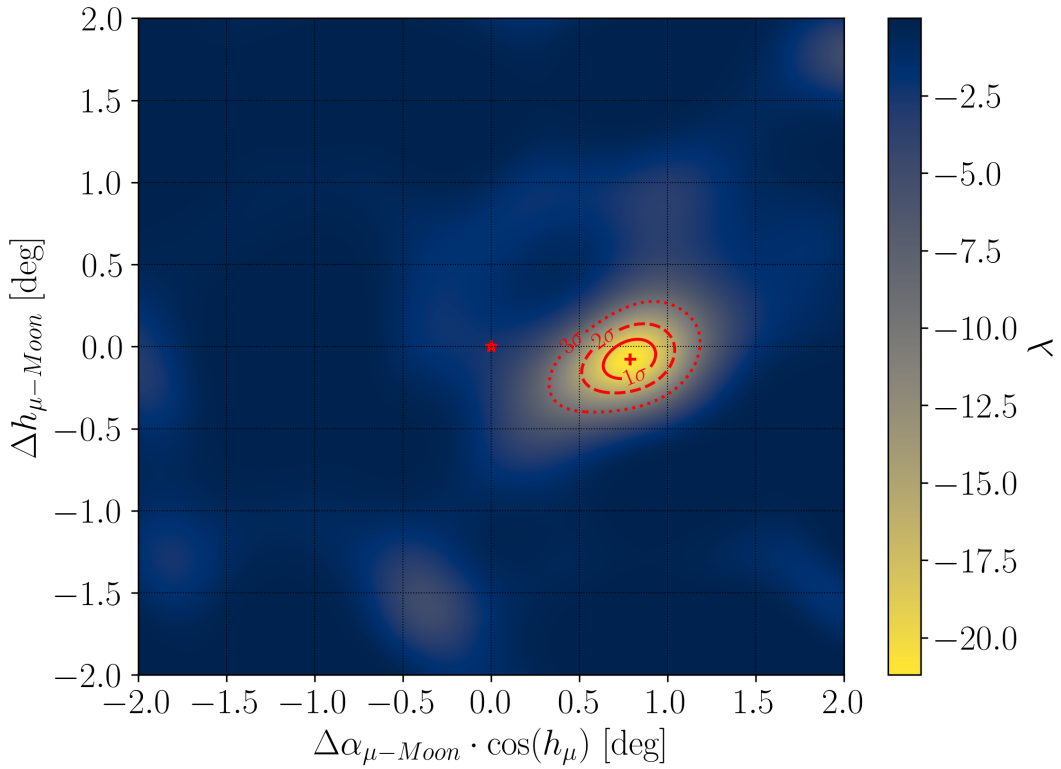

Figure 6.8: Distribution of the test statistic λ from Eq. 6.6 in the field of view (zoomed in the range $\pm 2°$) around the Moon nominal position $(x, y) = (0, 0)$, indicated by a red star. The red dot refers to the coordinates $(0.79°, -0.08°)$ where the minimum of the test statistic is located, with $\lambda_{min} = -21.21$. The contour levels corresponding to $1\sigma, 2\sigma, 3\sigma$ confidence levels are shown.

test statistic has a value of $\lambda_O = -11.27$: a difference of 2.6, which means that, with two degrees of freedom, the nominal position is contained in the 72.7% confidence level. The significance of the Moon shadow in the nominal position is 3.16σ. These results for the Moon shadow represent thus a cross-check of the validity of the nominal detector orientation, once corrected for the $-1.35°$ azimuth shift. This correction has therefore been applied by the Collaboration to the detected events, including KM3-230213A, to recover the nominal orientation of the detector and assign the correct event coordinates.

Another way to evaluate the offset in the azimuth of the events is to study the distribution of λ_O when the azimuth of the muon tracks is shifted: the shift for which the test statistic reaches the minimum value can be taken as the best estimate for the offset. The procedure is the same as the one performed on the 12 independent Monte Carlo samples in Sect. 6.2.1. Assuming now the shift of $-1.35°$ as the *nominal* orientation of the detector, I have performed the scan of λ_O varying the azimuth of the muon tracks in the range $[-3°, +3°]$ from the nominal orientation, with steps of $0.25°$. The step size has been chosen to be compliant to the $0.24°$ uncertainty associated to the best azimuth offset determined with this procedure. This uncertainty is the statistical error obtained from the analysis of the Monte Carlo simulations in Sect. 6.2.1. For each shift, the x coordinate of the events is computed, the fits of the H_0 and H_1 functions performed and the λ_O determined. The obtained λ_O distribution is shown in Fig. 6.11. The minimum value,

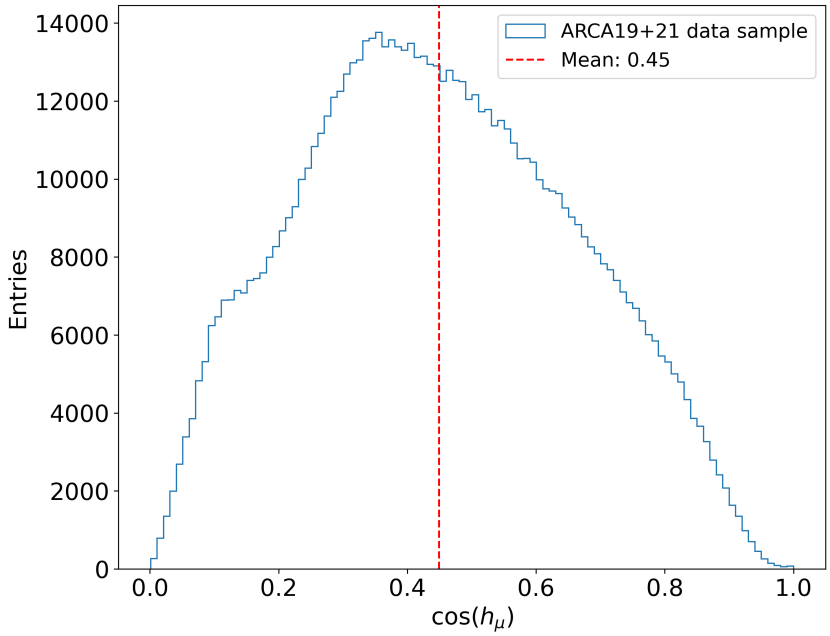

Figure 6.9: Distribution of the cosines of the altitude of the muon tracks for the ARCA19+21 data sample of the analysis. The mean value of the distribution is highlighted by the red dotted line, and is reported in the text box.

and the corresponding largest significance of 3.16σ, is found for the nominal assumption, with the associated error of 0.24°.

The deficit of muon tracks due to the Moon presence can be also observed studying the density of muon events, contained in annuli of the field of view centered on the Moon position, as a function of the angular distances from the Moon. Unfortunately, the statistics of the current dataset is too low to perform this kind of study (as a comparison, the event density in the KM3NeT/ORCA analysis [137] was $\rho \simeq 3000\,\text{events/deg}^2$, while for the present KM3NeT/ARCA19+21 dataset it is $\rho \simeq 1700\,\text{events/deg}^2$) which I will do once the dataset from KM3NeT/ARCA with 28 Detection Units will be available, adding another year of data to the current sample.

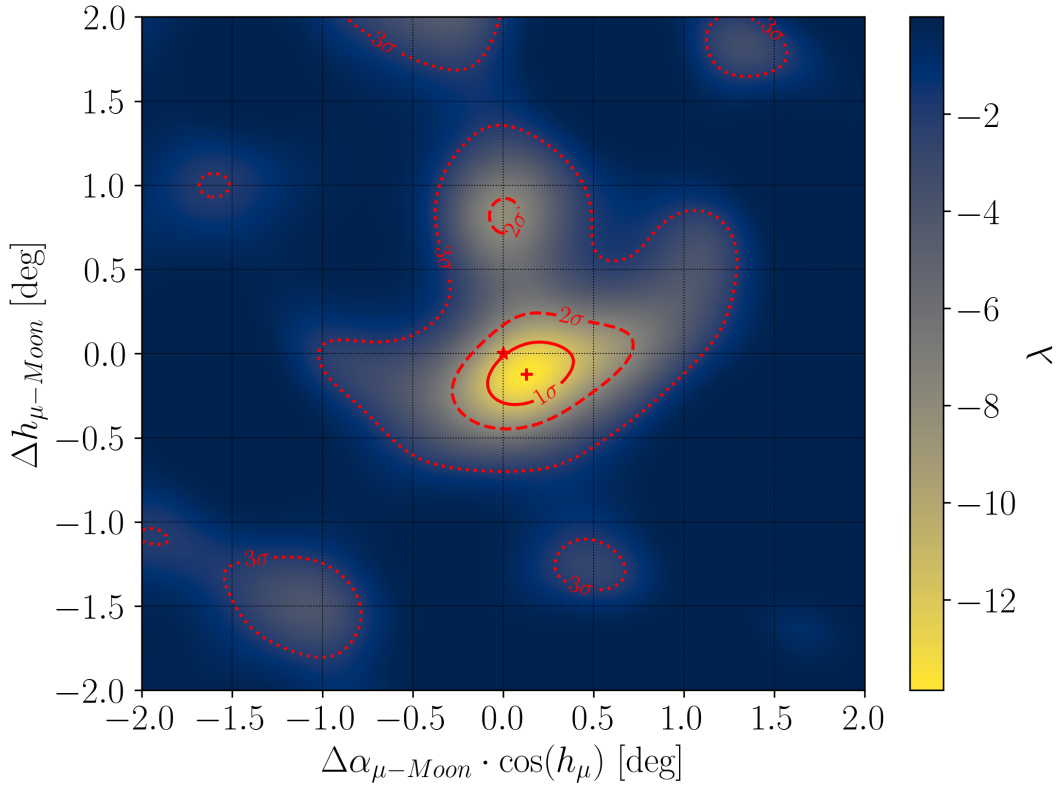

Figure 6.10: Distribution of the test statistic λ in the field of view (zoomed in the range $\pm 2°$) around the Moon nominal position $(x, y) = (0, 0)$, indicated by a red star, after performing a shift of $-1.35°$ of the azimuth α of the muon tracks. The red dot refers to the coordinates $(0.13°, -0.12°)$ where the minimum of the test statistic is located, with $\lambda_{min} = -13.87$. The contour lines corresponding to 1σ (68.3%), 2σ(95.4%), 3σ(99.7%) confidence levels around the minimum of the test statistic are shown.

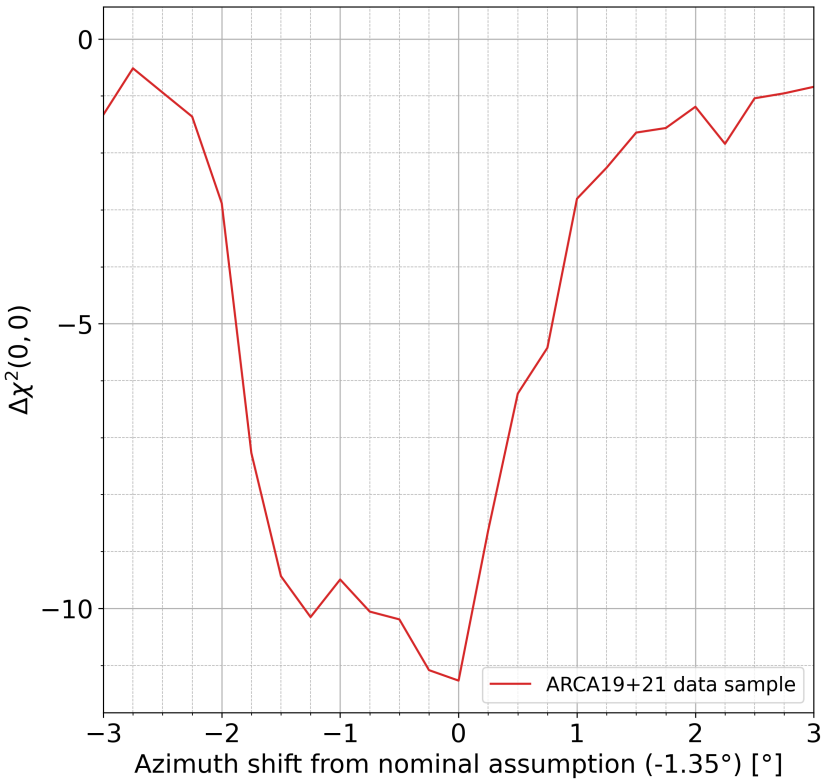

Figure 6.11: Distribution of the test statistic computed in the nominal Moon position $(x, y) = (0, 0)$, i.e., λ_O (here expressed as $\Delta\chi^2(0,0) \equiv \chi^2_{H_1}(0,0) - \chi^2_{H_0}(0,0)$), as a function of the shift applied to the azimuth, from the *nominal* assumption (here defined as a shift by $-1.35°$), of the muon tracks. The minimum of the distribution, or the largest significance, is found for the nominal assumption.

Conclusions

With the continuous deployment of new Detection Units, the KM3NeT experiment is rapidly evolving into one of the largest neutrino telescopes on Earth and will become a cornerstone of neutrino astronomy in the coming years. At present, in March 2025, its two detectors consist in 24 Detection Units, for KM3NeT/ORCA, and 34 Detection Units, for KM3NeT/ARCA. Despite the current limited sizes, corresponding to 16% and 12% of the respective detectors final configuration, KM3NeT early results have already demonstrated its potential. The recent announcement of the detection with KM3NeT/ARCA of the extremely energetic neutrino event KM3-230213A, with an estimated energy of 220 PeV, represents a breakthrough discovery in the neutrino astronomy field. In order to be operated with the required performances to reconstruct neutrino events with a sub-degree angular resolution, the accurate calibration of the telescope is essential: the time synchronization of the optical modules, the determination of their relative and absolute positions, as well as their orientation are the key parameters to do so.

This thesis gives an overview of the main current KM3NeT time and position calibration methods, and describes the work that I have done in the their most recent developments, which are going to enhance the detector performances in terms of angular resolution. In October 2024, the first 3 Detection Units constructed according to the new Standard White Rabbit network architecture and (partially) the Calibration Unit have been installed in KM3NeT/ARCA. The new network architecture implies a change of paradigm in the time synchronization and calibration of the optical modules, providing a simplified and more precise time calibration. From the early results of the time calibration of those Detection Units, illustrated in the thesis, the new approach has proven to be effective in synchronizing the optical modules with sub-nanosecond precision. Currently, the 3 Standard White Rabbit Detection Units are taking data and will soon mark the beginning of the Phase 2 of the detector where Detection Units with the Standard White Rabbit architecture will take data alongside Detection Units with the Broadcast architecture: the calibration approach which I contributed to design is such that the two different detector architectures will be synchronized among each other, in order to grant a reliable detection of events involving the Detection Units of the two kinds. At the same time, the measurements carried out by the oceanographic instruments of the Calibration Unit will improve the positioning calibration of the optical modules, by refining the sound velocity input parameter of the acoustic positioning system and providing information on sea currents. In the thesis, the description of the KM3NeT/ARCA Calibration Unit, along with the functional tests that I performed in order to prepare it for its installation of October 2024 and operation in the following months, are illustrated. Due to technical constraints, the inductive line of the Instrumentation Unit could not be installed and its deployment has been postponed to 2025. The next developments regarding the data

acquisition control of the Calibration Unit will be carried out at the dedicated setup in the *Bologna Laboratory for User-ports*, which I have arranged for this purpose.

Finally, the thesis illustrates the analysis that I have done to study the pointing of the KM3NeT/ARCA detector, exploiting the atmospheric muon deficit induced by the Moon presence, with data acquired with the detector consisting in 19 and 21 Detection Units. The analysis has initially suggested a mis-pointing of the detector of $\sim 1.6^\circ$ in the azimuth direction, which is consistent with the offset of 1.35° that was estimated independently by the Collaboration and that was assumed as the correction to recover the nominal detector orientation. After the correction of the event tracks by this offset, a significance of the Moon shadow in the expected Moon position of $3.2\,\sigma$ is observed. This is the largest value found when studying the distribution of the significance of the deficit as a function of the applied shift to the azimuth of the events, thus showing a confirmation of the nominal, corrected, pointing of the detector. The uncertainty on the azimuth shift determination has been evaluated via simulations to 0.24°. This analysis has represented a relevant cross-check for the detector pointing evaluation required to assess the correct coordinates of the KM3-230213A event.

Bibliography

[1] Wolfgang Pauli. Pauli letter collection: letter to Lise Meitner. Typed copy; https://cds.cern.ch/record/83282.

[2] Frederick Reines and Clyde L. Cowan. The Neutrino. *Nature*, 178(4531):446–449, 1956. DOI: 10.1038/178446a0.

[3] G. Danby, J. Gaillard, K. Goulianos, L. Lederman, N. Mistry, M. Schwartz, and J. Steinberger. Observation of high-energy neutrino reactions and the existence of two kinds of neutrinos. *Physical Review Letters*, 9:36–44, 1962.

[4] K. Kodama et al. (DONUT Collaboration). Observation of tau neutrino interactions. *Phys. Lett. B*, 504:218–224, 2001. DOI: 10.1016/S0370-2693(01)00307-0.

[5] C. Giunti and W. Kim Chung. *Fundamentals of Neutrino Physics and Astrophysics*. Oxford University Press, 2007.

[6] C.S. Wu, E. Ambler, R.W. Hayward, D.D. Hoppes, and R.P. Hudson. Experimental Test of Parity Conservation in β Decay. *Phys. Rev.*, 105:1413–1414, 1957. DOI: 10.1103/PhysRev.105.1413.

[7] J. A. Formaggio and G. P. Zeller. From eV to EeV: Neutrino cross sections across energy scales. *Rev. Mod. Phys.*, 84:1307–1341, Sep 2012. DOI: 10.1103/RevModPhys.84.1307.

[8] S. Braibant, G. Giacomelli, and M. Spurio. *Particles and Fundamental Interactions*. Springer-Verlag Italia, 2012.

[9] Donald H. Perkins. *Introduction to High Energy Physics*. Cambridge University Press, 2000.

[10] Raj Gandhi, Chris Quigg, Mary Hall Reno, and Ina Sarcevic. Ultrahigh-energy neutrino interactions. *Astropart. Phys.*, 5:81–110, 1996. DOI: 10.1016/0927-6505(96)00008-4.

[11] Markus Ackermann et al. High-energy and ultra-high-energy neutrinos: A Snowmass white paper. *JHEAp*, 36:55–110, 2022. DOI: 10.1016/j.jheap.2022.08.001.

[12] Guo-yuan Huang and Qinrui Liu. Hunting the Glashow Resonance with PeV Neutrino Telescopes. *JCAP*, 03:005, 2020. DOI: 10.1088/1475-7516/2020/03/005.

[13] Sheldon L. Glashow. Resonant Scattering of Antineutrinos. *Phys. Rev.*, 118:316–317, 1960. DOI: 10.1103/PhysRev.118.316.

[14] M. Aartsen et al. (IceCube Collaboration). Transient optical emission from the error box of the γ-ray burst of 28 February 1997. *Nature*, 591(7849):220–224, 2021. DOI: 10.1038/s41586-021-03256-1.

[15] Y. Fukuda and others (Super-Kamiokande Collaboration). Evidence for oscillation of atmospheric neutrinos. *Phys. Rev. Lett.*, 81:1562–1567, 1998. DOI: 10.1103/PhysRevLett.81.1562.

[16] Q.R. Ahmad and others (SNO Collaboration). Direct evidence for neutrino flavor transformation from neutral current interactions in the Sudbury Neutrino Observatory. *Phys. Rev. Lett.*, 89:011301, 2002. DOI: 10.1103/PhysRevLett.89.011301.

[17] B. Pontecorvo. Inverse beta processes and nonconservation of lepton charge. *Sov. Phys. JETP*, 7:172–173, 1958.

[18] Ziro Maki, Masami Nakagawa, and Shoichi Sakata. Remarks on the Unified Model of Elementary Particles. *Progress of Theoretical Physics*, 28(5):870–880, 11 1962. DOI: 10.1143/PTP.28.870.

[19] Thomas K. Gaisser, Ralph Engel, and Elisa Resconi. *Cosmic Rays and Particle Physics*. Cambridge University Press, 2 edition, 2016. DOI: 10.1017/CBO9781139192194.

[20] Marius S. Potgieter. Solar Modulation of Cosmic Rays. *Living Reviews in Solar Physics*, 10:3, 2013. DOI: 10.12942/lrsp-2013-3.

[21] Carmelo Evoli. The cosmic-ray energy spectrum, December 2020. DOI: 10.5281/zenodo.4396125.

[22] Benedetto D'Ettorre Piazzoli, Si-Ming Liu, Domenico della Volpe, Zhen Cao, Andrea Chiavassa, Benedetto D'Ettorre Piazzoli, Yi-Qing Guo, Leonid T. Ksenofontov, Olivier Martineau-Huynh, Diane Martraire, Ling-Ling Ma, Xin-Hua Ma, Yuri Stenkin, Qiang Yuan, Hou-Dun Zeng, Shou-Shan Zhang, Yi Zhang, and Hui Zhu. Chapter 4 cosmic-ray physics. *Chinese Physics C*, 46(3):030004, 2022. DOI: 10.1088/1674-1137/ac3faa.

[23] Mirko Boezio and Emiliano Mocchiutti. Chemical Composition of Galactic Cosmic Rays with Space Experiments. *Astropart. Phys.*, 39-40:95–108, 2012. DOI: 10.1016/j.astropartphys.2012.05.007.

[24] W.V. Zober et al. (CALET Collaboration). Results of the Ultra-Heavy Cosmic-Ray Analysis with CALET on the International Space Station. *PoS*, ICRC2023:088, 2023. DOI: 10.22323/1.444.0088.

[25] M. Spurio. *Probes of Multimessanger Astrophysics*. Springer International Publishing, 2018.

[26] A. Obermeier, P. Boyle, J. Hörandel, and D. Müller. The Boron-to-Carbon abundance ratio and galactic propagation of cosmic radiation. *The Astrophysical Journal*, 752(1):69, May 2012. DOI: 10.1088/0004-637X/752/1/69.

[27] Enrico Fermi. On the Origin of the Cosmic Radiation. *Phys. Rev.*, 75:1169–1174, Apr 1949. DOI: 10.1103/PhysRev.75.1169.

[28] K. Kawata et al. TA Anisotropy Summary. *EPJ Web Conf.*, 210:01004, 2019. DOI: 10.1051/epjconf/201921001004.

[29] O. Deligny, K. Kawata, and P. Tinyakov. Measurement of anisotropy and the search for ultra high energy cosmic ray sources. *PTEP*, 2017(12):12A104, 2017. DOI: 10.1093/ptep/ptx043.

[30] W. Hofmann and J. A. Hinton. *Cosmic Particle Accelerators*. Springer International Publishing, 2020. DOI: 10.1007/978-3-030-34245-6$_1$3.

[31] Kumiko Kotera and Angela V. Olinto. The Astrophysics of Ultrahigh-Energy Cosmic Rays. , 49(1):119–153, September 2011. DOI: 10.1146/annurev-astro-081710-102620.

[32] Arno A. Penzias and Robert Woodrow Wilson. A Measurement of excess antenna temperature at 4080-Mc/s. *Astrophys. J.*, 142:419–421, 1965. DOI: 10.1086/148307.

[33] G.T. Zatsepin and V.A. Kuzmin. Upper limit of the spectrum of cosmic rays. *JETP Lett.*, 4:78–80, 1966.

[34] Kenneth Greisen. End to the Cosmic-Ray Spectrum? *Phys. Rev. Lett.*, 16:748–750, Apr 1966. DOI: 10.1103/PhysRevLett.16.748.

[35] E. W. Mayotte et al. (Pierre Auger Collaboration). Measurement of the mass composition of ultra-high-energy cosmic rays at the Pierre Auger Observatory. *PoS*, ICRC2023:365, 2023. DOI: 10.22323/1.444.0365.

[36] Antonella Castellina (on behalf of the Pierre Auger Collaboration). AugerPrime: the Pierre Auger Observatory Upgrade. *EPJ Web Conf.*, 210:06002, 2019. DOI: 10.1051/epjconf/201921006002.

[37] Jakob Boettcher et al. (IceCube Collaboration). Search for the Prompt Atmospheric Neutrino Flux in IceCube. *PoS*, ICRC2023:1068, 2023. DOI: 10.22323/1.444.1068.

[38] A. Albert et al. (ANTARES Collaboration). Measurement of the atmospheric ν_e and ν_μ energy spectra with the ANTARES neutrino telescope. *Phys. Lett. B*, 816:136228, 2021. DOI: 10.1016/j.physletb.2021.136228.

[39] E. Richard et al. (Super-Kamiokande Collaboration). Measurements of the atmospheric neutrino flux by super-kamiokande: Energy spectra, geomagnetic effects, and solar modulation. *Phys. Rev. D*, 94:052001, Sep 2016. DOI: 10.1103/PhysRevD.94.052001.

[40] M. G. Aartsen et al. (IceCube Collaboration). Measurement of the ν_μ energy spectrum with icecube-79 - icecube collaboration. *Eur. Phys. J. C*, 77(10):692, 2017. DOI: 10.1140/epjc/s10052-017-5261-3.

[41] S. Adrian-Martinez et al. (ANTARES Collaboration). Measurement of the atmospheric ν_μ energy spectrum from 100 GeV to 200 TeV with the ANTARES telescope. *Eur. Phys. J. C*, 73(10):2606, 2013. DOI: 10.1140/epjc/s10052-013-2606-4.

[42] Andrea Palladino, Maurizio Spurio, and Francesco Vissani. Neutrino Telescopes and High-Energy Cosmic Neutrinos. *Universe*, 6(2):30, 2020. DOI: 10.3390/universe6020030.

[43] E. Yen. New Scaling Variable and Early Scaling in Single Particle Inclusive Distributions for Hadron-Hadron Collisions. *Phys. Rev. D*, 10:836, 1974. DOI: 10.1103/PhysRevD.10.836.

[44] Silvia Celli, Andrea Palladino, and Francesco Vissani. Neutrinos and γ-rays from the Galactic Center Region after H.E.S.S. multi-TeV measurements. *Eur. Phys. J. C*, 77(2):66, 2017. DOI: 10.1140/epjc/s10052-017-4635-x.

[45] S. Aiello et al. (KM3NeT Collaboration). Sensitivity of the KM3NeT/ARCA neutrino telescope to point-like neutrino sources. *Astropart. Phys.*, 111:100–110, 2019. DOI: 10.1016/j.astropartphys.2019.04.002.

[46] Zhen Cao et al. (LHAASO Collaboration). Ultrahigh-energy photons up to 1.4 petaelectronvolts from 12 γ-ray Galactic sources. , 594(7861):33–36, June 2021. DOI: 10.1038/s41586-021-03498-z.

[47] Zhen Cao et al. (LHAASO Collaboration). The First LHAASO Catalog of Gamma-Ray Sources. *Astrophys. J. Suppl.*, 271(1):25, 2024. DOI: 10.3847/1538-4365/acfd29.

[48] Eli Waxman and John N. Bahcall. High-energy neutrinos from astrophysical sources: An Upper bound. *Phys. Rev. D*, 59:023002, 1999. DOI: 10.1103/PhysRevD.59.023002.

[49] M. G. Aartsen et al. (IceCube Collaboration). Differential limit on the extremely-high-energy cosmic neutrino flux in the presence of astrophysical background from nine years of IceCube data. *Phys. Rev. D*, 98(6):062003, 2018. DOI: 10.1103/PhysRevD.98.062003.

[50] R. Aloisio, D. Boncioli, A di Matteo, A. F. Grillo, S. Petrera, and F. Salamida. Cosmogenic neutrinos and ultra-high energy cosmic ray models. *JCAP*, 10:006, 2015. DOI: 10.1088/1475-7516/2015/10/006.

[51] Ofelia Pisanti. Cosmic Neutrinos. *PoS*, NuFact2017:024, 2017. DOI: 10.22323/1.295.0024.

[52] S. Aiello et al. (KM3NeT Collaboration). Observation of an ultra-high-energy cosmic neutrino with KM3NeT. *Nature*, 638(8050):376–382, 2025. DOI: 10.1038/s41586-024-08543-1.

[53] R. Abbasi et al. (IceCube Collaboration). Improved Characterization of the Astrophysical Muon–neutrino Flux with 9.5 Years of IceCube Data. *Astrophys. J.*, 928(1):50, 2022. DOI: 10.3847/1538-4357/ac4d29.

[54] M. G. Aartsen et al. (IceCube Collaboration). Evidence for High-Energy Extraterrestrial Neutrinos at the IceCube Detector. *Science*, 342:1242856, 2013. DOI: 10.1126/science.1242856.

[55] M.G. Aartsen et al. (IceCube Collaboration). The IceCube Neutrino Observatory - Contributions to ICRC 2017 Part II: Properties of the Atmospheric and Astrophysical Neutrino Flux. *ArXiv: 1710.01191*, 10 2017.

[56] M. G. Aartsen et al. (IceCube Collaboration). Characteristics of the diffuse astrophysical electron and tau neutrino flux with six years of IceCube high energy cascade data. *Phys. Rev. Lett.*, 125(12):121104, 2020. DOI: 10.1103/PhysRevLett.125.121104.

[57] R. Abbasi et al. (IceCube Collaboration). Characterization of the astrophysical diffuse neutrino flux using starting track events in IceCube. *Phys. Rev. D*, 110(2):022001, 2024. DOI: 10.1103/PhysRevD.110.022001.

[58] Richard Naab, Erik Ganster, and Zelong (on behalf of the IceCube Collaboration) Zhang. Measurement of the astrophysical diffuse neutrino flux in a combined fit of IceCube's high energy neutrino data. In *38th International Cosmic Ray Conference*, 7 2023.

[59] A. Albert et al. (ANTARES Collaboration). All-flavor Search for a Diffuse Flux of Cosmic Neutrinos with Nine Years of ANTARES Data. *Astrophys. J. Lett.*, 853(1):L7, 2018. DOI: 10.3847/2041-8213/aaa4f6.

[60] V. A. Allakhverdyan et al. (BAIKAL-GVD Collaboration). Diffuse neutrino flux measurements with the Baikal-GVD neutrino telescope. *Phys. Rev. D*, 107(4):042005, 2023. DOI: 10.1103/PhysRevD.107.042005.

[61] M.G. Aartsen et al. (IceCube, Fermi-LAT, MAGIC, AGILE, ASAS-SN, HAWC, H.E.S.S., INTEGRAL, Kanata, Kiso, Kapteyn, Liverpool Telescope, Subaru, Swift NuSTAR, VERITAS, VLA/17B-403 Collaborations). Multimessenger observations of a flaring blazar coincident with high-energy neutrino IceCube-170922A. *Science*, 361(6398):eaat1378, 2018. DOI: 10.1126/science.aat1378.

[62] M.G. Aartsen et al. (IceCube Collaboration). Neutrino emission from the direction of the blazar TXS 0506+056 prior to the IceCube-170922A alert. *Science*, 361(6398):147–151, 2018. DOI: 10.1126/science.aat2890.

[63] R. Abbasi et al. (IceCube Collaboration). Evidence for neutrino emission from the nearby active galaxy NGC 1068. *Science*, 378(6619):538–543, 2022. DOI: 10.1126/science.abg3395.

[64] Robert Stein et al. A tidal disruption event coincident with a high-energy neutrino. *Nature Astron.*, 5(5):510–518, 2021. DOI: 10.1038/s41550-020-01295-8.

[65] Simeon Reusch et al. Candidate Tidal Disruption Event AT2019fdr Coincident with a High-Energy Neutrino. *Phys. Rev. Lett.*, 128(22):221101, 2022. DOI: 10.1103/PhysRevLett.128.221101.

[66] Sjoert van Velzen et al. Establishing accretion flares from supermassive black holes as a source of high-energy neutrinos. *Mon. Not. Roy. Astron. Soc.*, 529(3):2559–2576, 2024. DOI: 10.1093/mnras/stae610.

[67] EMODnet Bathymetry Consortium. EMODnet Digital Bathymetry (DTM 2022), 2022. DOI: 10.12770/ff3aff8a-cff1-44a3-a2c8-1910bf109f85.

[68] B.P. Abbott et al.(LIGO, Virgo Collaborations). Observation of Gravitational Waves from a Binary Black Hole Merger. *Phys. Rev. Lett.*, 116(6):061102, 2016. DOI: 10.1103/PhysRevLett.116.061102.

[69] B.P. Abbott et al. (LIGO Scientific, Virgo, Fermi GBM, INTEGRAL, IceCube, AstroSat Cadmium Zinc Telluride Imager Team, IPN, Insight-Hxmt, ANTARES, Swift, AGILE Team, 1M2H Team, Dark Energy Camera GW-EM, DES, DLT40, GRAWITA, Fermi-LAT, ATCA, ASKAP, Las Cumbres Observatory Group, OzGrav, DWF (Deeper Wider Faster Program), AST3, CAASTRO, VINROUGE, MASTER, J-GEM, GROWTH, JAGWAR, CaltechNRAO, TTU-NRAO, NuSTAR, Pan-STARRS, MAXI Team, TZAC Consortium, KU, Nordic Optical Telescope, ePESSTO, GROND, Texas Tech University, SALT Group, TOROS, BOOTES, MWA, CALET, IKI-GW Follow-up, H.E.S.S., LOFAR, LWA, HAWC, Pierre Auger, ALMA, Euro VLBI Team, Pi of Sky, Chandra Team at McGill University, DFN, ATLAS Telescopes, High Time Resolution Universe Survey, RIMAS, RATIR, SKA South Africa/MeerKAT Collaborations). Multi-messenger Observations of a Binary Neutron Star Merger. *Astrophys. J. Lett.*, 848(2):L12, 2017. DOI: 10.3847/2041-8213/aa91c9.

[70] A. Albert et al. (ANTARES, IceCube, Pierre Auger, LIGO Scientific, Virgo Collaborations). Search for High-energy Neutrinos from Binary Neutron Star Merger GW170817 with ANTARES, IceCube, and the Pierre Auger Observatory. *Astrophys. J. Lett.*, 850(2):L35, 2017. DOI: 10.3847/2041-8213/aa9aed.

[71] A. Albert et al. (ANTARES Collaboration). Search for neutrino counterparts to the gravitational wave sources from LIGO/Virgo O3 run with the ANTARES detector. *JCAP*, 04:004, 2023. DOI: 10.1088/1475-7516/2023/04/004.

[72] R. Abbasi et al. (IceCube Collaboration). IceCube Search for Neutrinos Coincident with Gravitational Wave Events from LIGO/Virgo Run O3. *Astrophys. J.*, 944(1):80, 2023. DOI: 10.3847/1538-4357/aca5fc.

[73] M.A. Markov. On high energy neutrino physics. In *10th International Conference on High Energy Physics*, pages 578–581, 1960.

[74] J. Babson et al. (DUMAND Collaboration). Cosmic ray muons in the deep ocean. *Nucl. Phys. B Proc. Suppl.*, 14:157–161, 1990. DOI: 10.1016/0920-5632(90)90413-O.

[75] V. Ayutdinov et al. (BAIKAL-GVD Collaboration). Results from the BAIKAL Neutrino Telescope. In *28th International Cosmic Ray Conference*, 5 2003.

[76] A. Karle (on behalf of the AMANDA Collaboration). The Path from AMANDA to IceCube. *Proc. IAU Symposium 288, Astrophysics from Antarctica*, 2012. DOI: 10.1017/S1743921312016730.

[77] Thomas Gaisser and Francis Halzen. IceCube. *Annual Review of Nuclear and Particle Science*, 64(1):101–123, 2014. DOI: 10.1146/annurev-nucl-102313-025321.

[78] M. Ageron et al. (ANTARES Collaboration). ANTARES: the first undersea neutrino telescope. *Nucl. Instrum. Meth. A*, 656:11–38, 2011. DOI: 10.1016/j.nima.2011.06.103.

[79] T. Chiarusi and M. Spurio. High-Energy Astrophysics with Neutrino Telescopes. *Eur. Phys. J. C*, 65:649–701, 2010. DOI: 10.1140/epjc/s10052-009-1230-9.

[80] M. G. Aartsen et al. (IceCube Collaboration). Measurement of the multi-TeV neutrino cross section with IceCube using Earth absorption. *Nature*, 551:596–600, 2017. DOI: 10.1038/nature24459.

[81] William R. Leo. *Techniques for Nuclear and Particle Physics Experiments*. Springer-Verlag Berlin Heidelberg, 1994.

[82] KM3NeT: Conceptual Design Report. `https://www.km3net.org/wp-content/uploads/2015/07/CDR-KM3NeT.pdf`.

[83] Juan Pablo Yáñez Garza. *Measurement of neutrino oscillations in atmospheric neutrinos with the IceCube DeepCore detector*. PhD thesis, Humboldt-Universität zu Berlin, Mathematisch-Naturwissenschaftliche Fakultät I, 2014. DOI: 10.18452/17016.

[84] Donald E. Groom, Nikolai V. Mokhov, and Sergei I. Striganov. Muon stopping power and range tables 10 mev–100 tev. *Atomic Data and Nuclear Data Tables*, 78(2):183–356, 2001. DOI: 10.1006/adnd.2001.0861.

[85] Evangelia Drakopoulou, Christos Markou, and Ekaterini Tzamariudaki (on behalf of the KM3NeT Collaboration). Muon and Neutrino Energy Reconstruction for KM3NeT. *PoS*, NEUTEL2015:071, 01 2016. DOI: 10.22323/1.244.0071.

[86] KM3NeT Website, `https://www.km3net.org`.

[87] S. Adrian-Martinez et al. (KM3NeT Collaboration). Letter of intent for KM3NeT 2.0. *J. Phys. G*, 43(8):084001, 2016. DOI: 10.1088/0954-3899/43/8/084001.

[88] S. Aiello et al. (KM3NeT Collaboration). The KM3NeT multi-PMT optical module. *JINST*, 17(07):P07038, 2022. DOI: 10.1088/1748-0221/17/07/P07038.

[89] S. Aiello et al. (KM3NeT Collaboration). The Power Board of the KM3NeT Digital Optical Module: design, upgrade, and production. *Electronics*, 13(11):2044, 2024. DOI: 10.3390/electronics13112044.

[90] A. Margiotta (on behalf of the KM3NeT Collaboation). Status of the KM3NeT project. *JINST*, 9:C04020, 2014. DOI: 10.1088/1748-0221/9/04/C04020.

[91] S. Aiello et al. (KM3NeT Collaboration). Characterisation of the Hamamatsu photomultipliers for the KM3NeT Neutrino Telescope. *JINST*, 13(05):P05035, 2018. DOI: 10.1088/1748-0221/13/05/P05035.

[92] Clara Gatius Oliver, Félix Bretaudeau, Maarten De Jong, and Lilian Martin (on behalf of the KM3NeT Collaboration). Dynamical position and orientation calibration of the KM3NeT telescope. *PoS*, ICRC2023:1033, 2023. DOI: 10.22323/1.444.1033.

[93] D. Calvo and D. Real (on behalf of the KM3NeT Collaboration). Status of the central logic board (CLB) of the KM3NeT neutrino telescope. *Journal of Instrumentation*, 10(12):C12027, dec 2015. DOI: 10.1088/1748-0221/10/12/C12027.

[94] D. Calvo and D. Real (on behalf of the KM3NeT Collaboration). The new CLBv4 for the KM3NeT Neutrino Telescope. *EPJ Web of Conferences*, 207:06003, 01 2019. DOI: 10.1051/epjconf/201920706003.

[95] Glenair website, `https://www.glenair.com/`.

[96] S. Aiello et al. (KM3NeT Collaboration). Deep-sea deployment of the km3net neutrino telescope detection units by self-unrolling. *Journal of Instrumentation*, 15(11):P11027, nov 2020. DOI: 10.1088/1748-0221/15/11/P11027.

[97] Rene Brun and Fons Rademakers. ROOT - An Object Oriented Data Analysis Framework. *Nucl. Inst. Meth. in Phys. Res.*, 389:81–86, 1997.

[98] S. Aiello et al. (KM3NeT Collaboration). The control unit of the km3net data acquisition system. *Computer Physics Communications*, 256:107433, 2020. DOI: 10.1016/j.cpc.2020.107433.

[99] White Rabbit website, `http://www.ohwr.org/projects/white-rabbit`.

[100] B. Bakker. Trigger studies for the Antares and KM3NeT neutrino telescopes. *Master thesis*, 2011.

[101] Francesco Benfenati, Francesco Filippini, and Tommaso Chiarusi (on behalf of the KM3NeT Collaboration). First scientific results of the km3net neutrino telescope. *EPJ Web of Conferences*, 283:04009, 04 2023. DOI: 10.1051/epjconf/202328304009.

[102] Rasa Muller, Aart Heijboer, and Thijs van Eeden (on behalf of the KM3NeT Collaboration). Search for cosmic neutrino point sources and extended sources with 6-21 lines of KM3NeT/ARCA. *PoS*, ICRC2023:1018, 2023. DOI: 10.22323/1.444.1018.

[103] S. Aiello et al. (KM3NeT Collaboration). Astronomy potential of KM3NeT/ARCA. *Eur. Phys. J. C*, 84(9):885, 2024. DOI: 10.1140/epjc/s10052-024-13137-2.

[104] Rosa Coniglione, Alexandre Creusot, Irene Palma, Daniel Guderian, Jannik Hofestaedt, Giorgio Riccobene, and Agustín Sánchez-Losa (on behalf of the KM3NeT Collaboration). KM3NeT Time Calibration. *PoS*, ICRC2019:868, 07 2019. DOI: 10.22323/1.358.0868.

[105] Salvatore Viola, Miguel Ardid, Vincent Bertin, Robert Lahmann, Carmelo Pellegrino, Giorgio Riccobene, Maria Saldaña, Piera Sapienza, and Francesco Simeone (on behalf of the KM3NeT Collaboration). Acoustic positioning system for KM3NeT. page 1169, 08 2016. DOI: 10.22323/1.236.1169.

[106] Maciej Lipinski, Tomasz Wlostowski, Javier Serrano, and Pablo Alvarez. White rabbit: a ptp application for robust sub-nanosecond synchronization. pages 25 – 30, 10 2011. DOI: 10.1109/ISPCS.2011.6070148.

[107] Karel Melis (on behalf of the KM3NeT Collaboration). In-Situ Calibration of KM3NeT. *PoS*, ICRC2017:1059, 08 2017. DOI: 10.22323/1.301.1059.

[108] Louis Bailly-Salins (on behalf of the KM3NeT Collaboration). Time, position and orientation calibration using atmospheric muons in KM3NeT. *PoS*, ICRC2023:218, 2023. DOI: 10.22323/1.444.0218.

[109] Agustín Sánchez Losa, Juan Palacios Gonzalez, Francisco Salesa Greus, Juan Zúñiga Román, Diego Real Máñez, and David Calvo Díaz-Aldagalán (on behalf of the KM3NeT Collaboration). KM3NeT Time calibration with Nanobeacons. *PoS*, ICRC2023:1062, 2023. DOI: 10.22323/1.444.1062.

[110] White Rabbit calibration application note 1, Q. Genoud, A. Wucjek, M. Lipinski, T. Chiarusi, F. Benfenati, `https://ohwr.org/project/white-rabbit/-/wikis/Documents/White-Rabbit-calibration-procedure`.

[111] White Rabbit calibration procedure, v.1.1, G. Daniluk, `https://ohwr.org/project/white-rabbit/-/wikis/Documents/White-Rabbit-calibration-procedure`.

[112] C. M. Mollo et al. A new instrument for high statistics measurement of photomultiplier characteristics. *JINST*, 11(08):T08002, 2016. DOI: 10.1088/1748-0221/11/08/T08002.

[113] S. Adrián-Martínez et al. (ANTARES Collaboration). The positioning system of the ANTARES Neutrino Telescope. *Journal of Instrumentation*, 7(8):T08002, August 2012. DOI: 10.1088/1748-0221/7/08/T08002.

[114] Chen-Tung Arthur Chen and Frank J. Millero. Speed of sound in seawater at high pressures. *The Journal of the Acoustical Society of America*, 62(5):1129–1135, 11 1977. DOI: 10.1121/1.381646.

[115] Viola, Salvatore (on behalf of the KM3NeT Collaboration). KM3NeT acoustic positioning and detection system. *EPJ Web Conf.*, 216:02006, 2019. DOI: 10.1051/epjconf/201921602006.

[116] Dídac D. Tortosa (on behalf of the KM3NeT Collaboration). Mechanical Line Fit Model to Monitor the Position of KM3NeT Optical Modules from the Acoustic and Compass/Accelerometer Sensor System Data. *Proceedings*, 42(1), 2020. DOI: 10.3390/ecsa-6-06583.

[117] Diego-Tortosa D. Martínez-Mora J.A. Ardid M., Bou-Cabo M. and Poirè C. (on behalf of the KM3NeT Collaboration). Underwater Acoustic Positioning System for the Monitoring of KM3NeT Optical Modules. *Proceedings of the INTER-NOISE19, Madrid, Spain, 16–19 June 2019*, 06 2019.

[118] Teledyne ODI website: http://www.teledynemarine.com/odi.

[119] NORSOK standard documentation: https://online.standard.no.

[120] Dídac Diego-Tortosa, Miguel Ardid, Manuel Bou-Cabo, Guillermo Lara, and Juan A. Martínez-Mora (on behalf of the KM3NeT Collaboration). Development of a Trigger for Acoustic Neutrino Candidates in KM3NeT. *PoS*, ARENA2022:060, 2023. DOI: 10.22323/1.424.0060.

[121] European Broadcast Union. NORSOK standard documentation: https://tech.ebu.ch/docs/tech/tech3250.pdf.

[122] Mediterraneo Senales Maritimas website: https://mesemar.com/en/home/.

[123] GISMA website: https://www.gisma-connectors.de/.

[124] EMSO website: https://emso.eu/.

[125] Seabird website: https://www.seabird.com/.

[126] Valeport website: https://www.valeport.co.uk/.

[127] Aandera website: https://www.aanderaa.com/.

[128] Paroscientific website: https://paroscientific.com/.

[129] KM3NeT/ARCA Calibration Base power and optics measurements: https://github.com/francescobenfenati/KM3NeT-ARCA-I.U.-devices/tree/main/power_measurements.

[130] M. Ambrosio et al. Moon and sun shadowing effect in the macro detector. *Astroparticle Physics*, 20(2):145–156, 2003. DOI: 10.1016/S0927-6505(03)00169-5.

[131] P. Achard et al. Measurement of the shadowing of high-energy cosmic rays by the moon: A search for tev-energy antiprotons. *Astroparticle Physics*, 23(4):411–434, 2005. DOI: 10.1016/j.astropartphys.2005.02.002.

[132] P. Adamson et al. Observation in the minos far detector of the shadowing of cosmic rays by the sun and moon. *Astroparticle Physics*, 34(6):457–466, 2011. DOI: 10.1016/j.astropartphys.2010.10.010.

[133] B. Bartoli and others (ARGO-YBJ Collaboration). Observation of the cosmic ray moon shadowing effect with the argo-ybj experiment. *Phys. Rev. D*, 84:022003, Jul 2011. DOI: 10.1103/PhysRevD.84.022003.

[134] Daniel W. Fiorino, Segev Benzvi, and James Braun (on behalf of the HAWC Collaboration). Observation of the Moon Shadow and Characterization of the Point Response of HAWC-30. In *International Cosmic Ray Conference*, volume 33 of *International Cosmic Ray Conference*, page 2715, January 2013.

[135] M. G. Aartsen et al. (IceCube Collaboration). Observation of the cosmic-ray shadow of the Moon with IceCube. *Phys. Rev. D*, 89(10):102004, 2014. DOI: 10.1103/PhysRevD.89.102004.

[136] A. Albert et al. (ANTARES Collaboration). The cosmic ray shadow of the Moon observed with the ANTARES neutrino telescope. *Eur. Phys. J. C*, 78(12):1006, 2018. DOI: 10.1140/epjc/s10052-018-6451-3.

[137] S. Aiello et al. (KM3NeT Collaboration). First observation of the cosmic ray shadow of the Moon and the Sun with KM3NeT/ORCA. *Eur. Phys. J. C*, 83(4):344, 2023. DOI: 10.1140/epjc/s10052-023-11401-5.

[138] Adrian Price-Whelan et al. Astropy Collaboration. The Astropy Project: Sustaining and Growing a Community-oriented Open-source Project and the Latest Major Release (v5.0) of the Core Package. *ApJ*, 935(2):167, August 2022. DOI: 10.3847/1538-4357/ac7c74.

[139] G. Carminati et al. MUPAGE: a fast atmospheric MUon GEnerator for neutrino telescopes based on PArametric formulas. *Computer Physics Communications*, 179(12):915–923, 2008. DOI: 10.1016/j.cpc.2008.07.014.

[140] J. T. Gosling. *Interplanetary magnetic field*, pages 342–342, in Encyclopedia of Planetary Science. Springer Netherlands, Dordrecht, 1997. DOI: 10.1007/1-4020-4520-4_189.

[141] Steve Baker and Robert D. Cousins. Clarification of the use of CHI-square and likelihood functions in fits to histograms. *Nuclear Instruments and Methods in Physics Research*, 221(2):437–442, 1984.

[142] F. James. *Statistical Methods in Experimental Physics*. World Scientific, 2006.

[143] G. Cowan. *Statistical data analysis*. Oxford University Press, USA, 1998.